UNIVERSITÉ DE SHERBROOKE

Faculté de génie

Département de génie électrique et de génie informatique

ON THE ORIGIN OF UV LASER-INDUCED QUANTUM WELL INTERMIXING IN III-V SEMICONDUCTOR HETEROSTRUCTURES

SUR L'ORIGINE DE L'INTERDIFFUSION DE PUITS QUANTIQUES PAR LASER UV DANS DES HETEROSTRUCTURES DE SEMI-CONDUCTEURS III-V

Thèse de Doctorat

Spécialité : Génie électrique

Neng LIU

Jury: Prof. Jan J. DUBOWSKI (directeur)

Prof. Vincent AIMEZ (Rapporteur)

Prof. Amr S. HELMY

Prof. J. Thomas DICKINSON

Sherbrooke (Québec), Canada 10/2013

SUMMARY

Photonic integrated circuits (PICs) which combine photonic devices for generation, detection, modulation, amplification, switching and transport of light on a chip have been reported as a significant technology innovation that simplifies optical system design, reduces space and power consumption, improves reliability. The ability of selective area modifying the bandgap for different photonic devices across the chip is the important key for PICs development. Compared with other growth methods, quantum well intermixing (QWI) has attracted amounts of interest due to its simplicity and effectiveness in tuning the bandgap in post-growth process. However, QWI has suffered problems of lack of precision in achieving targeted bandgap modification and uncontrollable up-taking of impurities during process which possibly degrade the quality of intermixed material.

In this thesis, we have employed excimer laser to create surface defects in the near surface region (~ 10 nm) of III-V e.g. InP and GaAs, based QW microstructure and then annealing to induce intermixing. The irradiation by ArF and KrF excimer lasers on the QW microstructure was carried out surrounded by different environments, including air, DI water, dielectric layers (SiO_2 and Si_3N_4) and InO_x coatings. To propose a more controllable UV laser QWI technique, we have studied surface defects generation and diffusion with various surface/interface characterization methods, like AFM, SEM, XPS and SIMS, which were used to analyse the QW surface/interface morphology and chemical modification during QWI. The quality of processed QW microstructure was represented by photoluminescence measurements and luminescence measurements of fabricated laser diodes.

The results shows that excimer laser induced amounts of surface oxides on the InP/InGaAs/InGaAsP microstructure surface in air and the oxygen impurities from oxides layer diffused to the active region of the QW microstructure during annealing, which enhance intermixing but also reduce the PL intensity. When irradiated in DI water environment, no obvious excessive oxygen impurities were found to diffuse to the active regions and the surface stoichiometry has been restored after intermixing. InO_x with large coefficient of thermal expansion was found inside the intermixed QW microstructure, which was supposed

to increase the compressive strain in active region and enhance the PL intensity to maximum 10 times on sample irradiated in DI water.

On microstructure coated with dielectric layers, bandgap modifications were always found on samples whose dielectric layers were ablated and InP surface was modified by excimer laser. On sample coated with 243 nm SiO_2 layer, the PL shifts were found on sample without ablation of the SiO_2 layer when irradiated by KrF laser. However, the InP interface morphology was modified, interface oxides were generated and oxygen impurities have diffused inside on the irradiated sites. The enhancements of interdiffusion on both non irradiated and irradiated sites of sample coated with InO_x layer have verified the importance of oxides in QWI.

The laser diodes fabricated from KrF laser intermixed material have shown comparable threshold current density with as grown material with PL shifted by 133 nm. Combined aluminum mask, we have created uniform 70 nm PL shifts on 40 μm x 200 μm rectangle arrays which presents UV laser QWI potential application in PICs.

In addition, excimer lasers have been used to create self organized nano-cone structures on the surface of InP/InGaAs/InGaAsP microstructure and enhance the PL intensity by ~1.4x. Excimer lasers have selective area modified wettability of silicon surface based on laser induced surface chemical modification in different liquid environments. Then the fluorescence nanospheres succeeded to specific pattern functions with silicon surface.

Key words: quantum well intermixing, excimer laser, InP/InGaAs/InGaAsP microstructure, XPS, SIMS

RÉSUMÉ

Les circuits photoniques intégrés qui combinent des dispositifs photoniques pour la génération, la détection, la modulation, l'amplification, la commutation et le transport de la lumière dans une puce, ont été rapportés comme étant une innovation technologique importante qui simplifie la conception du système optique et qui réduit l'espace et la consommation de l'énergie en améliorant ainsi la fiabilité. La capacité de modifier la bande interdite des zones sélectives des différents dispositifs photoniques à travers la puce est la clé majeure pour le développement de circuits photoniques intégrés. Comparé à d'autres méthodes d'épitaxie, l'interdiffusion de puits quantiques a attiré beaucoup d'intérêt en raison de sa simplicité et son efficacité en accordant la bande interdite durant le processus de post-épitaxie. Cependant, l'interdiffusion de puits quantiques a subi des problèmes reliés au manque de précision pour modifier convenablement la bande interdite ciblée et à l'incontrôlabilité de l'absorption des impuretés au cours du processus qui peut dégrader la qualité du matériel interdiffusé.

Dans cette thèse, nous avons utilisé les lasers excimer pour créer des défauts à proximité de la surface (~ 10 nm) des microstructures à base de puits quantiques III-V (par exemple InP et GaAs) et pour induire l'interdiffusion après le recuit thermique. L'irradiation par les lasers excimer (ArF et KrF) des microstructures à puits quantiques a été réalisée dans différents environnements, y compris l'air, l'eau déionisée, les couches diélectriques (SiO_2 et Si_3N_4) et les couches d'InO_x. Pour proposer un bon contrôle de la technique d'interdiffusion de puits quantiques par laser excimer, nous avons étudié la génération et la diffusion de défauts de surface en utilisant différentes méthodes de caractérisation de surface/interface, comme l'AFM, SEM, XPS et SIMS qui ont été utilisées pour analyser la modification de la morphologie de surface/interface et la modification chimique de la microstructure de ces puits quantiques. La qualité des microstructures à puits quantiques étudiées a été représentée par des mesures de photoluminescence et de luminescence des diodes lasers ainsi fabriqués.

Les résultats montrent que le laser excimer induit des quantités d'oxydes de surface dans les surfaces des microstructure à puits quantiques InP/InGaAs/InGaAsP dans l'air et des

impuretés d'oxygène des couches d'oxydes diffusées dans la région active de la microstructure lors du recuit, ce qui améliore l'interdiffusion mais réduit l'intensité de la photoluminescence. Par contre, l'irradiation dans un environnement d'eau déionisée n'a pas démontrée de diffusion des impuretés évidentes d'un excès d'oxygène vers les régions actives mais la stœchiométrie de surface a été restaurée après l'interdiffusion. L'InO_x a été trouvé avec un grand coefficient de dilatation thermique dans la microstructure interdiffusé qui était supposé d'augmenter la contrainte de compression dans la région active et ainsi d'augmenter l'intensité de photoluminescence de 10 fois dans l'échantillon irradié dans l'eau déionisée.

Concernant les microstructures avec une couche diélectrique, la modification de la bande interdite a été toujours réalisé sur des échantillons dont les couches diélectriques été irradié et la surface de InP a été modifié par le laser excimer. Pour l'échantillon avec une couche de 243 nm de SiO_2, les variations de la photoluminescence été mesurées sans l'ablation de cette couche de SiO_2 lors de l'irradiation par le laser KrF. Cependant, la morphologie de l'interface d'InP a été modifiée, les oxydes d'interface ont été générés et les impuretés d'oxygène se sont diffusées à l'intérieur des surfaces irradiées. Les améliorations de l'interdiffusion dans les deux surfaces non irradiées et irradiés de l'échantillon couvert de couche d'InO_x ont démontré l'importance des oxydes dans l'interdiffusion des puits quantiques.

Les diodes laser fabriquées à partir d'un matériau interdiffusé par un laser KrF ont montré un seuil de courant comparable à celui des matériaux non interdiffusés avec un décalage de photoluminescence de 100 nm. En combinant un masque d'aluminium, nous avons créé un déplacement uniforme de photoluminescence de 70 nm sur une matrice rectangulaire de 40 µm x 200 µm ce qui présente un potentiel d'application de l'interdiffusion des puits quantiques par les lasers excimer dans les circuits photoniques intégrés.

En outre, les lasers excimer été utilisés pour créer des structures de nano-cônes auto-organisées sur des surfaces de microstructure de InP/InGaAs/InGaAsP en augmentant l'intensité de PL par ~ 1.4 fois. Les lasers excimer ont été aussi utilisés pour modifier la mouillabilité sélective des zones d'une surface de silicium par une modification chimique de surface induite par laser dans différents milieux liquides. Ainsi, la fluorescence des

nanosphères a été réussie pour des fonctions de configuration spécifique avec une surface de silicium.

Mots clés: Interdiffusion de puits quantiques, laser excimer, microstructure InP/InGaAs/InGaAsP, XPS, SIMS

Acknowledgements

Firstly, I would like to thank sincerely to my thesis advisors Jan J. Dubowski, Professor from the Département de génie électrique et génie informatiques of the Université de Sherbrooke, for the quality of his patient, nice and professional supervision. His unconditional support and the experience and knowledge he shared with me insured the success of the different phases of my work. Without his guidance and encouragements, I would never have finished my PhD thesis.

I would also like to express my deepest thanks to Professor Tom Dickinson, from Department of Physics, in Washington State University, Professor Amr S. Helmy from Department of Electrical and Computer engineering of the University of Toronto, and Professor Vicent Aimez from Département de génie électrique et génie informatiques, Université de Sherbrooke for managing time to read the whole thesis exhaustively.

I would like to thank Professor JJ He of Zhejiang University, in China, who recommended me come to Université de Sherbrooke for my PhD studying. In addition, thanks to his discussion with me of some collaboration projects during my PhD projects.

I would like express gratitude to Dr Khalid Moumanis, the manager of the laboratory for Quantum Semiconductors and Photon-based BioNanotechnology, who helped and encouraged me when I met difficulties in my PhD studying. Many thanks to all the previous and present colleagues in my group for their friendly discussions and helps.

I would like to thank all the technicians in Centre de Caractérisation des Matériaux (CCM) of Université de Sherbrooke, especially Sonia Blais, who has taught me a lot about XPS. I would like to thank the technicians in École Polytechnique Laboratoire de service pour analysis de surface des materiaux, Montréal, especially Suzie Poulin, who helped me to collect SIMS measurements.

I also thank the rest of the academic and support staff of the previous Centre de recherche en nanofabrication et nanocaractérisation (CRN2) and present Interdisciplinary Institute for Technological Innovation (3IT) at the Université de Sherbrooke as well as the other

undergraduate and graduated students with whom I had the chance to interact during the last five years.

I thank the Merit Scholarship Program for Foreign Student, Fonds de recherche du Québec - Nature et technologies, for providing a graduate student scholarship.

I would like to thank all my Chinese friends in Sherbrooke during last five years, no matter wherever you are. You have given me a lot of happiness during my staying in Sherbrooke.

Finally, I would like to say sincerely 'Thank you' to my family in China. Thanks for their continuous encouragement during last five years.

Neng

October, 2013

Table of Contents

SUMMARY i
RÉSUMÉ iii
Acknowledgements vi
Table of Contents viii
List of Figures xi
List of Tables xvi
Chapter 1 Introduction 1
1.1 Photonic integrated circuits 1
1.2 UV laser QWI 4
1.3 Project description 6
1.4 Contribution of this research 7
1.5 Thesis Structure 9
1.6 Bibliography 10
Chapter 2 Background information 13
2. 1 Laser-matter interaction 13
2.1.1 Laser induced temperature estimation 14
2.1.2 Laser induced surface morphology modification 19
2.1.3 Laser induced surface chemical modification 23
2.2 Quantum well intermixing 25
2.2.1 General considerations 25
2.2.2 Quantum semiconductor 26
2.2.3 Principle of quantum well intermixing 28
2.2.4 Point defects influence on QWI 29
2.2.5 Strain influence on QWI 33
2.3 Summary 40
2.4 Bibliography 41
Chapter 3 Experimental Procedures 48
3.1 Excimer laser irradiation techniques 48
3.1.1 Excimer lasers and beam homogenization 48
3.1.2 Sample chamber and positioning 50
3.2 Studied heterostructures 51
3.2.1 InP based full laser QW microstructure 51
3.2.2 RAC82: InP based QW microstructure with shallow cap region 52
3.2.3 T0808: InGaAsP/GaAs QW microstructure 53
3.3 Rapid thermal annealing 54
3.4 Characterization methods 55
3.4.1 Photoluminescence measurements 55
3.4.2 Surface Morphology Characterization 57
3.4.3 Surface and interface chemical characterization 62
3.5 Summary 71
3.6 Bibliography 71
Chapter 4 Surface morphology of III-V semiconductor microstructures irradiated with excimer lasers and blueshift amplitudes 74

4.1 Surface morphology of InP/InGaAs/InGaAsP microstructures irradiated in air by excimer laser with a small number ($N < 100$) of pulses 74
4.2 Surface morphology of InP/InGaAs/InGaAsP microstructures irradiated in air by excimer laser with large number ($N \geq 100$) of pulses 77
4.2.1 Abstract 77
4.2.2 Introduction 78
4.2.3 Experimental details 79
4.2.4 Results and discussion 80
4.2.5 Conclusion 89
4.2.6 Acknowledgments 90
4.3 Surface morphology of InP/InGaAs/InGaAsP microstructures coated with dielectric layers and irradiated with ArF and KrF excimer lasers 90
4.3.1 Samples coated with SiO_2 and irradiated with ArF laser 90
4.3.2 Samples coated with SiO_2 and irradiated with KrF laser 93
4.3.3 Sample coated with Si_3N_4 layer irradiated by ArF laser 97
4.4 Surface morphology of InP/InGaAs/InGaAsP microstructure irradiated in DI water with ArF anf KrF excimer lasers 98
4.5 Blueshifting amplitude in InP/InGaAs/InGaAsP microstructure irradiated in air and through SiO_2, Si_3N_4 cap layers 100
4.6 Summary 102
4.7 Bibliography 103
Chapter 5 Excimer laser induced surface chemistry modification of InP/InGaAs/InGaAsP QW microstructures 106
5.1 XPS analysis of KrF laser irradiated InP/InGaAs/InGaAsP microstructures coated with SiO_2 layer 106
5.2 Chemical evolution of InP/InGaAs/InGaAsP microstructures irradiated in air and deionized water with ArF and KrF lasers 112
5.2.1 Abstract 112
5.2.2 Introduction 113
5.2.3 Experimental details 114
5.2.4 Results and Discussions 115
5.2.5 Conclusions 127
5.2.6 Acknowledgements 128
5.3 XPS analysis of KrF laser irradiated on InP/InGaAs/InGaAsP microstructures coated with InO_x layers 129
5.4 Summary 131
5.5 Bibliography 132
Chapter 6 Excimer laser induced quantum well intermixing amplitudes in III-V microstructures 138
6.1 QWI amplitudes in InP/InGaAs/InGaAsP microstructures coated with different oxides and irradiated with excimer lasers 138
6.1.1 InP/InGaAs/InGaAsP microstruture coated with SiO_2 140
6.1.2 InP/InGaAs/InGaAsP microstructure coated with Si_3N_4 142
6.1.3 InP/InGaAs/InGaAsP microstructure coated with InO_x 143

6.2 Study of excimer laser induced interface chemical modification InGaAs/InGaAsP/InP laser microstructures in DI water and air by SIMS 146
6.3 KrF laser induced QWI in GaAs based QW microstructure 157
6.3.1 Experiment 158
6.3.2 Results and discussions 158
6.4 Summary 160
6.5 Bibliography 161
Chapter 7 Laser diodes in KrF laser QWI InGaAs/InGaAsP/InP microstructures 165
7.1 KrF laser QWI for integrated laser diode fabrication 165
7.1.1 Experimental 165
7.1.2 Results and discussions 165
7.2 Laser diode fabricated on KrF laser intermixed material 168
7.3 Summary 170
7.4 Bibliography 171
Chapter 8 Conclusions and perspectives 173
8.1 Conclusions 173
8.2 Future work 176
8.3 Bibliography 177
Chapitre 8 Conclusions et perspectives 178
8.1 Conclusions 178
8.2 Les travaux futurs 181
8.3 Bibliographie 182
Appendix: Study of excimer laser control Si wettability in different aqueous environments 183
A.1 Si wettability and bionfunctionization 183
A.2 Contact angle measurement 187
A.3 Selective area in situ conversion of Si (001) hydrophobic to hydrophilic surface by excimer laser irradiation in hydrogen peroxide 188
A.3.1 Abstract 188
A.3.2 Introduction 189
A.3.3 Experimental 190
A.3.4 Results and discussions 192
A.3.4.5 Selective area immobilization of biotinylated nanospheres 200
A.3.5 Conclusion 201
A.3.6 Acknowledgement 202
A.4 Excimer laser assisted chemical process for formation of hydrophobic surface of Si (001) 202
A 4.1 Abstract 202
A 4.2 Introduction 203
A 4.3 Experimental 204
A 4.4 Results and Discussion 204
A 4.5 Conclusion 208
A 4.6 Acknowledgement 209
A.5 Summary 209
A.6 Bibliography 210

List of Figures

Figure 1. 1 Top view of a PIC chip fabricated on the Si platform [S. Jain*, et al.* 2011]. 3
Figure 1. 2 UV or excimer laser irradiation of a QW heterostructure allows selective area QWI [J. J. Dubowski 2003]. 5
Figure 2. 1 Reflectance (R) and absorption (α) and and of GaAs, InP and Si as a function of incident light photon energy extracted from reference [H. Philipp*, et al.* 1963, S. S. Vishnubhatla*, et al.* 1968] and [D. E. Aspnes*, et al.* 1983, D. Smith*, et al.* 1985]................ 14
Figure 2. 2 Geometry model (Temperature profile) of InP sample during KrF laser irradiation in air at 124 mJ/cm^2.. 16
Figure 2. 3 Time dependent temperature of InP sammple irradiated by KrF laser at 124mJ/cm^2 in air (a) and DI water (b)... 17
Figure 2. 4 Static temperature dependence on z of InP sample during KrF laser irradiation in air at 124 mJ/cm^2 18
Figure 2. 5 Time dependent temperature of SiO_2 and InP surface of InP sample coated with 240 and 150 nm SiO_2 layer irradiated by KrF laser at 124 mJ/cm^2....................................... 18
Figure 2. 6 (a) Light specularly reflecting from flat surface; (b) Multiple reflection from textured surface enhanced coupling into the material [P. Campbell 1993] 21
Figure 2. 7 SEM image of laser direct writing texturing features on Si substrate (a) before and (b) after etching of laser induced damage; (c) spontaneous formed Si surface features processed in vacuum with 800 nm, 100 fs pulses.(d) Square region of a Si wafer textured with spontaneously forming quasi-periodic microstructures appears black in contrast to the unprocessed regions [L. A. Dobrzanski*, et al.* 2008]... 22
Figure 2. 8 Typical bands profiles at 0K for a) insulator b) semiconductor and c) metal [B. G. Streetman*, et al.* 1995] 26
Figure 2. 9 Schematic of QW band structure.. 27
Figure 2. 10 Energy level, En, and wavefunctions, φn, in the infinite well [B. G. Streetman*, et al.* 1995] 28
Figure 2. 11 Schematic of the band-structure and epitaxy of a non-processed vs. a QWI InGaAs/GaAs QW. 28
Figure 2. 12 Simulation of composition profile (a) and conduction band (b) of interdiffused $In_{0.53}/Ga_{0.47}As$/InP QW with group III and V interdiffusion with identical rates for $\boldsymbol{Ld}$ =0, 10, 20, 30, 40Å. 29
Figure 2. 13 Point defect assisted diffusion. a) Vacancy initiated diffusion, b) an interstitial kicks an atom out of its lattice site, c) diffusion channelling through interstitial jumps [J. D. Plummer 2009].. 30
Figure 2. 14 Illustration of different point defects in a GaAs lattice. V stands for vacancy, i for interstitial for subtitutionnal, while the notation AB signifies that the atom A occupies the site of an atom B 31
Figure 2. 15 Valence band structure calculated for tensile, unstrained and compressive strained of InGaAs well grown on InP [A. R. Adams 2011]... 35
Figure 2. 16 Strain variation of identical interdiffusion v.s. interdiffusion length across a QW structure on the different positions: (a) well center (b) well close to the interface (c) barrier close to the interface (d) barrier center [H. Djie*, et al.* 2004]... 36
Figure 2. 17 View of oxygen adsorption on the InP (100). In, P, O, are indicated by brown, pink, and red spheres, respectively [K. Santosh*, et al.* 2013]... 40

Figure 3. 1 Schematic of excimer laser (ArF & KrF) irradiation setup ... 50
Figure 3. 2 ArF (a) and KrF (b) laser beam profiles ... 50
Figure 3. 3 Schematic cross-section of the investigated InP/InGaAs/InGaAsP microstructure (M1580) ... 51
Figure 3. 4 Schematic cross-section of the investigated InP/InGaAsP/InGaAsP microstructure (ZJU) ... 52
Figure 3. 5 Schematic cross-section of the investigated InP/InGaAs/InGaAsP microstructure (RAC82) ... 53
Figure 3. 6 Schematic cross-section of the investigated T0808 InGaAsP/GaAs quantum well microstructure ... 53
Figure 3. 7 Photograph of RTA setup ... 54
Figure 3. 8 Typical experimental set-up for PL measurements ... 56
Figure 3. 9 Schematic of atomic force microscope ... 58
Figure 3. 10 Multimode SPM ... 59
Figure 3. 11 SEM set up ... 60
Figure 3. 12 Schematic Olympus IX71 inverted microscope ... 61
Figure 3. 13 Illustration of XPS concept [B. V. Crist 2010] ... 62
Figure 3. 14 AXIS Ultra DLD XPS ... 64
Figure 3. 15 Schematic of SIMS components [I. Probe 2007] ... 67
Figure 3. 16 TOF-SIMS IV instrument ... 69
Figure 3. 17 Principle of FTIR [I. Sanchonx 2011] ... 70
Figure 4. 1 AFM image of InP/InGaAs/InGaAsP irradiated by ArF laser at 82 mJ/cm^2 in air ... 75
Figure 4. 2 AFM image of non irradiated and irradiated sites in by ArF laser in air after RTA ... 76
Figure 4. 3 Optical micrograph of the surface of an InP/InGaAs/InGaAsP microstructure irradiated with 400 pulses of a KrF laser at 142 mJ/cm^2 (a), along with high magnification images of the central (b) and edge (c) regions. ... 80
Figure 4. 4 AFM images of the central (a) and the edge (b) regions of a site irradiated with 400 pulses of the KrF ... 81
Figure 4. 5 Microscopic images of KrF laser irradiated sites at 109 mJ/cm^2 (left panel) and 142 mJ/cm^2 (right panel) with 100, 400 and 700 pulses. ... 81
Figure 4. 6 AFM images and profiles along indicated lines in the central region the KrF laser irradiated sites at 109 mJ/cm^2 (left panel) and 142 mJ/cm^2 (right panel). ... 82
Figure 4. 7 Average height (a), size (b) and period (c) of self-organized nanostructures vs. pulse number of the KrF laser operating at 109 mJ/cm^2, 124 mJ/cm^2 and 142 mJ/cm^2. ... 83
Figure 4. 8 PL peak intensity map and profile of the KrF laser irradiated spots with 400 pulses at 109 (a) and 142 mJ/cm^2 (b). ... 85
Figure 4. 9 Normalized PL intensity of the site central region vs. pulse number when irradiated with the KrF laser at 109 mJ/cm^2, 124 mJ/cm^2 and 142 mJ/cm^2. The inset shows PL spectra observed from the as-grown QW microstructure and the central region of the laser irradiated sites. ... 86
Figure 4. 10 AFM images and profiles along indicated lines of the central region of the ArF laser sites irradiated at 95 mJ/cm^2 with (a) 400 pulses and (b) 700 pulses. ... 87

Figure 4. 11 Average size, period and height of the nano-cone structures (a) and normalized PL intensity (b) in the central region of the ArF laser irradiated sites at 95 mJ/cm^2. 88
Figure 4. 12 AFM image of bulk InP irradiated with 400 (a) and 700 (b) pulses of the KrF laser operating at 142 mJ/cm^2. 89
Figure 4. 13 Room temperature PL maps and microscopic pictures of a series of spots on SiO_2 (50 and 150 nm thick) coated QW microstructures irradiated with ArF laser at 76 mJ/cm^2. 91
Figure 4. 14 AFM image of SiO_2 layer (a) and InP surface revealed after SiO_2 removed (b). The SiO_2 coated as-grown material and irradiated with ArF laser at 76 mJ/cm^2 underwent RTA at 700 °C for 2 min. 92
Figure 4. 15 Surface morphology of the InP cap layer exposed to the ArF laser radiation in the region where SiO_2 was removed. 93
Figure 4. 16 Microscopic images of samples coated with 243 nm thick layer of SiO_2 and irradiated with KrF excimer at 124 mJ/cm^2 (after RTA). 93
Figure 4. 17 AFM micrographs of SiO_2 (a) and InP (b) layer of non irradiated sites and irradiated sites 95
Figure 4. 18 High magnification InP surface morphology of irradiated sites with 25 pulses after RTA and removing SiO_2 layer. 95
Figure 4. 19 The RMS roughness of the InP layer irradiated with different pulses of the KrF at 124 mJ/cm^2, followed by the RTA step. The results are shown after the SiO_2 layer has been removed. 96
Figure 4. 20 SEM image of InP/InGaAs/InGaAsP QW sample (M1580) coated with a 243 nm thick layer of SiO_2 before KrF laser irradiation (a) and after irradiated with 25 pulses at 124 mJ/cm^2 (b). 97
Figure 4. 21 Microscopic picture of InP/InGaAs/InGaAsP microstructure coated with 40 nm (a) and 80 nm (b) Si_3N_4 layer after ArF laser irradiation at 70 mJ/cm^2. 98
Figure 4. 22 AFM image of non irradiated sites and sites irradiated by ArF laser in DI water 98
Figure 4. 23 AFM image of non irradiated sites and sites irradiated with ArF laser in DI water and after RTA. 99
Figure 4. 24 PL map of the sample irradiated by KrF laser at 124 mJ/cm^2 and RTA. 101
Figure 4. 25 Room temperature PL map of InP/InGaAs/InGaAsP sample coated with (a) 40 nm and (b) 80 nm Si_3N_4 after ArF laser irradiation and RTA. 101
Figure 5. 1 Si 2p (a), (d), O 1s (b), (e) and C 1s (c), (f) XPS spectra of no irradiated site and site irradiated with 25 pulses by KrF laser at 124mJ/cm^2 108
Figure 5. 2 In 3d 5/2 (a, b, c, d) and P 2s (e, f, g,h) XPS spectra of the SiO_2 layer, SiO_{2-x}/InP interface 1, SiO_{2-x}/InP interface 2 and the InP layer following KrF laser irradiation and RTA. 110
Figure 5. 3 XPS depth profiles of O, Si, C, In, N, P, Ga and As in non-irradiated (a) and laser irradiated (b) SiO_2/InP/InGaAs/InGaAsP microstructures following their RTA. 112
Figure 5. 4 PL shift dependence in the InP/InGaAs/InGaAsP microstructure on the laser pulse number after (a) ArF and (b) KrF laser irradiation in air and DI water that was followed by the RTA step. 116
Figure 5. 5 In 3d 5/2 and P 2p XPS spectra of as grown sample (a), (d), irradiated by ArF laser at 82mJ/cm^2 with 50 pulses in air (b), (e) and in DI water (c), (f). 118

Figure 5. 6 C 1s and O 1s XPS spectra of as grown sample (a), (d) and sample irradiated by ArF laser at 82mJ/cm^2 with 50 pulses in air (b), (e) and in DI water (c), (f)....................... 120
Figure 5. 7 Expanded O 1s XPS spectra of as grown sample (a) and sample irradiated by ArF laser at 82mJ/cm^2 with 50 pulses in air (b) and in DI water (c)... 121
Figure 5. 8 In 3d 5/2 and P 2p XPS spectra of as grown sample (a), (d) and sample irradiated by ArF laser at 82mJ/cm^2 with 50 pulses in air (b),(e) and DI water (c),(f), followed by the RTA step. 122
Figure 5. 9 C 1s and O 1s XPS spectra of as grown sample (a), (d) and sample irradiated by ArF laser at 82mJ/cm^2 with 50 pulses in air (b),(e) and DI water (c),(f), followed by the RTA step. 123
Figure 5. 10 Dependence of XPS atomic concentration of InP and surface adsorbates on pulse number in the samples irradiated with ArF laser in DI water (a), in air (b) and after RTA of the sample irradiated in DI water (c) and in air (d). 124
Figure 5. 11 TOF-SIMS oxygen concentration depth profile in as grown sample, and in samples irradiated with ArF laser in DI water and in air before (a) and after (b) RTA at 700°C for 2 minutes. 126
Figure 5. 12 Dependence of XPS atomic concentration of InP and surface adsorbates on pulse number in the sample irradiated with KrF laser in DI water (a), in air (b) and after RTA of the sample irradiated in DI water (c) and in air (d). 127
Figure 5. 13 O 1s and In 3d XPS spectra of InO_x layer coated sample before and RTA. 130
Figure 5. 14 In 3d 5/2 and P 2p XPS spectra of sample coated with 10 nm InO_x layer irradiated by KrF laser with 2 and 10 pulses. 131
Figure 6. 1 Net PL shifts dependence on RTA time 139
Figure 6. 2 Net blueshift amplitude dependence on the pulse number of the KrF laser at 124 mJ/cm^2 and RTA (InP/InGaAs/InGaAsP QW microstructure).................................... 140
Figure 6. 3 SIMS profiles of O, Si, P, Ga, As and In InP/InGaAs/InGaAsP microstructure coated with a 243 nm thick layer of SiO_2 after KrF laser irradiation and RTA 142
Figure 6. 4 Expanded view of SIMS analysis of InP/InGaAs/InGaAsP microstructure coated with 243 nm SiO_2 layer after KrF laser irradiation and RTA 142
Figure 6. 5 Dependence of amplitude of blueshift on pulse number of samples without Si_3N_4 and caoted with 40 nm Si_3N_4 layer after ArF laser irradiation and RTA. 143
Figure 6. 6 Blueshift of as grown and samples coated with different thickness InO_x layers dependence on RTA temperatures 144
Figure 6. 7 SIMS measurement of as grown samples from M1580 microstructure before and after RTA 144
Figure 6. 8 SIMS results of sample coated with 40 nm InOx layer before and after RTA at 725◦C for 2 minutes 145
Figure 6. 9 PL shift dependence on pulse number of as grown sample (0 nm) and samples coated with 10 and 40 nm InO_x layer irradiated by KrF laser at 124mJ/cm^2 145
Figure 6. 10 SIMS results of sample coated with 40 nm InO_x layer after KrF laser irradiation with 10 pulses and before and after RTA at 725°C for 2 minutes...................................... 146
Figure 6. 11 PL spectra of as grown material and sites irradiated in air (a) and DI water (b) following the RTA step... 151
Figure 6. 12 In $3d_{5/2}$ XPS spectra of sample irradiated by ArF laser at 82 mJ/cm^2 with 50 pulses in DI water and air before (I) and after (II) RTA... 152

Figure 6. 13 P (—), O (---), As (—) and InO (—) intensity profiles in the microstructure after RTA of as grown sample (a) and samples irradiated by ArF laser at 82mJ/cm^2 with 50 pulses in air (b) and DI water (c) investigated by ToF-SIMS.. 155
Figure 6. 14 Calculated strain dependence in the 32 nm blueshifted InGaAs/InGaAsP QW region on the thickness, d, of the InO_x stressing layer.. 156
Figure 6. 15 PL map of sample (T0808) irradiated in DI water (a) and air (b) by KrF laser and RTA at 825 °C measured PLM 159
Figure 6. 16 PL map measured by HI-PLM of investigated sample after KrF laser QWI and RTA.. 160
Figure 7. 1 PL spectra of as grown material, irradiated with 75 and 100 pulses by KrF laser at 153 mJ/cm^2 in air and RTA 166
Figure 7. 2 PL map of the sample before KrF laser QWI. The “1440 nm” signal is an arbitrary background corresponding to the region with the negligible PL emission. 166
Figure 7. 3 PL map (left) and PL scanning profile (right), line from A to B, of InGaAs/InP QW microstructure after KrF laser irradiation at 156 mJ/cm^2 with 200 pulses through Al film mask with 40 μm x 200 μm windows and RTA at 700°C for 2 minutes............................. 167
Figure 7. 4 Detailed PL map and scanning line of small windows of InGaAs/InP QW microstructure after KrF laser irradiation at 156 mJ/cm^2 with 200 pulses and RTA at 700 °C for 2 minutes 168
Figure 7. 5 PL map of a ZJU sample after KrF laser irradiation at 156 mJ/cm^2 and RTA. Sites A and B irradiated with 75 pulses (80 nm net blue shift) and sites C and D with 150 pulses (120 nm net blue shift). 168
Figure 7. 6 Emission spectra (a), L-J curve (b) and I-V (c) of LD devices fabricated in the QWI (Sample 1-3) and RTA as grown sample and RTA only sample................................ 170

List of Tables

Table 2. 1. Thermal and mechanical properties of GaAs, InP and Si 16
Table 2. 2 Thermal properties of water, air and SiO_2 19
Table 2. 3 Index of CTE (α), Ef and υf are the Young modulus and the Poisson coefficient, σ_{in} is the initial stress.. 37
Table 3. 1 Spin-orbit splitting j values and peak area ratios. 65
Table 4. 1 RMS roughness on non irradiated site and irradiated sites by KrF laser in air 77
Table 4. 2 RMS roughness on non irradiated site and irradiated sites by ArF (I) and KrF (II) laser in DI water... 100
Table 5. 1 Atomic percentage of elements of non irradiated sites and irradiated by KrF laser with 25 pulses 106
Table 6. 1 Blueshift amplitude vs. thickness of the SiO_2 layer for non-irradiated QW microstructures.. 141
Table 6. 2 XPS P/In ratio in the as grown InP-covered InGaAs/InGaAsP/InP microstructure and ArF irradiated sites before RTA.. 153
Table 6. 3 XPS P/In ratio in the as grown InP-covered InGaAs/InGaAsP/InP microstructure and ArF irradiated sites after 2 min RTA at 700 °C. 153
Table 7. 1 Laser diode fabrication steps 168
Table A. 1 Parameters of Si used in calculation of spatial and transient temperature profiles. 193
Table A. 2 Atomic percentage and CA of as-received, etched and KrF laser processed Si samples with 100 and 500 pulses of 250 mJ/cm^2. 199
Table A. 3 Atomic percentage and CA of as-received, etched and ArF laser processed Si samples with 100 and 500 pulses of 65 mJ/cm^2. 199

Chapter 1 Introduction

1.1 Photonic integrated circuits

The explosive "Moore's Law" development of integrated electronics devices along with the similarly explosive development of the Internet, has contributed to demand for communication systems providing increased bandwidth and flexibility at lower cost [R. Nagarajan*, et al.* 2005]. Optical communication systems can satisfy these demands, as they provide low-dispersion and low-loss (0.2 dB/km) transmission enabling higher-bit-rate and longer-distance data transport with reduced repeater spacing over that of electrical coaxial lines [G. P. Agrawal 2010]. Such systems consist of active components, used for light generation, detection, modulation and amplification, as well as passive components that serve as point-to-point links in the form of fibers or waveguides, wavelength multiplexers, wavelength demultiplexers, polarisers, isolators and switchers. A majority of present communications systems are assembled using discrete optoelectronic components as building blocks. However, there are several shortcomings with this method. The dominant optical loss is coupling loss between fiber and waveguide during communication between discrete components. The other drawback is the high cost involved with packaging discrete components separately. A reduction of the packaging cost can be accomplished by placing two or more optoelectronic chips into one package, but the device-to-device coupling issue still exists.

A new generation of high-functionality photonic integrated circuits (PICs) which combine generation, detection, modulation, amplification, switching and transport of light on a single chip can reduce power dissipation, cost and size. The monolithic integration of multiple optoelectronic devices onto a single chip eliminates the device-to-device coupling problem. Fewer packages are required as multiple components can be placed on a single chip within one package. Also, the reliability increases due to the elimination of possible mechanical movements among the elements of an optical train and the reduced driving currents allowed by the reduction in optical coupling loss between elements.

However, the integration of III-V semiconductor PICs does not develop along as the silicon-based integrated circuits (IC). There are severals factors that have contributed to this relatively

slow scaling of the PIC. In a PIC, there is a wide range of functions that need to be served, including light generation, amplification, modulation, detection and guiding. To optimize performance of each function, different material structures are likely required in the different components serving these functions. This is a difficult task for the common 2-dimensional growth and processing platforms used for device fabrication. This means that after the first growth, lithography and etching steps are applied on the sample before putting it back in the epitaxial reactor to make a second growth. Since growth processes are long, and the etching treatments can generate a considerable amount of defects at the surface and edges of the wafer, such a technique can be expensive with low production rates. The defects embedded in the interfaces formed during etching procedures often cannot be removed during the consecutive growth and they become responsible for diminishing quality of the devices [R. Nagarajan*, et al.* 2005, M. Smit*, et al.* 2007]. The growth techniques developed for multibandgap engineering include butt-joint regrowth, selective area growth, offset quantum wells and dual quantum wells [E. J. Skogen*, et al.* 2005]. Besides the common drawbacks discussed before, butt-joint regrowth has a difficulty in achieving high-quality interface that would avoid reflections and losses in axial waveguides [J. Binsma*, et al.* 1997]. The selective area growth technique is less flexible to achieve multibandgap wafer [B. Mason*, et al.* 1998]. The offset quantum wells and dual quantum wells approach suffers from limited quantities bandgaps on one platform [M. Aoki*, et al.* 1993]. Consequently, quantum well intermixing (QWI) has been investigated as one of the most promising approaches for the cost-effective fabrication of PICs [W. Laidig*, et al.* 1981, J. H. Marsh 1993, E. J. Skogen*, et al.* 2005, S. B. Estrella*, et al.* 2012]. It allows for the strategic, post growth, tuning of the quantum well (QW) band edge by inducing atomic interdiffusion between the well and barrier materials. This technique enables the generation of multiple QW bandgap on a chip without difficult growths steps or discontinuities in axial waveguide. QWI offers more design flexibilities than the offset QW method [B. Mason*, et al.* 1998] and offers a simpler fabrication scheme than the butt-joint regrowth method [J. Binsma*, et al.* 1997] or selective area growth method [M. Aoki*, et al.* 1993]. The known methods of QWI include impurity induced intermixing [W. Laidig*, et al.* 1981], impurity-free vacancy diffusion [J. Teng*, et al.* 2002], ion implantation induced QWI [V. Aimez*, et al.* 2002], and visible [J. Epler*, et al.* 1986], IR [B. S. Ooi*, et al.* 2004] and UV [J. J. Dubowski 2003] laser induced QWI. QWI obtained by annealing

of selective area coated QW wafers with different oxides, nitrides and fluorides (fabricated by conventional thin film deposition techniques) has also been investigated [P. Deenapanray*, et al.* 2002, A. Francois*, et al.* 2006].

To illustrate the QWI use in PICs application, scientists have first fabricated and studied external cavity laser diodes with integrated passive waveguides generated by impurity induced disordering in 1992 [S. Andrew*, et al.* 1992]. Then, high performance devices fabricated in QWI material, e.g. widely tunable, negative chirp, 10 Gb/s transmitter, sampled grating distributed Bragg reflector (SG-DBR) laser and electro absorption modulator (EAM) on QWI platform [E. J. Skogen*, et al.* 2005]. The band-edge of the EAM can be blue-shifted by QWI such that it maintains a high absorption coefficient, reasonable insertion loss and without severe degradation to the exciton peak. The passive component band-edge can be further blue-shifted for minimum loss [E. J. Skogen*, et al.* 2005]. Plasma bonding techniques have been used to bond the integrated laser-EAM device with already patterned tuned bandgap on to patterned SOI (silicon-on-insulator) substrate, as shown in Figure 1.1. Four bandgaps were generated on a single chip and used to realize a multi-channel distributed feedback (DFB) laser array and lasers-EAM modulators. A 150 μm long taper following the EAM is used to transit the optical mode from the III-V semiconductor to the Si. Thirteen CW operational lasers with 40-70 mA threshold current and four-channel laser-EAM arrays with 2 GHz bandwidth were fabricated [S. Jain*, et al.* 2011].

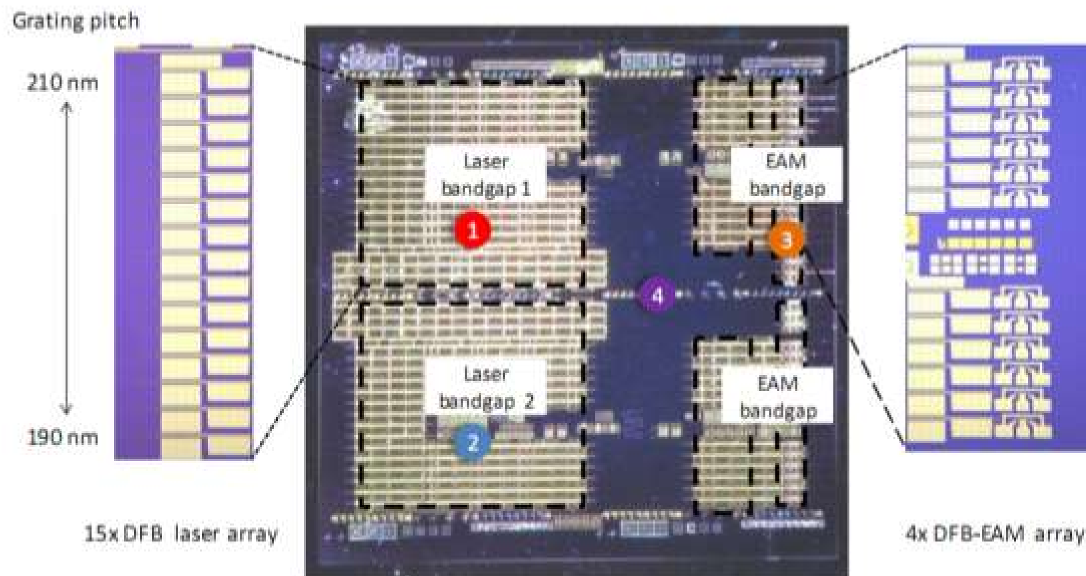

Figure 1. 1 Top view of a PIC chip fabricated on the Si platform [S. Jain*, et al.* 2011].

Characterization of intermixed material has typically been carried out by measuring optical properties of the intermixed material and photonic devices fabricated on the intermixed platforms [J. H. Marsh 1993, E. Li 2000]. Photoluminescence (PL) has frequently been employed to investigate QW bandgap modification and provides information about surface and interface modification/damage during the intermixing step [J. H. Marsh 1993]. The measurement of the laser diode threshold current increment also provides the information about the density of defects and modified quantum confinement in the intermixed active region [V. Aimez*, et al.* 2002]. To measure the atom or defect diffusion inside the QW microstructure, secondary ion mass spectroscopy (SIMS) was used to compare atomic profile depths of QW before and after QWI [J. Teng*, et al.* 2002]. In order to reduce the damage of the active region of QW in the intermixing, many studies focus on creating surface defects by means of capped stressor layers and low energy ion implantation. High resolution X-ray photoelectron spectroscopy (XPS) has been used to analyse the surface defects creation on non-stoichemical InP surface during ion induced QWI [C. Xu*, et al.* 2009]. In addition, XPS can also be used to study the indepth atom diffusion profile of QW [P. Deenapanray*, et al.* 2002, S. Barik*, et al.* 2007]. As the surface and interface morphology modification is directly related to these chemical modifications, the surface morphology investigation with atomic force microscope (AFM) and scanning electron microscope (SEM) can be used to verify the surface defect generation and diffusion process [D. G. Deppe*, et al.* 1988, J.-S. Lee*, et al.* 1998].

1.2 UV laser QWI

Despite significant advancements, QWI technology has remained the subject of ongoing investigation triggered, e.g., by the lack of precision in achieving targeted amplitudes of bandgap shifting, and it has suffered from unintentionally introduced impurities present on the surface of processed wafers. Such impurities could influence the QWI amplitude attempted with ion implantation, plasma exposure or with layers of different oxides, nitrides, fluorides, etc. Uncontrolled presence of impurities will also lead to the reduced quality of the QWI material and compromised performance of devices made from such material. In that context, the application of a strongly absorbed UV laser radiation for surface modification of III-V QW microstructures offers the possibility to investigate the role of surface impurities and that of chemical

composition of a laser-fabricated layer, typically thinner than 10 nm, in the QWI process. The UV laser QWI approach (UV-QWI), originally discussed in [J. J. Dubowski 2003], employs an excimer laser (λ = 248 nm) to alter the near-surface region (~10 nm) of the QW microstructure, as shown in Figure 1.2. The goal of this step is to create a “reservoir” of defects at the surface of a QW microstructure. Another form of the alteration could be chemical in nature, resulting from the irradiation in different environments. Processing with shaped UV laser beams, or using a mask projection technique, provides a direct method to achieve selective area processing required for manufacturing of PIC. Following the UV laser exposure, the QW microstructure needs to be annealed at a temperature sufficient to drive defects from the reservoir into the vicinity of the QW region where the intermixing (between well and barrier material) will take place. This step is carried out in a rapid thermal annealing (RTA) oven. In addition to driving impurities and/or point defects towards the QW region, typically located less than 2 μm below the surface, the high-temperature treatment could change the chemical composition of the laser-fabricated layer and induce/reduce stress in the QW region related to the presence of such a layer. Excimer laser has already been employed in the microelectronics industry for high resolution optical lithography. Thus, these tools could be relatively easily accommodated for industrial processes involving QWI.

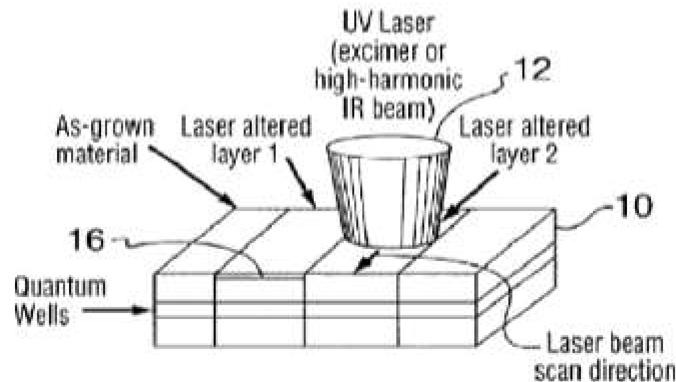

Figure 1. 2 UV or excimer laser irradiation of a QW heterostructure allows selective area QWI [J. J. Dubowski 2003].

UV laser QWI is applicable in both InP and GaAs based QW and QD microstructures. In InP based QWs microstructures, the UV-QWI process is based on the localized generation of point defects through UV laser pulse absorption. The excess concentration of point defects promotes intermixing between the barriers and wells during the annealing step. The blueshift strongly depends on the fluence and pulse number. A phenomenological model was developed to fit the

wavelength shift dependence up to 125 nm, which indicates that UV laser QWI technique is more efficient in defect generation than pulsed laser induced QWI [J. Genest*, et al.* 2008a]. Excimer laser QWI was also reported to induce significant blueshifts due to laser modification of surface chemistry of InP cap material irradiated in various environments, including air, DI water and dielectric layer coating [N. Liu*, et al.* 2011a, N. Liu*, et al.* 2013]. In GaAs based QW microstructure, the UV laser QWI process leads to the suppression of intermixing in InAlGaAs/AlGaAs/GaAs and AlGaAs/GaAs heterostructures due to stress from surface oxides initiated by UV laser irradiation and developed during the RTA step [J. Genest*, et al.* 2007a]. The short wavelength of the surface modifying laser radiation and the relatively shallow location of the QW allow suppression of QWI with a spatial resolution as high as 1 μm [J. Genest*, et al.* 2007b]. Thus, excimer laser has the potential to offer a highly efficient and controllable method of QWI.

1.3 Project description

The goal of the project was to investigate the role of excimer lasers in fabricating high-quality QWI material. The QW microstructures material mainly studied in this project are InP/InGaAs/InGaAsP microstructures with QW active region below surface cap layer around 76 nm or 1.5 μm. As dielectric layers of SiO_2 and Si_3N_4 are popular in semiconductor optoelectronic devices fabrication, we have studied properties of InP/InGaAs/InGaAsP microstructure coated with such layers and irradiated with an excimer laser before RTA. Furthermore, deionized water (DI) environment is known to be chemically "simple and clean" that could reduce the uptake of contamination of air environment during laser irradiation. For that reason, it was interesting to investigate if UV laser QWI by irradiating QW wafers in DI water environment could lead to the fabrication of the QWI material with improved optical properties. In our preliminary studies, we also found that UV laser created indium oxide (InO_x) played an important role in the QWI process. Following this lead, in this thesis I have investigated the QWI effect in QW microstructures coated with InO_x and irradiated with excimer laser. As the surface defects generation and surface chemical and morphology alteration could depend on the energy of laser emitted photons, two different wavelengths excimer lasers, ArF and KrF lasers, were used in this research. In addition, both InP (full and partially laser diode QW) and GaAs (partially laser diode

QW) based QW microstructures were investigated. The surface and interface formation during excimer laser irradiation and annealing were mainly measured by AFM. The surface and interface chemical modifications and atoms diffusions during process were characterized by surface XPS, indepth XPS and SIMS. The optical properties of all the QW microstructures after UV laser QWI were mainly characterized by PL measurements as well as by investigating luminescence quality from laser diodes fabricated in the intermixed full laser diode QW microstructures.

In summary, this thesis was addressed to study the mechanism of excimer laser QWI in III-V semiconductor microstructures and propose a novel controllable UV laser QWI recipe leading to the fabrication of high quality wafers required in the fabrication of PICs.

1.4 Contribution of this research

1.4.1 Excimer laser induced QWI in InP/InGaAs/InGaAsP microstructures coated with different dielectric layers

- Liu, N., Moumanis, Kh., and Dubowski, J. J. *ArF excimer laser-induced quantum well intermixing in dielectric layer coated InGaAs/InGaAsP microstructures,* 4th Pacific International Conference on Applications of Lasers and Optics (PICALO), Wuhan, China, March 23-25, 2010, PICALO 2010 Conference Proceedings, ISBN:978-0-912035-56-7, article number: M404, (2010);
- Liu, N., Moumanis, Kh., and Dubowski, J. J. *Surface morphology of SiO_2 coated InP/InGaAs/InGaAsP microstructures following irradiation with the ArF and KrF excimer lasers,* Photonics West Conference: Laser Application in Microelectronic and Optoelectronic Manufacturing (LAMOM) XVI, San Francisco, USA, January 22-27, 2011, (Oral Presentation), Proceeding of SPIE, Vol. **7920**, 7920C, (2011);
- Liu, N., Blais, S. and Dubowski, J. J. *Surface and interface study of SiO_{2-x} coated InP/InGaAs/InGaAsP semiconductor laser microstructures processed in the soft KrF laser irradiation regime,* Pacific RIM Laser Damage 2011: Optical Materials for High Power Lasers, Shanghai, China, November 6-9, 2011, Proceeding of SPIE, Vol. **8206**, 820609, (2012);

1.4.2 UV laser QWI of InP/InGaAs/InGaAsP microstructures irradiation in air and DI water

- Liu, N., Moumanis, Kh., Blais, S. and Dubowski, J. J. : *XPS study of InP/InGaAs/InGaAsP microstructures irradiated with ArF laser in air and deionized water,* Photonics West Conference: Synthesis and Photonics of Nanoscale Material IX, San Francisco, USA, January 21-26, 2012, Proceeding of SPIE, Vol. **8245**, 82450E, (2012);
- Liu, N. and Dubowski, J. J.: *Chemical evolution of InP/InGaAs/InGaAsP microstructures irradiated in air and deionized water with ArF and KrF lasers,* Applied Surface Science **270**, 13, 16-24, (2013);
- Liu, N., Poulin S. and Dubowski, J. J.: *Enhanced photoluminescence from UV laser quantum well intermixed InGaAs/InGaAsP/InP laser microstructures*, Journal of Physics D: Applied Physics, **46**, 445103, (2013);
- Liu, N., Moumanis, Kh., and Dubowski, J. J.: *Self-organized Nano-cone Arrays in InP/InGaAs/InGaAsP Microstructures by Irradiation with ArF and KrF Excimer Lasers*, Journal of Laser Micro/Nano Engineering **7,** 2,130-136, (2012);

1.4.3 Application of excimer laser QWI for photonic device fabrication

- Béal, R., **Liu, N.** Moumanis, Kh., Aimez, V. and Dubowski, J.J. *Multi Section Bandgap Tuned Superluminescent Diodes Fabricated by UV Laser Induced Quantum Well Intermixing, International Conference on Information Photonics (IP), Ottawa, Canada, May, 2011, IEEE Proceeding of IP2011, ISBN:* 978-1-61284-315-5*, article number:* 5953731, (2011);
- Kaleem, M., Zhang, X., Zhuang, Y., He, J.J., Liu, N., and Dubowski, J. J. *UV laser induced selective-area bandgap engineering for fabrication of InGaAsP/InP laser devices*, Optics & Laser Technology **51**, 36-42, (2013);

1.4.4 Excimer laser induced modification of silicon wettability

- Liu, N., Hassen W. and Dubowski, J.J.: *Excimer laser assisted chemical process for formation of hydrophobic surface of Si (001),* Applied Physics A, (published on line), DOI: 10.1007/s00339-014-8380-9, (2014);
- Liu, N, Huang X. and Dubowski, J.J.: Selective area in situ conversion of hydrophobic to hydrophilic surface of Si by excimer laser irradiaiton in hydrogen peroxide, Journal of Physics D: Applied Physics, (submitted);

1.4.5 **XPS and AFM analysis of semiconductor surfaces** (My contribution was to the semi-quantitative analysis of XPS data and collection of AFM images)

- Arudra, P., Marshall**,** G. M., Liu**, N.,** and Dubowski, J. J. :*Enhanced Photonic Stability of GaAs in Aqueous Electrolyte Using Alkanethiol Self-Assembled Monolayers and Postprocessing with Ammonium Sulfide,* Journal of Physical Chemistry **C116**, 2891-2895, (2012);
- Huang, X., Liu, N., Moumanis, Kh., and Dubowski, J. J.: *Water-Mediated Self-Assembly of 16-Mercaptohexadecanoic acid on GaAs(001),* Journal of Physical Chemistry **C117**, 1590-1597, (2013).

1.5 Thesis structure

The topics of the remaining eight chapters of the current thesis are as following:

Chapter 2: covers the concepts of laser-matter interaction, including laser induced surface temperature, morphology and chemical modification; discusses the principle of QW and QWI and the role of strain and point defects in the QWI process;

Chapter 3: presents excimer laser irradiation setups; introduces the investigated semiconductor microstructures and discusses characterization techniques used during my work;

Chapter 4: discusses UV laser induced InP/InGaAs/InGaAsP microstructure surface morphology modification in air and presents self-organized nanocone structures created outside of QWI laser parameters and its effect in PL intensity enhancement; discusses surface morphology of microstructure coated with dielectric layers (SiO_2 and Si_3N_4) and in DI water;

Chapter 5: XPS analysis of chemical evolution of InP/InGaAs/InGaAsP microstructure after ArF and KrF laser irradiation in air and DI water; XPS analysis of surface and interface of the microstructure coated with SiO_2 and InO_x layer during KrF laser QWI;

Chapter 6: summarizes the PL shift dependence on laser parameters when irradiated in the discussed environments, including in air, DI water and dielectric layers (SiO_2, Si_3N_4 and InO_x) coated; SIMS analysis of atoms diffusion of the interface of InP/InGaAs/InGaAsP microstructure after UV laser QWI in air and DI water and studies the atoms diffusion influence on PL shift and PL intensity of intermixed microstructures; SIMS analysis of atoms diffusion in UV laser QWI in the other different environments;

Chapter 7: investigates laser diode fabrication on KrF laser QWI material; KrF laser QWI on GaAs based QW and measured with a novel HI-PLM setup developed by our group;

Chapter 8: presents the conclusion of this thesis and future direction for the project.

Appendix: discusses UV laser induced Si wettability modification, including excimer laser induced selective area hydrophilic Si surface by irradiation in hydrogen peroxide and hydrophobic surface by irradiation in methanol solution.

1.6 Bibliography

Agrawal, G.P.: (2010), Fiber-optic communication systems (Wiley), 587p.

Aimez, V., Beauvais, J., et al., (2002), Low-energy ion-implantation-induced quantum-well intermixing, *IEEE Journal of Selected Topics in Quantum Electronics*, vol. 8, n°4, 870-879.

Andrew, S., Marsh, J., et al., (1992), Quantum-well laser with integrated passive waveguide fabricated by neutral impurity disordering, *IEEE Photonics Technology Letters*, vol. 4, n°5, 426-428.

Aoki, M., Suzuki, M., et al., (1993), InGaAs/InGaAsP MQW electroabsorption modulator integrated with a DFB laser fabricated by band-gap energy control selective area MOCVD, *IEEE Journal of Quantum Electronics*, vol. 29, n°6, 2088-2096.

Barik, S., Fu, L., et al., (2007), Impurity-free disordering of InAs/ InP quantum dots, *Applied Physics Letters*, vol. 90, 243114.

Binsma, J., Thijs, P., et al., (1997), Characterization of butt-joint InGaAsP waveguides and their application to 1310 nm DBR-type MQW gain-clamped semiconductor optical amplifiers, *IEICE transactions on electronics*, vol. 80, n°5, 675-681.

Deenapanray, P., Gong, B., et al., (2002), Impurity-free disordering mechanisms in GaAs-based structures using doped spin-on silica layers, *Applied Physics Letters*, vol. 80, 4351.

Deppe, D.G., and Holonyak, N., (1988), Atom diffusion and impurity induced layer disordering in quantum well III-V semiconductor heterostructures, *Journal of applied physics*, vol. 64, n°12, R93-R113.

Dubowski, J.J.: 'Laser-induced bandgap shifting for photonic device integration', US Patent 6,514,784, 2003.

Epler, J., Burnham, R., et al., (1986), Laser induced disordering of GaAs AlGaAs superlattice and incorporation of Si impurity, *Applied Physics Letters*, vol. 49, 1447.

Estrella, S.B., Johansson, L.A., et al., (2012), Widely Tunable Compact Monolithically Integrated Photonic Coherent Receiver, *IEEE Photonics Technology Letters*, vol. 24, n°5, 365-367.

Francois, A., Aimez, V., et al., (2006), Enhancement of quantum well intermixing on InP/InGaAs/InGaAsP heterostructures using titanium oxide surface stressors to induce forced point defect diffusion, *Applied Physics Letters*, vol. 89, 164107.

Genest, J., Dubowski, J.J., et al., (2007a), Suppressed intermixing in InAlGaAs/AlGaAs/GaAs and AlGaAs/GaAs quantum well heterostructures irradiated with a KrF excimer laser, *Applied Physics A: Materials Science & Processing*, vol. 89, n°2, 423-426.

Genest, J., Dubowski, J.J., et al., (2007b), UV laser controlled quantum well intermixing in InAlGaAs/GaAs heterostructures, *Journal of Physics: Conference Series*, vol. 59, 605-609.

Genest, J., Beal, R., et al., (2008), ArF laser-based quantum well intermixing in InGaAs/InGaAsP heterostructures, *Applied Physics Letters*, vol. 93, 071106.

Jain, S., Sysak, M., et al., (2011), Integrated hybrid silicon DFB laser-EAM array using quantum well intermixing, *Optical express*, vol. 19, n°14, 13692-13699.

Laidig, W., Holonyak, N., et al., (1981), Disorder of an AlAs/GaAs superlattice by impurity diffusion, *Applied physics letters*, vol. 38, n°10, 776-778.

Lee, J.-S., Ren, H.-W., et al., (1998), InGaAs quantum dot intermixing and evaporation in GaAs capping layer growth, *Journal of applied physics*, vol. 84, 6686.

Li, E.: (2000), Semiconductor quantum wells intermixing (CRC), 669p.

Liu, N., Blais, S., et al., (2011), Surface and interface study of SiO_{2-x} coated InP/InGaAs/InGaAsP semiconductor laser microstructures processed in the soft KrF laser irradiation regime, *Proceeding of SPIE*, vol. 8206, 820609.

Liu, N., and Dubowski, J.J., (2013), Chemical evolution of InP/InGaAs/InGaAsP microstructures irradiated in air and deionized water with ArF and KrF lasers, *Applied Surface Science*, vol. 270, n°13, 16-24.

Marsh, J.H., (1993), Quantum well intermixing, *Semiconductor Science and Technology*, vol. 8, n°6, 1136.

Mason, B., Fish, G.A., et al., (1998), Ridge waveguide sampled grating DBR lasers with 22-nm quasi-continuous tuning range, *IEEE Photonics Technology Letters*, vol. 10, n°9, 1211-1213.

Nagarajan, R., Joyner, C.H., et al., (2005), Large-scale photonic integrated circuits, *IEEE Journal of Selected Topics in Quantum Electronics*, vol. 11, n°1, 50-65.

Ooi, B.S., Ong, T.K., et al., (2004), Multiple-wavelength integration in InGaAs-InGaAsP structures using pulsed laser irradiation-induced quantum-well intermixing, *IEEE Journal of Quantum Electronics*, vol. 40, n°5, 481-490.

Skogen, E.J., Raring, J.W., et al., (2005), Monolithically integrated active components: a quantum-well intermixing approach, *IEEE Journal of Selected Topics in Quantum Electronics*, vol. 11, n°2, 343-355.

Smit, M., Bente, E., et al., (2007), Current status and prospects of photonic IC technology, *IEEE 19th International Conference on Indium Phosphide & Related Materials, 2007 (IPRM'07)*, IEEE, 3-6

Teng, J., Dong, J., et al., (2002), Controlled group V intermixing in InGaAsP quantum well structures and its application to the fabrication of two section tunable lasers, *Journal of Applied Physics*, vol. 92, 4330.

Xu, C., and Mei, T., (2009), Inductively Coupled Argon Plasma-Enhanced Quantum-Well Intermixing: Cap Layer Effect and Plasma Process Influence, *IEEE Journal of Quantum Electronics*, vol. 45, n°8, 920-926.

Chapter 2 Background information

In this chapter, first I review the fundamental laser material interaction. I discuss laser induced surface temperature, morphology and chemical modification of materials. The focus is on mechanisms of UV laser interaction with semiconductor surfaces. I also discuss the band structure of QW, the principle of QWI and the influence of defects and mechanical strain on the QWI effect.

2. 1 Laser-matter interaction

The interaction mechanism between laser light and material depends on the parameters of laser beam and properties of the material. Laser parameters contain laser wavelength, intensity, spatial and temporal coherence, polarization, angle of incidence and irradiation time (e.g. pulse width and number of pulses for pulse laser). The material is characterized by its chemical composition and physical microstructures, which determines the type of elementary excitations and interactions between them. Laser processing can be classified into two groups, at least in principle : conventional laser processing and laser chemical processing [D. Bauerle 2010]. Conventional laser processing can be performed in an inert atmosphere and takes place without any changes in the overall chemical composition of the material being processed. Laser chemical processing is characterized by overall change in the chemical composition of material or the activation of a chemical reaction, as well as morphological changes in the surface and near surface region.

When laser beam irradiates the surface of a material, a fraction of laser beam is reflected; the penetrating radiation is absorbed inside the bulk material where the intensity decreases for linear absorption corresponding to Beer's law [R. F. Haglund*, et al.* 1997]:

$$I(x) = (1 - R)I_0 e^{(-\alpha x)}, \quad (2.\ 1)$$

where $I_0$is intensity at surface at x=0, α is absorption coefficient and R is reflectance.

The inverse of the absorption coefficient (α) can be regarded as the optical penetration depth, which is the depth where the intensity has fallen to 1/e of the incoming value. Both α and R are important in a laser irradiation process, but they can vary with laser wavelength and material

composition. Figure 2.1 (a) and (b) shows the R and α of Si, GaAs and InP as a function of photon energy extracted from [H. Philipp*, et al.* 1963, S. S. Vishnubhatla*, et al.* 1968, D. E. Aspnes*, et al.* 1983, D. Smith*, et al.* 1985]. For the photon energy exceeding the bandgap, α increases rapidly to around 10^6-10^7 cm^{-1}, so the penetration depth of Si, GaAs and InP is very shallow. However, heat diffusion processes can spread laser generated defects to depths significantly exceeding those of the penetration depth α^{-1}. Note that the InP absorption at 248 nm (1.78×10^6 /cm) is slightly stronger than that at 193 nm (1.28×10^6 /cm). Thus, for a comparable reflection of this material at 193 and 248 nm, it is expected that the KrF laser radiation would be absorbed in shallower layer than that of the ArF laser.

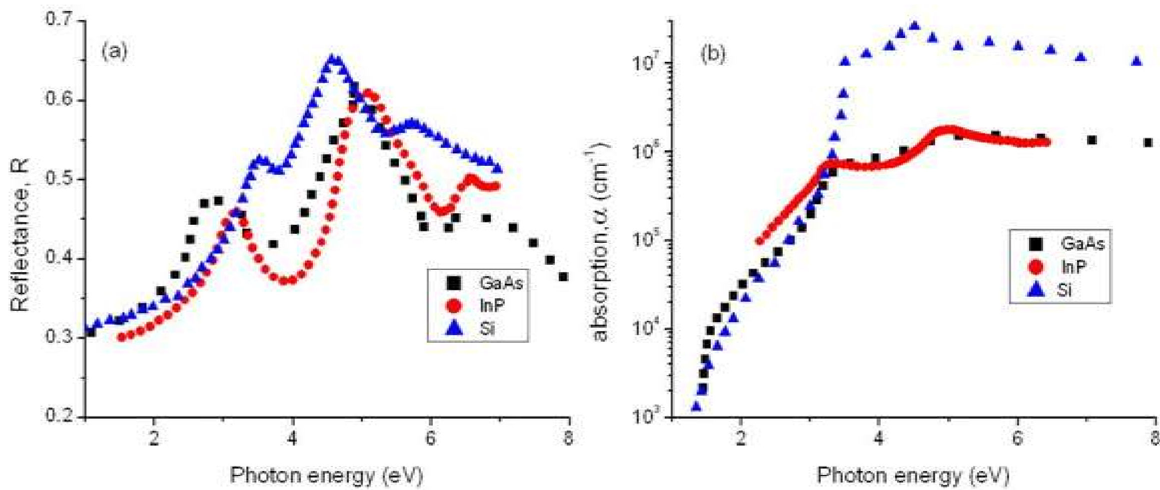

Figure 2. 1 Reflectance (R) and absorption (α) and and of GaAs, InP and Si as a function of incident light photon energy extracted from reference [H. Philipp*, et al.* 1963, S. S. Vishnubhatla*, et al.* 1968] and [D. E. Aspnes*, et al.* 1983, D. Smith*, et al.* 1985]

2.1.1 Laser induced temperature estimation

The primary effect of an intense laser pulse absorbed into a solid material with high absorption is heating of the surface layer to relatively high temperatures in only a few nanoseconds. The most important parameters in understanding thermal effects are the temperature distribution in the material and its development in time. Reasonable estimates of the surface temperature distribution can be made from solution to the thermal diffusion equation:

$$Q - \nabla(k(T)\nabla T) = \rho C \frac{\partial T}{\partial t} \tag{2. 2}$$

Where the inward heat source Q

$$Q = (1 - R)\alpha FP(t)e^{-\alpha z}G(r) \quad (2.3)$$

where ρ: material density; C: specific heat; k: thermal conductivity; F: laser fluence; *P(t)*: temporal pulse shape ($\int_0^\infty \frac{P(t)}{t_\ell}dt = 1$), t_ℓ is the pulse duration; *G(r)*: spatial laser beam shape, e.g. circular Gaussian beam is $G(r) = \exp\left(-\frac{2r^2}{{w_0}^2}\right)$; w_0: beam waist at the sample; *r*: beam radius coordinate; *z*: direction into the material; *T* and *t*: temperature and time, respectively. Although exact calculations have suffered from the problems of temperature dependent physical parameters that often are not easily predicated, good agreements between experiment and calculation are obtained when defining parameters function from experiments [R. F. Haglund*, et al.* 1997].

The boundary condition in the heat transfer process is as follows:

$$q_0 - h(T_{inf} - T) + Const({T_{amb}}^4 - T^4) = k\nabla T \quad (2.4)$$

Where q_0: inward flux; h: heat transfer coefficient; T_{inf}: temperature far away from the modeled domain; T_{amb} : ambient temperature (heat radiation); $Const$: Emissivity·sigma (Stefan Boltzman's heat radiation constant).

Numerical techniques such as finite difference or elemental analysis are required and succeeded to solve these equations [Radoslaw Stanowski*, et al.* 2006]. In most cases, there are assumptions that can be applied to simplify analytic solutions, e.g. treating material properties independent of T. In this project, commercial finite element method (FEM) software, (COMSOL group), was used to solve the heat transfer partial differential equation and calculate temperature temporal and spatial profiles. The FEM approach takes advantage of the finite element discretization of the calculated model's geometry into mesh elements. The properties of adjacent elements in the nodes of the generated net are shared during progressive iteration steps, so the energy flux phenomena could be calculated for, e.g. diffusion or heat transfer. The FEM method (Comsol software) allows generating mesh elements of various sizes and shapes, depending on the calculated physical process. The size of mesh elements is not only a critical factor for accuracy of the calculated results, but also it affects the total time of calculations. To simplify the calculations, we assumed that the irradiated samples are of circular shape. This allowed us to use a 2D model employing circular axial symmetry to investigate temperature modification in depth

of the microstructures (r-z). Calculations were carried out to determine the temporal temperature behavior in the middle of the laser irradiated spot as well as both spatial temperature profiles. The laser spot was situated in the center axis of the model's geometry. After designing the multilayer geometrical microstructure, the main material properties parameters in the above equations were defined in the software using the values in Table 2.1.

Table 2. 1. Thermal and mechanical properties of GaAs, InP and Si

	GaAs	InP	Si
k	0.425* (300/T)	0.68 (T=300)	1.3
ρ (g/cm^3)	5.31	4.81	2.329
C (J/g.K)	0.303+0.015 *(T/300)	0.31 (T=300)	0.7
*T_{melt} (K)	1520	1333	1680

*T_{melt} is the material melting temperature.

Figure 2.2 shows the geometry model of InP sample during KrF laser irradiation in air. In this model, (0, 0) is the laser spot center on the InP surface and the laser beam direction is along minus Z direction. The circular laser pulse duration is 23 ns, and repetition rate is 2 Hz. The circle laser spot size and sample size are $r_{laser} = 0.75 \times 10^{-3}$ m and $r_{InP} = 2.5 \times 10^{-3}$ m.

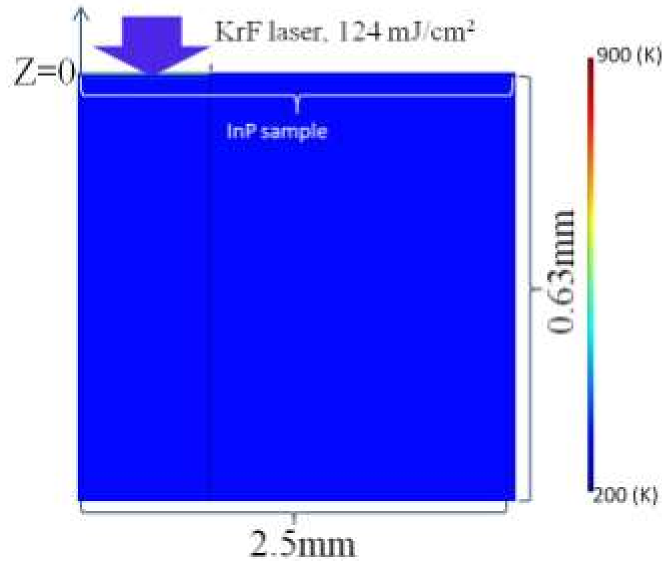

Figure 2. 2 Geometry model (Temperature profile) of InP sample during KrF laser irradiation in air at 124 mJ/cm^2

As the reflectance depends on laser wavelength, the heat source absorbed by the sample was comparable when it was irradiated by KrF laser at 124 mJ/cm^2 (R ~ 0.6) and by ArF laser at 82 mJ/cm^2 (R ~ 0.43). Here we take KrF laser irradiation at 124 mJ/cm^2 as an example for

numerical analysis of excimer laser induced temperature modification on samples. Figure 2.3 (a) and (b) shows the temperature dependence on time (t ≤ 1000 ns) in one pulse of center (0, 0) on InP surface after KrF laser irradiation in air and DI water at 124 mJ/cm^2. It shows that during laser pulses dwelling time, the temperature increases as time increases and reaches the maximum at 23 ns, then the temperature decreases. The temperature in the air quickly dropped back to room temperature (293 K) in 1000 ns while the temperature in DI water decreases more slowly to room temperature in 5000 ns (which is not shown here). As the time difference between two pulses is 30 s, there is no heat accumulation between two pulses. The maximum temperature is much lower than InP melting temperature 1333 K, so there is no obvious laser induced surface damage at 124 mJ/cm^2. It can be seen that the maximum temperature of 384 K is significantly lower in DI water than that irradiated in air.

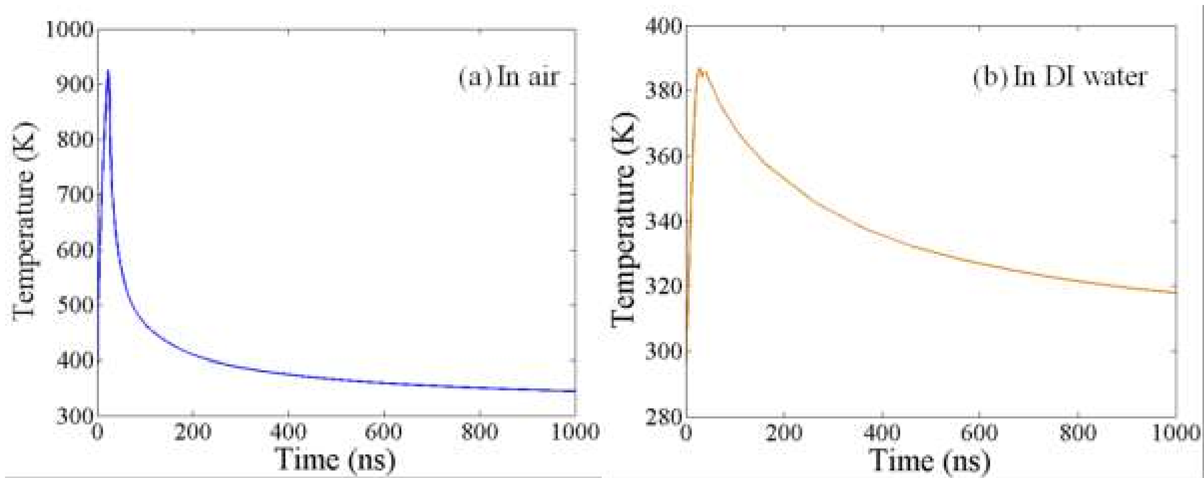

Figure 2. 3 Time dependent temperature of InP sammple irradiated by KrF laser at 124mJ/cm^2 in air (a) and DI water (b)

Figure 2.4 shows the temperature of InP surface dependence on z after KrF laser irradiation in air at 124 mJ/cm^2. It demonstrates that laser induced high temperature is only in the near surface region (~4 μm), due to high α. The thermal diffusion length which has obvious temperature increment is many times of absorption depth (~10 nm), as semiconductor is thermal conductive [J. E. Bjorkholm 1985]. The thermal diffusion length can measure how far the energy can spread during laser irradiation. The spread in energy during laser pulse or after laser pulse can change material properties. Therefore, for material with smaller absorption depth when irradiated with short pulse laser irradiation, the confinement can be relaxed by increasing the absorption and thermal diffusion length by changing of laser wavelength and pulse width.

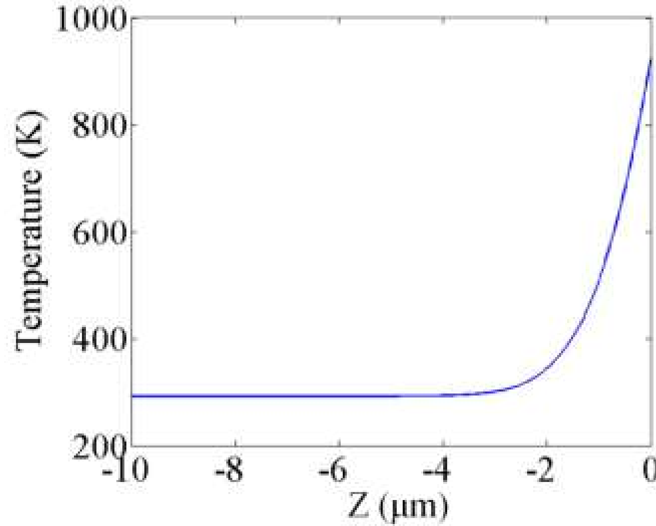

Figure 2. 4 Static temperature dependence on z of InP sample during KrF laser irradiation in air at 124 mJ/cm^2

Figure 2.5 shows the temperature of InP and SiO_2 surface dependence on time when InP surface was coated with 240 and 150 nm SiO_2 layer irradiated by KrF laser in air at 124 mJ/cm^2. SiO_2 layer is transparent to UV laser with low absorption (2.5 x 10^{-5}/cm) [D. Bauerle 2010]. The temperature of SiO_2 coated InP layer is lower than InP layer irradiated in air, which is possibly caused by higher reflection and thermal conductivity of SiO_2 layer. There is a time delay for SiO_2 layer reaches the maximum temperature compared to InP layer. The maximum temperature on SiO_2 surface is lower than that on InP surface. The maximum temperatures on InP are the same while the maximum temperature of SiO_2 layers decreases as the thickness of SiO_2 layer increases.

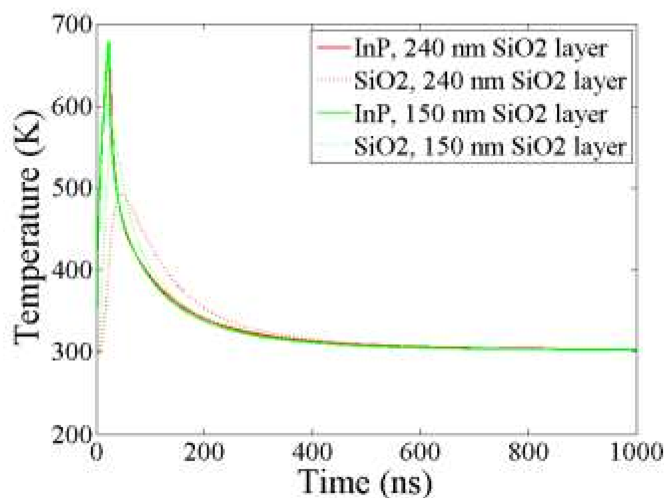

Figure 2. 5 Time dependent temperature of SiO_2 and InP surface of InP sample coated with 240 and 150 nm SiO_2 layer irradiated by KrF laser at 124 mJ/cm^2.

KrF laser induced different temperature on InP sample irradiated in air, DI water and through SiO_2 layer are due to different values of specific heat, k, and thermal conductivity, C,, as shown in Table 2.2. As the thermal conductivity of SiO_2 layer is greater than air, the heat transfers faster into SiO_2 than into air, and the peak temperature of the InP surface is lower. For the sample irradiated in DI water, both specific heat and thermal conductivity of water are higher than those of air. Specific heat is the ratio of heat energy transferred to an object and the resulting increase in temperature of the object: $C \equiv \frac{Q}{\Delta T}$. So, due to the higher specific heat, it is more difficult to increase the interface temperature when irradiated in DI water with same laser energy.

Table 2. 2 Thermal properties of water, air and SiO_2

	k, Specific heat(J/g.K)	C, Thermal conductivity (W/m.K)	Ref.
water	4.187	0.58	[E. toolbox 2005]
air	1	0.024	[E. toolbox 2005]
SiO_2	0.73	1.4	[A. S. Grove, *et al.* 1967]

For a sample coated by dielectric layers with higher absorption in UV, e.g. Si_3N_4 (~1.5×10^5 /cm) [D. Bauerle 2010] and InO_x layer (> 2×10^5 /cm) [S. Ray, *et al.* 1983], the temperature is very high (~ 1000 K) and even higher than that of InP material. Therefore, these dielectric layers were supposed to be easily ablated during excimer laser irradiation.

2.1.2 Laser induced surface morphology modification

Even if the laser induced temperature is below the threshold of melting, a variety of thermally activated processes could be observed. For instance, the rapid generation of large temperature gradients can induce thermal stress and thermo elastic excitation of acoustic waves. The stresses can contribute to the mechanical response of the material, such as work hardening, warping, or cracking [A. Hick 1983]. When the laser fluence is above the laser melting threshold, there will be formation of transient pools of molten material on the surface. High self-quenching rates with solidification front velocities up to several m/s can be achieved by rapid dissipation of heat into the cooler surrounding bulk material [W. M. Steen, *et al.* 2010]. At temperatures far above the melting temperature, hydrodynamic motion can reshape and redistribute material.

Convective and thermo capillary forces can cause significant deformations that are frozen in during solidification [J. Eizenkop*, et al.* 2008].

The laser ablation occurs above laser ablation threshold fluence. During this laser ablation, material removal rates typically exceed one-tenth monolayer per pulse; surface is structurally or compositionally modified at mesoscopic length scales; particle yields are superlinear functions of the density of excitation. A variety of mechanisms for material removal may be active during laser ablation depending on the particular material system and laser processing parameters [B. N. Chichkov*, et al.* 1996a]. At lower fluences, photo-electronic effects mechanism was first defects driven. Then photo thermal mechanisms for ablation include material evaporation and sublimation. With higher fluence, heterogeneous nucleation of vapor bubbles leads to normal boiling. If material heating is sufficiently rapid to approach its thermo dynamic critical temperature, rapid homogenous nucleation and expansion of vapor bubbles lead to explosive boiling (phase explosion) carrying off solid and liquid material fragments [N. M. Bulgakova*, et al.* 2001]. When the excitation time is shorter than the thermalization time in the material, non-thermal, photo chemical ablation mechanisms can occur. Overall, material removal is accompanied by a highly directed plume ejected from the irradiated zone. Recoil from the plume can generate shockwaves in the material, causing plastic deformation and work hardening of solid [A. H. Clauer*, et al.* 1977, A. H. Clauer*, et al.* 1981]. Resolidification of expelled liquid and condensation of plume material into thin films and clusters of nanoparticles can alter the topography at the rim and surrounding areas of the ablated region [N. G. Semaltianos*, et al.* 2008] .

One of the most important technologically applications related to laser induced surface morphology modification is laser surface texturing. Laser texturing of semiconductor surfaces can be utilized to decrease reflections and increase absorption for enhanced device performance, e.g. emission intensity of semiconductor LED surface, without altering bulk properties [T. Fujii*, et al.* 2005]. As shown in Figure 2.6 (a), a portion of light will specularly reflect from a flat surface, and have no further interaction with the material. Compared with this, protruding features on texturing surface can reflect and scatter light back on to the surface, as seen in Figure 2.6 (b). Light can effectively become trapped in devices and holes where multiple reflections enhance the coupling into the material. Once inside these protruded structures, multiple internal

reflections can guide the light into the bulk [E. Yablonovitch, *et al.* 1982]. Refraction at the surface of these structures also leads to transmission at oblique angles, effectively increasing the optical path length enhancing absorption [P. Campbell 1993]. Compared with other surface texturing techniques, like lithographic techniques combined with isotropic etching, laser texturing is a non-contact technique which can be utilized on both crystalline and polycrystalline material. There are two different methods which have been investigated for surface texturing to enhance the absorption. One is laser direct writing using a focused beam scanning across a surface in a pattern to selectively ablate material and define the structures, as shown in Figure 2.7 (a) and (b) [M. Halbwax, *et al.* 2008]. Laser direct writing has a great flexibility in defining surface structures; however, feature dimensions are limited by the focus size of the beam.

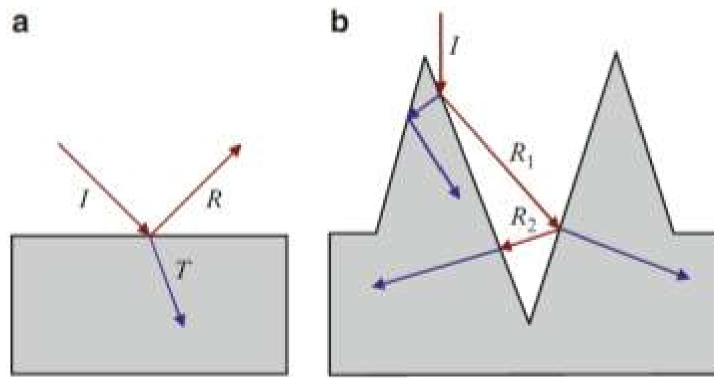

Figure 2. 6 (a) Light specularly reflecting from flat surface; (b) Multiple reflection from textured surface enhanced coupling into the material [P. Campbell 1993]

The second method is spontaneously forming quasi periodical structures on laser irradiated region. Arrays of high-aspect-ratio features such as cones or pillars will generate in the irradiated region, as shown in Figure 2.7 (c). Unlike laser direct writing, large areas can be textured with high absorbance features at once irradiation with unfocused beams during this process [L. A. Dobrzanski, *et al.* 2008]. The formation of laser induced periodical surface structures (LIPSS) has been investigated since 1960s. Low spatial frequency LIPSS were generally well understood and attributed to interference between the incident beam and a surface scattered wave resulting in an inhomogeneous energy deposition. The spacing period (Λ) is [Z. Guosheng, *et al.* 1982]:

$$\Lambda = \frac{\lambda}{1 \pm \sin\Theta} \tag{2.5}$$

where Θ is the incidence angle measured from the normal to the surface, λ is incident wavelength.

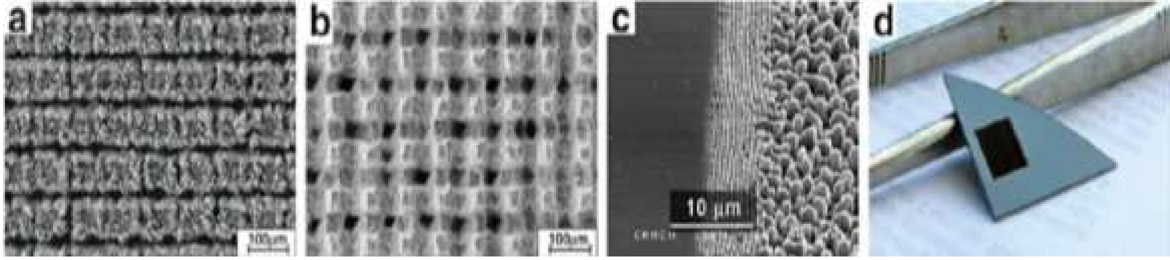

Figure 2. 7 SEM image of laser direct writing texturing features on Si substrate (a) before and (b) after etching of laser induced damage; (c) spontaneous formed Si surface features processed in vacuum with 800 nm, 100 fs pulses.(d) Square region of a Si wafer textured with spontaneously forming quasi-periodic microstructures appears black in contrast to the unprocessed regions [L. A. Dobrzanski, *et al.* 2008]

The formation mechanisms of high spatial frequency LIPSS remains a topic of debate in the current literatures and explanations, including nonlinear interactions, transient optical properties during irradiation, self-organization, and Coulombic explosion. E.g. Coulomb explosion has been reported to induce strong ionization of the surface and underlying region, which could be followed by particle ejection, and eventually forming nano-craters distributed inhomogeneously over the surface [Y. Dong, *et al.* 2004]. With a large number of additional pulses, reflections from the sides of these features will concentrate light into the surrounding valleys, activating a positive feedback mechanism where material is removed from the valleys and partially deposited onto the peaks. This can lead to the formation of high-aspect-ratio features such as cones or columns [F. Sanchez, *et al.* 1996]. Figure 2.7 c shows the LIPSS with periodicity equal to $\lambda \sim$ 800 nm, at the edge of their radiated region which transitions to cones in the irradiation center. These structures are highly efficient at trapping light and suppressing reflections. Figure 2.7 d shows the laser-textured square region of a Si wafer, which appears black in contrast to the highly reflecting unprocessed regions [L. A. Dobrzanski, *et al.* 2008]. The nature of the process and the details of the final microstructure, such as the shape of the cones or columns, the irregularity and density on the surface, chemical composition, and presence of nanostructure, depend strongly on the variables involved in the laser parameters and the ambient environment [D. H. Lowndes, *et al.* 2000]. This enhanced absorbance features has resulted, e.g., in high-sensitivity infrared photo detectors [J. E. Carey, *et al.* 2005] and high-quantum-efficiency avalanche photodiodes (APDs) [R. A. Myers, *et al.* 2006].

2.1.3 Laser induced surface chemical modification

Laser can induce a chemical reaction in two ways: raise temperature of the substrate (and/or reactants) to exceed the activation energy of a reaction, or electronically excite a material with photons to create bond breaking. These are termed as pyrolytic and photolytic processing, respectively. In a pyrolytic reaction, the laser serves as a heat source, which affects the reaction rate. In laser processing, two possibilities can limit the pyrolytic reaction rate: reaction kinetics and mass transport. At low laser fluences, kinetics is usually more important; at higher fluences, mass transport tends to become more important. In the kinetic limited mode, the reaction rate is given by Arrhenius type equation [L. V. Zhigilei*, et al.* 1999]:

$$R(t) = Const.n(t)exp\left\{-\frac{E_a}{K_B T(t)}\right\} \quad (2.6)$$

Where $n(t)$: density of reactants at the surface; E_a: activation energy; $T(t)$: surface temperature; K_B: Boltzman constant. The reaction rate is directly proportional to the density of reactants and temperature dependent reactants diffusion rate. Mass transport is of primary consideration in self terminating reactions like thermal oxidation where oxide grows on the surface, and prevents the oxygen from reaching the bulk material.

In photolytic reactions, direct photochemical bond breaking in an ambient, absorbate, or substrate occurs when a molecule absorbs a photon or multiple photons with sufficient energy. Bond energies, typically several eV, require UV photons or multiphoton absorption of longer wavelengths. The mechanism of photon dissociation involves an electronic transition from a ground state to an excited dissociative state. In many cases, both pyrolytic and photolytic reactions work simultaneously in laser processing and one reaction is dominating in the processing. Frequently, the laser chemical reaction is initiated photolytically and then proceeds pyrolytically. The change in the optical, thermal, mechanical and chemical properties of material surface and ambient environment will cause different results.

Due to their high photon energy (≥3.5 eV), excimer laser radiation is always reported to have high absorption in semiconductor material. When the laser light is absorbed by the semiconductor, the photon energy is converted to electronic vibrational energy [R. F. Haglund*, et al.* 1997]. The transformation of those photoexcited states into kinetic energy leads to the

ejection of atoms, ions, molecules and clusters from the material surface, which is called laser sputtering. In this process, laser desorption is defined as ejection of particles occurring without causing detectable mesoscopic modification to the surface composition or structure; and particle yield is a linear function of the density of electronic and vibrational excitation, without any significant gas dynamics effects in the steam of particles leaving the surface. This is different from laser ablation process discussed in 2.1.2, but the distinctions between each other are not very sharp.

Under vacuum environments, as the vapour pressure of V column is higher than that of III column, arsenic and phosphorous are preferentially sputtered from GaAs and InP. This will change the surface stoichiometry of semiconductor during laser irradiation [L. Vivet*, et al.* 1997] and the InP and GaAs surface becomes more metallic rich after laser irradiation [R. F. Haglund*, et al.* 1997]. However, it has also been found that the group III rich surface reduces the desorption rate of group V atoms which leads to an equal desorption of groups III and V atoms [M. Raff*, et al.* 1994]. The desorption rates of atoms also depend on laser irradiation environments. For example, a GaAs sample irradiated in a Cl_2 environment has its gallium and arsenic removed at the same rate. For example, a GaAs sample irradiated in a Cl_2 environment leads to the formation of $GaCl_3$. It results in the generation of Ga vacancies that further promotes desorption of Ga and, consequently, leads to the equal removal of surface As and Ga atoms [S. Takatani*, et al.* 1995].

Laser induced oxidation is based on thermal or non-thermal molecular-surface excitation. Single-photo dissociation of O_2 starts at around 5.1 eV ($\lambda \leq 240$ nm) [D. Bauerle 2010] when performed in air and O_2 atmosphere. Laser enhanced pyrolytic oxidation is similar as thermal oxidation. The laser induced temperature rise enhances the diffusion flux and the reaction rate of species within the irradiated area. However, the growth rate, composition, thickness, morphology and microstructure of laser fabricated oxide layers are different from thermal oxide layers fabricated at same temperature in the oven. Far-UV radiation results in gas phase formation of atomic oxygen (O) and ozone, which can efficiently react with many semiconductor surfaces. UV and far-UV laser can generate high concentration of O vacancies which increase the mobility of species, lower the temperature for surface melting. If photon energy exceeds the bandgap,

electron-hole pairs are generated within the oxides layer or substrate. Photoelectrons and holes can modify O adsorption on the surface, reaction with surface atoms or migration into surface to promote O dissociation. For semiconductors, these photoelectrons may be directly ejected into the oxides layer and modify the electric field. Laser enhanced oxidation of compound semiconductors, in particular of GaAs and InP, has been demonstrated with VIS- and UV- laser light. Light with photon energies $h\upsilon > E_g$ (GaAs, ~1.43 eV) increases O surface sticking coefficient by a factor of 10^3. This is related to the increase of electron transfer, which favors chemisorptions of O_2 and enhance the oxidation [Z. Lu*, et al.* 1990]. An increase in oxidation rate observed with 193 nm ArF laser irradiation is related to photodissociation of O_2. The stoichiometry of oxides depends on the laser parameters. After laser irradiation, the oxides layer mainly consists of Ga_2O_3 and variable amounts of As_2O_3 and As_2O_5. These amorphous oxide mixtures may crystallize and form stable Ga_2O_3 and $GaAsO_4$ [B. Schwartz 1975].

2.2 Quantum well intermixing

The optical properties, such as refractive index and absorption spectrum of III-V heterostructures are determined by the bandgap of QW. QWI is a process designed to change the bandgap of QW and reshape the potential profiles of QW, without the need of multiple etching and epitaxial regrowth steps.

2.2.1 General considerations

Solids can be separated into three categories depending on the relative positions of valence and conduction bands: metals, semiconductors and insulators, as shown in Figure 2.8 [B. G. Streetman*, et al.* 1995]. Metal's valence and conduction bands overlap and are partially filled, so electrons can move freely in the presence of an external force. In semiconductors and insulators, the bands are separated by a bandgap (E_g) empty of available energy states. Therefore, the bandgap is an energy barrier that an electron needs to overcome to jump to the conduction band where it can contribute to the electric conduction. Materials with bandgap below 2 eV are considered semiconductors while insulators have higher bandgap. The relatively small bandgap of semiconductors allows the excitation of electrons to the conduction band by a reasonable amount of thermal or optical energy.

The formation and the position of the bands are directly related to the coupling of electronic orbitals in a crystal. All elemental semiconductors (Si, Ge, C) can be found in the IV column of Mendeleev's periodic table and all have a crystalline structure similar to that of a diamond. Compound semiconductors are made of elements that, when combined, have a mean number of valence electrons equal to four. These compound semiconductors are either made of atoms from the III and V columns of the periodic table (III-V semiconductors: GaAs, GaP, GaSb, GaN, InAs, InP, InSb, InN, AlP, AlAs, AlSb, AlN), from II and VI columns (II-VI semiconductors: ZnO, ZnS, ZnSe, ZnTe, CdS, CdSe, CdTe, HgS, HgSe, HgTe), from IV group (IV-IV semiconductors: SiGe, SiC), or less known semiconductors from II and V groups (II-V semiconductors: Zn_3As_2, Cd_3As_2, Cd_3P_2). The combination of more than one binary compounds leads to the formation of ternary and quaternary compound semiconductors such as AlGaAs, InGaAs, InGaAsP and InAlGaAs.

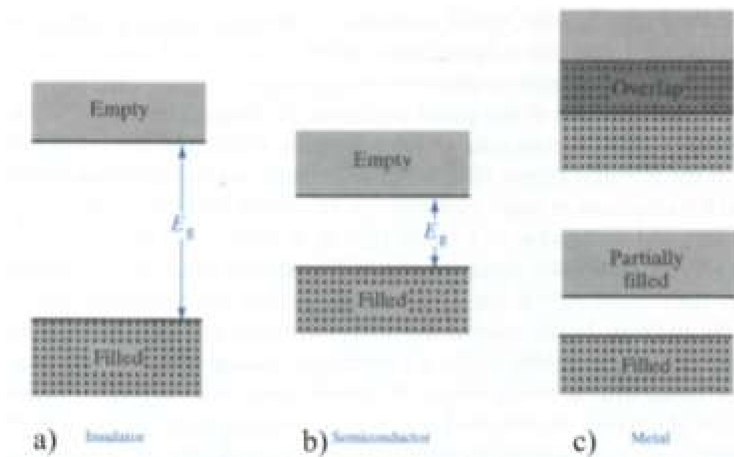

Figure 2. 8 Typical bands profiles at 0K for a) insulator b) semiconductor and c) metal [B. G. Streetman, *et al.* 1995]

2.2.2 Quantum semiconductor

QW is the result of a successive stacking of different materials, in which one thin "well" layer with a relatively small bandgap is surrounded by two "barrier" layers with larger bandgap, as shown in Figure 2.9 [B. G. Streetman, *et al.* 1995]. By extension, a quantum wire confines the carriers in two dimensions while a quantum dot confines them in three dimensions.

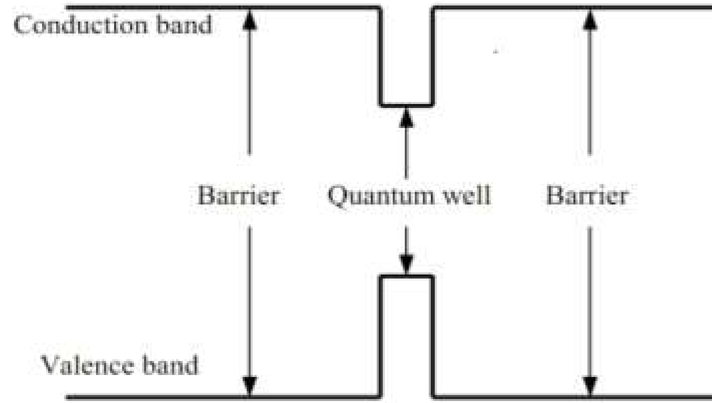

Figure 2. 9 Schematic of QW band structure

To minimize their energy, charge carriers tend to migrate toward the central region. Since the well thickness is of the order of electron wavelength inside the material, the well confines the charge carriers in the growth direction. The confinement leads to a discretisation of the energy levels inside the well. The levels position depends on the material composition and on the well thickness. The energy levels inside the well can be calculated through a simple "particle-in-a-box" model using Schrödinger equation in one dimension for particular particles (e.g. electrons or holes) [B. G. Streetman*, et al.* 1995]:

$$-\frac{\hbar^2}{2\mathrm{m_{eff}}}\frac{d^2\varphi_n(z)}{dz^2}+\mathrm{U}(z)\varphi_n=E_n\varphi_n(z) \tag{2. 7}$$

where U(z) is structural potential along epitaxial growth direction z, $\mathrm{m_{eff}}$ is effective mass of particle interest, E_n and φ_n are the eigenenergy and eigenfunction related to the n'th solution to the equation, ħ is reduced Plank's constant. If the barrier side of well is simply presumed infinitely high (infinite well), the solutions to E_n and φ_n are

$$E_n=\frac{-\hbar^2}{2\mathrm{m_{eff}}}\left[\frac{n\pi}{L_z}\right]^2, n=1,2\cdots\cdots, \varphi_n=\mathrm{A}\sin\left(\frac{\mathrm{n}\ \pi \mathrm{z}}{L_z}\right) \tag{2. 8}$$

where L_z is the width of the well. The energy levels are quadratically spaced and the wavefunctions are sine waves. The energy levels and wavefunctions in 'infinite well' are shown in Figure 2.10. As implied by equation 2.8, the spacing between energy levels is large for the narrow wells and small effective mass. For very large L, the distrubition of energies approaches a continuum. For the accurate QW with finite barrier side height, the solution of E_n and φ_n can

be calculated by choosing precise boundary conditions, e.g. wavefunctions must be continuous at boundary.

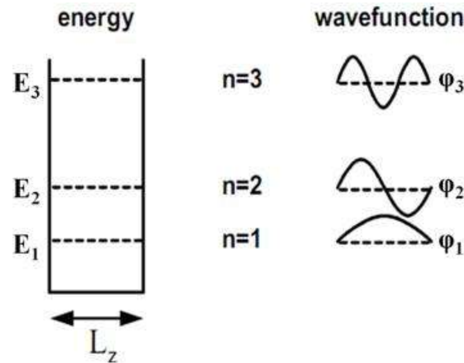

Figure 2. 10 Energy level, E_n, and wavefunctions, φ_n, in the infinite well [B. G. Streetman, *et al.* 1995]

2.2.3 Principle of quantum well intermixing

Since the QWs and barriers are made of different materials, there is atomic concentration gradient between the wells and barriers. At sufficiently high temperature, the diffusion forces associated with concentration gradient initiate the intermixing process [J. H. Marsh 1993]. This partially homogenizes the wells and barriers layers and changes the well shape. Figure 2.11 illustrates the changes in composition, in the potential well shape and in the position of energy level of conduction and valence band associated with the intermixing process. The major emission wavelength ($\lambda \sim 1/(E_g+E_e+E_h)$) shifts to shorter wavelength after intermixing, which is called blueshift, while the opposite is redshift.

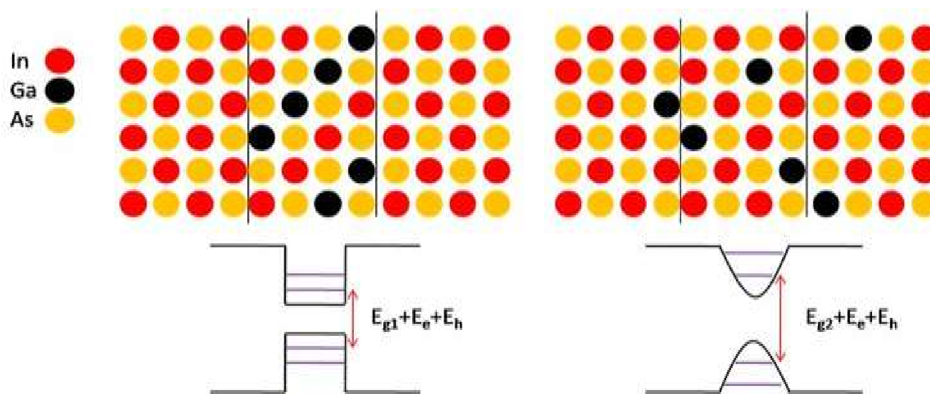

Figure 2. 11 Schematic of the band-structure and epitaxy of a non-processed vs. a QWI InGaAs/GaAs QW.

The interdiffusion process is characterized by a diffusion length L_d, which is defined as $L_d = \sqrt{D * t}$, where D is the interdiffusion coefficient and t is the annealing time of

processing [E. Li 2000]. In GaAs based QW, only group-III atoms diffuse between wells and barriers. In InP based QW, both the group III and group V can interdiffuse, each with their own diffusion lengths, ${L_d}^{III}$ and ${L_d}^{V}$. The compositions of group III element A, $w(z)$, and group V element C, $v(z)$ after interdiffusions are given by [E. Li 2000]:

$$w(z) = 1 - \frac{1-w}{2}\left[erf\left(\frac{L_z + 2z}{4{L_d}^{III}}\right) + erf\left(\frac{L_z - 2z}{4{L_d}^{III}}\right)\right] \tag{2. 8}$$

$$v(z) = \frac{v}{2}\left[erf\left(\frac{L_z + 2z}{4{L_d}^{V}}\right) + erf\left(\frac{L_z - 2z}{4{L_d}^{V}}\right)\right] \tag{2. 9}$$

Figure 2.12 illustrates the composition profile and conduction band optical confinement of interdiffused $In_{0.53}Ga_{0.47}As/InP$ QW, estimated from the equation (2.8) to (2.9) using our Comsol model. The charge carriers' energy levels in the intermixed well are determined by solving the Schrödinger equation in an envelope function:

$$-\frac{\hbar^2}{2}\frac{d\varphi_C(z)}{dz}\frac{d}{dz}\frac{1}{m_C(w(z),v(z))} + U_C(z)\varphi_C(z) = E\varphi_C(z) \tag{2. 10}$$

Where $m_C\big(w(z), v(z)\big)$ is effective mass of conduction band, which depends on composition $w(z), v(z)$, $U_C(z)$. So the position dependent potential energy due to changes in the conduction band edge can be calculated.

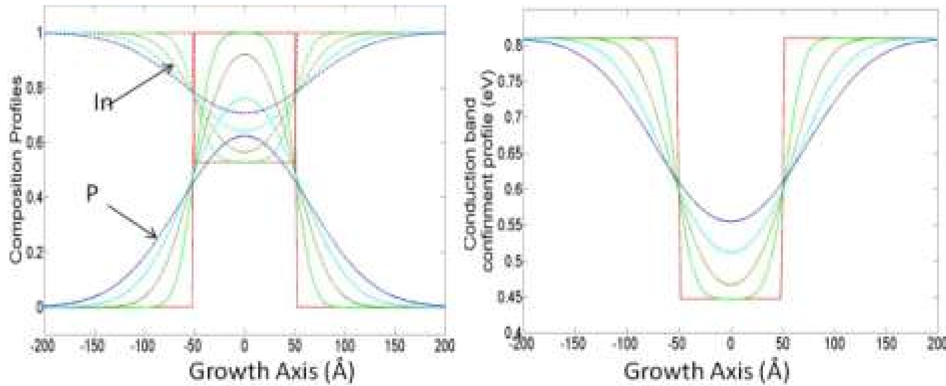

Figure 2. 12 Simulation of composition profile (a) and conduction band (b) of interdiffused $In_{0.53}/Ga_{0.47}As/InP$ QW with group III and V interdiffusion with identical rates for $\boldsymbol{L_d}$ =0, 10, 20, 30, 40Å.

2.2.4 Point defects influence on QWI

Defects, especially point defects, play an important role in QWI. For a given temperature, the concentration of a particular type of point defect will tend to reach its thermo-equilibrium concentration [R. Cohen 1997]. The defects diffusion follows Fick's law:

$$J = -D\nabla C_d \qquad (2.\ 11)$$

$$\frac{dC_d}{dt} = D[\nabla^2 C_d] + s \qquad (2.\ 12)$$

where J: point defects flux; D: diffusion coefficient; C_d: composition of defects; s: generation-annihilation term. The concentration gradient directs the point defects diffusion. The newly created defects will diffuse through active region to reach equilibrium. The passing through of point defects through the active region reduces the active energy needed for intermixing and increase the intermixing coefficient (D_{in}), given by following equation:

$$D_{in} = D_0 exp(-E_A/K_B T) \qquad (2.\ 13)$$

where D_0 : intermixing coefficient at infinite temperature; E_a: intermixing active energy; K_B: Boltzman constant; T: temperature. Three basic point defects assisted diffusion is shown in Figure 2.13 [J. D. Plummer 2009].

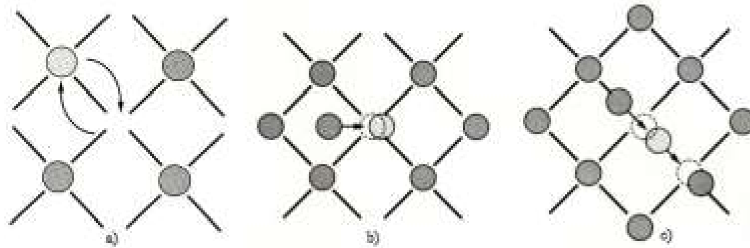

Figure 2. 13 Point defect assisted diffusion. a) Vacancy initiated diffusion, b) an interstitial kicks an atom out of its lattice site, c) diffusion channelling through interstitial jumps [J. D. Plummer 2009]

These included: lattice vacancies, interstitials, impurities, Frenkel defects, and anti-site defects, see Figure 2.14. Vacancies are empty lattice sites; interstitials are atoms, which occupy sites in the crystal between the regular lattice periods. Also of interest are: Frenkel pair (a pair of nearby interstitial and vacancy); impurities (atoms which don't belong to the pure crystal and can occupy interstitial sites or substitute themselves to regular atomic sites); anti-site defects (occur in ordered compound material when an atom of the sublattice A occupies a site on the sublattice B).

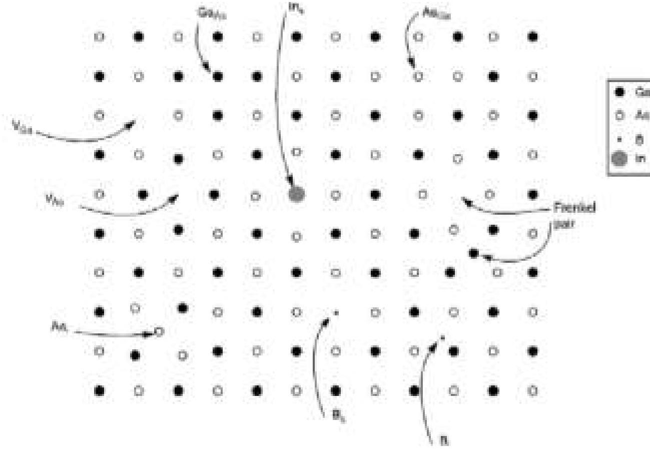

Figure 2. 14 Illustration of different point defects in a GaAs lattice. V stands for vacancy, i for interstitial for subtitutionnal, while the notation AB signifies that the atom A occupies the site of an atom B

If some external force is present, Fick's law (2.11) and (2.12) will change to

$$J = -D\nabla c + \frac{D}{k_B T} F * C_d \quad (2.14)$$

$$\frac{dC_d}{dt} = D[\nabla^2 C_d - (\nabla C_d * \nabla F + C_d \nabla^2 F)] + s \quad (2.15)$$

where F is the external force, which can be from i.e. an electric field, temperature gradient and mechanical stress inside the bulk. In the case of mechanical stress, the elastic force exerted on a defect depends strongly on the symmetry of the defect itself [J. D. Eshelby*, et al.* 1951]. This is due to the interaction of the applied strain field with the one produced by the defect. In the case of point defects in an isotropic material, the defect symmetry is spherical. We define the defect volume V as a function of the mean atomic site volume V_0 and mismatch parameter β:

$$V = V_0(1 + \beta) \quad (2.16)$$

Using this nomenclature, an interstitial constitutes a dilation center ($\beta > 0$), while a vacancy causes the lattice to compress ($\beta < 0$). The applied force on the defect can then be expressed as:

$$F = \beta \frac{4}{3} \pi r_0^3 \nabla T_r(\sigma) \quad (2.17)$$

where r_0 is the defect radius and $T_r(\sigma)$ is the trace of the stress tensor. It demonstrates that shear stress doesn't apply any force on a point defect; a stress gradient is required, under the same conditions, vacancies and interstitials are forced to drift in different direction. Under a stress gradient, Fick's laws are then expressed as:

$$J = -D\nabla C_d + \frac{D}{k_B T}\alpha\frac{4}{3}\pi r_0^3 \nabla T_r(\sigma) * C_d \tag{2. 18}$$

$$\frac{dC_d}{dt} = D\left[\nabla^2 C_d - \frac{4\alpha}{3}\pi r_0^3\left(\nabla C_d * \nabla^2 T_r(\sigma) + C_d \nabla^3 T_r(\sigma)\right)\right] + s \tag{2.19}$$

According to this equation interstitials are driven away from stress field maximum position while vacancies migrate toward it where they will cluster [D. T. Britton*, et al.* 2002].

Point defects can be generated in semiconductors by ion implantation or bombardment [S. Charbonneau*, et al.* 1998], oxidation or nitridation [T. Y. Tan*, et al.* 1985], pulsed laser irradiation [V. I. Emel'yanov*, et al.* 1992]. In ion implantation method, the collision between implanted ion and lattice atoms displaces the lattice atoms out of its site and creates defects and then following by rapid thermal annealing (RTA) to induce QWI [S. Charbonneau*, et al.* 1998]. Low acceleration energy (<500 keV), which creates defects above QW and induces less damage to the active region, and high acceleration energy (>500 keV), which penetrates deeper and creates defects directly in QWs, have been investigated in QWI process [V. Aimez*, et al.* 2002].

It was well established that pulse laser irradiation of elemental and compound semiconductors, even for energies $W = (0.05\sim0.1)W_m$, where W_m is the melting threshold, leads to the formation of defect. The defect formation on semiconductors under laser irradiation is due to heating [S. Akhmanov*, et al.* 1985], acoustical deformation [G. K. Celler*, et al.* 1984] and local electronic excitation of the surface [S. Karjagin*, et al.* 1984]. The electronic excitation is only for certain solid-normally and requires formation of unique excitations (e.g., self trapped excitation or direct band to band excitation into anti-bonding states - requires particular laser wavelengths). However, under $W < W_m$, this mechanism does not cause the formation of defects separately. When the energy of pulse laser is greater than the bandgap energy, the fraction of the energy of the photo-excited electron-hole pairs is transferred in the process of electron-phonon relaxation to the lattice and heats it. The strong rise in temperature (up to the melting point) leads to the generation of defects by thermal fluctuation, which are frozen at the end of the laser pulse due to the very rapid cooling (101 K/s). With the increase of the number of pulses, the density of the thermo fluctuation defects reaches its stationary value [J. Bourgoin*, et al.* 1983] :

$$N_d = Const.\exp[-\frac{E_d}{K_B(T_0 + \Delta T)}] \quad (2.20)$$

where T_0 : initial temperature; ΔT: laser induced temperature rise; E_d: defect formation energy; K_B: Boltzman constant.

The defect formation energy can be substantially reduced due to the localization of the electronic energy E_{ee} and laser induced lattice deformation, $E_d s \frac{\delta a}{a}$[J. Corbett, *et al.* 1975], where a is lattice constant, δa is the deviation of constant and s denotes to the type of a collision ($s \cong 4$ for elastic collision). Taking into account all these effects, the static defects concentration has the following equation:

$$N_d = Const.\exp[-\frac{E_A - E_{ee} - E_d s \frac{\delta a}{a}}{k_B(T_0 + \Delta T)}] \quad (2.21)$$

2.2.5 Strain influence on QWI

2.2.5.1 Strain and stress on semiconductors

Strain is the distortion of a material from its position in equilibrium. More generally, if we consider a deformation vector $\overrightarrow{(u_i)}$, linear strain (ε_{ii}) becomes:

$$\varepsilon_{ii} = \frac{\partial u_i}{\partial x_i}, \text{ i=1,2,3} \quad (2.22)$$

And the shear strain ($\varepsilon_{i,j}$) becomes:

$$\varepsilon_{i,j} = \frac{1}{2} * (\frac{\partial u_i}{\partial x_j} + \frac{\partial u_j}{\partial y_i}) \quad (2.23)$$

The presence of an exclusive shear strain does not alter the material volume while linear strain results in compression or dilation. The material dilation $div\vec{u}$:

$$div\vec{u} = \varepsilon_{xx} + \varepsilon_{yy} + \varepsilon_{zz} \quad (2.24)$$

Stress is the force associated with an elastic distortion:

$$\vec{F} = -div(\sigma) \quad (2.25)$$

Like strain, we define stress tensor σ

$$\sigma = \begin{bmatrix} \sigma_{xx} & \sigma_{xy} & \sigma_{xz} \\ \sigma_{yx} & \sigma_{yy} & \sigma_{yz} \\ \sigma_{zx} & \sigma_{zy} & \sigma_{zz} \end{bmatrix} \quad (2.26)$$

Strain and stress relate to each other through the Poisson ratio υ, the Young modulus Y_0 and the Shear modulus C':

$$\varepsilon_{xx} = \frac{1}{Y_0}(\sigma_{xx} - \upsilon(\sigma_{yy} + \sigma_{zz})) \quad (2.27)$$

$$\varepsilon_{xy} = \frac{\sigma_{xy}}{C'} = \frac{(1+\nu)\sigma_{xy}}{Y_0} \quad (2.28)$$

There are two specific stress configurations. The hydrostatic stress has identical linear components σ_{xx}=σ_{yy} =σ_{zz} and no shear component. The strain counterpart is a diagonal matrix with all non-null components $\varepsilon_{ii} = \sigma_{ii}(1-2\nu)/2Y_0$. Another is the baxial stress,

$$\sigma = \begin{bmatrix} \sigma_\perp & 0 & 0 \\ 0 & \sigma_\perp & 0 \\ 0 & 0 & 0 \end{bmatrix} \quad (2.29)$$

where $\sigma_\perp$ is the strain component in the material plane perpendicular to the growth direction. The corresponding strain tensor is:

$$\varepsilon_{baxial} = \frac{1}{Y_0}\begin{bmatrix} \sigma_\perp(1-\nu) & 0 & 0 \\ 0 & \sigma_\perp(1-\nu) & 0 \\ 0 & 0 & -2\nu\sigma_\perp \end{bmatrix} \quad (2.30)$$

In semiconductor materials, strain affects the band structure by shifting the conduction and valence band energies and modification of the trapping rate of carriers and excitons that change their effective masses [E. P. O'Reilly*, et al.* 1994]. To illustrate the effects of strain and stress on a real heterostructure, a single $In_xGa_{1-x}As$ well grown on InP substrate is taken as an example [A. R. Adams 2011]. In this case, thin $In_xGa_{1-x}As$ well with lattice constant a_f adapts itself to form a pseudomorphic strained layer with a new lattice parameter $a_\perp$ perpendicular to growth direction equal to the one of the substrate. The perpendicular (biaxial) strain in the QW

$$\varepsilon_\perp = \varepsilon_{xx} = \varepsilon_{yy} = \frac{a_s - a_f}{a_s} \quad (2.31)$$

In this case, when x < 0.53, $a_s > a_f$, the well lattice expands itself in the *xy* plane, contracts in the growth direction *z*. When x > 0.53, $a_s < a_f$, $\varepsilon_\perp < 0$, it is under compressive strain. A lattice matched QW is obtained for x = 0.53. To define strain effect on electron-hole recombination, we first need to define the biaxial strain tensor $\boldsymbol{\varepsilon}$,

$$\varepsilon = \begin{bmatrix} \varepsilon_{\perp} & 0 & 0 \\ 0 & \varepsilon_{\perp} & 0 \\ 0 & 0 & -2[{}^{c_{12}}/{c_{11}}]\varepsilon_{\perp} \end{bmatrix} \qquad (2.\ 32)$$

where $\varepsilon_{\perp}$ is the strain in the xy plan, it is negative for compressive strain and positive for tensile strain. c_{ij} are elastic deformation constants with $c_{12}/c_{11} = \nu/(1-\nu)$. The change in the bandgap is given by:

$$\triangle E_g(x) = -2a(\mathrm{x})(1 - \frac{c_{12}}{c_{11}})\varepsilon_{\perp} \qquad (2.\ 33)$$

and the splitting energy between heavy hole and light hole is expressed by:

$$S(x) = -b(x)(1 + 2c_{12}/c_{11})\varepsilon_{\perp} \qquad (2.\ 34)$$

where $a(\mathrm{x})$ is the hydrostatic deformation potential, and $b(x)$ is shear deformation potential. Therefore, in the form of compressive strain, the bandgap increases and the valence band splitting increases. In the case of tensile strain, the bandgap decreases by the baxial strain, as shown in Figure 2.15 [A. R. Adams 2011].

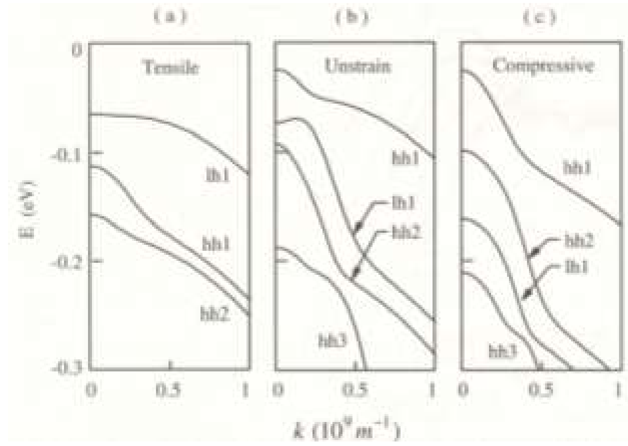

Figure 2. 15 Valence band structure calculated for tensile, unstrained and compressive strained of InGaAs well grown on InP [A. R. Adams 2011].

2.2.5.2 Strain and stress effects in intermixed QW

The interdiffusion of III and V column atoms modifies the atomic concentration profile between the wells and barriers. The composition profiles changes always lead to the strain generation or reduction in the wells thickness [E. Li 2000]. Figure 2.16 shows in-plane strain variation vs. interdiffusion length across a QW of a single lattice matched InGaAs/InGaAsP QW microstructure [H. Djie*, et al.* 2004]. The compressive strain appears in the well center, since the

lattice constant of $In_{0.53}Ga_{0.47}As$ well is always larger than barrier $In_{0.77}Ga_{0.23}As_{0.49}P_{0.51}$. The maximum compressive strain in the well center is 0.018%. As the interdiffusion length increases, the increase of lattice constant in the well is attributed to the compositional change in the wells, which corresponds to the increase of the In and P contents and the decrease of the Ga and As contents coherently. The compressive strain decreases almost entirely to 0 with increasing interdiffusion length, since the compositional profile tends to homogenize.

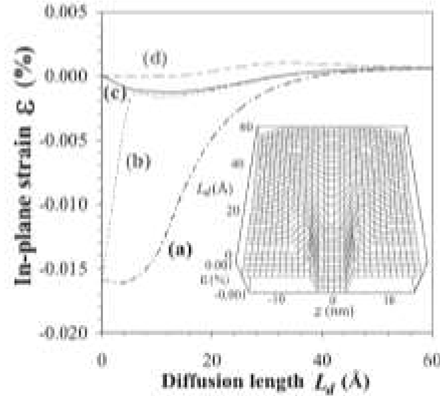

Figure 2. 16 Strain variation of identical interdiffusion v.s. interdiffusion length across a QW structure on the different positions: (a) well center (b) well close to the interface (c) barrier close to the interface (d) barrier center [H. Djie, *et al.* 2004].

2.2.5.3 External stressor layer effects on the QWI

The external stressors, such as oxide layers, have been reported to affect the point defects diffusion which modify the bandgap during annealing [D. T. Britton, *et al.* 2002]. This could result in the change of the luminescence properties of QW [M. Aumer, *et al.* 2000]. A well known stressor layer in the QWI process is SiO_xN_y [J. H. Marsh 1993, E. Li 2000, I. McKerracher, *et al.* 2012]. In this process, the generation of Ga vacancies takes place by two possible mechanisms: 1) outdiffusing of Ga atoms to the SiO_2 layer during RTA; 2) metallurgical reaction between Ga atoms and SiO_x layer. The Ga vacancies are driven away from the interface by the thermal stress [A. Pepin, *et al.* 1997a].

In the QWI process, a sample is annealed at high temperature to induce interdiffusion. The initial stress field in the microstructure is modified by the thermal stress due to coefficient of thermal expansion (CTE) mismatch between surface layers and substrates. The thermal stress or strain generated in the thin homogenized oxide film deposited on a thick microstructure substrate is given by:

$$\sigma_{th} = (\frac{E_f}{1-\upsilon_f})\Delta\delta\Delta T \quad (2.35)$$

where E_f and υ_f are the Young modulus and the Poisson coefficient, $\Delta\delta$ is the CTE mismatch between the film and substrate. Table 2.2 shows the index of CTE (δ), E_f and υ_f and the initial stress (σ_{in}) of some materials. At low temperature, SiO_2 films are under compressive stress, due to low CTE, and they become tensile at the annealing temperature. For Si_3N_4 films, the situation is different: films are under tensile stress at low temperature, as well as at the annealing temperature where a very high tensile stress is expected. So for SiO_2 layer, the tensile stress provides the driving force for Ga atoms diffusion away from the interface and leaves Ga vacancies (V_{Ga}) to cause intermixing. The semiconductor below the SiO_2 film is under compressive stress during annealing. In the second step, V_{Ga} is injected in a compressive region (active region) according to Fick's law with external force in equation (2.18) and (2.19) discussed in section 2.2.3. According to Table 2.2, the compressive stress generated by Si_3N_4 was obviously smaller and Si_3N_4 film is not porous to Ga or As atoms as SiO_2. This may lead to less efficient vacancy creation at the interface and later less intermixing. The stress effect is also verified by depositing Ga_2O_3 layer on top of the SiO_2 layer, as CTE of Ga_2O_3 is larger, which reduces the microstructure compressive stress below the SiO_2 layer. This suppresses the diffusion of this V_{Ga} and the intermixing [R. M. Cohen*, et al.* 1998].

Table 2. 3 Index of CTE (α), E_f and υ_f are the Young modulus and the Poisson coefficient, σ_{in} is the initial stress

Material	$\alpha(/K)$	$\left(\frac{E_f}{1-\upsilon_f}\right)$ (GPa)	σ_{in} (GPa)
SiO_2	0.52×10^{-6}	85.4	-0.2
Si_3N_4	2.8×10^{-6}	370	+2.26
GaAs	6.86×10^{-6}	…	…

As InP CTE ($4.6X10^{-6}$ /K) is larger than that of SiO_xN_y, the thermal stress (strain) also plays a similar role in InP based QW microstructure as in GaAs based QW microstructure. However, the initial defects generation processes varies with capping layers. When applying RTA between 650°C to 750°C, an InGaAs layer was usually required to induce the intermixing in the InGaAs/InP microstructures coated with SiO_xN_y [S. K. Si*, et al.* 1998, J. Teng*, et al.* 2002]. The

initial III or V defects were reported to generate on the InGaAs-oxide layer interface during SiO_xN_y deposition [M. K. Lee*, et al.* 2001]. The magnitude of PL shift is usually larger in samples coated with SiO_2 layer and InGaAs capping than that coated with Si_xN_y [S. Sudo*, et al.* 1996, J. H. Lee*, et al.* 1997]. In samples coated with Si_xN_y, P atom outdiffusion was reported to play an important role in the generation of defects [H. T. Yi*, et al.* 2002]. The blueshift amplitude, in that case, depended on the capping layer in the following order: InP>InGaAsP>InGaAs. After generation of defects with different capping layers, the thermal strain between dielectric layer and substrate promotes the diffusion of defects.

When a coating oxide layer has a larger CTE, the structure is under tensile stress during annealing at high temperature. A variety of layers, such as TiO_x (δ_{TiO2}=8.2 x 10^{-6} /K) [P. Gareso*, et al.* 2004], SrF_2 (δ_{SrF2}=37.5 x 10^{-6} /K) [J. Beauvais*, et al.* 1992] and Ga_2O_3 (δ_{Ga2O3}=7.3 x 10^{-6} /K) [L. Fu*, et al.* 2002] have been reported to suppress QWI by slowing down V_{Ga} diffusion due to the tensile stress induced during annealing on GaAs based QW microstructures. The similar suppression effect has also been observed in GaAs capped QW microstructure after KrF laser irradiation and annealing and explained as due to the formation of thick Ga oxide layer on irradiated sites [J. Genest*, et al.* 2007a]. Although the diffusion of vacancies is slowed down, interstitials were enhanced to diffuse from the interface to the active region according to (2.16) and (2.17) [D. T. Britton*, et al.* 2002]. This mechanism has also been used to induce bandgap engineering. For example, TiO_x has been proven to be effective to induce intermixing in InP based microstructures due to its large CTE [A. Francois*, et al.* 2006]. For InGaAs/InGaAsP/InP microstructure, different thicknesses TiO_x stressor layer is reported to promote both the native interstitials and externally injected P interstitials diffusion in the microstructure, resulting in enlarged wavelength shift [A. Francois*, et al.* 2006].

The strain can increase the heavy and light holes splitting gap as well as in-plane heavy hole effective mass and density of states. This will improve the optical properties, including PL intensity, laser diode gain and threshold current density of QW microstructure [E. P. O'Reilly*, et al.* 1994, M. Aumer*, et al.* 2000]. For InGaAsP/InP QW, the PL intensity was reported to be enhanced almost 10 times, when the compressive strain was increased from 0.8% to 1.4% [T. Tsuchiya*, et al.* 1994b]. Besides a lattice mismatched $In_xGa_{1-x}As_yP_{1-y}$ strain layer [A. R. Adams 2011], strain can also be generated into heterostructure by adding a surface stressor. The strain

induced by cooling from high deposition temperature to room measurement temperature always remains inside the QW microstructure [A. Pepin, *et al.* 1997a]. The compressive strain in the active region induced by TiO_x stressor in InGaAs/InGaAsP/InP cooled from a deposition temperature at 700°C to room temperature have been calculated from PL and Raman spectra measurements [A Francois, *et al.* 2006]. The similar compressive strain of anodic Ga oxides has been reported to enhance PL and cathode luminescence intensity by 2-3 times in intermixed GaAs based QW or quantum wire microstructures after RTA at high temperature [Y. Kim, *et al.* 1996, S. Yuan, *et al.* 1998]. Similarly, 2.6X and 1.5X enhancement of PL intensity has been found in InAlGaAs/AlGaAs/GaAs and AlGaAs/GaAs microstructure after KrF laser irradiation and annealing due to the formation of a thick Ga_2O_3 layer and a possible strain induced in the QW region [J. Genest, *et al.* 2007a]. The enhanced PL intensity was also found after XeCl laser processing of InGaAs/InGaAsP microstructure and RTA at 750°C for 10 s without bandgap modification. Auger electron spectroscopy showed the formation of thicker GaO_x layer in the processed microstructure, which could be a possible cause of enhanced PL intensity [J. J. Dubowski, *et al.* 1999b].

2.2.5.4 Laser induced InO_x stressor and QWI

Laser was reported to induce surface oxidation of InP substrate and formation of oxides that can be indentified on the In-P-O phase diagrams [G. Schwartz, *et al.* 1982]. During heating, O atoms penetrate the bulk InP and are adsorbed through In-O, P-O and In-O-P bond formation, as shown in Figure 2.17 [K. Santosh, *et al.* 2013]. When the sample is heated above 560°C, the relative low binding energy the P-O bond results in bond breaking and P is evaporated from the surface. This leads to the formation of polycrystalline In_2O_3 that represents the main oxide on the surface of irradiated and annealed InP [M. Yamaguchi, *et al.* 1980]. The free O atoms in III-V alloys disappear when heated above 520°C [R. Stall, *et al.* 1985]. In In-P-O, the O atom substitutes P sites in the InP host at certain level of coverage. As the O atomic radius (60 pm) is smaller than P atomic radius (100 pm), and O atoms have higher vibration frequency than that of P atoms, which results in a smaller lattice parameters and larger CTE [S. Qadri, *et al.* 2011]. As InP is zinc blend crystal and In_2O_3 is a cubic crystal, CTE of In-P-O mixture cannot be linearly extrapolated from the percentage of III-V alloy compound and In-metal-oxide [S. Adachi 1982, S. Qadri, *et al.* 2011]. However, it appears that CTE depends very weakly on the lattice structure

as SiO_2 and Si_3N_4 represents different in lattice structure, trigonal and hexagonal, respectively [I. McKerracher, *et al.* 2010]. CTE in SiO_xN_y is measured to increase monotonically with N composition and the maximum value of $\delta_{SiOxNy} = 2.3 \times 10^{-6}$ /K (y = 4/3) approach that of Si_3N_4 [I. McKerracher, *et al.* 2010]. Therefore, we can suppose that the CTE of the In-P-O after QWI can also increase in the similar linear way from ($\delta_{InP} = 4.6 \times 10^{-6}$/°C) to approach the higher value of In_2O_3 ($\delta_{In2O3} = 10.2 \times 10^{-6}$/°C) depending on the composition [R. Singh, *et al.* 1978]. Therefore, this altered layer causes the compressive strain in the intermixed QW microstructure when cooling from high RTA temperature to the room temperature. The thermal strain (stress) of thin film caused by temperature variation spatial profile can be calculated and simulated with COMOSOL [N. DeRoller, *et al.* 2010], following the equation (2.34).

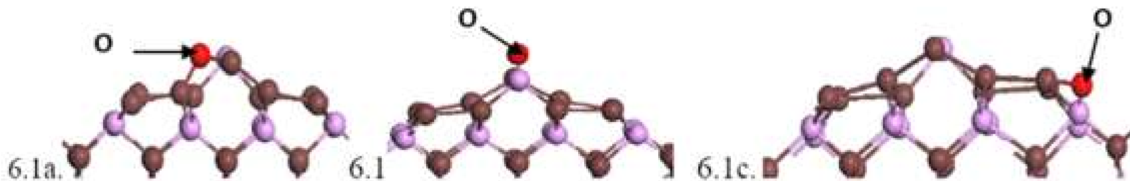

Figure 2. 17 View of oxygen adsorption on the InP (100). In, P, O, are indicated by brown, pink, and red spheres, respectively [K. Santosh, *et al.* 2013].

2.3 Summary

In the first part, it has shown some of the versatile capabilities of laser processing to modify the surface properties of materials in order to enhance their performance for a variety of applications. A variety of different material responses (temperature rise, surface modification) can be achieved depending on the material system and the laser parameters, allowing processes to be designed and optimized to permanently alter the material's surface chemistry, crystal structure, and morphology to suite its desired function. Laser processing offers new and unique processing possibilities that are impossible with currently available technologies.

In the second part, I describe the QWI concept. I have discussed the point defects generation and diffusion influence on QWI. The effects of strain from intermixed QW and external stressor layer (oxides layer) on the QWI process and the performance of QWI material have also been discussed.

2.4 Bibliography

Adachi, S., (1982), Material parameters of InGaAsP and related binaries, *Journal of Applied Physics*, vol. 53, 8775.

Adams, A.R., (2011), Strained-Layer Quantum-Well Lasers, *IEEE Journal of Selected Topics in Quantum Electronics,*, vol. 17, n°5, 1364-1373.

Aimez, V., Beauvais, J., et al., (2002), Low-energy ion-implantation-induced quantum-well intermixing, *IEEE Journal of Selected Topics in Quantum Electronics*, vol. 8, n°4, 870-879.

Akhmanov, S., Emel'yanov, V.I.i., et al., (1985), Interaction of powerful laser radiation with the surfaces of semiconductors and metals: nonlinear optical effects and nonlinear optical diagnostics, *Physics-Uspekhi*, vol. 28, n°12, 1084-1124.

Aspnes, D.E., and Studna, A.A., (1983), Dielectric functions and optical parameters of Si, Ge, GaP, GaAs, GaSb, InP, InAs, and InSb from 1.5 to 6.0 eV, *Physical Review B*, vol. 27, n°2, 985-1009.

Aumer, M., LeBoeuf, S., et al., (2000), Effects of tensile and compressive strain on the luminescence properties of AlInGaN/InGaN quantum well structures, *Applied Physics Letters*, vol. 77, n°6, 821-823.

Bauerle, D. (2010), Laser processing and chemistry (Springer Berlin), 788p.

Beauvais, J., Marsh, J., et al., (1992), Suppression of bandgap shifts in GaAs/AlGaAs quantum wells using strontium fluoride caps, *Electronics Letters*, vol. 28, n°17, 1670-1672.

Bjorkholm, J.E.: ‘Light induced etching of InP by aqueous solutions of H_3PO_4’, US Patent 4,518,456,, 1985.

Bourgoin, J., and Lannoo, M. (1983), Point defects in semiconductors: Experimental aspects (Springer), 301p.

Britton, D.T., and Härting, M., (2002), The Influence of Strain on Point Defect Dynamics, *Advanced Engineering Materials*, vol. 4, n°8, 629-635.

Bulgakova, N.M., and Bulgakov, A.V., (2001), Pulsed laser ablation of solids: transition from normal vaporization to phase explosion, *Applied Physics A*, vol. 73, n°2, 199-208.

Campbell, P., (1993), Enhancement of light absorption from randomizing and geometric textures, *JOSA B*, vol. 10, n°12, 2410-2415.

Carey, J.E., Crouch, C.H., et al., (2005), Visible and near-infrared responsivity of femtosecond-laser microstructured silicon photodiodes, *Optics Letters*, vol. 30, n°14, 1773-1775.

Celler, G.K., and Leamy, H.J., (1984), Modification of Silicon properties with lasers, Electron beams, and incoherent light, *Critical Reviews in Solid State and Material Sciences*, vol. 12, n°3, 193-265.

Charbonneau, S., Koteles, E.S., et al., (1998), Photonic integrated circuits fabricated using ion implantation, *IEEE Journal of Selected Topics in Quantum Electronics*, vol. 4, n°4, 772-793.

Chichkov, B.N., Momma, C., et al., (1996), Femtosecond, picosecond and nanosecond laser ablation of solids, *Applied Physics A: Materials Science and Processing*, vol. 63, n°2, 109-115.

Clauer, A.H., Fairand, B.P., et al., (1977), Laser shock hardening of weld zones in aluminum alloys, *Metallurgical Transactions A*, vol. 8, n°12, 1871-1876.

Clauer, A.H., Holbrook, J.H., et al. (1981), Shock waves and high-strain-rate phenomena in metals,chapter 38, Effects of laser induced shock waves on metals, Springer,p. 675-702.

Cohen, R., (1997), Point defects and diffusion in thin films of GaAs, *Materials Science and Engineering: R: Reports*, vol. 20, n°4, 167-280.

Cohen, R.M., Li, G., et al., (1998), Native defect engineering of interdiffusion using thermally grown oxides of GaAs, *Applied Physics Letters*, vol. 73, n°6, 803-805.

Corbett, J., and Bourgoin, J. (1975), Point Defects in Solids 2. Semiconductors and Molecular Crystals. (Plenum Press, New York), 480p.

DeRoller, N., Qazi, M., et al., (2010), Characterization of an AlGaN/GaN Electrostatically Actuated Cantilever using Finite Element Method, *Proceedings of COMSOL Conference 2010* vol., 101.

Djie, H., Mei, T., et al., (2004), Experimental and theoretical analysis of argon plasma-enhanced quantum-well intermixing, *IEEE Journal of Quantum Electronics*, vol. 40, n°2, 166-174.

Dobrzanski, L.A., Drygata, A., et al., (2008), Laser surface treatment of multicrystalline silicon for enhancing optical properties, *Journal of Materials Processing Technology*, vol. 201, n°1-3, 291-296.

Dong, Y., and Molian, P., (2004), Coulomb explosion-induced formation of highly oriented nanoparticles on thin films of 3C–SiC by the femtosecond pulsed laser, *Applied Physics Letters*, vol. 84, n°1, 10-12.

Dubowski, J.J., Poole, P.J., et al., (1999), Enhanced quantum-well photoluminescence in InGaAs/InGaAsP heterostructures following excimer-laser-assisted surface processing, *Applied Physics A: Materials Science & Processing*, vol. 69, 299-303.

Eizenkop, J., Avrutsky, I., et al., (2008), Single-pulse excimer laser nanostructuring of silicon: A heat transfer problem and surface morphology, *Journal of Applied Physics*, vol. 103, n°9, 094311-094311-094316.

Emel'yanov, V.I., and Kashkarov, P.K., (1992), Laser-induced defect formation in semiconductors, *Applied Physics A*, vol. 55, n°2, 161-166.

Eshelby, J.D., and Eshelby, J., (1951), The force on an elastic singularity, *Philosophical Transactions of the Royal Society of London. Series A, Mathematical and Physical Sciences*, vol. 244, n°877, 87-112.

Francois, A., Aimez, V., et al., (2006), Measurements ofTiOx stress induced on InP/InGaAs InGaAsP quantum well heterostructures, *Journal of Vacuum Science & Technology A: Vacuum, Surfaces, and Films*, vol. 24, n°3, 797-801.

Francois, A., Aimez, V., et al., (2006), Enhancement of quantum well intermixing on InP/InGaAs/InGaAsP heterostructures using titanium oxide surface stressors to induce forced point defect diffusion, *Applied Physics Letters*, vol. 89, 164107.

Fu, L., Wong-Leung, J., et al., (2002), Suppression of interdiffusion in GaAs/AlGaAs quantum-well structure capped with dielectric films by deposition of gallium oxide, *Journal of Applied Physics*, vol. 92, n°7, 3579-3583.

Fujii, T., David, A., et al., (2005), Cone-shaped surface GaN-based light-emitting diodes, *physica status solidi (c)*, vol. 2, n°7, 2836-2840.

Gareso, P., Buda, M., et al., (2004), Suppression of thermal atomic interdiffusion in C-doped InGaAsAl/GaAs quantum well laser structures using TiO_2 dielectric layers, *Applied Physics Letters*, vol. 85, n°23, 5583-5585.

Genest, J., Dubowski, J.J., et al., (2007a), Suppressed intermixing in InAlGaAs/AlGaAs/GaAs and AlGaAs/GaAs quantum well heterostructures irradiated with a KrF excimer laser, *Applied Physics A: Materials Science & Processing*, vol. 89, n°2, 423-426.

Genest, J., Dubowski, J.J., et al., (2007b), UV laser controlled quantum well intermixing in InAlGaAs/GaAs heterostructures, *Journal of Physics: Conference Series*, vol. 59, 605-609.

Grove, A.S., and Grove, A. (1967), Physics and technology of semiconductor devices (Wiley New York), 143p.

Guosheng, Z., Fauchet, P., et al., (1982), Growth of spontaneous periodic surface structures on solids during laser illumination, *Physical Review B*, vol. 26, n°10, 5366.

Haglund, R.F., Miller, J.C., et al. (1997), Laser ablation and desorption (Academic Press), 641p.

Halbwax, M., Sarnet, T., et al., (2008), Micro and nano-structuration of silicon by femtosecond laser: Application to silicon photovoltaic cells fabrication, *Thin Solid Films*, vol. 516, n°20, 6791-6795.

Hick, A., (1983), Rapid Surface Heat Treatments--a Review of Laser and Electron Beam Hardening, *Heat Treat Metal*, vol. 10, n°1, 3-11.

Karjagin, S., Kashkarov, P., et al., (1984), Jahn-Teller effect on silicon surface under laser irradiation, *Surface Science*, vol. 146, n°2, L582-L586.

Kim, Y., Yuan, S., et al., (1996), Effects of anodic oxide induced intermixing on the structural and optical properties of quantum wire structure grown on nonplanar GaAs substrate, *Journal of applied physics*, vol. 80, n°9, 5014-5020.

Lee, J.H., Si, S.K., et al., (1997), Bandgap tuning of $In_{0.53}Ga_{0.47}As$/InP multiquantum well structure by impurity free vacancy diffusion using $In_{0.53}Ga_{0.47}As$ cap layer and SiO_2 dielectric capping, *Electronics Letters*, vol. 33, n°13, 1179-1181.

Lee, M.K., Song, J.D., et al., (2001), Intermixing behavior in InGaAs/InGaAsP multiple quantum wells with dielectric and InGaAs capping layers, *Applied Physics A*, vol. 73, n°3, 357-360.

Li, E. (2000), Semiconductor quantum wells intermixing (CRC), 669p.

Lowndes, D.H., Fowlkes, J.D., et al., (2000), Early stages of pulsed-laser growth of silicon microcolumns and microcones in air and SF_6, *Applied Surface Science*, vol. 154-155, n°0, 647-658.

Lu, Z., Schmidt, M., et al., (1990), Ultraviolet-light-induced oxide formation on GaAs surfaces, *The Journal of Chemical Physics*, vol. 93, 7951.

Marsh, J.H., (1993), Quantum well intermixing, *Semiconductor Science and Technology*, vol. 8, n°6, 1136.

McKerracher, I., Fu, L., et al., (2010), Thermal expansion coefficients and composition of sputter-deposited silicon oxynitride thin films, *Journal of Physics D: Applied Physics*, vol. 43, n°33, 335104.

McKerracher, I., Fu, L., et al., (2012), Intermixing of InGaAs/GaAs quantum wells and quantum dots using sputter-deposited silicon oxynitride capping layers, *Journal of Applied Physics*, vol. 112, n°11, 113511.

Myers, R.A., Farrell, R., et al., (2006), Enhancing near-infrared avalanche photodiode performance by femtosecond laser microstructuring, *Applied Optics*, vol. 45, n°35, 8825-8831.

O'Reilly, E.P., and Adams, A.R., (1994), Band-structure engineering in strained semiconductor lasers, *IEEE Journal of Quantum Electronics*, vol. 30, n°2, 366-379.

Pepin, A., Vieu, C., et al., (1997), Evidence of stress dependence in SiO2/Si3N4 encapsulation-based layer disordering of GaAs/AlGaAs quantum well heterostructures, *Journal of Vacuum Science & Technology B: Microelectronics and Nanometer Structures*, vol. 15, n°1, 142-153.

Philipp, H., and Ehrenreich, H., (1963), Optical properties of semiconductors, *Physical Review*, vol. 129, n°4, 1550.

Plummer, J.D. (2009), Silicon VLSI technology: fundamentals, practice, and modeling (Pearson Education India), 817p.

Qadri, S., Fahed, C., et al., (2011), Thermal expansion studies of indium-iron oxide, *Physica Status Solidi (b)*, vol. 248, n°4, 928-930.

Raff, M., Schutze, M., et al., (1994), Laser-stimulated nonthermal particle emission from InP and GaAs surfaces, *Physical Review B*, vol. 50, n°15, 11031.

Ray, S., Banerjee, R., et al., (1983), Properties of tin doped indium oxide thin films prepared by magnetron sputtering, *Journal of Applied Physics*, vol. 54, n°6, 3497-3501.

Sanchez, F., Morenza, J., et al., (1996), Whiskerlike structure growth on silicon exposed to ArF excimer laser irradiation, *Applied Physics Letters*, vol. 69, n°5, 620-622.

Santosh, K., Wang, W., et al., (2013), First principles study on InP (001)-(2X 4) surface oxidation, *Journal of Applied Physics*, vol. 113, n°10, 103705-103705-103708.

Schwartz, B., (1975), GaAs surface chemistry review, *Critical Reviews in Solid State and Material Sciences*, vol. 5, n°4, 609-624.

Schwartz, G., Sunder, W., et al., (1982), The In-P-O Phase Diagram: Construction and Applications, *Journal of Electrochemical Society*, vol. 129, n°6, 1361-1367.

Semaltianos, N.G., Perrie, W., et al., (2008), Nanoparticle formation by the debris produced by femtosecond laser ablation of silicon in ambient air, *Materials Letters*, vol. 62, n°14, 2165-2170.

Si, S.K., Deok Ho, Y., et al., (1998), Area selectivity of InGaAsP-InP multiquantum-well intermixing by impurity-free vacancy diffusion, *IEEE Journal of Selected Topics in Quantum Electronics*, vol. 4, n°4, 619-623.

Singh, R., and Shewchun, J., (1978), A possible explanation for the photovoltaic effect in indium tin oxide on InP solar cells, *Journal of Applied Physics*, vol. 49, n°8, 4588-4591.

Smith, D., Shiles, E., et al. (1985), Handbook of Optical constants of Solids (Academic Press), 999p.

Stall, R., Wunder, R., et al., (1985), Effect of oxygen on In0.53Ga0.47As films grown by molecular beam epitaxy, *Applied Physics Letters*, vol. 47, n°5, 518-520.

Stanowski, R., Voznyy, O., et al., (2006), Finite element model calculations of temperature profiles in Nd: YAG laser annealed GaAs/AlGaAs quantum well microstructures, *Journal of Laser Micro/Nanoengineering*, vol. 1, 17-21.

Steen, W.M., and Mazumder, J. (2010), Laser material processing (Springer), 401p.

Streetman, B.G., and Banerjee, S. (1995), Solid state electronic devices (Prentice-Hall Englewood Cliffs, NJ), 476p.

Sudo, S., Onishi, H., et al., (1996), Impurity-free disordering of InGaAs/InGaAlAs quantum wells on InP by dielectric thin cap films and characterization of its in-plane spatial resolution, *Japanese Journal of Applied Physics*, vol. 35, n°part 1, 1276-1279.

Takatani, S., Yamamoto, S., et al., (1995), Excimer laser assisted etching of AlGaAs and GaAs, *Journal of Vacuum Science & Technology B: Microelectronics and Nanometer Structures*, vol. 13, n°6, 2340-2343.

Tan, T.Y., and Gesele, U., (1985), Point defects, diffusion processes, and swirl defect formation in silicon, *Applied Physics A*, vol. 37, n°1, 1-17.

Teng, J., Dong, J., et al., (2002), Controlled group V intermixing in InGaAsP quantum well structures and its application to the fabrication of two section tunable lasers, *Journal of Applied Physics*, vol. 92, 4330.

http://www.engineeringtoolbox.com/

Tsuchiya, T., Komori, M., et al., (1994), Investigation of effect of strain on low-threshold 1.3 um InGaAsP strained-layer quantum well lasers, *Electron. Lett.*, vol. 30, n°10, 788-789.

Vishnubhatla, S.S., and Woolley, J.C., (1968), Reflectance spectra of some III-V compounds in the vacuum ultraviolet, *Canadian Journal of Physics*, vol. 46, n°16, 1769-1774.

Vivet, L., Dubreuil, B., et al., (1997), Laser irradiation of GaAs/GaAlAs multi-quantum well structure, *Applied Surface Science*, vol. 119, n°1, 117-126.

Yamaguchi, M., and Ando, K., (1980), Thermal oxidation of InP and properties of oxide film, *Journal of Applied Physics*, vol. 51, n°9, 5007-5012.

Yablonovitch, E., and Cody, G.D., (1982), Intensity enhancement in textured optical sheets for solar cells, *IEEE Transactions on Electron Devices*, vol. 29, n°2, 300-305.

Yi, H.T., Cho, J., et al., (2002), Dielectric cap quantum well disordering for band gap tuning of InGaAs/InGaAsP quantum well structure using various combinations of semiconductor-dielectric capping layers, *Journal of Materials Science Letters*, vol. 21, n°22, 1739-1741.

Yuan, S., Jagadish, C., et al., (1998), Anodic-oxide-induced intermixing in GaAs-AlGaAs quantum-well and quantum-wire structures, *IEEE Journal of Selected Topics in Quantum Electronics*, vol. 4, n°4, 629-635.

Zhigilei, L.V., and Garrison, B.J., (1999), Molecular dynamics simulation study of the fluence dependence of particle yield and plume composition in laser desorption and ablation of organic solids, *Applied Physics Letters*, vol. 74, n°9, 1341-1343.

Chapter 3 Experimental procedures

In this chapter, I describe excimer laser (ArF, KrF) setups employed for processing of QW wafers and I provide details about investigated semiconductor microstructures and about the characterization methods used in the project.

3.1 Excimer laser irradiation techniques

3.1.1 Excimer lasers and beam homogenization

The name of **excimer** comes from **exci**ted di**mer** molecules used as a lasing medium [D. Basting, *et al.* 2005]. Many different excimer lasers have been developed at wavelengths from 126 to 660 nm. The most commonly used excimer lasers are xenon chloride (XeCl, 308 nm), krypton flouride (KrF, 248 nm), argon fluoride (ArF, 193 nm) and fourine (F_2, 157 nm). The production of excited dimer molecules in an electric discharge is based on a complex plasma reaction process. These reactions take place on nanosecond scale and leave the excited molecule at rather unstable upper state. The excited molecule decays after a few nanoseconds into atoms and emits photons. The ground states components atoms are then available for another lasing circle. Because of the unstable ground state, excimer lasers do not have ground state saturation effect and have relatively high efficiency. Because of short spontaneous lifetime of laser transition and fast loss process in nanoseconds, laser requires an excitation pump source with power density exceeding 1 MW/cm^2 which can only be obtained in pulsed systems. This limits excimer laser to a pulse mode operation.

The various applications of excimer laser are related to its unique short UV and deep UV wavelengths, high pulse energy and high average power. The application of excimer laser can be divided into three areas: material processing, medical therapeutics and basic research. In material processing, the most widely industrial application of excimer laser is high resolution photolithography up to below 45 nm by KrF and ArF laser, called as ‘excimer laser lithography’ [B. La Fontaine 2010]. Excimer lasers have also been used for laser deposition of film coating [P. Willmott, *et al.* 2000]. In addition to these application in material processing, there exists great amount application of excimer laser, like chemical surface alteration, heating, laser assisted

chemical surface cleaning and semiconductor processing [D. Basting*, et al.* 2005, D. Bauerle 2010]. Semiconductor processing has been considered as the largest and fastest growing market for excimer laser applications.

The raw beam coming out of an excimer laser is of low coherence and spatially non-uniform. To avoid the formation of spots of increased intensity (hot spots), it is necessary to homogenize the laser beam. A device made of arrays of fly-eye microlenses is one of the most efficient homogenizing systems. Typically, it consists of two parallel arrays of cylindrical lenses. The incoming laser beam is first divided into many beamlets by the first array. The beamlets converge in a focal plane between the two arrays where they form an array of point images. The second array brings back the incoming beamlets to a parallel configuration and then are all refocused by a collector lens. The homogenized laser beam is focused in the focal plane of the objective and it consists of the sum of all the collected beamlets. Fly-eye beam homogenizers are specially used for mask projection lithography and in micromachining tools [X. Zhang*, et al.* 1996].

ArF and KrF lasers setup used in this project employ GSI Lumonics Pulse Master laser delivering pulses of ~20 ns length with energy up to 230 and 450 mJ/pulse, respectively. A schematic idea of an excimer laser setup is shown in Figure 3.1. A variable attenuator controls the incident beam intensity of the laser. The laser beam is homogenized by a double micro-lens fly-eye-array homogenizer and delivered to the place of the projection mask holder. Figure 3.2 shows the intensity profile of homogenized (top-hat profile) ArF (a) and KrF (b) laser beams that have been used to irradiate different masks. The masks are placed in the focal plane of the objectives that allows a delivering of 1.8 and 2.6 demagnifications with ArF and KrF laser, respectively. Metallic stainless steel masks have been used in our experiments, because UV light is highly absorbed in the metal and it can be totally blocked in the unwanted region of the masks. As these metal masks can be usually damaged by laser sputtering, melting or mechanical damage, and high quality dielectric masks that can sustain high laser fluences could be used for application requiring high power irradiation.

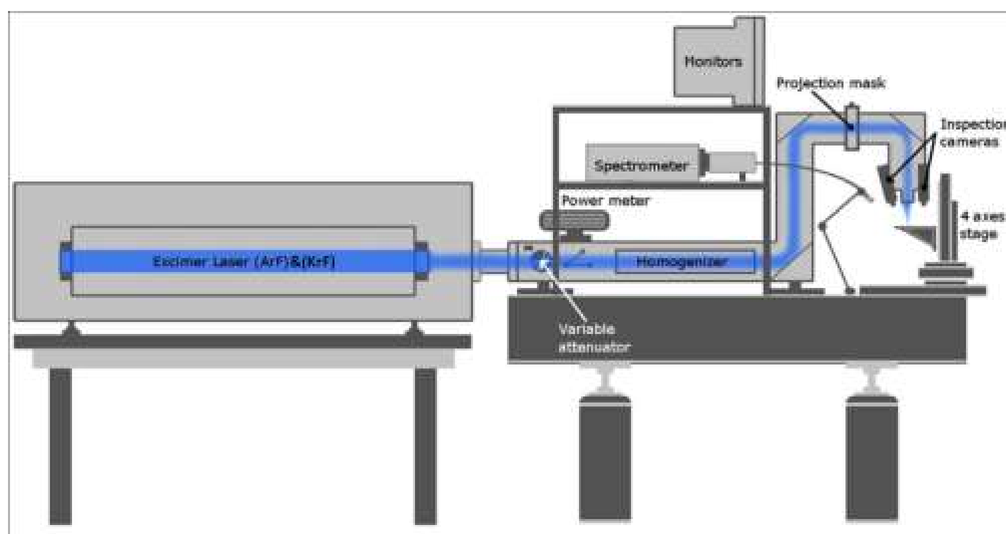

Figure 3. 1 Schematic of excimer laser (ArF & KrF) irradiation setup

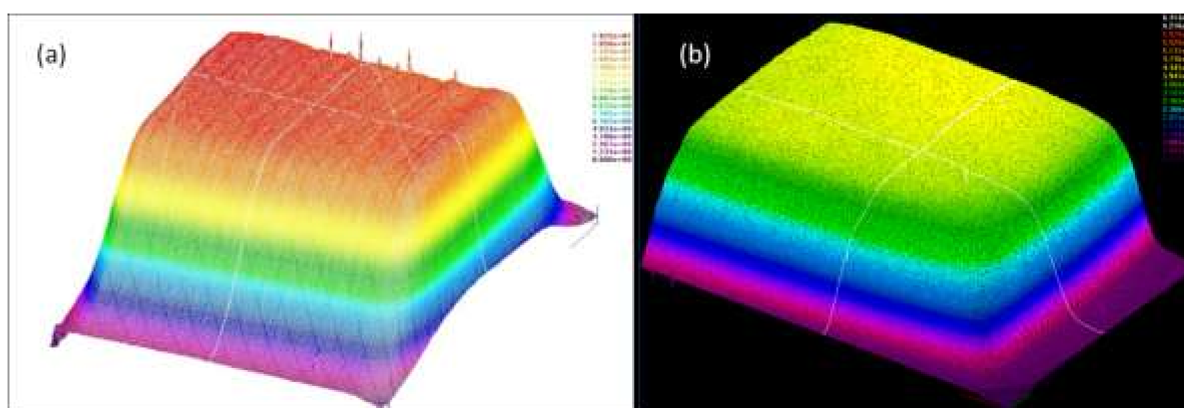

Figure 3. 2 ArF (a) and KrF (b) laser beam profiles

3.1.2 Sample chamber and positioning

A microchamber for holding samples surrounded by different environments is built by inserting a 0.74 mm thick silicone rubber between an UV transparent (T > 90%) fused silica glass and normal glass slide. The chamber was filled with different liquid solutions (e.g. DI water, methanol, etc) with samples immersed in the liquid before sealing. Due to low evaporation temperature of organic liquid, a fused silica glass slide with microfluidic tubes was used to provide continuing liquid environments during experiment. The chamber was installed on a sample stage equipped with computer controlled X-Y-Z-Theta stage. The setup allowed for the processing of the same sample at numerous sites with a lateral resolution of 10 µm. An inspection camera was used to monitor in situ macroscopic changes of the sample surface during irradiation.

3.2 Studied heterostructures

3.2.1 InP based full laser QW microstructure

3.2.1.1 M1580 : InP/InGaAs/InGaAsP QW microstructures

A schematic cross-section of the InP/InGaAs/InGaAsP QW microstructure (M1580) is shown in Figure 3.3. The microstructure was deposited on an S-doped InP substrate covered with a 1400 nm thick InP (Si: $2x10^{18}cm^{-3}$) buffer. The active region, consisting of five 5.5-nm-thick intrinsic InGaAs QWs separated by four 12 nm thick intrinsic InGaAsP barriers, was designed to emit at 1.55 µm at room temperature. The active region was confined by two 142-nm-thick graded bandgap InGaAsP layers, $\leq 5 \times 10^{15}$ cm^{-3} top side and from 5×10^{15} cm^{-3} to 5×10^{17} cm^{-3} graded bottom, Zn doped. The top cladding InP layer (Zn: 6×10^{17} cm^{-3}) was separated by a 10-nm-thick InGaAsP (Zn: 6×10^{17} cm^{-3}) etch stop layer. A 100 nm thick InGaAs (Zn: 8×10^{18} cm^{-3}) contact layer on top of the microstructure was separated from the InP cladding layer by a second 50-nm-thick InGaAsP etch stop layer (Zn: 5×10^{18} cm^{-3}). The whole microstructure was covered with a 400-nm-thick undoped InP sacrificial layer.

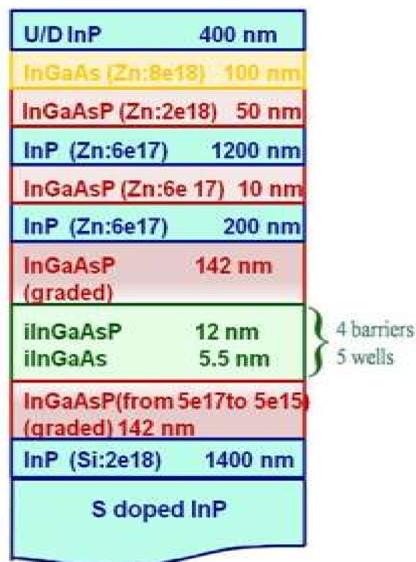

Figure 3. 3 Schematic cross-section of the investigated InP/InGaAs/InGaAsP microstructure (M1580)

3.2.1.2 ZJU : InP/InGaAsP/InGaAsP QW microstructure

The investigated sample of InP/InGaAsP/InGaAsP (ZJU) is a 1.2 % compressive strained laser structure containing five $In_{0.8}Ga_{0.2}As_{0.8}P_{0.2}$ QWs with 1.25Q InGaAsP barriers. From the surface the layers are a 0.5 µm Zn-doped (10^{18} cm^{-3}) InP sacrificial layer, 0.2 µm Zn-doped (10^{19} cm^{-3}) $In_{0.53}Ga_{0.47}As$ cap, 1.5 µm Zn-doped (10^{18} cm^{-3}) InP cladding, 0.004 µm Zn-doped (4 x 10^{17} cm^{-3}) 1.3Q InGaAsP etch-stop layer, five repeats of 10 nm undoped $In_{0.8}Ga_{0.2}As_{0.8}P_{0.2}$ barriers and 5.5 nm undoped strained $In_{0.8}Ga_{0.2}As_{0.8}P_{0.2}$ wells which is sandwiched by 60 nm and 80 nm InGaAsP step-graded index confining layers, and 1.5 µm Si-doped (2 x 10^{18} cm^{-3}) InP buffer on Si-doped (4 x 10^{18} cm^{-3}) InP substrate. It emits at 1530 nm at room temperature.

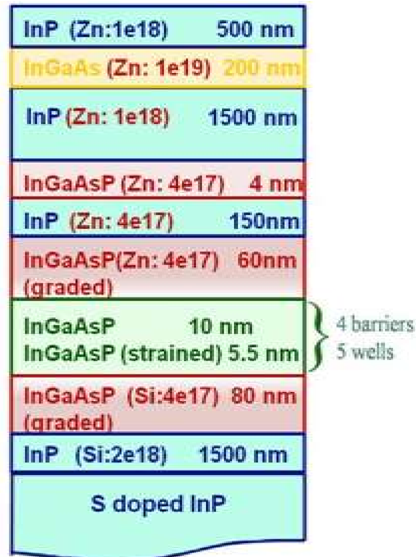

Figure 3. 4 Schematic cross-section of the investigated InP/InGaAsP/InGaAsP microstructure (ZJU)

3.2.2 RAC82: InP based QW microstructure with shallow cap region

An InGaAs/InGaAsP/InP microstructure with shallow cap region was grown on n-doped InP (001) substrate and it was designed to emit at 1.540 µm at room temperature. The microstructure comprises five (5) 6-nm-thick strained (1%) $In_{0.47}Ga_{0.53}As$ QWs (Si: 6 x 10^{17} cm^{-3}) separated by four (4) 10-nm-thick $In_{0.74}Ga_{0.26}As_{0.57}P_{0.43}$ barriers (Zn: 6 x 10^{17} cm^{-3}). The optical confinement is provided by 110 (Si: from 8 x 10^{17} cm^{-3} to 1 x 10^{18} cm^{-3}) and 20 nm (Zn: 5 x 10^{17} cm^{-3}) thick InGaAsP graded bandgap materials interfacing the substrate and surface side of the QW stack. The whole microstructure was capped with a 30-nm thick P doped InP layer (Zn: 5 x 10^{17} cm^{-3}). Another 40 nm InP layer (Zn: 5 x 10^{17} cm^{-3}) was separated by a thin layer InGaAsP (Zn: 5 x 10^{17}

cm^{-3}) from the cap. There is 1500 nm InP buffer layer (Si: 5 x 10^{18} cm^{-3}) between the heterostructure and substrate.

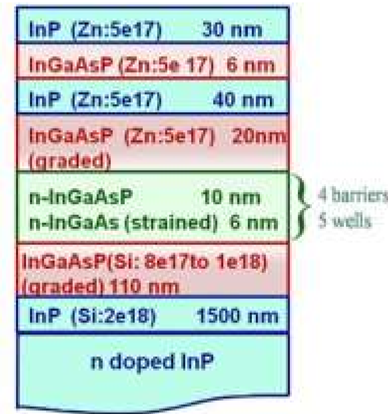

Figure 3. 5 Schematic cross-section of the investigated InP/InGaAs/InGaAsP microstructure (RAC82)

3.2.3 T0808: InGaAsP/GaAs QW microstructure

T0808 InGaAsP/GaAs contains single 8.5 nm GaAs well were confined by two 100 nm thick InGaAsP layers with graded Si doped from 6 x 10^{17} cm^{-3} to 6 x 10^{16} cm^{-3}. On top of this QW, there is 200 nm InGaP layer (Si: 6 x 10^{17} cm^{-3}) capped with 5 nm n doped GaAs QW layer (Si: 6 x 10^{17} cm^{-3}). Below the QW, there is 1 μm InGaAs layer (Si: 6 x 10^{17} cm^{-3}). The whole microstructure is grown on semi-insulating GaAs substrate separated by 50 nm intrinsic GaAs buffer layer. The microstructure was designed to emit at 920 nm.

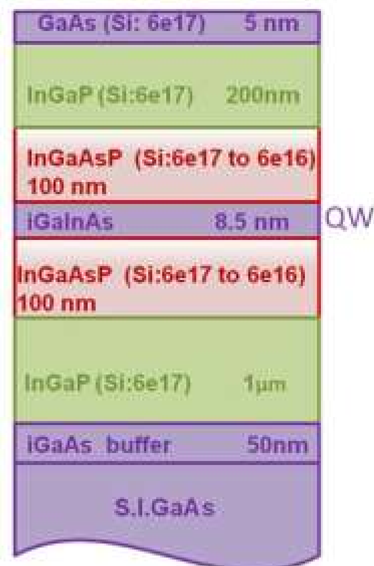

Figure 3. 6 Schematic cross-section of the investigated T0808 InGaAsP/GaAs quantum well microstructure

3.3 Rapid thermal annealing

Rapid thermal annealing (RTA) is a process used in semiconductor device fabrication that, unlike a normal furnace heating, can increase the temperature of a whole wafer rapidly (in 10s of seconds). Wafers can be heated in order to activate dopants, change film-to-film or film-to-wafer substrate interfaces, densify deposited films, change states of grown films, repair damage from ion implantation, move dopants or drive dopants from one film into another or from a film into the wafer substrate. Figure 3.7 is the RTA setup (Jetfirst, Jipelec) used in our project. An array of lamps provides the heat and the temperature is measured by a thermocouple and pyrometer combination. Computer controlled with a temperature range up to maximum 1000 °C at a ramp rate from 1 to 30°C/sec. Single 4" semiconductor wafers can be rapidly heated to a set temperature at a controllable recipe. Piece parts can also be annealed by resting them on a 4" silicon platform. Samples can be processed in 3 atmospheres, including oxygen, nitrogen and forming gas (N_2:H_2 = 9:1). In our case, forming gas atmosphere were used in order to prevent oxidation of the samples from residual adsorbed water vapor or oxygen [D. Paine*, et al.* 1993].

Figure 3. 7 Photograph of RTA setup

3.4 Characterization methods

3.4.1 Photoluminescence measurements

Photoluminescence (PL) is a process of photons emission by a semiconductor that absorbs photons whose energy exceeds that of the semiconductor bandgap (E_g). In a direct bandgap (E_g) semiconductor, the electrons are excited from valence band to conduction band when it was excited by excitation source with photon energy than semiconductor, $hv > E_g$. The electrons relax to the bottom of the conduction band through phonon emission. Then the recombination of the electrons with holes at the top of valence band results in the emission of photons with a wavelength corresponding to the semiconductor bandgap. In addition to interband transition, PL can probe transitions between impurities levels, interband traps, defects and bound quasi-particles. PL intensity offers qualitative information on the quality of the studied material. For example, a weaker signal is usually attributed to a high density of surface states and other non-radiative processes associated with the presence of defects. Other non-radiative processes associated with the presence of defects are also responsible for quenching PL signal. The full width at half-maximum (FWHM) of the PL signal is often considered as an indicator of the quality of the studied sample. As suggest by the Heisenberg uncertainty principle,

$$\Delta E \Delta t = \hbar/2 \quad (3.\ 1)$$

Where $\hbar$ is the reduced Plank constant, a broadening in of the PL peak is associated with shorter carrier's lifetime. In QW microstructure, the broadening of FWHM is always associated with variation in the of confinement energies in different wells [T. H. Gfroerer 2000] and the generation of trapping defects or the relaxation of strain [A. Lee*, et al.* 2001]. When the quality of investigated semiconductor varies spatially, the PL signal will change with sample position.

The instrumentation required for PL measurement is modest, which includes excitation source (laser), objective lens, spectrometer and photodector, as shown in Figure 3.8. The excitation source intensity controls the density of photoexcited electrons and holes, which has great influence of the PL signal intensity. The incident light wavelength determines the photon penetration depth in the semiconductor microstructure. Therefore, the laser source should be carefully chosen to probe PL signal of QW structure in particular depth. Although PL signal

depends strongly on temperature, liquid helium low temperature being required for the highest spectral resolution, room temperature measurement is sufficient for most purposes.

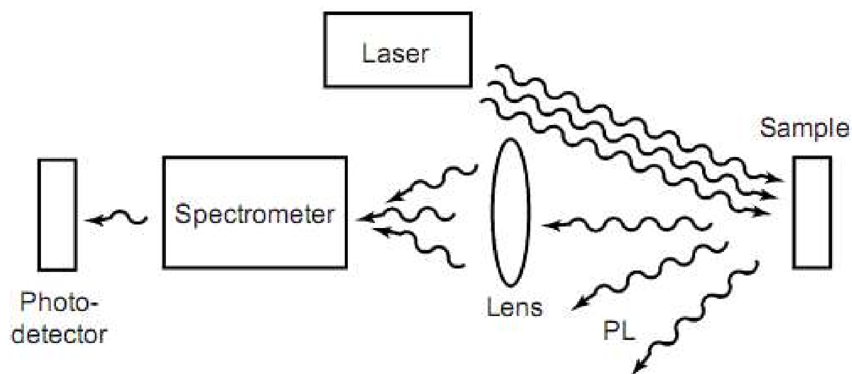

Figure 3. 8 Typical experimental set-up for PL measurements

Room temperature PL measurements were carried out with a commercial mapper (Philips PLM-150) equipped with Nd: YAG laser (λ=1064 nm and λ=532 nm) to excite the sample. PL signal was dispersed by a monochromator and detected by an InGaAs photodiode array. The minimum spatial scanning resolution is 10 μm and the spectral resolution is 0.6 nm.

Hyperspectral photoluminescence mapper (HI-PLM) developed by our group was operated to test its application in the high resolution mapping of PL signal variation on one sample after UV laser QWI. HI-PLM is a specially modified microscope system. The instrument captures 2D images of a sample (XY image) spectrally dispersed in a 3rd dimension as a function of the collected light's energy (E). The final images produced by the system are stored within a cube of data, generating a "hyperspectral" cube in which each volume pixel (voxel) corresponds to a coordinate in (x, y, E). In the normal mode of imaging, the images recorded by the camera are direct images of the sample, XY image. The HI-PLM system possesses a second imaging which allows creating images in the 2th conjugate space (conjugate space imaging). Thus, the camera of the system can record K_xK_y images instead of XY images. The full sample area is excited with a continuous wave 532 nm laser in this system, and mapping acquisition in the spectral region of interest, typically 200 nm, takes about 70 s. The computer-based interface of the HI-PLM system allows for an automated the collection of a time series of PL maps in 10 min intervals. Sample illumination was controlled by a computer-programmed shutter that opened during PL integration time only. Dark maps were also recorded and used for background subtraction. A

fused silica window reflected 4% of the excitation source to a Centronic OSD100–7Q calibrated silicon photodiode for power normalization, establishing PL stability within 3% variation.

3.4.2 Surface morphology characterization

3.4.2.1 Profilometry

A commercial profilometer (KLA AlphaStep® D-120 system) was used to measure small variations in the vertical direction. When the stylus of the contact profilometer scans over the sample surface, small surface variations cause the stylus to move up or down, which is transformed to an analog signal with an accelerometer. A contact profilometer can usually measure vertical features from nm to µm. The lateral resolution, however, is limited by the stylus size (~ 5 to 25 µm). The applied instruments has an 800 µm Z range, sub-angstrom resolution, 6 angstrom step height repeatability, and a manual x-y theta sample positioning stage. The graphical user interface permits the user to analyze the data while acquiring additional measurements.

3.4.2.2 Atomic Force microscopy

Atomic Force microscopy (AFM) is a popular tool to image, measure and manipulate material in nanoscale [F. J. Giessibl 2003]. As shown in Figure 3.9, AFM consists of a cantilever, typically Si or Si_3N_4, with a sharp tip (probe) with radius of nm at its end that is used to scan the sample surface. When the tip is brought into proximity of a sample surface, forces between the tip and the sample lead to a deflection of the cantilever according to Hooke's law [B. Cappella*, et al.* 1999],

$$F = -k_s * z \qquad (3.\ 2)$$

where F is the force, k_s is the stiffness of the lever, and z is the distance the lever is bent. A feedback mechanism is employed to adjust the tip-to-sample distance to maintain a constant force between the tip and sample. Images are created by scanning the tip in the x, y plane and recording the z position required to keep force constant. The resulting map of the area $z = f(x,y)$ represents the surface morphology of the sample.

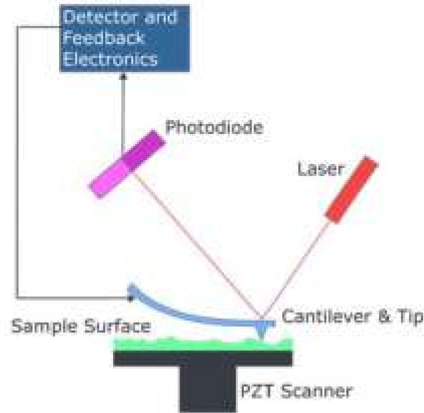

Figure 3. 9 Schematic of atomic force microscope [L. Gross*, et al.* 2009]

In general, AFM can be divided into static (contact) and dynamic (non-contact or tapping) modes [L. Gross*, et al.* 2009]. In static mode, the cantilever is dragged across the sample surface and the contours of the surface are measured directly using the deflection of the cantilever. In non-contact mode, the cantilever is oscillated in the attractive regime, quite close to the sample without touching it. The detection is based on measuring changes to the resonant frequency or amplitude of the cantilever. In tapping mode, the cantilever is driven to oscillate up and down near its resonance frequency similar to non-contact mode. However, the amplitude of this oscillation (100 to 200 nm) is greater than non contact mode (10 nm), so the tip intermittently taps the surface. Tapping mode reduces the damage to the surface and the tip compared to contact mode. It also has higher lateral resolution than non contact mode.

AFM has also been used to determine the surface roughness, such as Root-mean-square roughness (RMS) which is calculated from height variations from a mean surface level,

$$R_q = \sqrt{\sum_{i=1}^{N} \frac{(Z_i - Z_m)^2}{(N-1)}} \tag{3. 3}$$

where N is the number of pixels in the image, Z_i is the height of the i_{th} pixel, and Z_m is the mean height. As tapping mode tips response faster than contact mode tips to surface features, it offers a more accurate roughness measurement [G. Simpson*, et al.* 1999].

Figure 3.10 shows MultiMode™ scanning probe microscope (MM-SPM, Digital Instrument) used in our project for tapping mode AFM image. Typically, samples are fixed to metal disks, and then magnetically attached to the top of the scanner tube. The scanner with sample moves

back and forth, allowing the probe to extract information from the sample surface. The piezo stack continuously excites the cantilever's oscillation, and the tip is deflected in its encounter with the surface. The reflected laser beam reveals information of the sample surface. The AFM is in-situ controlled by Nanoscope software (Digital Instrument). An etched single-crystal Si tip with rectangular cantilever (TESP, Digital Instruments) was used for collecting images. The tip radius is around 5-20 nm, the cantilever stiffness is 20-100 N/m and the resonance frequency is around 200-400 kHz. The information collected can be analysed off-line to yield sectional profiles, depth, roughness, grain size.

Figure 3. 10 Multimode SPM

3.4.2.3 Scanning electron microscope

Scanning electron microscope (SEM) produces images of a sample by scanning it with a focused beam of electrons. The electrons interact with electrons in the sample, producing various signals that contain information about the sample's surface topography and composition. SEM can achieve resolution better than 1 nm. SEM generates a beam of incident electrons in an electron column above the sample chamber. The electrons are produced by a thermal emission source, such as a heated tungsten filament, or a field emission cathode. The electrons are focused into a small beam by a series of electromagnetic lenses in the SEM column. The electron beam is scanned in a raster pattern over the surface for imaging. The incident electrons cause electrons

to be emitted from the sample due to elastic and inelastic scattering events within the sample's surface and near-surface. The topography of surface features influences the number of electrons that reach the secondary electron detector. This local variation in electron intensity creates the image contrast that reveals the surface morphology. The secondary electron image resolution for an ideal sample is about 3.5 and 1.5 nm for a tungsten-filament electron source and field emission SEM, respectively. There is also backscatter electron imaging **w**hich provides function of elemental composition. For SEM, samples must be electrically conductive. Nonconductive materials can be coated with a thin film of carbon, gold or other conductive material to obtain conductivity without significantly affecting observed surface morphology.

In our case, the SEM images were collected by LEO Zeiss Supra 55VP SEM, see Figure 3.12. It has an ultra high resolution at 1 nm/20kV, 3 nm/1kV, and magnification from 20X to 900,000X. The sample stage can be manual controlled in 5 axis direction, including X, Y, Z, rotation angle (360°) and tilting angle (-15° to 65°).

Figure 3. 11 SEM set up

3.4.2.4 Fluorescence microscopy

A fluorescence microscope is an optical microscope that uses fluorescence and phosphorescence instead of, or in addition to, reflection and absorption to study properties of organic or inorganic substances. The principle of fluorescence microscope is that the sample is illuminated with light of a wavelength which excites fluorescence in the sample. The fluoresced light, which is usually at a longer wavelength than the illumination, is then imaged through a

microscope objective. Two filters are normally used in this technique: an illumination (excitation) filter which ensures the illumination is near monochromatic at the correct wavelength, and a second emission (barrier) filter which ensures none of the excitation light source reaches the detector. Typical components of a fluorescence microscope are a light source, the excitation filter, the dichroic mirror (or dichroic beamsplitter), and the emission filter. The main light source includes xenon arc or mercury-vapor lamps, lasers and high-power LEDs.

In this project, Olympus IX71 inverted microscope with a DP71 digital camera was used, as shown in Figure 3.13. This microscope equipped with a super high signal/noise ratio aperture objectives to effectively detect the weak excitation fluorescence signal to the autofluorescence. The light source of this system is xenon arc lamp emitting at 470 and 490 nm, whose power can be manually tuned. The Q-capture software can be used to in-situ capture the fluorescence image from the sample. The fluorescent nanospheres (FPs) allow almost any protein or peptide to become fluorescent inside cells and thereby to be visible within a bio-logical context. In our project, the fluorescence microscopy image was collected from 40 nm FPs (Invitrogen, Burlington), emitting at 515 nm. These FPs are manufactured using high-quality, ultraclean polystyrene nanospheres and loaded with specific dyes which can be excited efficiently at 488 nm. These nanospheres are coated with a hydrophilic polymer containing multiple carboxylic acids for covalent attachment of ligands.

Figure 3. 12 Schematic Olympus IX71 inverted microscope

3.4.3 Surface and interface chemical characterization

3.4.3.1 X-ray photoelectron spectroscopy

i. XPS setup

XPS is a well-established surface analysis technique capable of providing elemental and chemical state information from the outer 5 to 10 nm of a solid surface. The technique is based on the photoelectric effect, discovered by Hertz in 1887. When a X-ray of known energy (hν), e.g. Al Kα (1486.7 eV) or Mg Kα (1253.6 eV), interacts with an atom, a photoelectron can be emitted via the photoelectric effect. The emitted electron's kinetic energy (E_k) can be measured and the atomic core level binding energy (BE) relative to the Fermi level (E_F) of the sample can be determined using the equation [J. F. Moulder*, et al.* 1995] :

$$BE = h\nu - E_k - \emptyset_{sp} \tag{3.4}$$

where ϕ_{sp} is the work function of the spectrometer (typically 4 to 5 eV), see Figure 3.13.

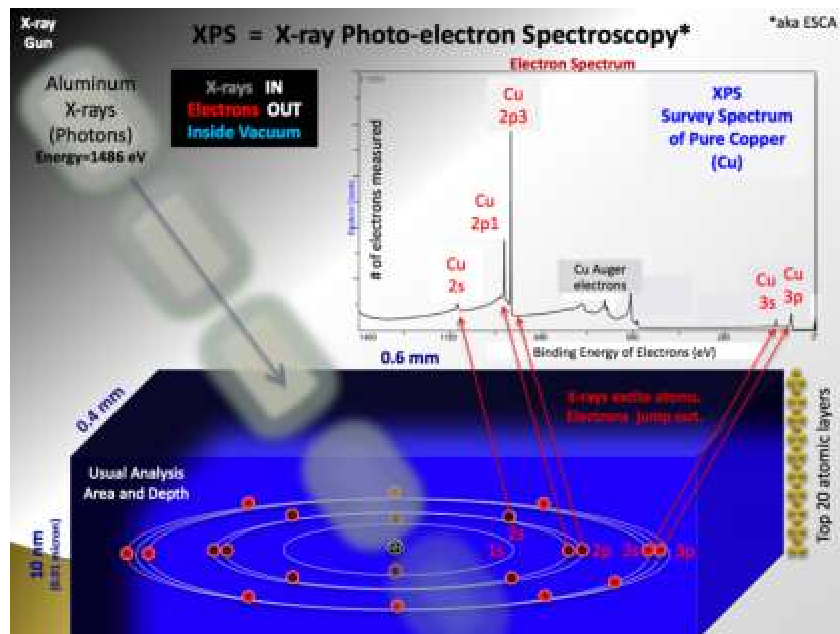

Figure 3. 13 Illustration of XPS concept [B. V. Crist 2010]

Usually, XPS spectra were shown as a graph of electron count as a function on the electron BE, as shown in Figure 3.13. The various core levels BEs observed in a spectrum can be used to identify all the elements of the periodic table except for hydrogen and helium. Chemical

composition information can also be extracted, as the chemical environments in which the core electron is found (the type of bonding, the oxidation state, the presence of adsorbates) results in distinctive BE shift. The number of detected electrons for each peak is related to the density of related atoms in the detection volume. By normalizing the count with relative sensitivity factor (RSF), it is possible to establish the relative ratio of each atom and thus determine the chemical composition of studied compound. Therefore, XPS is used to measure: elemental composition of the surface (1–10 nm), chemical or electronic state of each element in the surface, empirical formula of pure materials, contamination elements, uniformity of elemental composition across the top surface (line profiling or mapping) and in depth (depth profiling). In depth profiling, an ion gun is used to etch the material for a period. Each ion gun etch cycle exposes a new surface and the XPS spectra provide information of the composition of these new surfaces. Then the trend of the quantification values is plotted as a function of etch-time. The actual profiling depth depends on the etch-rate of the ion-gun, which may vary between the layers of material. XPS can also be used to investigate the deposited or passivation thin overlayers by takeoff angle measurement following equation [P. Gunter*, et al.* 1992]:

$$\frac{I_O}{I_S} = \frac{n_O \ell_O}{n_S \ell_S}\left[\exp\left(\frac{d}{\ell_O \cos\Theta}\right) - 1\right] \tag{3. 5}$$

where I is peak intensity, n is the volume density of electron-emitting atoms, ℓ is the inelastic mean free path of the photoelectrons, O and S in the subscripts present overlayer and substrate, Θ is the takeoff angle with respect to the surface normal and d is the thickness of the over-layer. The passivation layer thickness can be calculated from equation. Also, the intensity ratio (I_O/I_S) and overlay analysis sensitivity increase with the takeoff angle, as the thin overlay information is more interesting sometimes [S. Arabasz*, et al.* 2006].

In this project, XPS measurements were carried out in a spectrometer (Kratos Analytical, AXIS Ultra DLD) equipped with a 150 W Al Kα source and operating at a base pressure of $1x10^{-9}$ Torr. It integrates a magnetic immersion lens and charge neutralization system with a spherical mirror analyser. This means that electrically non-conductive samples can be easily analyzed, and high quality XPS spectra can be obtained. The spherical mirror analyser provides real-time chemical state and elemental imaging using a full range of pass energies. A micro-channel plate and phosphor detection system are incorporated into the system to provide parallel

imaging capability with high spatial resolution and high sensitivity. Advanced zoom optics enables a variable viewing area for the identification of macro or micro features.

Figure 3. 14 AXIS Ultra DLD XPS

ii. XPS data processing

The data collected by XPS spectrometer was processed by Computer aided surface analysis for X-ray photoelectron spectroscopy (CasaXPS) software [N. Fairley 2009]. In practice, to produce accurate atomic concentrations from XPS spectra is not straight forward, so quantification of XPS spectra is highly required. In CasaXPS, the quantification of surface is always beginning with survey spectra, which measured the intensity over a relative wide range of energies using a relative low energy resolution. A first step to quantifying survey spectra is to identify the elements by assigning each peak to an element via element library. The peak positions maybe offset due to charging of the sample, so charge compensation is needed. The important issue is to define a background (Liner, Shirley and Tougaard), as quantification regions are energy intervals over the defined background. The parameters, like region start and end BE position, start and end offset affect analysis.

Once the element identification of a sample is known in survey spectra, high-energy resolution spectra analysis can be carried out to investigate the chemical states of elements on the surface. This step includes creating quantification regions by choosing appropriate background,

charging compensation and constructing peak models. The first two are similar as the steps in the survey spectra. Constructing peak models is key to study the chemical compositions of specific element. Without careful model construction, the resulting fit, regardless of how accurate a measurement of the data, may be of no significance from a physical perspective. A peak model is determined by the specific parameters, like line shape, BE position, FWHM and area. The most commonly used line shapes in CasaXPS are product GL(p), (Gaussian/Lorentzian mix), A(a,b,n)GL(p) (Gaussian/Lorentzian mix modified by an asymmetric form, A(a,b,n)) and LA(α, β, m), (Asymmetric line-shape where α and β define the spread of the tail on either side of the Lorentzian component). As identification of chemical state based on BE position, it requires careful analysis according to database. FWHM is useful indicators of chemical state changes and physical influences. By iteratively building these parameters constraints for the peaks in a peak model to satisfy the data envelopes, the precise area for specific chemical composition can finally be obtained. There are some important tips and skills during data fitting with CasaXPS software:

a) Spin orbit splitting

Core levels in XPS use the nomenclature nl_j where n is the principal quantum number, l is the angular momentum quantum number (where j is the spin angular momentum number and can be ±½). All orbital levels except the *s* levels ($l = 0$) give rise to a doublet with the two possible states having different BEs, which is known as spin-orbit splitting. The peaks have specific area ratios based on the degeneracy of each spin state, which always share equal FWHM, as shown in Table 3.1. These ratios must be taken into account when analyzing spectra of the core levels. Spin-orbit splitting values can be found in data base and Handbook.

Table 3. 1 Spin-orbit splitting j values and peak area ratios.

subshell	*j* values	Area ratio
s	1/2	
p	1/2, 3/2	1:2
d	3/2, 5/2	2:3
f	5/2, 7/2	3:4

b) Carbon

A thin layer of carbonaceous material is usually found on the surface of most air exposed samples. Its presence makes it a convenient charge compensation for most investigated samples in our project. The charge compensation of spectra from samples is carried out by shifting all peaks relative to the adventitious C 1s spectral component (C-C, C-H) BE set to 285.0 ±0.2 eV. There are also three kinds other C absorbates, alcohol/ether (–COH, –COC–), carbonyl (–C=O), and ester (O=CO–) functionalities, which have their peak position at BE of 286.2±0.1 eV, 287.7±0.1 eV, and 288.6±0.2 eV, respectively [B. Payne*, et al.* 2011], when the area at lower BE of 286.2±0.1 eV must larger than or minimum equal to the (O=CO–) functionality at BE of 288.6±0.2 ev. If not, the alcohol/ether spectra intensity is required to split into –COH, -COC. Following fitting all the C species, these C absorbates contributions to Oxygen (O) intensity is calculated depending on the O/C ratio of individual species, e.g. 1:1 in COH group [B. P. Payne*, et al.* 2009]. Then by fixed the O intensities and peak positions of these C absorbates in the O spectra, the O intensities and peak positions from other investigated oxidation states, like metal oxides, can be more precisely calculated and estimated.

3.4.3.2 Secondary ion mass spectroscopy (SIMS)

SIMS is a technique used in materials and surface science to analyze the composition of solid surfaces and thin films by sputtering the surface of the specimen with a focused primary ion beam and collecting and analyzing ejected secondary ions. The mass/charge ratios of these secondary ions are measured with a mass spectrometer to determine the elemental, isotopic, or molecular composition of the surface to a depth of 1 to 2 nm. SIMS is generally considered to be a qualitative technique, with elemental detection limits ranging from parts per million (ppm) to parts per billion (ppb) [A. Bennighoven*, et al.* 1987]. A basic SIMS instrument consists of, as shown in Figure 3.16: 1) primary beam source (usually O_2^+, O^-, Cs^+, Ar^+, Ga^+ or neutrals) to bombard species; 2) target or sample that must be solid and stable in a vacuum;3) a method of collecting the ejected secondary ions; mass analyser to isolate the ion of interest (quadrupole, magnetic sector, double focusing magnetic sector or time of flight (TOF)); ion detection system to record the magnitude of the secondary ion signal (photographic plate, Faraday cup, electron multiplier, CCD camera and image plate).

The depth SIMS profiling is aim to obtain information on the variation of composition with depth below the initial surface. It can be obtained simply by recording sequential SIMS spectra as the surface is gradually eroded away by the incident ion beam probe [S. Hofmann 2004]. A plot of the intensity of a given mass signal as a function of time is a direct reflection of the variation of its abundance/concentration with depth below the surface. To convert the time axis into depth, profilometry was used to measure the sputter crater depth. One of the main advantages that SIMS over other depth profiling techniques (e.g. Indepth XPS analysis) is its sensitivity to very low concentrations (sub-ppm or ppb) of elements, which is particularly important in semiconductor industry where dopants are often present at very low concentrations.

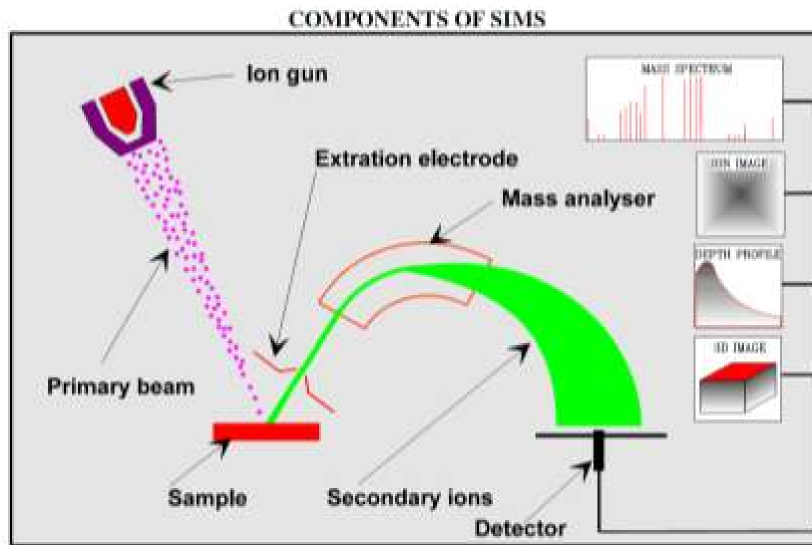

Figure 3. 15 Schematic of SIMS components [I. Probe 2007]

TOF mass analyzer separates the ions in a field-free drift path according to their velocity. It is based on the fact that ions with the same energy but different masses travel with different velocities. Basically, ions formed by a short ionisation event are accelerated by an electrostatic field to a common energy and travel over a drift path to the detector. The lighter ones arrive before the heavier ones and a mass spectrum is recorded. Measuring the flight time for each ion allows the determination of its mass. Combinations of linear drift paths and electrostatic sectors or ion mirrors, results with mass resolutions, M/dM, above 10,000 can be achieved. Major advantages of this approach over quadrupole and magnetic sector analysers are the extremely high transmission, the parallel detection of all masses and the unlimited mass range.

In TOF-SIMS, a start time of all secondary ions is defined by using a pulsed primary ion guns. Three basic types of ion guns are employed [P. Williams 1985]. The first ions of gaseous elements are usually generated with duoplasmatrons or by electron ionization, for instance noble gases (Ar^+, Xe^+), oxygen (O^-, O_2^+), or even ionized molecules such as SF_5^+ (generated from SF_6) or C_{60}^+. This type of ion gun is easy to operate and generates roughly focused but high current ion beams. O is commonly used because it enhances the yield of electropositive elements such as Al, Si. A second source type, the surface ionization source, generates Cs^+ primary ions. Cs ion beams are used to enhance the yield of electronegative elements (C, O, and S, etc.) within the target. The Cs gun can only operate in positive mode. In general Cs beams are smaller than those generated by the duoplasmatron, and sputter material more effectively because of their greater mass. A third source type, the liquid metal ion gun (LMIG), operates with metals or metallic alloys, which are liquid at room temperature or slightly above. The developed LIMIG source includes gallium (Ga), gold (Au), indium (In) and bismuth (Bi), whose melting temperature has been lowered. The LMIG provides a tightly focused ion beam (< 50 nm) with moderate intensity and is additionally able to generate short pulsed ion beams. Compared with other LIMIG source, the Bi ion has higher mass (209) and it has higher intensity of cluster emission Bi_n^+ (n=1-7) and Bi_n^{2+} (n=3 and 5). It also has significant higher proportion of doubly charged Bi_3^{2+}, which gives double impact energy and more secondary ions. The Bi ion beam has good focusing characteristics giving 100 nm lateral resolutions. One of the limitations of TOF-SIMS is that the sputtering process is poorly understood. No quantitative model currently exists that can accurately predict the secondary ionisation process [J. Grams 2007]. In order to obtain quantitative information a suitable standard has to be used and empirical corrections applied.

In our projects, TOF-SIMS (TOF-SIMS IV, IONTOF) equipped with a dual stage reflectron ToF-analyser and a Bi as primary ion source mounted at 45° with respect to the sample surface at pressure $3x10^{-9}$ Torr was used, as shown in Figure 3.16. It has a range of ion sources (Cs, O, Bi, Ar). It has high surface spectroscopy sensitivity ppm, high lateral resolution for surface image (<100 nm) and high depth resolution (<1 nm). For depth profiling, a dual beam principle were applied, The samples were sputtered over an area of 500 μm x 500 μm in the irradiated center by 3 keV Cs ion source at sputtering rate 0.08 nm/second. An area of 50 μm x 50 μm from sputtered region center was analysed by a 10 keV Bi ion beam.

Figure 3. 16 TOF-SIMS IV instrument

3.4.3.3 Fourier transformer infrared spectroscopy

Fourier transformer infrared spectroscopy (FTIR) is a preferred infrared (IR) spectroscopy. IR spectroscopy bases on the fact that molecules absorb specific frequencies that are characteristic of their structure and matches the transition energy of the bond or group that vibrates in the molecular. The energies are determined by the shape of the molecular potential energy surfaces, the masses of the atoms, and the associated vibronic coupling. Usually, a broadband IR light source, containing the full spectrum of wavelengths, passes through a sample. Part of the radiation is absorbed and the other is transmitted. The resulting spectrum represents a fingerprint of sample with absorption peaks which correspond to the frequencies of vibrations between the bonds of the atoms making up the material. Because each different material is a unique combination of atoms, no two compounds produce the exact same infrared spectrum. IR can result in a positive identification of every different kind of material. In addition, the intensity of the peaks in the spectrum is a direct indication of the amount of material present. Therefore, IR spectroscopy can identify unknown materials and determine the quality or consistency of a sample and the amount of components in a mixture.

FTIR was developed overcome limitation of original IR dispersive spectroscopy. As shown in Figure 3.18, Michelson interferometer was employed in FTIR, which was used to create interfergrom between split beam from stationary mirror and split beam delay from moving mirror, encoding information about passing sample with every infrared frequency. Infrared light is guided through the interferometer and then through the sample. The moving mirror alters the

distribution of infrared light that passes through the interferometer. The interferogram represents light output as a function of moving mirror position. Because of the complicated nature of interferogram signal, it has to be decoding with Fourier transformation function to obtain the desired frequency spectral information for analysis. Because there needs to be a relative scale for the absorption intensity, a background spectrum must also be measured, which is normally a measurement with no sample in the beam. The resolution of FTIR in wavenumber per cm is equal to the reciprocal of retardation of interferometer in cm. So, FTIR can measure all the frequency simultaneously with high signal to noise ratio and reduce the time element per sample, compared with dispersive methods. Other than interferometer, laser source, beamsplitter and optical throughput will affect the performance of FTIR. One of the most important components is detector, and the popular used liquid N_2 cooled mercury-cadmium telluride (MCT) photoconductive detector is reported to with high sensitivity. Now, FTIR can be used to obtain an infrared spectrum of absorption, emission, photoconductivity or Raman scattering of a solid, liquid or gas [P. R. Griffiths 1983].

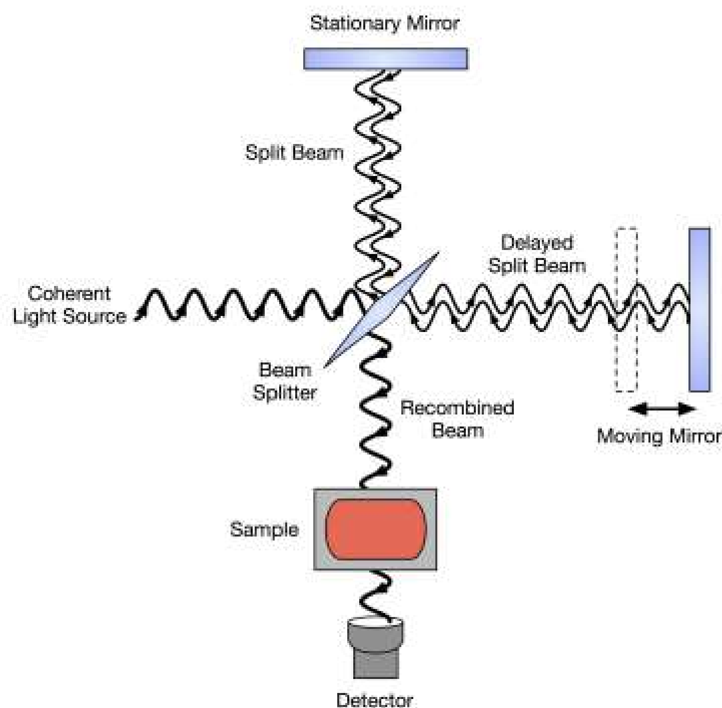

Figure 3. 17 Principle of FTIR [I. Sanchonx 2011]

In our project, FTIR spectrometer (Brucker Optics, Vertex80) under ambient conditions was used. The signal was collected and focused into a liquid N_2 cooled HgCdTe (MCT) broad band

detector with a resolution of 4 cm^{-1}. The analyzed area was approximately 3 mm in diameter. It can cover the spectra range from the mid and near IR and visible and up to the ultraviolet spectral range. It provides a spectral resolution at 0.2 cm^{-1}.

3.5 Summary

In this chapter, I describe the experimental setup, excimer lasers, used in my thesis projects, including principles of the excimer laser, the beam delivery system, the homogenizer and sample chamber and positioning.

The four studied heterostructures were described. Three QW structures is based on InP substrate including a uncompleted QW laser diode microstructure with thin cap layers, one lattice match laser diode QW heterostructure and one strain Zn doped laser diode QW heterostructure. The other one is based on GaAs substrate.

The characterization methods, which were used to test the quality of intermixed QW like PL-mapper and HI-PLM, were presented. I also discussed the principle and equipments that are used to measure the surface morphology during processing, like profilometry, SEM, AFM and fluorescence microscope. Then the setup used to measure the surface chemical modification during process, such as XPS, SIMS, and FTIR were studied.

3.6 Bibliography

Arabasz, S., Bergignat, E., et al., (2006), XPS study of surface chemistry of epiready GaAs surface after $(NH_4)_2S_x$ passivation, *Vacuum*, vol. 80, n°8, 888-893.

Basting, D., and Marowsky, G.: (2005), Excimer Laser Technology (Springer), 433p.

Bauerle, D.: (2010), Laser processing and chemistry (Springer Berlin), 788p.

Benninghoven, A., Rudenauer, F., et al., (1987), Secondary Ion Mass Spectrometry: Basic Concepts, Instrumental Aspects, Applications and Trends, *Chemical Analysis*, vol. 86, 1-7.

Cappella, B., and Dietler, G., (1999), Force-distance curves by atomic force microscopy, *Surface Science Reports*, vol. 34, n°1, 1-104.

http://commons.wikimedia.org/wiki/File:XPS_PHYSICS.png

Fairley, N.: (2009), CasaXPS Manual 2.3. 15 (Casa Software Limited), 177p.

Gfroerer, T.H., (2000), Photoluminescence in analysis of surfaces and interfaces, *Encyclopedia of Analytical Chemistry*, vol., 9209-9231.

Giessibl, F.J., (2003), Advances in atomic force microscopy, *Reviews of Modern Physics*, vol. 75, n°3, 949-983.

Grams, J.: (2007), New trends and potentialities of ToF-SIMS in surface studies (Nova Science Pub Incorporated), 273p.

Griffiths, P.R., (1983), Fourier transform infrared spectrometry, *Science*, vol. 222, n°4621, 297-302.

Gross, L., Mohn, F., et al., (2009), The Chemical Structure of a Molecule Resolved by Atomic Force Microscopy, *Science*, vol. 325, n°5944, 1110-1114.

Gunter, P., De Jong, A., et al., (1992), Evaluation of take-off-angle-dependent XPS for determining the thickness of passivation layers on aluminium and silicon, *Surface and interface analysis*, vol. 19, n°1-12, 161-164.

Hofmann, S., (2004), Sputter-depth profiling for thin-film analysis, *Philosophical Transactions of the Royal Society of London. Series A: Mathematical, Physical and Engineering Sciences*, vol. 362, n°1814, 55-75.

La Fontaine, B., (2010), Lasers and Moore's Law, *SPIE Professional*, vol., 20.

Lee, A., MacKenzie, M., et al., (2001), Enhanced band-gap blueshift due to group V intermixing in InGaAsP multiple quantum well laser structures induced by low temperature grown InP, *Applied Physics Letters*, vol. 78, n°21, 3199-3201.

Moulder, J.F., Chastain, J., et al.: (1995), Handbook of X-ray photoelectron spectroscopy: a reference book of standard spectra for identification and interpretation of XPS data (Physical Electronics Eden Prairie, MN), 261p.

http://www.geos.ed.ac.uk/facilities/ionprobe/SIMS4.pdf

Paine, D., Caragianis, C., et al., (1993), Visible photoluminescence from nanocrystalline Ge formed by H reduction of SiGeO, *Applied Physics Letters*, vol. 62, 2842.

Payne, B., Biesinger, M., et al., (2011), X-ray photoelectron spectroscopy studies of reactions on chromium metal and chromium oxide surfaces, *Journal of Electron Spectroscopy and Related Phenomena*, vol. 184, n°1, 29-37.

Payne, B.P., Biesinger, M.C., et al., (2009), The study of polycrystalline nickel metal oxidation by water vapour, *Journal of Electron Spectroscopy and Related Phenomena*, vol. 175, n°1-2, 55-65.

http://en.wikipedia.org/wiki/File:FTIR_Interferometer.png

Simpson, G., Sedin, D., et al., (1999), Surface roughness by contact versus tapping mode atomic force microscopy, *Langmuir*, vol. 15, n°4, 1429-1434.

Williams, P., (1985), Secondary ion mass spectrometry, *Annual Review of Materials Science*, vol. 15, n°1, 517-548.

Willmott, P., and Huber, J., (2000), Pulsed laser vaporization and deposition, *Reviews of Modern Physics*, vol. 72, n°1, 315.

Zhang, X., Grigoropoulos, C.P., et al., (1996), Excimer laser projection micromachining of polyimide thin films annealed at different temperatures, *IEEE Transactions on Components, Packaging, and Manufacturing Technology, Part C*, vol. 19, n°3, 201-213.

Chapter 4 Surface morphology of III-V semiconductor microstructures irradiated with excimer lasers and blueshift amplitudes

In this chapter, I will discuss the UV laser induced surface morphology modification of InP-capped III-V semiconductor microstructure surrounded by air, dielectric layers (SiO_2 and Si_3N_4) and DI water during irradiation. I will discuss the importance of the InP surface morphology in the QWI process. In majority of the experiments, regardless of the surrounding environment, the conditions for observing maximum blueshift have been recorded for samples (sites) irradiated with less than 100 pulses. I will present the results of formation of self-organized nano-cone arrays created by the irradiation with ArF and KrF excimer lasers of a relatively large ($N \geq 100$) number of pulses with. These results have been published in *Journal of laser micro/nano engineering*, Vol. 7, No. 2, pp.130 -136, 2012. Finally, I will provide a preliminary review of blueshifting amplitudes achieved in the investigated microstructures following the irradiation with ArF and KrF lasers.

4.1 Surface morphology of InP/InGaAs/InGaAsP microstructures irradiated in air by excimer laser with a small number ($N < 100$) of pulses

As the material ablation threshold was reported to decrease as the laser pulse number increases, InP surface was found to be damaged when the pulse number is large [B. Kumar*, et al.* 2008]. The PL shift decreases at large pulse number ($N \geq 100$) related to the reduced 'reservoir' of laser induced surface defects caused by surface damage [J. Genest*, et al.* 2008a]. Within small pulse number ($N < 100$), the PL shift always increases with the pulse number and reaches the maximum. Therefore, we always employed UV laser QWI within the pulse number ($N < 100$).

Figure 4.1 shows 3 μm x 3 μm AFM images of non-irradiated InP and sites irradiated by ArF laser at 82 mJ/cm^2 in air with 20 and 40 pulses. It can be seen that surface morphology has been

modified after irradiation and there are amounts of nanofeatures on the irradiated sites. The σ_{RMS} roughness on non-irradiated material is ~0.49 nm, which is similar to σ_{RMS} of 0.52 nm that represents the as-grown material. The σ_{RMS} roughness of 20- and 40-pulse irradiated sites is 4.83 and 5.36 nm, respectively.

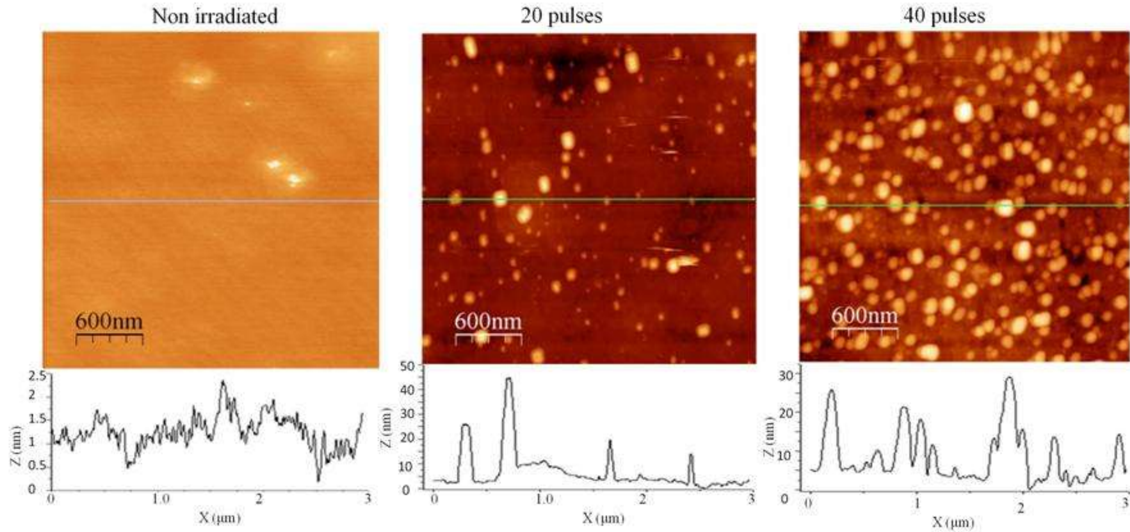

Figure 4. 1 AFM image of InP/InGaAs/InGaAsP irradiated by ArF laser at 82 mJ/cm^2 in air

Figure 4.2 shows AFM images of a non-irradiated material and the sites irradiated with ArF laser with 20 and 40 pulses following the RTA step. The σ_{RMS} roughness of 2.17 and 2.59 nm observed for 20- and 40-pulse irradiated sites indicates a 50% reduced amplitude in comparison to that of the ArF excimer irradiates sites. The most likely mechanism responsible for smoothing the surface morphology of laser irradiated samples is related to mass transport during the RTA step [J. J. Dubowski, *et al.* 1999b]. However, σ_{RMS} of the as-grown material has increased to 0.9 nm following the RTA treatment.

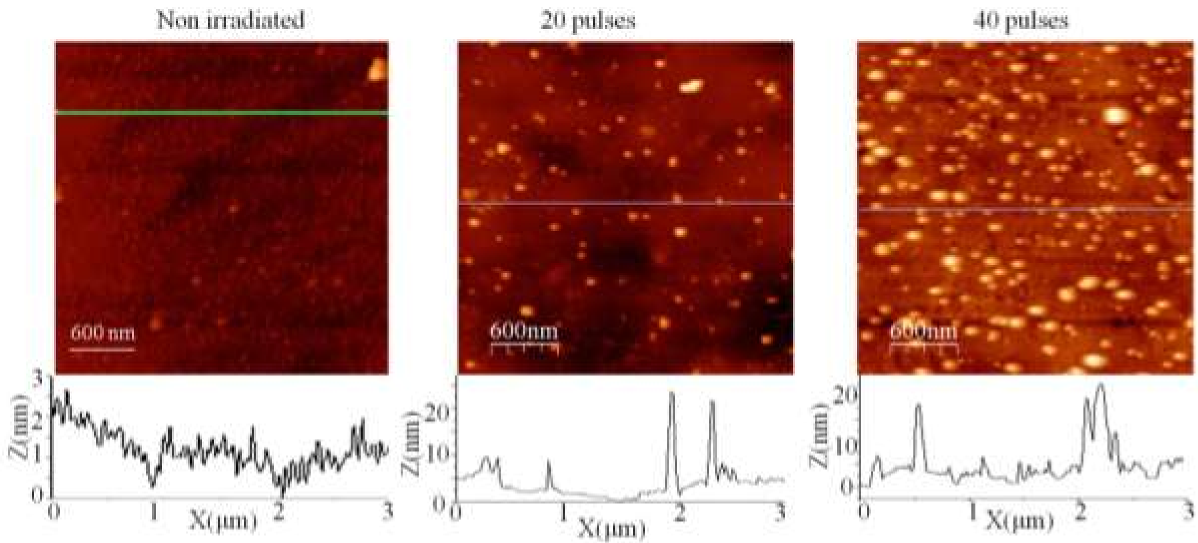

Figure 4. 2 AFM image of non irradiated and irradiated sites in by ArF laser in air after RTA

In UV laser QWI, UV laser was used to generate surface defects. When the KrF laser fluence is above 142 mJ/cm^2, the surface temperature is estimated above 1050 K. As the damage threshold decreases with increasing pulse number, InP surface could be easily ablated within 100 pulses above 142 mJ/cm^2 [O. Musaev, et al. 2008]. Therefore, the sacrificial layer designed to serve as a “reservoir” for defects would also be ablated. E.g. when the sites on InP/InGaAs/InGaAsP microstructure (M1580) were irradiated at 158 mJ/cm^2 by KrF laser, the PL shifts quickly increased to maximum 77 nm at 50 pulses and decreased to 65 nm at 100 pulses. However, on the same sample, when the sites were irradiated at 142 mJ/cm^2, the PL shift gradually increased to maximum 108 nm at 100 pulses. When the laser fluence is below 109 mJ/cm^2, the temperature is estimated below 800 K. As P evaporation from InP was found above 818 K [R. F. C. Farrow 1974], there will be no obvious laser-induced P atom evaporation or related chemical reaction. There will be no sufficient defects generated in this process to induce QWI. So, in our experiment, we limited the range of investigated KrF laser fluence to 109-142 mJ/cm^2. Table 4.1 shows σ_{RMS} of as-received sample and that of KrF laser irradiated sites at 124 mJ/cm^2 with 10 and 25 pulses in air before and after RTA. Qualitatively, similar results were observed for KrF laser irradiated samples. The increase of surface roughness with pulse number is evident. Furthermore, following the RTA step, we observe some smoothing of the irradiated surface, which is especially evident for the 25-pulse irradiated site. Note that for comparable number of pulses, σ_{RMS} of sites irradiated with KrF laser is significantly greater than that of sites

irradiated with ArF laser. This seems to be related to the greater pulse fluence of the KrF laser (124 mJ/cm^2) in comparison to that of the ArF laser (82 mJ/cm^2) used in the experiment (see discussion of InP absorption in the UV region, Chapter II).

Table 4. 1 RMS roughness on non irradiated site and irradiated sites by KrF laser in air

	In air before RTA σ_{RMS} (nm)	In air after RTA σ_{RMS} (nm)
Non irradiated	0.5	0.78
10 pulses	3.44	3.18
25 pulses	10.81	4.12

4.2 Surface morphology of InP/InGaAs/InGaAsP microstructures irradiated in air by excimer laser with large number (N ≥ 100) of pulses

Self-organized Nano-cone Arrays in InP/InGaAs/InGaAsP Microstructures by Irradiation with ArF and KrF Excimer Lasers

Neng Liu, Khalid Moumanis, Jan J. Dubowski, J. Laser Micro/Nano-engineering, Vol. 7(2), pp. 130-136 (2012)

4.2.1 Abstract

We discuss the effect of ArF (λ_{laser} =193 nm) and KrF (λ_{laser} = 248 nm) excimer laser irradiation of InP/InGaAs/InGaAsP QW microstructures on surface morphology of the top InP layer. The irradiation was carried out in air with lasers delivering up to 700 pulses of fluence from 82 to 142 mJ/cm^2. We observe the formation of nano-cone structures having their period increasing from 450 to 1080 nm for KrF laser, and from 675 to 875 nm for ArF laser, in proportion to the laser fluence and pulse number. The chemical and structural modification of the laser irradiated surface has resulted in the enhancement of the QW photoluminescence emission up to 1.4 times when compared to the non-processed material. Thus, the excimer laser processing of the surface of InP capped InP/InGaAs/InGaAsP QW microstructures using relatively low

pulse fluence, has been found attractive for the fabrication of enhanced optical emission semiconductor devices.

4.2.2 Introduction

Laser processing of semiconductor materials has attracted continuous interest due to its potential in delivering microfabrication solutions of interest for advanced photonic and electronic devices. Due to the relatively low thermal and chemical stability of III-V compound semiconductors, laser irradiation at a relatively moderate pulse fluence can alter the surface morphological, chemical and physical properties of these materials [D. Bauerle 2010]. For instance, the formation of nano-cone arrays was observed on the surface of InGaAs cap of the InGaAs/InGaAsP/InP QW microstructure irradiated with an excimer laser [J. J. Dubowski*, et al.* 1999b]. Following the annealing in a RTA furnace, the laser irradiated sites exhibited an enhanced PL emission from InGaAs QWs. The sub-micrometer surface features have also been observed on the surface of bulk InP [N. L. Abbott*, et al.* 1995] and diamond-like films irradiated with femtosecond (fs) lasers, which illustrates that the formation of surface nanostructures does not require a strong thermal component typical of nanosecond lasers [B. N. Chichkov*, et al.* 1996b]. It has also been reported that the irradiation of bulk InP with a low fluence ($F \approx 80$ mJ/cm^2) of a nanosecond UV laser ($\lambda = 337$ nm) leads to the formation of mounds and increased surface roughness of this material in proportion to the number of irradiating laser pulses [O. Musaev*, et al.* 2008].

Excimer lasers offer wafer level processing and these tools have been successfully applied by the microelectronics industry for sub-micrometer resolution photolithography. We have been investigating the application of 308 [J. J. Dubowski*, et al.* 1999b], 248 [J. Genest*, et al.* 2007b] and 193 nm [J. Genest*, et al.* 2008a] excimers for surface modification and bandgap engineering of III-V quantum semiconductors. This approach is attractive for processing of large size wafers, often in a single step, and without the need of using photolithography masks. Depending on the laser used, the investigated microstructure and the irradiation environment both enhanced QWI, leading to blue shifting (shorter wavelength emission of the QW microstructure) [J. Genest*, et al.* 2008a], and, as well, suppressed QWI processes have been reported in [J. Genest*, et al.* 2007b]. The surface morphology of intermixed QW microstructures affects their PL and other optical

properties [R. Hey, *et al.* 1997]. For instance, it is known that inductively coupled argon plasma processing yields QWI material with decreased PL intensity [C. Xu, *et al.* 2009]. Typically, excimer laser-induced surface modification of InP-capped QW microstructures results in the preferential loss of P atoms [J. Genest, *et al.* 2008a] and generation of different surface defects that promote the QWI process during the RTA step. Thus, it is of paramount importance to investigate both the morphology and chemical composition of altered III-V semiconductor surfaces as a function of laser parameters, such as pulse fluence and pulse number.

We have reported that the maximum band gap blue shift of the InP/InGaAs/InGaAsP microstructure irradiated in air with KrF [N. Liu, *et al.* 2011c] and ArF [J. Genest, *et al.* 2008a] lasers takes place for a relatively small number of pulses ($N < 100$) and low pulse fluence ($F < 124$ mJ/cm^2). In this paper, we investigate surface morphology of such microstructures irradiated in air with up to 700 pulses of KrF and ArF excimer lasers delivering pulse fluence in the range of 95 to 142 mJ/cm^2.

4.2.3 Experimental details

A series of 5 mm x 5 mm samples from M1580 InP/InGaAs/InGaAsP QW microstructure was cleaved and cleaned with standard solvents. The whole microstructure was covered with a 400-nm-thick undoped InP sacrificial layer. The samples were then irradiated with ArF and KrF lasers delivering ~16 ns pulses of fluence in the range of 82 - 95 mJ/cm^2 and 109 - 142 mJ/cm^2, respectively. The absorption depth in InP is about 8 and 5 nm for ArF ($\delta = 1.3 \times 10^6$ /cm) and KrF ($\delta = 1.8 \times 10^6$ /cm) laser, respectively [D. Aspnes, *et al.* 1983]. The ablation threshold of bulk InP is ~100 mJ/cm^2 [A. Bulgakov, *et al.* 2010] and ~140 mJ/cm^2 [O. Musaev, *et al.* 2008] for ArF and KrF laser, respectively. Room temperature PL measurements were carried out with a commercial mapper (Philips PLM-150). A Nikon microscope (Eclipse LV100) was used to collect optical images of the laser irradiated sites on the cap layer of the InP material. The sample surface morphology was also investigated with AFM (Digital Instruments Nanoscope III) operating in a tapping mode. A commercial profiler (Tencore Alphastep 200) was used to measure the ablation depth of laser irradiated sites.

4.2.4 Results and discussion

4.2.4.1 KrF laser irradiation of InP/InGaAs/InGaAsP microstructures

An optical microscope image of a ~ 1400 μm diameter site obtained by the irradiation with 400 pulses of a KrF laser at 142 mJ/cm^2 is shown in Figure 4.3. The presence of a darker region, of a diameter about 780 μm, can be seen in the center of the laser irradiated site. A closer inspection revealed that the whole surface of the laser irradiated site is covered with regularly organized nano-cone arrays, while in the central region (Figure 4.3 b) the nanostructure height is found greater and their periodicity shorter in comparison to the edge region (Figure 4.3 c).

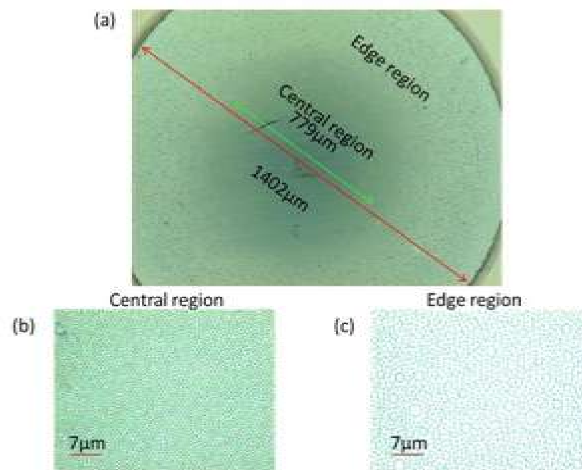

Figure 4. 3 Optical micrograph of the surface of an InP/InGaAs/InGaAsP microstructure irradiated with 400 pulses of a KrF laser at 142 mJ/cm^2 (a), along with high magnification images of the central (b) and edge (c) regions.

Figure 4.4 shows an AFM micrograph of a site irradiated with the KrF laser at 142 mJ/cm^2 with 400 pulses. An array of nano-cones is clearly observed in this figure. As indicated by cross-section scans, the nano-cones are denser and taller in the central region (a) in comparison to the edge region (b). The average period of the nano-cones in the central region is 870 nm, which compares to that of the edge region of 1320 nm. The average height of the nano-cone structures decreases from 188 nm in the central region to 141 nm in the edge region.

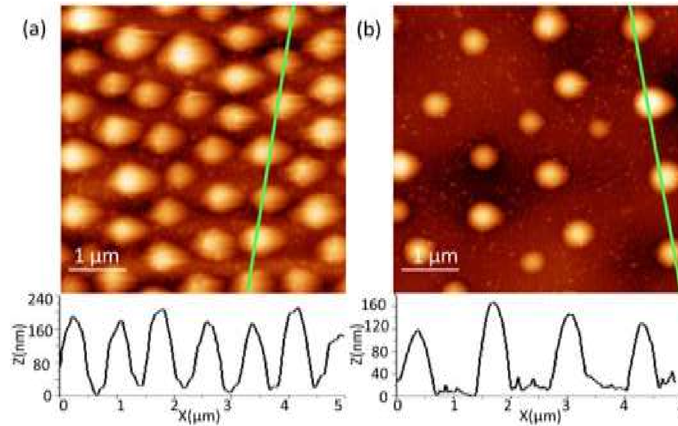

Figure 4. 4 AFM images of the central (a) and the edge (b) regions of a site irradiated with 400 pulses of the KrF

Figure 4.5 compares optical microscopic images of sites irradiated with 100, 400 and 700 pulses of the KrF laser at fluence of 109 mJ/cm^2 (left panel) and 142 mJ/cm^2 (right panel). The central dark region is clearly observed in all cases, increasing in its intensity with both the pulse number and fluence.

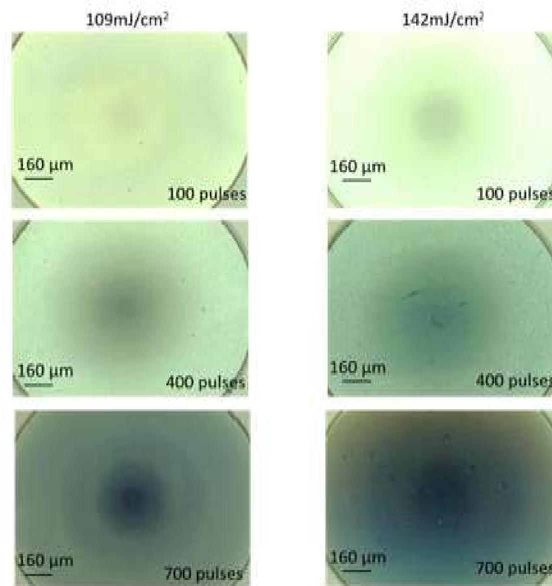

Figure 4. 5 Microscopic images of KrF laser irradiated sites at 109 mJ/cm^2 (left panel) and 142 mJ/cm^2 (right panel) with 100, 400 and 700 pulses.

More details concerning these microstructures can be observed in Figure 4.6 that presents the AFM data. The site irradiated with 100 pulses of the KrF laser at 109 mJ/cm^2 (Figure 4.6 a) shows some evidence of surface roughening, but no obvious nano-cone structures. However, irradiation with the same number of pulses at 142 mJ/cm^2 leads to the formation of nano-cones,

approximately 250 nm wide and up to 90 nm tall (Figure 4.6b). The nano-cones increase in height and diameter with increasing pulse fluence and number, as evidenced in Figure 4.6 c-f.

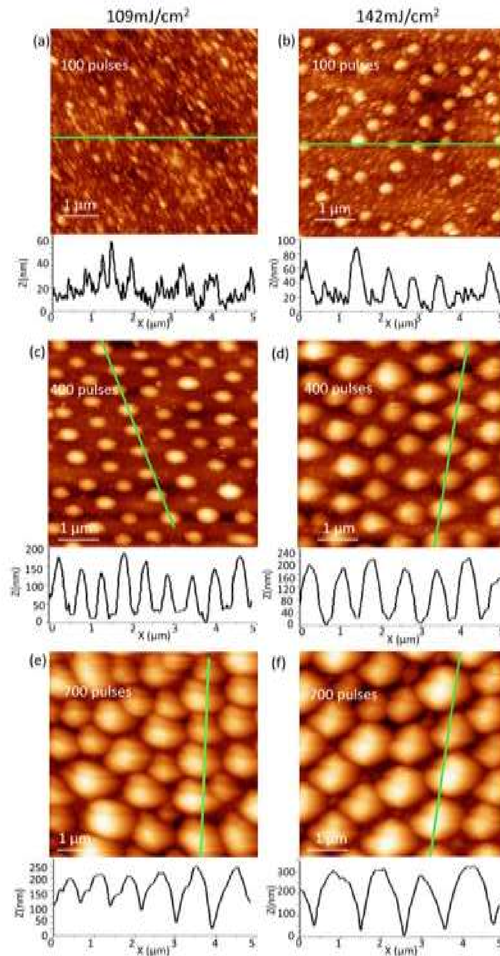

Figure 4. 6 AFM images and profiles along indicated lines in the central region the KrF laser irradiated sites at 109 mJ/cm^2 (left panel) and 142 mJ/cm^2 (right panel).

Figure 4.7 shows the average height (a), size (b) and period (c) of the self-organized nano-cone structures observed in this experiment. The amplitude of these parameters increases with the pulse number and fluence, and saturates at 600 pulses. Nano-cones with a maximum average height of 274 nm have been observed, which demonstrates that some material of the InP cap layer has been ablated with the laser (from the initial 400 nm thickness).

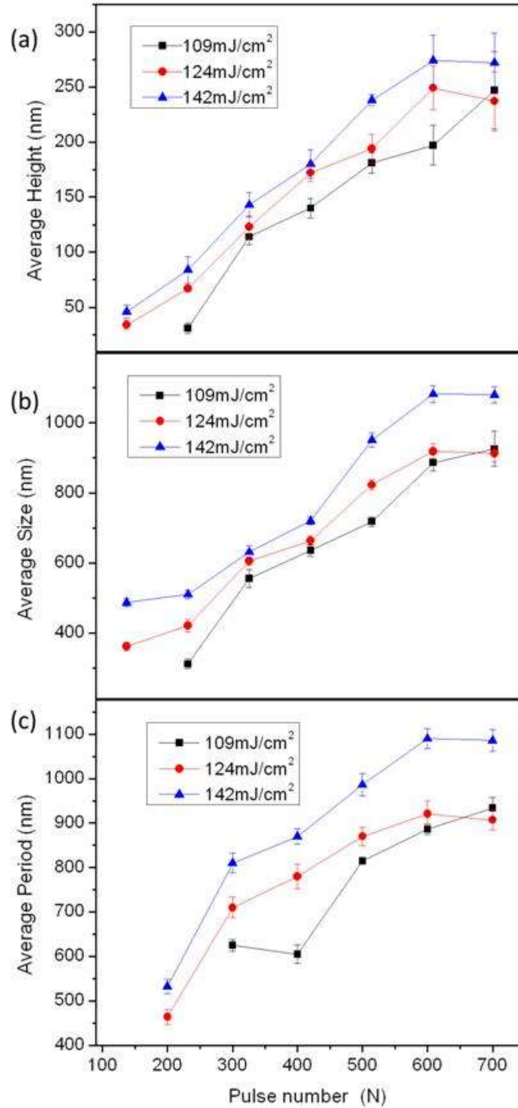

Figure 4. 7 Average height (a), size (b) and period (c) of self-organized nanostructures vs. pulse number of the KrF laser operating at 109 mJ/cm^2, 124 mJ/cm^2 and 142 mJ/cm^2.

It has been reported that preferential removal of P takes place from InP at high temperatures due to the significantly higher vapor pressure of that element in comparison to In [O. Musaev, *et al.* 2008]. Our XPS results of an excimer laser irradiated InP/InGaAs/InGaAsP microstructure in air showed that In/P ratio increases with the pulse number [J. Genest, *et al.* 2008a], which is also associated with the formation of indium oxide as reported in literature [M. Fathipour, *et al.* 1985].

The oxide is under significant stress due to lattice mismatch with the InP layer*. The stress accumulates on the sample surface as the number of laser pulses increases. The release of this mechanical stress, and related plastic deformation, are likely responsible for the formation of nano-cone structures through the modified Stranski-Krastanov growth [A. Medvid*, et al.* 2010]. Additionally, the surface temperature and the deformation strain are expected to increase with the laser fluence [O. Musaev*, et al.* 2008]. Thus, nano-cone structure size, height and period increase with laser fluence and pulse number. The saturation behavior of these nano-cone structures growth at large pulse number (≥ 600) indicates that the strain generated by the laser is relieved after a certain level of surface modification and material removal [O. Musaev*, et al.* 2008]. The quantitative description of the mechanism responsible for the formation of nano-cone structures and especially the formation of the zones of different density nano-cones observed within same laser irradiated sites requires a dedicating modeling. It is possible that formation of distinctly different zones of nano-cone structures is due to the intensity modulation of a coherent image of the mask projected through an aperture of the objective [D. S. Shin*, et al.* 2006]. The effect observed in Figure 4.5 (left panel, bottom image), where several concentred zones of different density material can clearly be seen, seems to support this hypothesis. Alternatively, a strong temperature gradient at the edge of the site, resulting from the diffraction on the mask, could contribute to the radial mass transfer – an effect that deserves further investigation.

Figure 4.8 shows the PL peak intensity map of the KrF laser irradiated spots with 400 pulses at 109 mJ/cm^2 (a) and 142 mJ/cm^2 (b). The PL intensity has been expressed in calibrated units (CU) that refer to the intensity obtained after subtracting the background signal. The corresponding PL intensity profiles show that the PL intensity is significantly enhanced in the center of the irradiated sites, coinciding with the presence of the 130 and 180 nm tall nano-cone structures as seen in Figure 4.4. The central region of the 109 mJ/cm^2 irradiated site (Figure 4.8 a) emits a PL signal about 2 times stronger than the edge region of that site. This difference is reduced to about 1.5 times for the 142 mJ/cm^2 irradiated site (Figure 4.8 b), although the maximum PL intensity in that case appears to be 10% greater than in Figure 4.8 a. The likely role

---

* XPS and SIMS results have shown that there is a more than 30 nm of InP oxides layer generated during UV laser irradiation. The InP-O layer (a = 10.12 Å) has larger lattice constant than InP (a = 5.87Å) [S. Qadri*, et al.* 2011]. Thus, this laser formed layer is under a significant stress due to lattice mismatch with InP.

of the nano-cone structures in enhancing the PL signal is related to the reduced reflection of the incident light (1064 nm) and, consequently, an enhanced laser pumping efficiency of the InP/InGaAs/InGaAsP microstructure. An increased light extraction efficiency has been reported for GaN-based light-emitting diodes (LEDs) with cone-shape surfaces [T. Fujii*, et al.* 2005]. The light output from InGaN/GaN LEDs with an KrF laser fabricated nano-cone surface structure has been reported to increase by 1.55 times in comparison to the conventionally fabricated LEDs [H. W. Huang*, et al.* 2005].

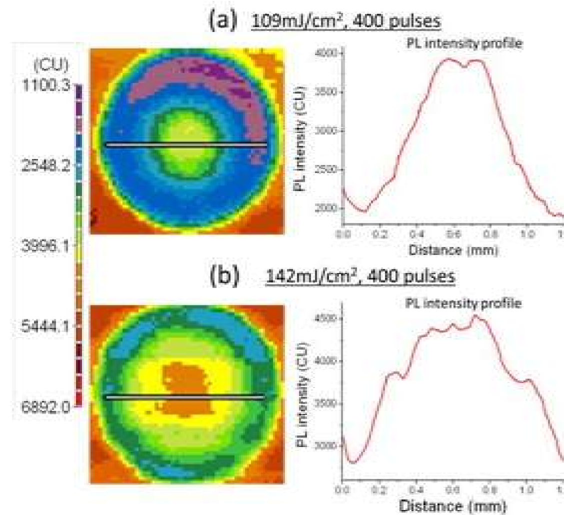

Figure 4. 8 PL peak intensity map and profile of the KrF laser irradiated spots with 400 pulses at 109 (a) and 142 mJ/cm^2 (b).

Figure 4.9 shows normalized PL intensities of the central region vs. the non-irradiated material for KrF laser operating at 109, 124 and 142 mJ/cm^2. Initially, the PL intensity decreases, primarily due to the laser induced structural and chemical surface damage [M. Takai*, et al.* 1988]. This coincides with no obvious nano-cone structures formation at sites irradiated with low pulse laser numbers ($N \leq 100$). However, the PL intensity increases for $N > 300$, i.e., for the samples with nano-cone microstructures as summarized in Figure 4.7. The PL intensity variation with different laser fluences at the same pulse numbers is due to the different average height, size and period of the created self-organized nano-cone structures. With 124 mJ/cm^2 and 142 mJ/cm^2, when $N \geq 400$, the PL intensity is greater than that in the non-irradiated material. The same results have been observed for the 109 mJ/cm^2 irradiated sites with $N \geq 500$. This is obviously related to the nano-cones formation because the average height (181 nm), size (670 nm) and period (870 nm) of these structures at 500 pulses has increased to the values corresponding to the

sites irradiated with 400 pulses at 142 mJ/cm^2 and 124 mJ/cm^2. The maximum normalized PL intensity enhancement factor of around 1.35 is observed for pulse number N ≥ 600. The inset in Figure 4.9 shows PL spectra observed from the as-grown QW microstructure and central region of the sites irradiated with 400 pulses at 109 and 142 mJ/cm^2 and 700 pulses at 142 mJ/cm^2.

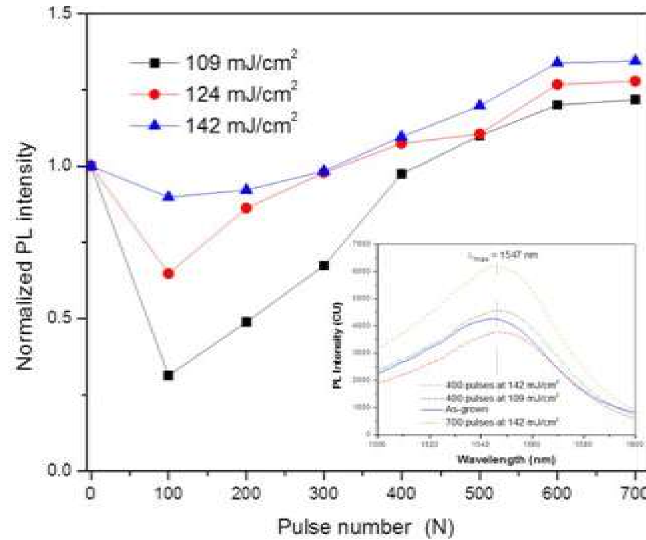

Figure 4. 9 Normalized PL intensity of the site central region vs. pulse number when irradiated with the KrF laser at 109 mJ/cm^2, 124 mJ/cm^2 and 142 mJ/cm^2. The inset shows PL spectra observed from the as-grown QW microstructure and the central region of the laser irradiated sites.

4.2.4.2 ArF laser irradiation of InP/InGaAs/InGaAsP microstructures

Similar surface morphology of the InP cap layer was observed following irradiation with the ArF laser. The 'darker' central and 'lighter' edge regions with different density and size of the nano-cone structures were observed by an optical microscope and AFM. Figure 4.10 shows an AFM image and line profile of the central region of the ArF laser irradiated spots with 400 (a) and 700 (b) pulses at 95 mJ/cm^2. The average height, size and period of nano-cone structures are larger in the 700 pulses irradiates sites than with 400 pulses.

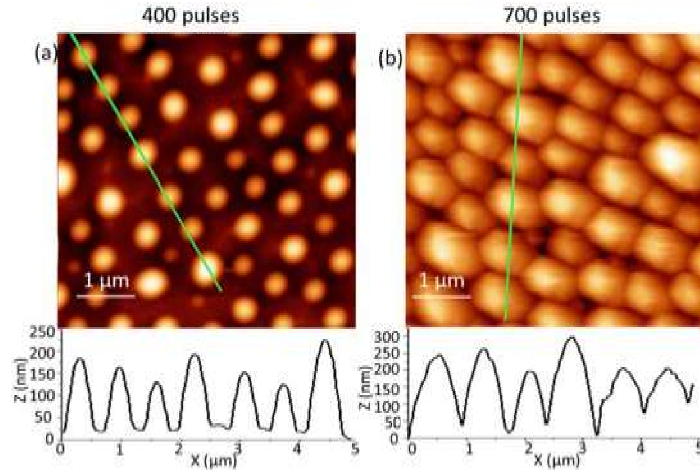

Figure 4. 10 AFM images and profiles along indicated lines of the central region of the ArF laser sites irradiated at 95 mJ/cm^2 with (a) 400 pulses and (b) 700 pulses.

Figure 4.11 summarizes the average height, size (diameter) and period of nano-cone structures (a) along with the normalized PL intensity (b) in the central region of ArF laser irradiated sites as a function of pulse number at 95 mJ/cm^2. It can be seen that the average size and period of nano-cone structures increase with the pulse number and saturate at 600 pulses, while the average height continues increasing up to 700 pulses. The average size and period of these nano-cones are smaller than those corresponding to the sites irradiated with the KrF laser. We did not identify any visible nano-cone structures at sites irradiated with the low number of pulses ($N \leq 200$) of the ArF laser. Related to this is the absence of an enhanced PL. As illustrated in Figure 4.11 (b), the PL signal decays rapidly with pulse number, indicating that significant surface damage occurs in this case. An inset in Figure 4.11 (b) shows an AFM image of the InP surface after it was irradiated with 200 pulses. Randomly distributed nanoparticles of maximum height nearing 40 nm can clearly be seen in the image. The σ_{RMS} roughness [N. Liu*, et al.* 2011c] of that sample was estimated at 7.5 nm, which compares to $\sigma_{RMS} \approx 0.9$ nm for the surface of a non-processed sample. A qualitatively similar surface morphology and reduced PL intensity has also been observed for the site irradiated with 100 pulses of a KrF laser operating at 109 mJ/cm^2 (see Figure 4. 6 a). An increasing PL intensity with increasing pulse number is observed in the $300 \leq N \leq 700$ range. The PL intensity of the 600-pulse irradiated site is about 25% greater than that on a non-irradiated site. This is related to the ArF laser-induced formation of nano-cone structures, as illustrated in Figure 4.10. The average height, diameter and periodicity of the 600-pulse created nano-cones are 188, 837 and 874 nm, respectively. These results are comparable to

those obtained with the KrF laser at 400 pulses and fluence of 142 mJ/cm^2. No formation of nano-cone structures was observed for the ArF laser operating at 82 mJ/cm^2, up to 700 pulses.

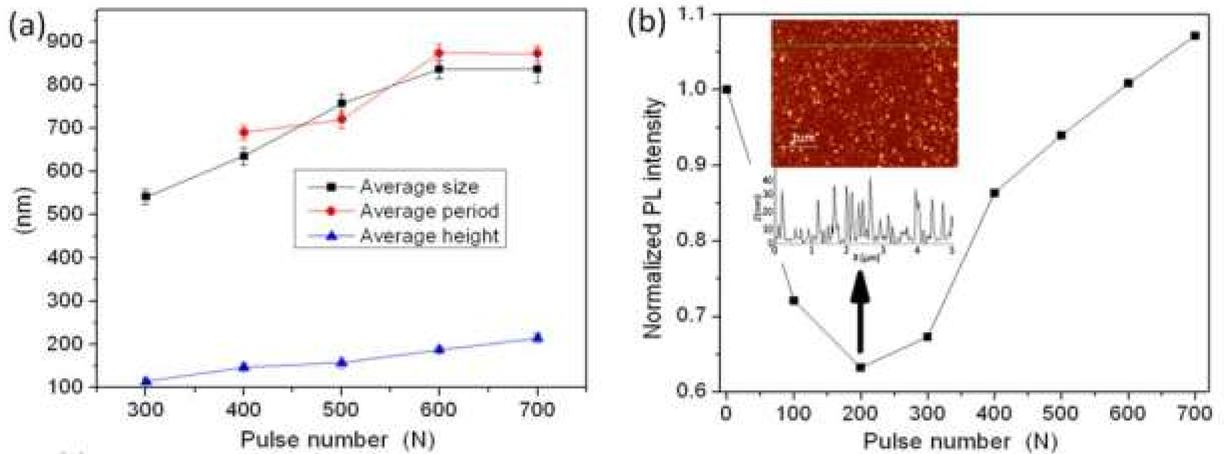

Figure 4. 11 Average size, period and height of the nano-cone structures (a) and normalized PL intensity (b) in the central region of the ArF laser irradiated sites at 95 mJ/cm^2.

4.2.4.3 KrF and ArF laser irradiation of bulk InP wafer

We have also irradiated bulk InP material with KrF and ArF laser using the same laser fluence and pulse number conditions as applied on InP/InGaAs/InGaAsP microstructures. Figure 4.12 shows AFM images of a bulk InP sample irradiated with 400 and 700 pulses of the KrF laser at 142 mJ/cm^2. No obvious nano-cone structure is present in this case. Instead, a randomly formed pattern of nanoparticles is observed. These nanoparticles are approximately 160 nm wide and their average height is around 10 and 20 nm for the 400- and 700-pulse irradiated spots, respectively. Similar surface morphology was also observed during KrF laser assisted etching of bulk InP in Cl_2 environment at 40 mJ/cm^2 with 600 pulses [O. Musaev*, et al.* 2008], although an even smoother surface of InP was reported in the XeCl excimer laser etching experiment of InP at 55 mJ/cm^2 with 2000 pulses in a Cl_2/H_2 environment[J. J. Dubowski*, et al.* 1995]. No measurable changes to the surface morphology of bulk InP samples was observed following their irradiation with the KrF laser at 124 mJ/cm^2 and 109 mJ/cm^2. This suggests that the ablation threshold of bulk InP irradiated in air with ~ 16 ns pulses at 248 nm is greater than 124 mJ/cm^2. For the ArF laser irradiated bulk InP, no evidence of material ablation was found for the pulse fluence of 95 mJ/cm^2 and up to 700 pulses. These differences in the observed ability of both ArF and KrF excimer lasers to modify the surface of the InP epi-layer interfaced with

InGaAs/InGaAsP QW microstructure and that of the bulk InP material are related to different optical properties of these materials, as well as to different temperature profiles and heat dissipation processes in bulk InP and epi-layer microstructures.

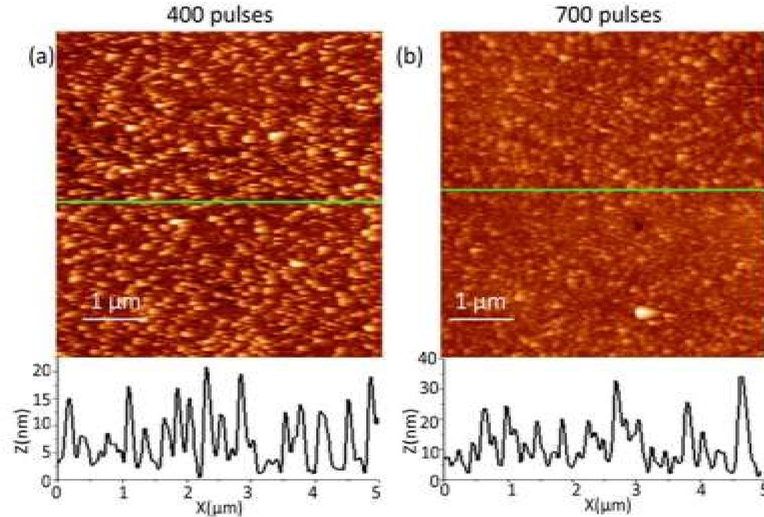

Figure 4. 12 AFM image of bulk InP irradiated with 400 (a) and 700 (b) pulses of the KrF laser operating at 142 mJ/cm^2.

We note that the formation of the nano-cone structures observed in this experiment has been obtained with the ArF and KrF lasers operating above the fluence and pulse number used for the formation of the QWI material. Therefore, these nano-cone structures, while contributing to the enhanced PL emission from the InP/InGaAs/InGaAsP QW heterostructures, do not perturb the QWI process.

4.2. 5 Conclusion

Laser-induced formation of self-organized nano-cone arrays has been observed in InP/InGaAs/InGaAsP microstructures irradiated with KrF and ArF lasers at pulse fluence of 95 - 142 mJ/cm^2 and pulse number from 100 to 700. The average size, height and period of these nano-cone structures increase with laser fluence and pulse number and saturates at larger pulse numbers ($N \geq 600$). No such surface structures have been observed in bulk InP irradiated with lasers under similar conditions. An enhanced QW PL emission has been observed from samples showing nano-cone structures, in proportion to their size and period. The maximum enhancement of ~ 1.4x has been observed for samples irradiated with KrF laser. The formation of relatively weaker developed nano-cones in samples irradiated with the ArF laser is likely related to the

weaker absorption of the 193 nm radiation in comparison to the 248 nm radiation by the investigated InP epi-film.

4.2. 6 Acknowledgments

This work was supported by the Natural Science and Engineering Research Council of Canada and the Canada Research Chair in Quantum Semiconductors program (JJD). One of the authors (NL) wishes to acknowledge the support from the Merit Scholarship program for Foreign Students of the Fonds de Recherche sur la Nature et les Technologies du Québec. The help from the Centre de recherche en nanofabrication et en nanocaracterisation (CNR^2) and Centre de Caractérisation des Matériaux (CCM) of Université de Sherbrooke is greatly appreciated.

4.3 Surface morphology of InP/InGaAs/InGaAsP microstructures coated with dielectric layers and irradiated with ArF and KrF excimer lasers

4.3.1 Samples coated with SiO_2 and irradiated with ArF laser

Figure 4.13 shows PL maps of samples coated with 50 and 150 nm thick PECVD deposited SiO_2 layers that were irradiated with the ArF laser at 76 mJ/cm^2. PL maps and microscopy images are shown in top and bottom rows of each series. It can be seen that SiO_2 layers were not ablated completely, even with 400 pulses. An obvious blueshift takes places only in the regions where the SiO_2 layer is ablated.

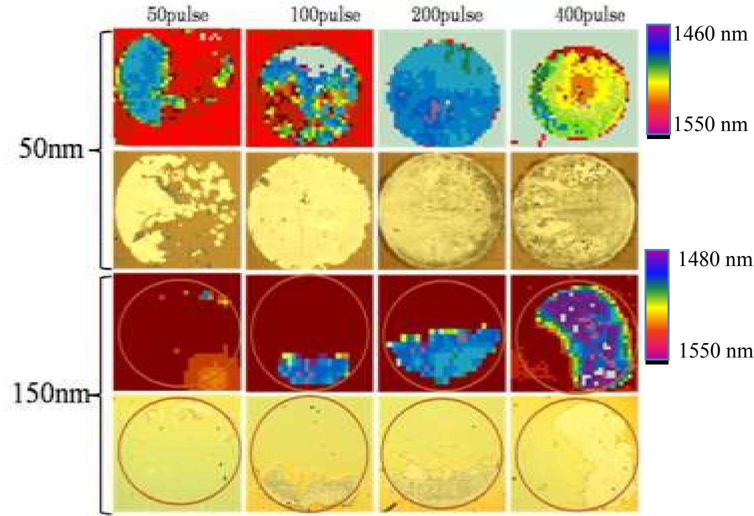

Figure 4. 13 Room temperature PL maps and microscopic pictures of a series of spots on SiO_2 (50 and 150 nm thick) coated QW microstructures irradiated with ArF laser at 76 mJ/cm^2.

Figure 4.14 shows 2.5 μm x 2.5 μm AFM images of 150 nm thick, SiO_2 layer before and after irradiated with 20 and 100 pulses of the ArF laser, followed by RTA. One notices that the laser-irradiated sites have, qualitatively, similar grain structures as that of the as-grown material. The grain structure is formed during PECVD with the grain size depending on the SiO_2 layer thickness [D. S. Wuu*, et al.* 2005]. The corresponding cross-section profiles, below each AFM image, indicate that the grain size of the investigated SiO_2 layer is around 60 nm. AFM measured surface roughness amplitude (σ_{RMS}) decreases from 1.31 nm for the as-grown sites to 1.07 nm for the 150-pulse-irradiated sites. As the SiO_2 melting temperature is around 1873 K, it is much higher than ArF laser induced temperature at 76 mJ/cm^2 (700 K), which was discussed in chapter 2. It is likely that laser-induced densification and surface cleaning of SiO_2 is the mechanisms responsible for this surface smoothing effect, as shown in XPS analysis in chapter 5. The surface morphology of InP after the SiO_2 layer was etched with the HF: H_2O solution (10%) is shown in Figure 4.14 (b). It can be seen that surface morphology of irradiated and non irradiated sites is comparable, while the σ_{RMS} of those surfaces fluctuates around 0.4 nm, which is representative of a high-quality surface of InP. The bandgap energy of SiO_2 (9 eV) is greater than photon energy of both ArF (~ 6.4 eV) and KrF (~ 5.0 eV) lasers. Hence, the SiO_2 layer should absorb only weakly the radiation of these lasers [F. Messina*, et al.* 2008]. However, our results indicate that SiO_2 layer protected InP surface against ArF laser irradiation, and prevented formation of

surface defects - consistent with the absence of the laser-induced intermixing process observed in this case.

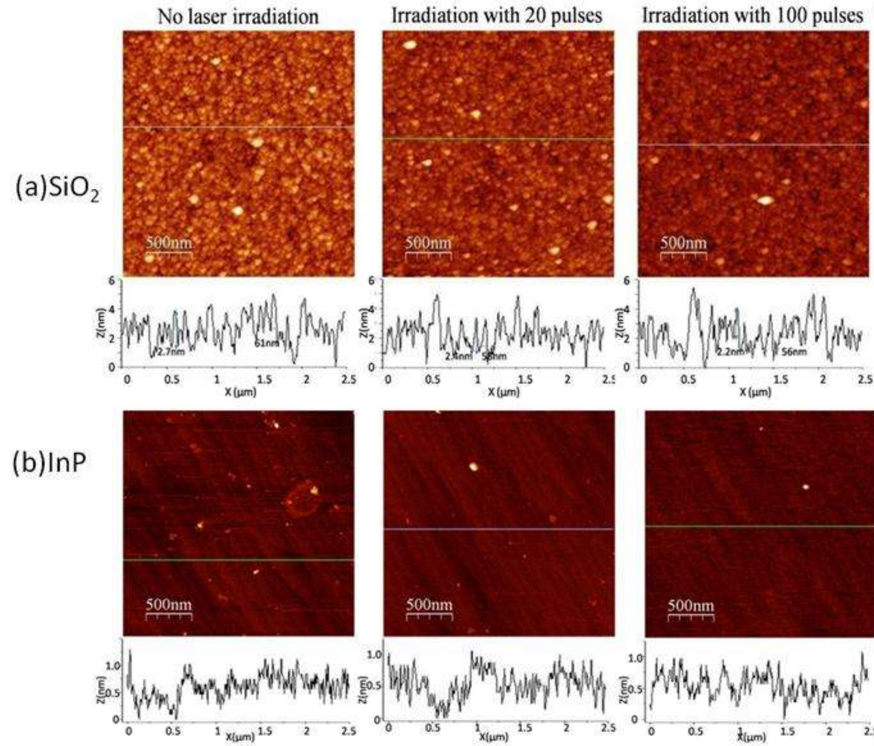

Figure 4. 14 AFM image of SiO_2 layer (a) and InP surface revealed after SiO_2 removed (b). The SiO_2 coated as-grown material and irradiated with ArF laser at 76 mJ/cm^2 underwent RTA at 700 °C for 2 min.

Figure 4.15 shows the 5 μm x 5 μm 2D and 3D AFM images of the InP surface revealed after the 150-nm-thick SiO_2 layer was ablated with 100 pulses of the ArF laser. There are ripples whose period and height are around 1 μm and 10 nm, respectively. The spacing is larger than laser induced period surface structures (LIPSS),$\Lambda = \frac{\lambda}{1 \pm \sin \Theta}$, as we discussed in chapter 2. This periodical ripple structure is possibly laser induced capillary wave, whose period is no dependence on incidence angle and polarization and is reported to between 1 and 3 μm [S. E. Clark*, et al.* 1989]. Figure 4.15 (a) also shows the presence of numerous 12 nm deep nano-holes on the processed surface. The roughness of this region is 2.11 nm, which compares to ~ 0.5 nm of the as-grown InP surface. We note that following the RTA step, the surface defects created during the ArF laser interaction with the InP layer induced a 38 nm blueshift.

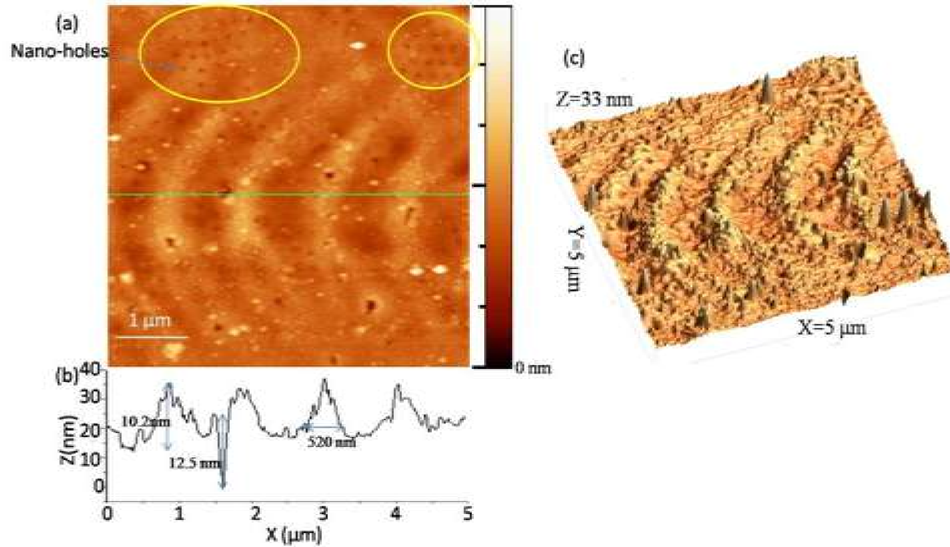

Figure 4. 15 Surface morphology of the InP cap layer exposed to the ArF laser radiation in the region where SiO_2 was removed.

4.3.2 Samples coated with SiO_2 and irradiated with KrF laser

For samples coated with 50, 150 and 190 nm thick SiO_2 layer and irradiated with KrF laser at 156 mJ/cm^2, ablation and partial removal of SiO_2 were observed with up to 200 pulses. Numerous laser-induced structural defects (microcracks) have been observed for these samples. However, the irradiation with low number of pulses at fluence reduced to 124 mJ/cm^2 produced more uniform results. This is illustrated in Figure 4.16 that shows microscopic images of a sample coated with a 243-nm-thick SiO_2 layer ($d_{SiO2} \approx \lambda_{KrF}$) and irradiated with 2, 25, 75 and 100 pulses. The color change of the SiO_2 layer is likely related to the laser-induced densification and, consequently, change of the refractive index of this material [S. Mao*, et al.* 2004]. The profilometry measurements have indicated a reduction of the overall thickness of the irradiated SiO_2 layer by up to 10 nm at 75 pulses.

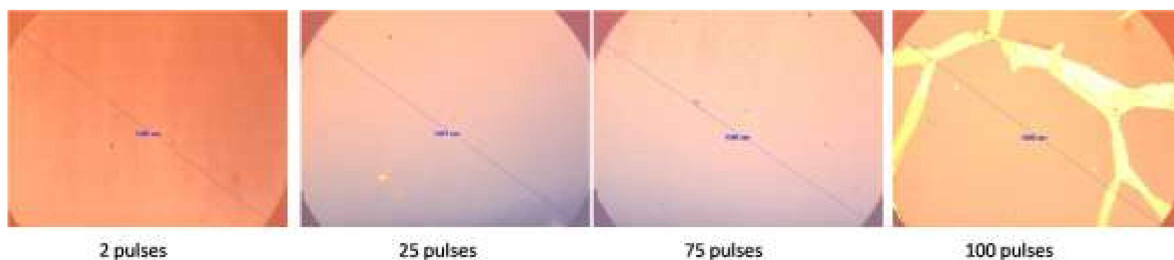

Figure 4. 16 Microscopic images of samples coated with 243 nm thick layer of SiO_2 and irradiated with KrF excimer at 124 mJ/cm^2 (after RTA).

Figure 4.17 (a) shows AFM micrographs of as-grown, 243 nm thick SiO_2 layer and those of the sites irradiated with 2 and 25 pulses of the KrF laser at 124 mJ/cm^2, and all are before RTA. The grain structure of the material is well seen for both non-irradiated material and irradiated sites. The average grain size of this SiO_2 layer is around 50 nm, which is smaller than that of the 150 nm thick SiO_2 layer (~ 60 nm). The average grain height decreases from 5.22 nm to 4.02 nm as the pulse number increases to 25 pulses due to laser surface cleaning of SiO_2 layer. The surface morphology of the sample after RTA and removing the SiO_2 layer is illustrated in Fig. 4.17 (b). Numerous nano-holes created in InP can be seen for the 2-pulse and, especially, for the 25-pulse irradiated surface. None of these nano-holes have been found on the non irradiated site, hence, the role of the KrF laser is evident in the formation of these nano-holes. It can be seen that the nano-hole depth increases from 2.5 nm to 3.3 nm and the width increases from 39 nm to 73 nm as the pulse number increases from 2 to 25 pulses. The density of nano-holes is also greatly increased for the 25 pulse irradiated site. The high magnification of InP surface morphology of sites irradiated with 25 pulses was shown in Figure 4.18 and the nano-holes is clearly found on the InP surface. We observed 8 nm deep, 83 nm wide nano-holes on sites irradiated with 100 pulses of the KrF laser. The formation of nano-holes leads to the increased average roughness of the irradiated surface, while the density of nano-holes saturation is observed at a large pulse number. As will be discussed in Sec. 4.5, the blueshift amplitude dependence on pulse number follows the same behaviour (see Figure 4.22). Therefore, it seems that the presence of nano-holes is somehow responsible for the intermixing process. The nano-holes may enhance defect creation and diffusion, similarly to microcracks reported in QW irradiated with CW laser RTA [C. Chia, *et al.* 2005].

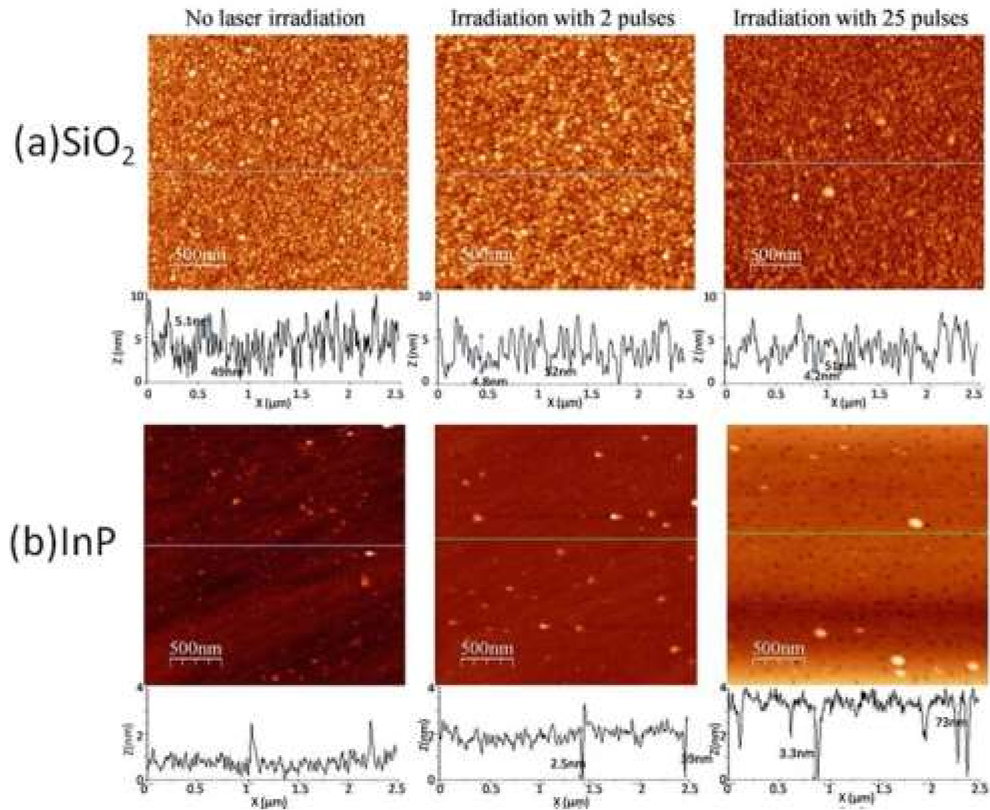

Figure 4. 17 AFM micrographs of SiO_2 (a) and InP (b) layer of non irradiated sites and irradiated sites

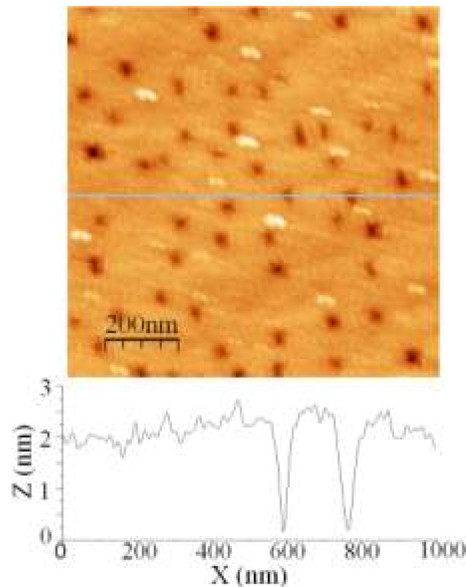

Figure 4. 18 High magnification InP surface morphology of irradiated sites with 25 pulses after RTA and removing SiO_2 layer

Figure 4.19 shows the RMS roughness of InP interface dependence on pulse number after KrF laser irradiation at 124 mJ/cm^2. The relevance of these results is that it correlates with the

blueshift amplitude dependence on the laser pulse number, as illustrated in Figure 6.1 in chapter 6.

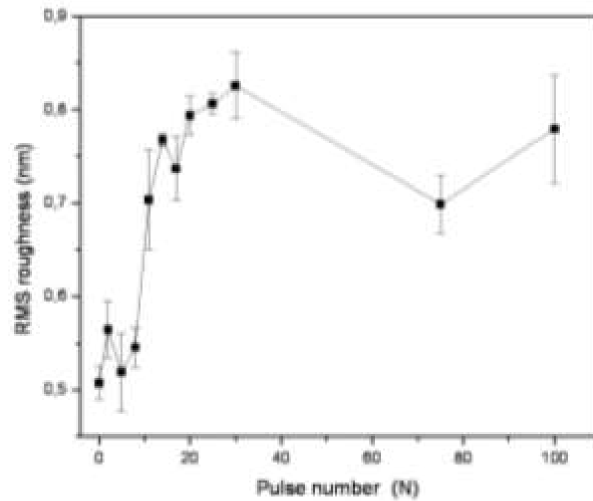

Figure 4. 19 The RMS roughness of the InP layer irradiated with different pulses of the KrF at 124 mJ/cm^2, followed by the RTA step. The results are shown after the SiO_2 layer has been removed.

Figure 4.20 (a) and (b) shows SEM micrograph of the SiO_{2-x}/InP cross sections region before and after KrF laser irradiation at 124 mJ/cm^2 with 25 pulses. It shows that there is approximately 8.65 nm thick, interface layer between SiO_{2-x} and InP, before KrF laser irradiation. This is an In_2O_{3-x} layer that was reported forming on the InP surface coated with a PECVD SiO_2 [Z. Liliental, *et al.* 1985]. The SEM observation has been corroborated by the ellisopmetry measurements indicating that the total thickness of that interface layer is ~ 7.7 nm. A thicker interface layer of ~ 53.05 nm has been observed in the sample irradiated with the KrF laser, see Figure 4.20 (b), compared to a 45.3 nm thick interface layer suggested by the elliposometry. The ellipsometry measurements have also indicated that the laser irradiation leads to a 6 - fold growth of the InP-oxide layer, while as large as a 14 - fold growth of the In_2O_{3-x} layer has been suggested. The SEM observations confirms that KrF laser has induced interface morphology modification which consist with what was observed by AFM in Figure 4.17.

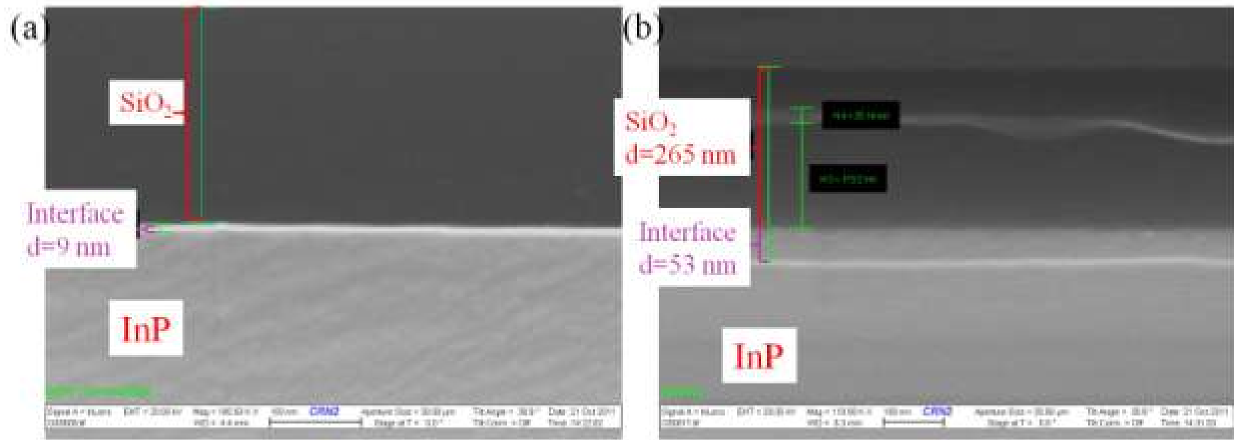

Figure 4. 20 SEM image of InP/InGaAs/InGaAsP QW sample (M1580) coated with a 243 nm thick layer of SiO_2 before KrF laser irradiation (a) and after irradiated with 25 pulses at 124 mJ/cm^2 (b).

For samples coated with 263 nm thick SiO_2 layer and irradiated with KrF laser at 124 mJ/cm^2 and followed by RTA, no obvious laser ablation of SiO_2 was observed for up to 100 pulses. This is because that the SiO_2 layer temperature decreases as the thickness increased when irradiated at same laser fluences, as discussed in chapter 2. At 200 pulses, the color of the SiO_2 layer changes significantly, which suggests that some structural changes take place in the laser irradiated SiO_2.

4.3.3 Sample coated with Si_3N_4 layer irradiated by ArF laser

In this experiment, different thicknesses Si_3N_4 layers were deposited on top of the QW (RAC82) microstructure. Here, we choose 40 nm and 80 nm thick Si_3N_4 to investigate surface morphology modification during ArF laser irradiation. Figure 4.20 shows the microscopic pictures of samples coated with (a) 40 and (b) 80 nm thick Si_3N_4 after ArF laser irradiation at 70 mJ/cm^2 with 20 pulses. The different background colour is due to different reflectivity of Si_3N_4 and that of the semiconductor substrate [J. Kvavle*, et al.* 2004]. The ablated depth of the sample with 40 nm Si_3N_4 is 45 nm (as determined by the profilometry measurements). On the sample coated with 80 nm Si_3N_4 layer, as Figure 4.21 (b), there is no obvious ablation effect. It is because that the absorption coefficient of Si_3N_4 layer is about 1.5 x 10^5 /cm in the UV wavelength range, which corresponds to the absorption depth of 65 nm.

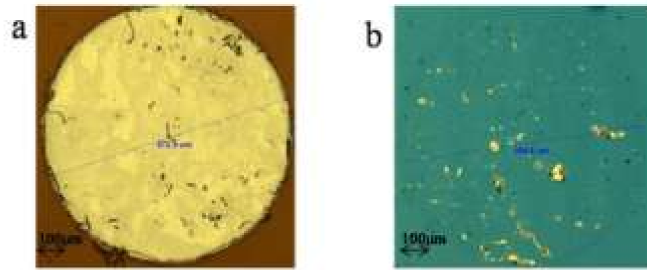

Figure 4. 21 Microscopic picture of InP/InGaAs/InGaAsP microstructure coated with 40 nm (a) and 80 nm (b) Si_3N_4 layer after ArF laser irradiation at 70 mJ/cm^2.

4.4 Surface morphology of InP/InGaAs/InGaAsP microstructure irradiated in DI water with ArF anf KrF excimer lasers

Figure 4.22 shows AFM image of non irradiated site and sites irradiated by ArF laser at 82 mJ/cm^2 in DI water with 20 and 40 pulses. Similar as irradiated by ArF laser in air, the roughness increases to 5.24 and 7.11 nm on sites irradiated in DI water with 20 and 40 pulses due to generation of nanofeatures. The interesting things were found on non irradiated sites in DI water, there are numbers of nanodots whose size is around 10 nm with roughness around 1.28 nm. They are possibly generated by the laser sputtered material from irradiated sites then recoiling back to the non irradiated sites surface after cooling and suspension in DI water [B. Kumar, *et al.* 2010].

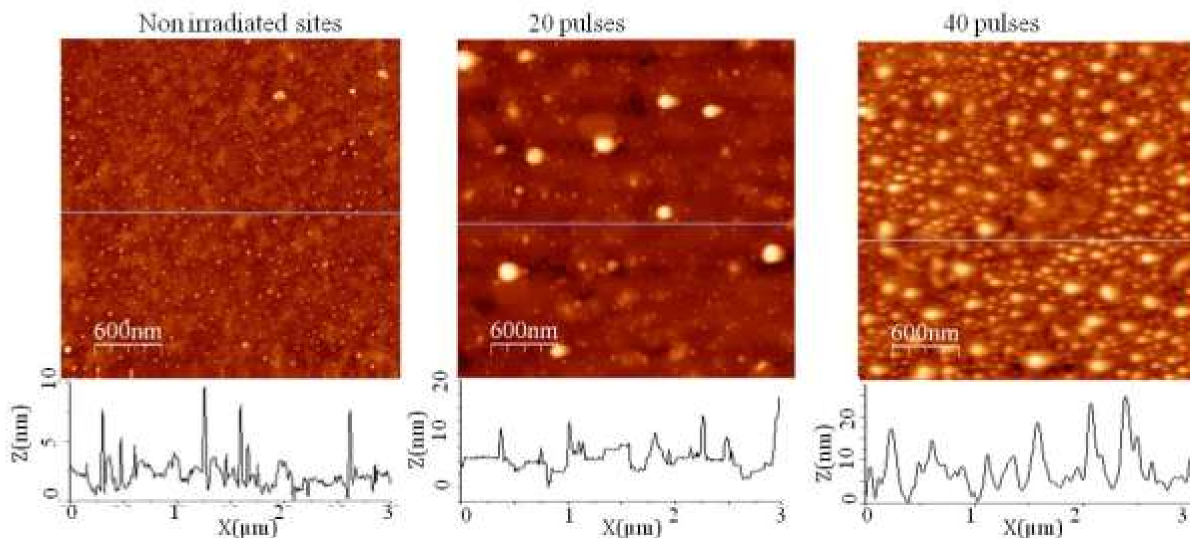

Figure 4. 22 AFM image of non irradiated sites and sites irradiated by ArF laser in DI water

Figure 4.23 shows the AFM image of non irradiated and irradiated site with 20 and 40 pulses by ArF laser in DI water (a) and air (b) and then after RTA. The roughness on all the irradiated sites decreases due to mass transport during RTA [J. J. Dubowski*, et al.* 1999b]. On sites irradiated in DI water, the roughness is 3.01 and 3.71 nm for 20 and 40 pulses. There are nanoholes on samples irradiated sites in DI water after RTA, which were not observed in air. This is possible due to the different defects created during laser irradiation and diffusion during annealing in these two environments. On the non irradiated sites in DI water, the surface morphology is similar as in air with roughness around 0.9 nm. The roughness variation dependence on pulse number and RTA is shown in Table 4.2 (I).

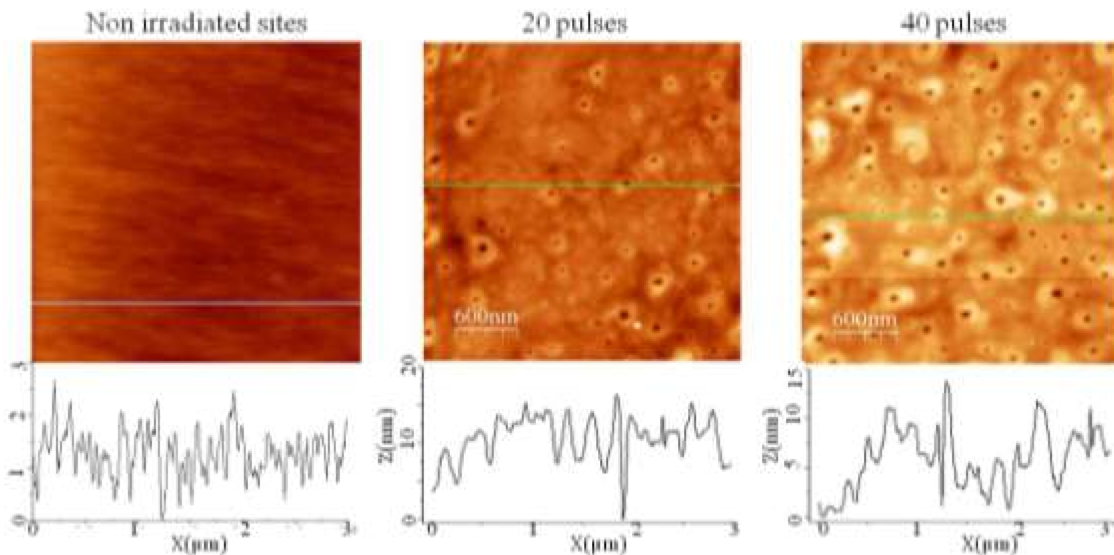

Figure 4. 23 AFM image of non irradiated sites and sites irradiated with ArF laser in DI water and after RTA.

Table 4.2 (II) shows RMS roughness of non irradiated sites and sites irradiated by KrF laser at 124 mJ/cm^2 with 10 and 25 pulses in DI water and air and then after RTA. The roughness increases with pulse numbers. However, after RTA, we found that all the roughness decrease the approximate value on sites irradiated in air and DI water, similar as sample irradiated by ArF laser in Table 4.3 (I). It suggested that the surface morphology effects on optical properties, e.g PL signal, is negligible on sites irradiated in DI water and air and then following RTA to induce intermixing. There are also nanodots on nonirradiated sites in DI water, which cause the roughness increase from as grown sites after irradiation before RTA. When irradiated in DI water, the surface morphology on laser irradiated sites has modified and the roughness increases

with pulse number. The roughness on the sites irradiated in DI water after RTA is comparable to sites irradiated in air.

Table 4. 2 RMS roughness on non irradiated site and irradiated sites by ArF (I) and KrF (II) laser in DI water

(I)

RMS (nm)	In DI water before RTA	In DI water after RTA
Non irradiated	1.28	0.9
20 pulses	5.235	3.01
40 pulses	7.11	3.71

(II)

RMS (nm)	In DI water before RTA	In DI water after RTA
Non irradiated	1.17	0.89
10 pulses	4.86	2.36
25 pulses	12.02	2.78

4.5 Blueshifting amplitude in InP/InGaAs/InGaAsP microstructure irradiated in air and through SiO_2, Si_3N_4 cap layers

On the sample coated with different thickness dielectric layers during excimer laser QWI, we found that the intermixing only happens when the dielectric layers were ablated and the surface morphology of top InP layer is altered by excimer lasers. However, PL shift was observed on KrF laser irradiated at 124 mJ/cm^2 on samples coated with 243 nm SiO_2 layer without ablation of SiO_2 layer, as shown in Figure 4.24. The upper and lower numbers shown for each site in this figure indicate the laser pulse number and the average amplitude of blueshift, respectively. We note that a uniform blueshift of 57 nm has been achieved following the irradiation with only 2 laser pulses. The maximum PL shift of 74 nm was get on sites irradiated with 100 pulses. The PL shift increase with pulse number was consisting with the increment of density of manholes (roughness), as shown in AFM image in Figure 4.17.

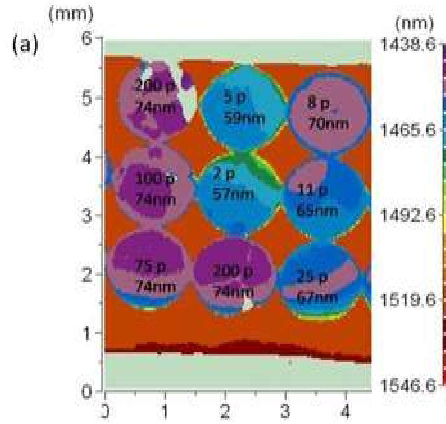

Figure 4. 24 PL map of the sample irradiated by KrF laser at 124 mJ/cm^2 and RTA.

Figure 4.25 shows the PL map of samples coated with 40 (a) and 80 nm (b) Si_3N_4 layer after ArF laser irradiation at 70 mJ/cm^2 and RTA at 700 °C for 120 seconds. It can be seen that for the sample coated with 40 nm Si_3N_4, there is an obvious array of sites with different bandgaps. On the same QW microstructure coated with 80 nm Si_3N_4 layer, there are no distinguishable blueshifted sites. This is because the 40 nm Si_3N_4 layer is ablated completely during laser irradiation while the 80 nm Si_3N_4 layer is almost not damaged, as shown in Figure 4.21. Thus, the blueshifts of these sites are related to the ArF laser created defects after the Si_3N_4 layer is ablated. It has been reported that laser irradiation could densify the coating Si_3N_4 layer [M. Delfino 1985] and reduce its porosity. This could lead to the formation of a stress at the Si_3N_4/InP interface and suppressed intermixing of the QWI process [A. Pepin*, et al.* 1997b] . As shown in Figure 4.25, the site irradiated with 100 pulses demonstrates a 2 nm red shift on sample coated with 80 nm Si_3N_4, which likely indicates the stress related effect.

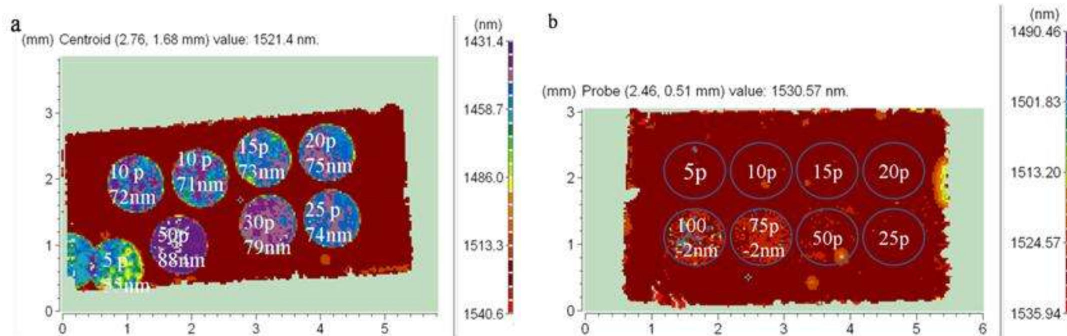

Figure 4. 25 Room temperature PL map of InP/InGaAs/InGaAsP sample coated with (a) 40 nm and (b) 80 nm Si_3N_4 after ArF laser irradiation and RTA.

4.6 Summary

In this chapter, I have presented the surface morphology modification of excimer laser processed InP/InGaAs/InGaAsP microstructure surrounded by air, dielectric layers (SiO_2 and Si_3N_4) and DI water.

When irradiated in air, the sample surface morphology is modified obviously. The roughness increases with pulse numbers and decreases after RTA when irradiated by ArF and KrF laser. Self organized nanocone surface structures were created on as grown material when it was irradiated with KrF and ArF lasers with larger pulse numbers up to 700 pulses, which is outside of UV laser QWI range. The average size, height and period of the nano-cone structures increase with laser fluence and pulse number and saturates at larger pulse numbers ($N \geq 600$). No such surface structures have been observed in bulk InP irradiated under similar conditions. The maximum enhancement of ~ 1.4x was found on samples with the laser induced nanocone structures.

We have investigated morphology of dielectric layer (SiO_2 and Si_3N_4) and InP layers of QW microstructure that were irradiated with the ArF and KrF lasers. For sample coated with 50 or 150 nm SiO_2 layer irradiated by the ArF laser, the blueshift is observed only in the region where the SiO_2 layer is ablated and InP surface morphology is modified. Similar results were founded on sample coated with Si_3N_4 during ArF laser QWI. On the other hand, the maximum blueshift of 74 nm was achieved on sample coated with a 243 nm thick SiO_2 layer ($d_{SiO2} \approx \lambda_{KrF}$) showing a smooth surface after 100-pulse-radiation with the KrF laser at 124 mJ/cm^2. A relatively large number of nano-holes have been observed in the InP layer irradiated with the KrF laser. The presence of these nano-holes coincides with the enhancement of the QWI process.

When irradiated in DI water, the InP surface morphology is modified during excimer laser irradiation. The roughness on non irradiated and irradiated sites after excimer laser irradiation and RTA is comparable to sample irradiated in air. However, on non irradiated sites in DI water, there are nanodots created on the surface.

Therefore, during UV laser QWI process, laser induced surface defects generation is always consist with InP surface morphology modification. The modification varies with surrounded environments.

4.7 Bibliography

Abbott, N.L., Gorman, C.B., et al., (1995), Active control of wetting using applied electrical potentials and self-assembled monolayers, *Langmuir*, vol. 11, n°1, 16-18.

Aspnes, D., and Studna, A., (1983), Dielectric functions and optical parameters of Si, Ge, GaP, GaAs, GaSb, InP, InAs, and InSb from 1.5 to 6.0 eV, *Physical Review B*, vol. 27, n°2, 985.

Bauerle, D.: (2010), Laser processing and chemistry (Springer Berlin), 788p.

Bulgakov, A., Evtushenko, A., et al., (2010), Pulsed laser ablation of binary semiconductors: mechanisms of vaporisation and cluster formation, *Quantum Electronics*, vol. 40, 1021.

Chia, C., Chua, S., et al., (2005), Group-V intermixing in InAs/ InP quantum dots, *Applied Physics Letters*, vol. 86, 051905.

Chichkov, B.N., Momma, C., et al., (1996), Femtosecond, picosecond and nanosecond laser ablation of solids, *Applied Physics A: Materials Science & Processing*, vol. 63, n°2, 109-115.

Clark, S.E., and Emmony, D.C., (1989), Ultraviolet-laser-induced periodic surface structures, *Physical Review B*, vol. 40, n°4, 2031-2041.

Delfino, M.: 'Laser treatment of silicon nitride', 1985.

Dubowski, J.J., Rosenquist, B.E., et al., (1995), Structure damage in reactive ion and laser etched InP/GalnAs microstructures, *Journal of Applied Physics*, vol. 78, n°3, 1488-1491.

Dubowski, J.J., Poole, P.J., et al., (1999), Enhanced quantum-well photoluminescence in InGaAs/InGaAsP heterostructures following excimer-laser-assisted surface processing, *Applied Physics A: Materials Science & Processing*, vol. 69, 299-303.

Fathipour, M., Boyer, P., et al., (1985), Photoenhanced thermal oxidation of InP, *Journal of Applied Physics*, vol. 57, n°2, 637-642.

Fujii, T., David, A., et al., (2005), Cone-shaped surface GaN-based light-emitting diodes, *Physica Status Solidi (c)*, vol. 2, n°7, 2836-2840.

Genest, J., Dubowski, J., et al., (2007a), UV laser controlled quantum well intermixing in InAlGaAs/GaAs heterostructures, *Journal of Physics: Conference Series*, vol. 59, 605-609.

Genest, J., Dubowski, J.J., et al., (2007b), Suppressed intermixing in InAlGaAs/AlGaAs/GaAs and AlGaAs/GaAs quantum well heterostructures irradiated with a KrF excimer laser, *Applied Physics A: Materials Science & Processing*, vol. 89, n°2, 423-426.

Genest, J., Beal, R., et al., (2008), ArF laser-based quantum well intermixing in InGaAs/InGaAsP heterostructures, *Applied Physics Letters*, vol. 93, 071106.

Hey, R., Gorbunova, I., et al., (1997), Growth-mode-induced surface morphology and its relation to optical properties of GaAs single quantum wells, *Journal of Crystal Growth*, vol. 175-176, n°Part 2, 1167-1172.

Huang, H.W., Chu, J., et al., (2005), Enhanced light output of an InGaN/GaN light emitting diode with a nano-roughened p-GaN surface, *Nanotechnology*, vol. 16, 1844.

Kumar, B., and Soni, R., (2008), Submicrometre periodic surface structures in InP induced by nanosecond UV laser pulses, *Journal of Physics D: Applied Physics*, vol. 41, 155303.

Kumar, B., and Soni, R., (2010), Synthesis of InP nanoparticles by pulsed laser ablation in ethanol, *Materials Chemistry and Physics*, vol. 121, n°1, 95.

Kvavle, J., Bell, C., et al., (2004), Improvement to reflective dielectric film color pictures, *Optics Express*, vol. 12, n°23, 5789-5794.

Liliental, Z., Krivanek, O., et al., (1985), Structure of the InP/SiO_2 interface, *Applied Physics Letters*, vol. 46, n°9, 889-891.

Liu, N., Moumanis, K., et al., (2011), Surface morphology of SiO2 coated InP/InGaAs/InGaAsP microstructures following irradiation with the ArF and KrF excimer lasers, *Proceeding of SPIE*, vol. 7920, 79200C.

Mao, S., F, Q., et al., (2004), Dynamics of femtosecond laser interactions with dielectrics, *Applied Physics A*, vol. 79, n°7, 1695-1709.

Medvid, A., Mychko, A., et al., (2010), Mechanism of nano-cone formation on $Cd_{0.9}Zn_{0.1}Te$ crystal by laser radiation, *Optical Materials*, vol. 32, n°8, 836-839.

Messina, F., Cannas, M., et al., (2008), Generation of defects in amorphous SiO2 assisted by two-step absorption on impurity sites, *Journal of Physics: Condensed Matter*, vol. 20, 275210.

Musaev, O., Kwon, O., et al., (2008), Evolution of InP surfaces under low fluence pulsed UV irradiation, *Applied Surface Science*, vol. 254, n°18, 5803-5806.

Pepin, A., Vieu, C., et al., (1997), Evidence of stress dependence in SiO/SiN encapsulation-based layer disordering of GaAs/AlGaAs quantum well heterostructures, *Journal of Vacuum Science & Technology B: Microelectronics and Nanometer Structures*, vol. 15, 142.

Shin, D.S., Lee, J.H., et al., (2006), Correction of a coherent image during KrF excimer laser ablation using a mask projection, *Optics and Lasers in Engineering*, vol. 44, n°6, 615-622.

Takai, M., Tsuchimoto, J., et al., (1988), Laser-induced thermochemical maskless-etching of III–V compound semiconductors in chloride gas atmosphere, *Applied Physics A: Materials Science & Processing*, vol. 45, n°4, 305-312.

Wuu, D.S., Lo, W.C., et al., (2005), Plasma-deposited silicon oxide barrier films on polyethersulfone substrates: temperature and thickness effects, *Surface and Coatings Technology*, vol. 197, n°2-3, 253-259.

Xu, C., and Mei, T., (2009), Inductively Coupled Argon Plasma-Enhanced Quantum-Well Intermixing: Cap Layer Effect and Plasma Process Influence, *IEEE Journal of Quantum Electronics*, vol. 45, n°8, 920-926.

Chapter 5 Excimer laser induced surface chemistry modification of InP/InGaAs/InGaAsP QW microstructures

In this chapter, I will present surface and interface analysis of InP/InGaAs/InGaAsP microstructures coated with 243 nm SiO_2 layer irradiated with KrF laser. Then I will present the results of XPS analysis of chemical evolution of InP/InGaAs/InGaAsP microstructure after ArF and KrF laser irradiation in air and DI water (published in Applied Surface Science *270*(13), 16-24, (2013)). I will also discuss chemical modification of InP/InGaAs/InGaAsP microstructure coated with InO_x layer, irradiated with KrF and RTA.

5.1 XPS analysis of KrF laser irradiated InP/InGaAs/InGaAsP microstructures coated with SiO_2 layer

In this experiment, KrF laser was used to irradiate InP/InGaAs/InGaAsP microstructure (M1580) coated with 243 nm PECVD deposited SiO_{2-x} layer. The irradiation was carried out at 124 mJ/cm^2 and RTA at 700 °C for 2 minutes. Table 5.1 show the atomic percentage of Si, O and C in SiO_{2-x} layer of non-irradiated and 25-pulse irradiated sites, 73 nm blue shifted. The O/Si ratio for both sites is less than 2, which suggests that the film is a mixture of different Si oxides. It can also be seen that the O/Si ratio of 1.52 increases to 1.54 in the irradiated site. A slight increase in the O content is expected, as the irradiation was carried out in an atmospheric environment. A decrease of C on the surface of laser irradiated SiO_{2-x} suggests that some laser cleaning of the adventitious C took place [P. Neves*, et al.* 2002].

Table 5. 1 Atomic percentage of elements of non irradiated sites and irradiated by KrF laser with 25 pulses

Atomic %	Si	O	C
Non irradiated	35.92	54.50	9.58
Irradiated with 25 pulses	35.74	55.14	9.12

The detailed Si 2p, O 1s and C 1s XPS spectra for this sample are shown in Figure 5.1. Following the typical order BE of Si oxides, the Si 2p peak can be deconvolved into SiO_2

(BE=104.0 ± 0.1 eV, FWHM = 1.28 eV) and SiO_x (BE = 103.5 ± 0.1 eV, FWHM = 1.28 eV) [C. Wagner*, et al.* 1982]. On the site irradiated with 25 pulses, there is additional peak at lower binding energy (BE = 101.9 eV) in the Si 2p XPS spectrum in Figure 5.1 (d) that is accompanied by the peak at lower BE (282.8 eV) in the C 1s spectrum in Figure 5.1 (f). This peak in C 1s spectra always corresponds to carbon in carbides or carbon-oxygen-metal complexes [T. P. Nguyen*, et al.* 2003]. Therefore, according to the peak position of both C 1s and Si 2p spectra, this chemical bond was assigned to Si-C created by the KrF laser [T. Tsvetkova*, et al.* 2010]. All the Si oxides are referenced to the same BE (533.0 eV) in the O 1s spectra shown in Figure 5.1 (b), (e) as the position of this peak is less sensitive to the presence of all oxides in contrast to the Si 2p peak [B. Gallas*, et al.* 2002]. There is also a weak O 1s peak at the lower BE (BE = 531.116 eV) that could be ascribed to O 1s in non-stoichiometric Si oxides. On the irradiated site, there is another Si-O peak observe at 533.7 eV, which is similar to the reported results [I. Stavarache*, et al.* , T. A. Clarke*, et al.* 1976]. Besides the Si-O peak, there is a H_2O related peak (BE = 534.2 ± 0.2 eV), whose amount has been reduced after laser irradiation due to KrF laser heating as shown in Figure 5.1 (b) and (e). Also, in C 1s spectra in Figure 5.1 (c) and (f), the quantities of –COH (BE = 286.6 ± 0.2 eV), -CO (BE = 287.8 ± 0.2 eV), -COO- (BE = 289.2 ± 0.2 eV) absorbates have decreased following the laser irradiation, i.e., the carbon contained absorbates have been partly eliminated by the KrF laser surface cleaning [P. Neves*, et al.* 2002].

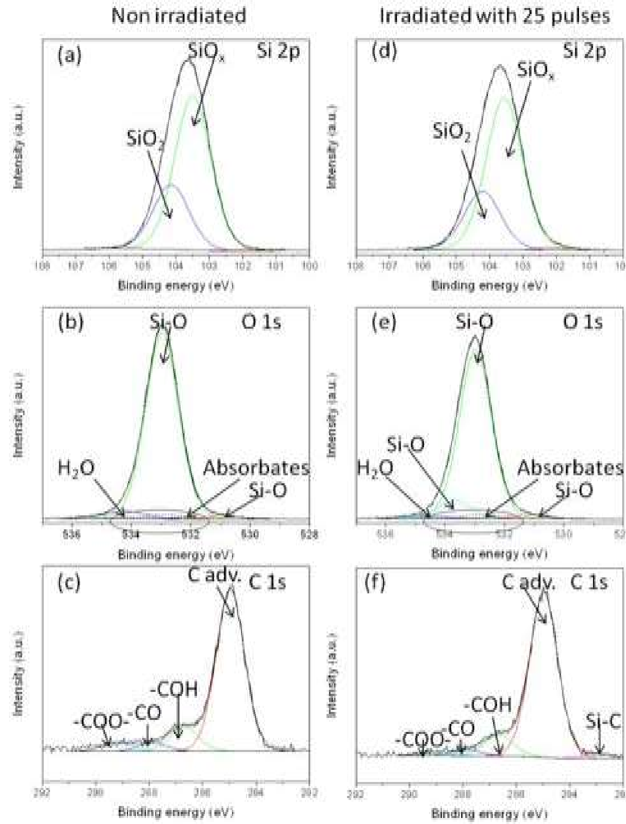

Figure 5. 1 Si 2p (a), (d), O 1s (b), (e) and C 1s (c), (f) XPS spectra of no irradiated site and site irradiated with 25 pulses by KrF laser at $124mJ/cm^2$

The outdiffusion of different atoms from top InP layer to the SiO_{2-x} layer was analyzed by XPS depth profiling that employed Ar ion sputtering. The depth resolution for profiling is 12~24 nm. In contrast to the reported earlier results [C. Chia*, et al.* 2005, S. Barik*, et al.* 2007], no In 3d and P 2s are found in the SiO_{2-x} layer after KrF laser irradiation and RTA in XPS survey. No obvious Si 2p is found in the InP cap material, so the negligible role of Si impurities (if any) is suggested. Figure 5.2 shows high resolution XPS scans in the In 3d and P 2s spectral regions recorded from the SiO_{2-x} layer (a, d), SiO_{2-x}/InP *interface 1*(b, e), SiO_{2-x}/InP *interface 2* (c, f) and InP layer (d, h). SiO_{2-x}/InP *interface 2* is the surface which is ion sputtered for another 60 seconds after reaching the SiO_{2-x}/InP *interface 1*. No In 3d (445 eV) and P 2s (187 eV) peaks are found in the SiO_{2-x} layer. No P 2s peak is found at the SiO_2/InP *interface 1*. However, the presence of In $3d_{5/2}$ peak is clearly observed in this interface 1 region. It has been reported that the charging effect caused by X-ray irradiation changes as sputtering time changes in depth profiling of SiO_{2-x} film coated semiconductor system [S. Iwata*, et al.* 1996, Y. Liu*, et al.* 2006]. Here we find that both C1s and Si 2p core level have shifted 0.7 eV from surface to interface 1.

The peak at 445.1 eV in In spectra in Figure 5.2 (b) reference to the C peak at 285 eV after correcting the charging effect can be assigned to In-O peak [N. Shibata*, et al.* 1992, J. Pan*, et al.* 1999]. This In-O may contains plasma oxides grown during exposure to an oxygen plasma in the PECVD reaction chamber which has been verified in indepth XPS analysis on PECVD deposited SiO_{2-x}/InP interface and it is always close to SiO_{2-x} layer [Z. Liliental*, et al.* 1985]. It also may come from laser induced metallurgic oxidation in the interface. In the SiO_{2-x}/InP interface 2, there are two additional peaks in the P 2s spectra. The peak at lower binding energy (186.3 eV) is fixed to InP or elemental P and the peak at higher binding energy (191.3 eV) is fixed to be P oxides [R. Franke*, et al.* 1991]. These P oxides layer are created by the reaction between the outdiffused P atom from InP layer and SiO_{2-x} during QWI process and this layer is reported to be closer to the InP surface [J. Wager*, et al.* 1982]. There are obvious In 3d (444.5) and P 2s (186.3 eV) peaks in the InP layer spectra in Figure 5.2 (d) and (h) [R. Franke*, et al.* 1991]. However, the peaks of In-O at 445.1 eV in InP spectra and P oxides peak at 191.3 eV in P 2s spectra has disappeared.

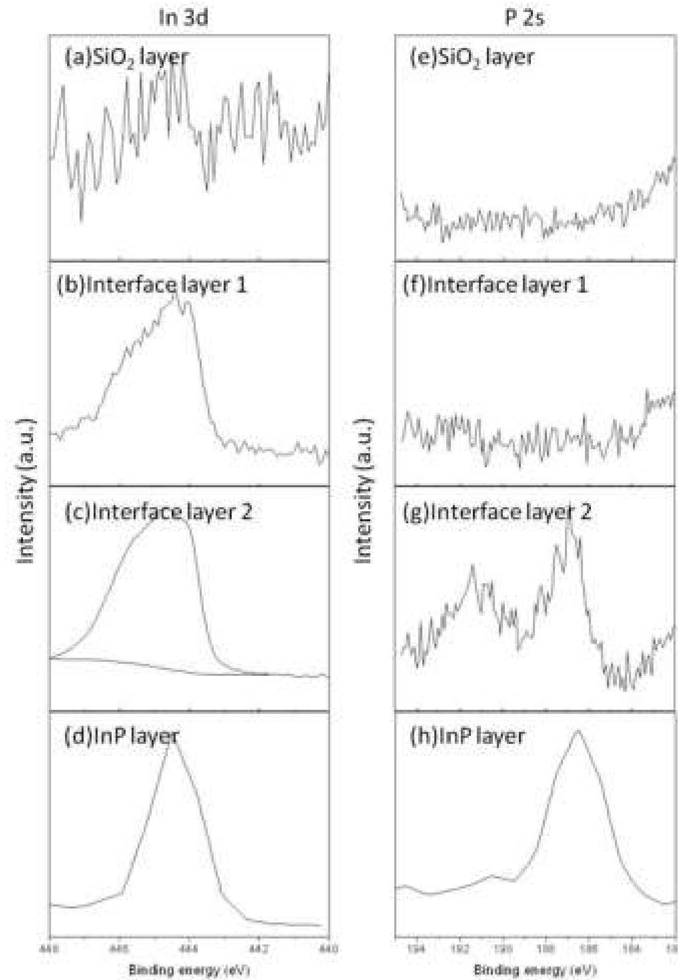

Figure 5. 2 In 3d 5/2 (a, b, c, d) and P 2s (e, f, g,h) XPS spectra of the SiO_2 layer, SiO_{2-x}/InP interface 1, SiO_{2-x}/InP interface 2 and the InP layer following KrF laser irradiation and RTA.

Figure 5.3 shows XPS depth profiles of O, Si, C, In, N, P, Ga and As in the SiO_{2-x}/InP top portion of the InP/InGaAs/InGaAsP microstructure following irradiation with KrF laser and a RTA processing step. It can be seen that the concentration of Si and O remains almost constant for the sputtering time $0 \leq t_{sp} < 2500$ sec. This indicates a relatively uniform SiO_{2-x} layer. However, the O/Si ratio inside the layer is about 1.43, which is less than this ratio measured at the surface of the SiO_{2-x} layer (see Table 5.1). The possible reason for this decrease could be related to the preferential sputtering of oxygen [S. Oswald, *et al.* 2004]. They indicate no presence of In and/or P atoms in the SiO_{2-x} layer during our RTA conditions. It is different from that reported in IFVD intermixing on InP based MQW after RTA at 800 °C or 850°C for 2 or 3 minutes [J. Teng, *et al.* 2002, S. Barik, *et al.* 2007]. They reported there is always ≥ 0.5% In or Ga atom outdiffuse to the SiO_2 layer which created III vacancies or V interstitials at the interface

to enhance the intermixing. The percentage of 0.5% is larger than our XPS detection sensitivity 0.1% and we have easily detected the N atom in the SiO_{2-x} layer around 0.5% as shown in the inset of Figure 5.3 (a) and (b). This is possibly caused by the relative lower temperature (700°C) of our RTA process and different quality of deposited SiO_{2-x} layer. However, this does not exclude the possibility of the presence of these atoms at the impurity level, as the XPS sensitivity is limited at 0.1 %. The concentration of In and P atoms increases at the SiO_{2-x}/InP interface. The results show a significantly greater concentration of In than it would be expected for a stoichiometric InP similar as reference. [S. Barik, *et al.* 2007] It was reported that in XPS depth profiling, the ion sputtering always cause chemical modification such as disorder, reduction and surface segregation [G. Hollinger, *et al.* 1987]. On InP based material, the In/P ratio is always larger than 1 (~1.4) due to the preferential removal of P during sputtering [S. Thurgate, *et al.* 1990]. The XPS depth profile of the InP layer region reveals that, at the maximum, the In/P ratio in the laser irradiated sample is significantly greater (2.3) than that in the non-irradiated sample (1.8). Then, they will decrease due to Ga and As atom percentage increase in InP layer. The increase of Ga and As in InP layer is caused by interdiffusion from InGaAs and InGaAsP layer under during RTA. Compared with Figure 5.3 (a) and (b), it shows that interdiffusion level is higher on laser irradiated sites than those on non irradiated sites. This consists with higher PL shift on laser irradiated sites. Because the sample is RTA in the N_2:H_2 environment, there is small amount of N on the SiO_2 layer. Also, the amount of C contained absorbates decreased, from 6.7% to 1.66%, and disappeared as investigating deep. The presence of In-O and InP-oxides confirmed what we find in high resolution XPS scan in the interface 1 and inteface 2 in Figure 5.2. It is reasonable to associated the QWI effect observed in such samples with the InO_x layer, as the InO_x layer has higher thermal expansion coefficient (CTE) (6.15×10^{-6} /°C) [R. Weiher, *et al.* 1963], which is more favourable to enahnce III atoms outdiffusion [J. McLaren, *et al.* 1983]. The surface morphology modification observed by AFM in Chapter 4, is possible due to the great amount of thermal oxides (InO_x and InP_xO_y) created by KrF laser in the interface. The difference in CTE of oxides and InP layer possibly cause internal stress to modify the interface morphology [J. McLaren, *et al.* 1983].

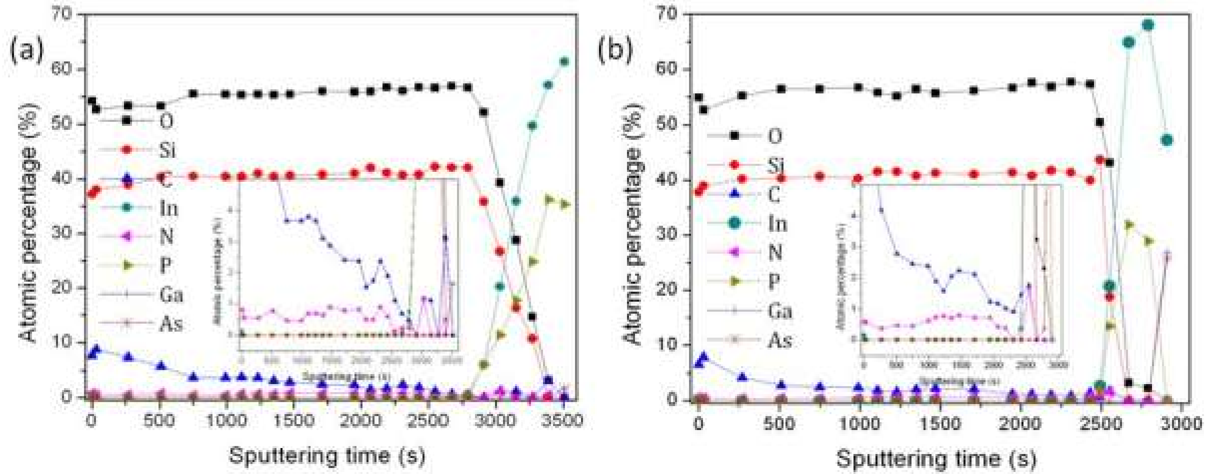

Figure 5. 3 XPS depth profiles of O, Si, C, In, N, P, Ga and As in non-irradiated (a) and laser irradiated (b) SiO_2/InP/InGaAs/InGaAsP microstructures following their RTA.

Therefore, surface and interface XPS findings have provided significant evidences; we have built addressing modification of the SiO_2/InP interface and its stability upon irradiation with the KrF laser. This modified interface works as a ‘defective layer’ that could contribute to the QWI process in the laser irradiated sites.

5.2 Chemical evolution of InP/InGaAs/InGaAsP microstructures irradiated in air and deionized water with ArF and KrF lasers

N. Liu, J.J. Dubowski, Applied Surface Science 270(13), 16-24 (2013)

5.2.1 Abstract

Irradiation of quantum semiconductor microstructures with ultraviolet pulsed lasers could induce surface defects and modify chemical composition of the microstructure capping material that during high-temperature annealing leads to selected area bandgap engineering through the process known as QWI. In this work, we investigate the role of both ArF and KrF excimer lasers in the QWI process of InP/InGaAs/InGaAsP microstructures irradiated in air and deionized (DI) water. XPS and SIMS analysis was employed to study the chemical composition of the irradiated surface and investigate the chemical evolution of ArF and KrF laser irradiated microstructures. The results indicate that InP_xO_y oxides are the dominating surface products of the ArF and KrF lasers interaction with InP. Consistent with this observation is a relatively greater bandgap blue

shift of ~ 124 nm found in the microstructures irradiated in air, in comparison to a maximum of 65 nm blue shift observed in the microstructures irradiated in a DI water environment.

Keywords: Quantum well intermixing, bandgap engineering, InP/InGaAs/InGaAsP microstructures, ArF and KrF excimer lasers, X-ray photoelectron spectroscopy, secondary ion mass spectroscopy, indium and InP oxides

5.2.2 Introduction

QWI has been reported as a potentially efficient method for the fabrication of some photonic integrated circuits due to its ability to selective area modify the bandgap of QW and quantum dot microstructures [J. Teng, *et al.* 2002, H. Lianping, *et al.* 2011, I. McKerracher, *et al.* 2012]. InP/InGaAs/InGaAsP QW microstructures, due to their ability to address device fabrication for fiber optic communication at 1.3 and 1.55 μm wavelengths, i.e., where the optical fibres exhibit the minimum of optical attenuation, have attracted a significant volume of QWI investigations [J. Arokiaraj, *et al.* 2004, J. Heo, *et al.* 2007a, S. C. Du, *et al.* 2011]. In addition to traditionally investigated QWI techniques, excimer lasers were found attractive as they were able to induce surface defects and modify chemical composition of the microstructures capping material that during rapid thermal annealing (RTA) could lead to QWI-based selective area bandgap engineering [J. J. Dubowski 2003, J. Genest, *et al.* 2004, J. Genest, *et al.* 2007b, J. Genest, *et al.* 2008a]. Depending on whether a QW microstructure is irradiated directly in air [J. Genest, *et al.* 2008a, N. Liu, *et al.* 2012a] or through a dielectric cap layer [N. Liu, *et al.* 2011b, N. Liu, *et al.* 2011c] different bandgap shifts have been observed, indicating the importance of the environment on the nature of surface defects and their role in the QWI mechanism. The role of surface defects, including P vacancies and In interstitials created in the InP cap layer irradiated with Ar ions, has been investigated with X-ray photoelectron spectroscopy (XPS) [C. L. Chiu, *et al.* 2009] and revealed that, indeed, the modification of the surface chemical composition plays an important role in the QWI process. The XPS and Auger spectroscopy techniques have also been employed to study surface chemistry of excimer laser irradiated InP [J. Genest, *et al.* 2008a] and InGaAs/InGaAsP microstructures [J. Dubowski, *et al.* 1999], indicating that the amount of surface oxides normally increases with the laser pulse number if the irradiation is carried out in an air atmosphere. Although the influence of the presence of different oxides, such as SiO_2,

SiO_xN_y and TiO_x deposited on quantum semiconductor (QS) microstructures on the QWI effect has been reported in literatures [J. Teng*, et al.* 2002, A. Francois*, et al.* 2006, I. McKerracher*, et al.* 2008], the correlation between the amplitude of the QWI effect (bandgap shifting) and the concentration of specific oxides induced with lasers has remained a relatively weakly investigated problem.

The presence of various atomic species in QW microstructures at the impurity level (< 10^{19} cm^{-3}) is known to contribute to the QWI effect[D. G. Deppe*, et al.* 1988, N. Holonyak, Jr. 1998]; therefore the investigation of excimer laser induced QWI effect has to address the problem of impurities distribution in irradiated microstructures. With this in mind, we have employed the time of flight secondary ion mass spectroscopy (TOF-SIMS) due to its high sensitivity and possibility of providing depth profiles of impurities in multilayer microstructures [L. L. Yang*, et al.* 2011, C. A. A. Ghumman*, et al.* 2012]. Of particular interest to us was the influence of the irradiation environments of air and deionized (DI) water on the amplitude of bandgap shifting and the quality of the intermixed material.

5.2.3 Experimental details

The investigated InP/InGaAs/InGaAsP microstructure (RAC 82) is covered with a 40-nm thick InP and a 6-nm-thick etch-stop InGaAsP layer and, finally, capped with a 30-nm thick InP layer. Small samples, typically 10 mm x 10 mm, were cleaved from the QW wafer and degreased in opticlear, acetone and isopropyl alcohol, each for 5 minutes at room temperature. For the laser irradiation experiments, the samples were installed in a 0.74 mm high chamber made of UV transparent (T > 90%) fused silica glass. The sample chamber was filled either with air or DI water. The irradiation was carried out with ArF (λ = 193 nm) and KrF (λ=248 nm) excimer lasers (Lumonics, Pulse Master 800). Following the laser irradiation, the samples were installed in a sealed nitrogen container to limit their exposure to an atmospheric environment, and transported for further processing. After laser irradiation, the samples were annealed for 2 min at 700°C with a RTA furnace (JIPELEC, Jetfirst) in an forming gas (N_2:H_2=1:9). Room temperature PL measurements of investigated samples were carried out with a commercial mapper (Philips, PLM-150).

The XPS measurements were carried out in a spectrometer (Kratos Analytical, AXIS Ultra DLD) equipped with a 150 W Al Kα source and operating at a base pressure of $1x10^{-9}$ Torr. The surface survey scan and high resolution scans were observed in constant energy modes at 50 eV and 20 eV pass energy, respectively. The size of an analyzed area on the investigated samples was set at 220 µm x 220 µm. The XPS spectra were recorded for samples after laser irradiation and after the RTA step. The collected data were processed using Casa XPS 2.3.15 software. To compensate for the surface charging effect, all XPS data binding energies were referenced to the adventitious C (C_{adv}) 1s peak at the BE of 285.0 eV. For spectral fitting, Gaussian-type and asymmetric peaks with constant FWHM were used for all components at a particular peak envelope. The RSF used for In 3d, P 2p and O 1s were set at 13.3, 1.19 and 2.93, respectively.

TOF-SIMS (TOF-SIMS IV, ION-TOF GmbH) measurements were performed to record information about the chemical composition and obtain depth profiles of atoms in non-irradiated sites, and sites irradiated in air and DI water before and after RTA. A 10 keV Bi ion beam was used as an analysis gun and a 3 keV Cs ion source was used as a sputtering gun. The sputtering beam was rastered over an area of 500 µm x 500 µm in the center of irradiated spots and the analysis signal was taken from a 50 µm x 50 µm area in the center of the sputtered region. [†]

5.2.4 Results and discussions

5.2.4.1 PL in InP/InGaAs/InGaAsP microstructure irradiated in air and DI water

Figure 5.4 illustrates the PL shift dependence on pulse number in InP/InGaAs/InGaAsP microstructure after ArF laser irradiation at 82 mJ/cm^2 (Figure 5.4.a) and KrF laser irradiation at 124 mJ/cm^2 (Figure 5.4.b) in air and DI water and RTA at 700°C for 2 minutes. For samples irradiated in air by both lasers, the PL shift continues to increase with the pulse number and it saturates for $N \geq 25$ pulses for KrF irradiated samples, while no such saturation is visible for the ArF irradiated samples, even for $N = 100$ pulses. The maximum blue shift of 130 nm observed for the ArF irradiated samples compares to 90 nm of the maximum blue shift observed for the KrF irradiated samples. In contrast, for samples irradiated in DI water, the saturation of the blue

[†] The depth resolution in SiO_2 layer is around 0.06 nm and the depth resolution in InP/InGaAs/InGaAsP microstructure is around

shift amplitude is observed at N ≥ 20 and N ≈ 5 for ArF and KrF irradiated samples, respectively. The blue shift saturation amplitude of 50-60 nm seems to be related to the limited concentration of the intermixing inducing defects that both lasers can generate during the irradiation in a DI water environment.

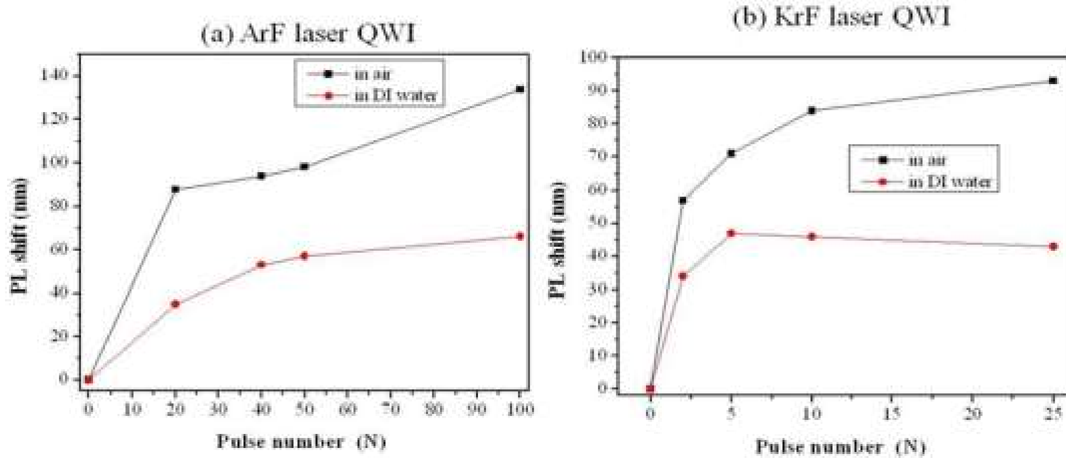

Figure 5. 4 PL shift dependence in the InP/InGaAs/InGaAsP microstructure on the laser pulse number after (a) ArF and (b) KrF laser irradiation in air and DI water that was followed by the RTA step.

A slightly stronger absorption of InP at 4.99 eV (~ 1.77 x 10^6 cm^{-1}) than at 6.4 eV (~1.25 x 10^6 cm^{-1}) [D. Aspnes, *et al.* 1983] could result in a modification of the thicker surface layer achieved with the ArF laser and, as a result, lead to a greater QWI amplitude as illustrated in Fig. 1a. Note that even though the microstructure was irradiated with 50% more intense pulses of the KrF laser when compared to those of the ArF laser (124 vs 82 mJ/cm^2), the energy absorbed by the samples was comparable in both cases due to a greater reflectivity of InP at 4.99 eV (R ~ 0.6) in comparison to that at 6.4 eV (R ~ 0.43) [D. Aspnes, *et al.* 1983] . Nevertheless, the role of the irradiation environment is clear, as the maximum blue shift amplitudes achieved with both lasers are significantly smaller for samples irradiated in DI water than for samples irradiated in air.

5.1.4.2 XPS analysis of sample irradiated by ArF laser in air and in DI water

Figure 5.5 shows In 3d 5/2 and P 2p XPS spectra of cap InP surface for as grown (non-irradiated) sample (a, d), irradiated by ArF laser in air (b, e) and DI water (c, f) with 50 pulses at 82 mJ/cm^2. The In 3d 5/2 spectra from all the samples have been fitted with elemental In (BE = 443.5 ± 0.2 eV, FWHM = 0.67 eV), InP (BE = 444.4 ± 0.2 eV, FWHM = 0.67 eV), indium oxide (InO_x) (BE = 445.2 ± 0.2 eV, FWHM = 0.67 eV), $In(PO_3)_y$ (BE = 445.6 ± 0.2 eV, FWHM = 0.67

eV), $In_x(PO_4)$ (BE = 446.3 ± 0.2eV, FWHM = 0.67 eV) [N. Shibata*, et al.* 1992, J. Pan*, et al.* 1999, V. Mikushkin*, et al.* 2004]. All the peaks have been fitted with Gaussian functions, except for In, where an asymmetric function has been used[A. M. Salvia*, et al.* 1998]. A peak at the highest binding energy (BE=446.4±0.2eV, FWHM=0.67eV) observed for the as-grown and air irradiated samples, has been attributed to $In(PO_3)_3$. This peak disappeared in the spectra of samples irradiated in DI water, consistent with the high solubility of InP_xO_y oxides in water [S. Ingrey*, et al.* 1987]. Also, for these two samples, as illustrated in Figure 5.5 a and b, an additional peak has been observed at the lowest binding energy (443.0 ± 0.2 eV). As this peak appears accompanied with the appearance of the carbide peak in C 1s spectrum, we ascribed it to indium carbide, InC_x [Y. Feurprier*, et al.* 1997, Z. Jin*, et al.* 2001]. This peak is absent in the sample irradiated in DI water, as shown in Figure 5.5 c.

A comparison between Figure 5.5 a, b and c shows that the concentration of InO_x and InP_xO_y has significantly increased in the air-irradiated sample, and additional oxides, such as $In(PO_3)_y$, $In_x(PO_4)$ and $In(PO_3)_3$, have also been created by the ArF laser irradiation in air. Using a model reported in the literature [Radoslaw Stanowski*, et al.* 2006], our COMSOL calculations indicated that the peak temperature of InP irradiated with the ArF laser at 82 mJ/cm^2 in air is about 500 K. This condition leads to the formation of InO_x and InP_xO_y by adsorption of oxygen that enters the In-In and In-P bonds [G. Chen*, et al.* 2002]. In contrast, the irradiation in DI water with the same laser fluence induces a peak temperature of about 360 K. At this temperature, no significant oxidation of InP is expected. Besides, laser heated DI water environments will enhance desorption of phosphorous oxides by the dissolution process[S. Ingrey*, et al.* 1987]. The oxygen concentration in DI water is lower than that in air[G. Truesdale*, et al.* 1955], which is consistent with the low XPS intensity of InO_x and InP_xO_y components observed in Figure 5.5 c. We note that the binding energy of InO_x created in DI water has been reduced by 0.3 eV and the In/O ratio has decreased from 1.3 in air to 0.8 in DI water. This indicates that another In sub-oxides are created in the sample irradiated in DI water [V. Golovanov*, et al.* 2005]. The P 2p spectra in Figure 5.5 d, e and f show 2p 3/2 (solid line) and 2p 1/2 (dash dot line) doublets of InP and P, respectively. To fit the experimental data, we fixed the doublet separation and branch ratio of P 2p 3/2 to P 2p 1/2 at 0.85 eV and 2.0, respectively. The peaks at low binding energy (BE = 128.6 ± 0.2 eV, FWHM=0.56±0.1eV) were assigned to InP and the peaks at secondary higher binding

energy (BE=129.2±0.1eV, FWHM=0.56±0.1eV) were assigned to P [T. Som*, et al.* 2009]. The oxides at the higher binding energy can be ascribed to $In(PO_3)_y$ (BE = 133.1 ± 0.2eV, FWHM = 1.1 ± 0.1 eV), $In_x(PO_4)$ (BE = 133.8 ± 0.2eV, FWHM = 1.1 ± 0.1eV) and $In(PO_3)_3$ (BE=134.4±0.2eV, FWHM=1.1±0.1eV), consistent with those in the In 3d 5/2 spectra [G. Hollinger*, et al.* 2009]. For the sample irradiated in air (Figure 5.5 e), the XPS intensity of InP_xO_y increased significantly. However, for the sample irradiated in DI water (Figure 5.5 f), the quantity of InP_xO_y has reduced and $In(PO_3)_3$ has clearly disappeared due to dissolution. The P 2p XPS spectra are consistent with the In 3d 5/2 XPS.

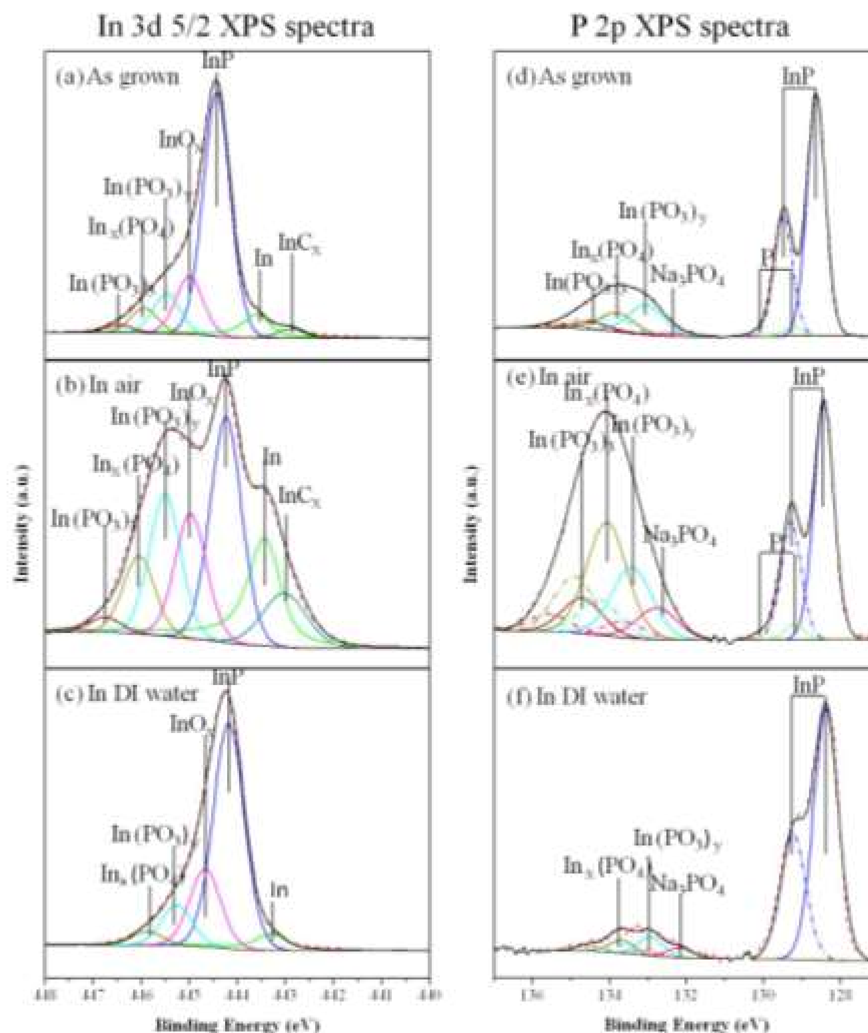

Figure 5. 5 In 3d 5/2 and P 2p XPS spectra of as grown sample (a), (d), irradiated by ArF laser at 82mJ/cm^2 with 50 pulses in air (b), (e) and in DI water (c), (f).

Figure 5.6 shows the C 1s and O 1s XPS spectra of as-grown sample (a, d) and sample irradiated by ArF laser at 82 mJ/cm^2 with 50 pulses in air (b, e) and DI water (c, f). The C 1s

XPS spectra are dominated by the C_{adv} peak that was assigned to 285.0 eV and used for the calibration of the charging effect. All the C 1s spectra showed the presence of three additional C adsorbate species: alcohol –COH (286.5±0.2eV), carbonyl –CO (287.9 ± 0.1 eV) and ester –COO- (288.8±0.1eV) [D. Miller*, et al.* 2002a]. The peak at lower binding energy (≤ 284 eV) in the C 1s XPS spectra of the as-grown and air irradiated samples could be assigned to metal carbide [T. P. Nguyen*, et al.* 1997]. Here, we attributed it to InC_x, which is consistent with the results shown by the In 3d 5/2 spectra that also show the increased quantity of this carbide in the sample irradiated in air. The binding energy of the InC_x peak observed for the laser-irradiated sample (Fig5.6 b) has been increased by 0.5 eV, in agreement with the reported high-temperature reconstruction of this compound [A. Baranzahi*, et al.* 1995]. However, the InC_x peak disappeared in the sample irradiated in DI water, similarly to what has been observed in the In 3d 5/2 spectra.

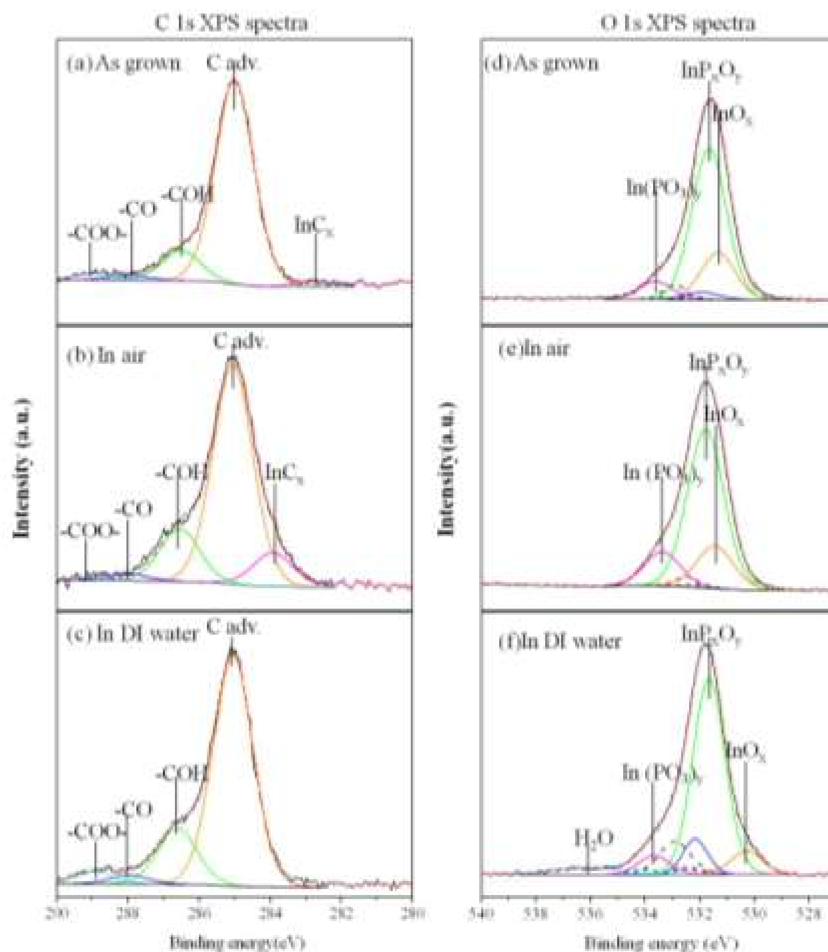

Figure 5. 6 C 1s and O 1s XPS spectra of as grown sample (a), (d) and sample irradiated by ArF laser at 82mJ/cm^2 with 50 pulses in air (b), (e) and in DI water (c), (f).

Four small peaks corresponding to the O-containing C adsorbates have been observed in the O 1s spectra in Figure 5.6 d, e and f. The intensities of these peaks are related to the corresponding species in C 1s spectrum in Figure 5.6 a, b and c. Identification of these C adsorbates species in the O 1s peak is important for the analysis of the quantities of InO_x and InP_xO_y. The expanded portion of the O 1s peak at higher binding energy of the as grown and irradiated in air and DI water samples are shown Figure 5.7 a, b and c. In addition to the C adsorbate peaks, the peak at 532.0 ± 0.2 eV has been ascribed to absorbed oxygen species (see Figure 5.7) and the other peak at 533.7 ± 0.2 eV has been ascribed to bridging oxygen atoms in $In(PO_3)_y$(see Figure 5.7) [G. Hollinger*, et al.* 2009]. The expanded view of the O1s spectrum (Figure 5.7 c) of the sample irradiated in DI water shows the presence of the H_2O peak at BE=536.0±0.2 eV. A similar peak has been reported for a rhenium sample irradiated in DI water [P. Schulze*, et al.* 1983]. Note that the binding energy of InO_x created in DI water (Figure 5.6 c) has been reduced by ~ 1.2 eV and the In/O ratio has decreased from 1.3 to 0.8 in DI water, which means another kind of indium oxides created [J. C. C. Fan*, et al.* 1977]. This is consistent with the formation of a low binding energy non-stoichiometric suboxide compound that is energetically more stable, even annealing at higher temperature (~1000 °C) [V. Golovanov*, et al.* 2005] .

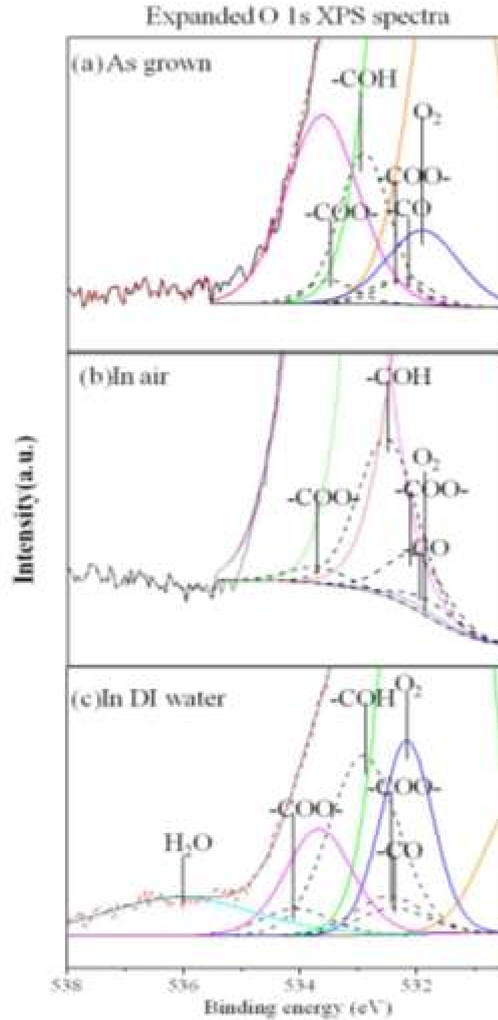

Figure 5. 7 Expanded O 1s XPS spectra of as grown sample (a) and sample irradiated by ArF laser at 82mJ/cm^2 with 50 pulses in air (b) and in DI water (c)

5.1.4.3 XPS analysis of sample irradiated by ArF laser in air and DI water and RTA

The In 3d 5/2 and P 2p XPS spectra of RTA as-grown samples and RTA ArF laser irradiated samples at 82 mJ/cm^2 with 50 pulses in air and DI water are shown in Figure 5.8. Compared with Figure 5.5, these spectra demonstrate that the RTA step has drastically reduced the concentration of surface oxides in all samples. This reduction is primarily related to the decomposition process of P-oxides as it is known that P atoms evaporate at 650°C [M. Yamaguchi, *et al.* 1980] and InP_xO_y decomposes at 458°C [W. Lau, *et al.* 1988]. Some presence of InC_x can be seen in the air irradiated samples (Figure 5.8 b), but the carbide disappeared in the RTA as-grown sample (Figure 5.8 a) and in the RTA sample laser-irradiated in DI water (Figure 5.8 c). It is possible that surface oxides and carbides could be the source of O and/or C diffusing into the QW region,

which would promote the QWI process. However, the role of C in the intermixing process seems negligible due to a relatively small concentration of this impurity at the surface of laser-irradiated samples, especially those processed in the DI water environment. Furthermore, the diffusion coefficient of C in GaAs is relatively low (< 10^{-16} cm^2s^{-1}) [C. Abernathy, *et al.* 1989] in comparison to the defect diffusion rate of $2.3*10^{-15}$ $cm^{-2}s^{-1}$ reported for a similar InGaAs QW structure during pulsed Nd:YAG laser QWI [O. Gunawan, *et al.* 2000].

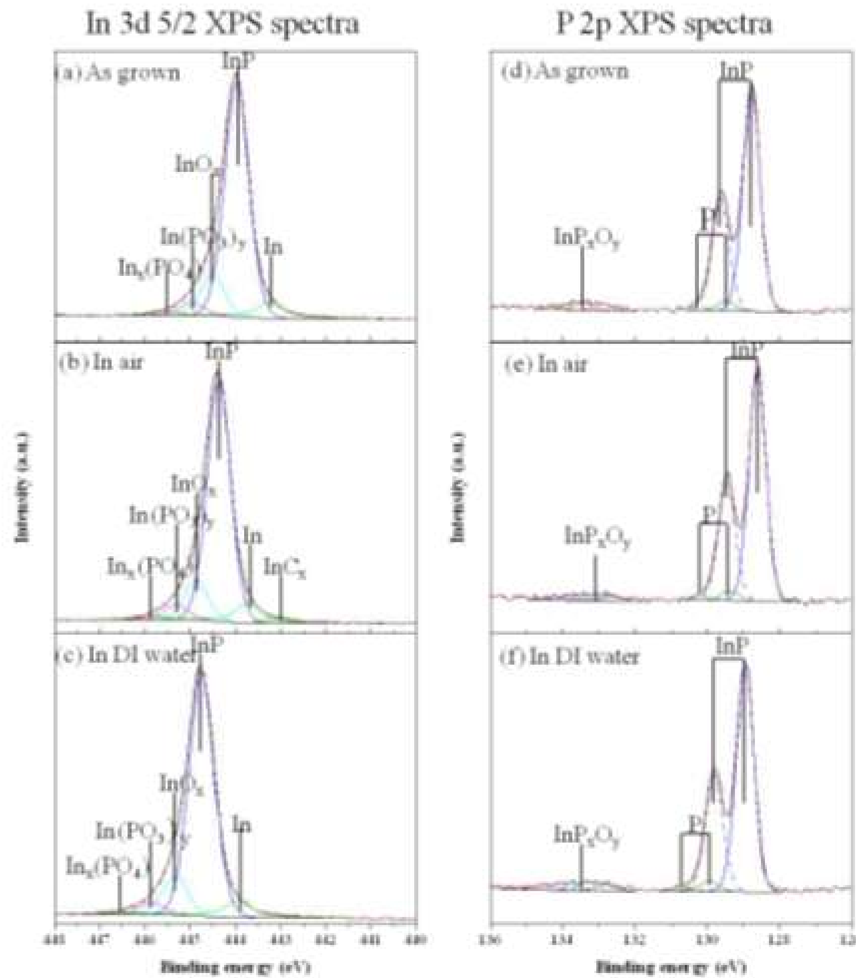

Figure 5. 8 In 3d 5/2 and P 2p XPS spectra of as grown sample (a), (d) and sample irradiated by ArF laser at 82mJ/cm^2 with 50 pulses in air (b),(e) and DI water (c),(f), followed by the RTA step.

Figure 5.9 shows the C 1s and O 1s XPS spectra of the as-grown sample (Figure 5.9 a and d) and the sample irradiated with the ArF laser in air (Figure 5.9 b and e) and DI water (Figure 5.9 c and f) with 50 pulses at 82 mJ/cm^2 and then RTA at 700°C for 2 minutes. It can be seen that the trace of H_2O, previously observed for a sample irradiated in DI water (see Figure 5.9 f) has disappeared following the high temperature treatment. The intensity of the InO_x peak observed in

the O 1s spectra has also decreased considerably, especially in the as-grown sample and that was irradiated with the laser in air. However, the InO_x peaks in the as-grown sample and irradiated in air has shifted to low binding energy (530.0 ± 0.2eV), which is similar as that in the sample irradiated in DI water, consistent with the more stable form of In sub-oxide after high temperature treatment [V. Golovanov*, et al.* 2005]. The InC_x feature in the C 1s spectrum of the sample irradiated in air is practically invisible.

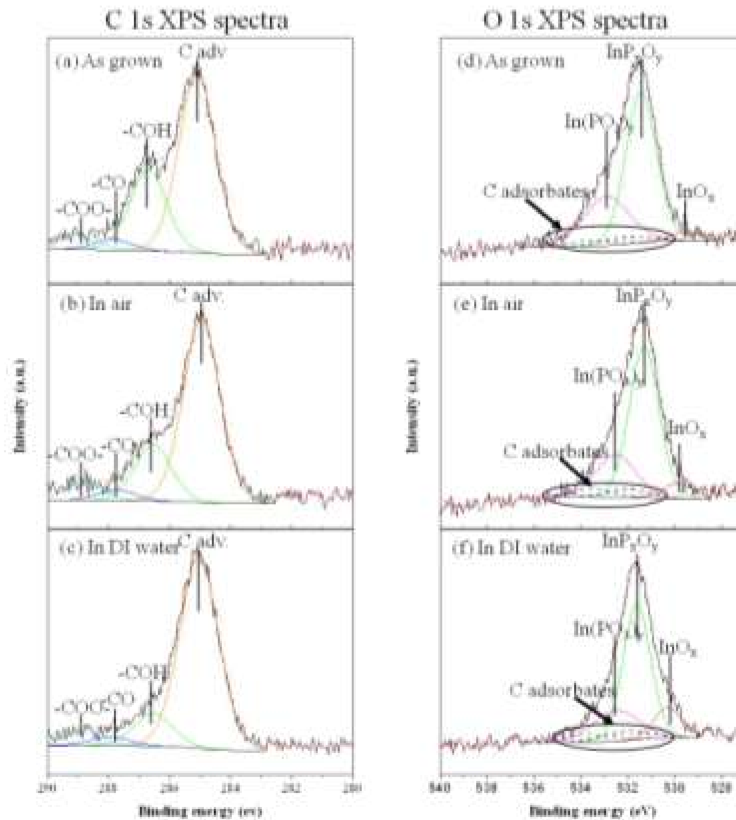

Figure 5. 9 C 1s and O 1s XPS spectra of as grown sample (a), (d) and sample irradiated by ArF laser at 82mJ/cm^2 with 50 pulses in air (b),(e) and DI water (c),(f), followed by the RTA step.

Figure 5.10 presents a dependence of the XPS atomic concentrations of In, InP, oxides compounds and major adsorbates observed at the surface of the InP capping layer as a function of the laser irradiation pulses. The results are presented for samples irradiated in DI water (Figure 5.10 a and c) and air (Figure 5.10 b and d) using 82 mJ/cm^2 pulses of the ArF laser. It can be seen that the InP_xO_y XPS signal from the sample irradiated in air increases rapidly with the number of laser pulses to reach a plateau at $N \geq 40$. This increase is mirrored by a decrease of the InP XPS signal observed for the same range of laser pulses. In contrast, the concentration of InP_xO_y in the sample irradiated in DI water increases weakly (about 5%) for $0 < N \leq 50$. At the

same time, the O_2 XPS signal remains relatively unchanged, or even slightly reduced for $0 < N \leq 40$ in comparison to that in the sample irradiated in air (compare Figure 5.7 a and b). Similarly, the InO_x concentration increased by 6% in the sample irradiated in air while the quantity of this compound in the sample irradiated in DI water does not show an obvious increase. Thus, the weaker formation of oxides on the surface of samples processed in DI water, as well as water dissolution of oxides appear the main reason for the pulse dependent behavior of the InP XPS signal observed in Figure 5.10 a.

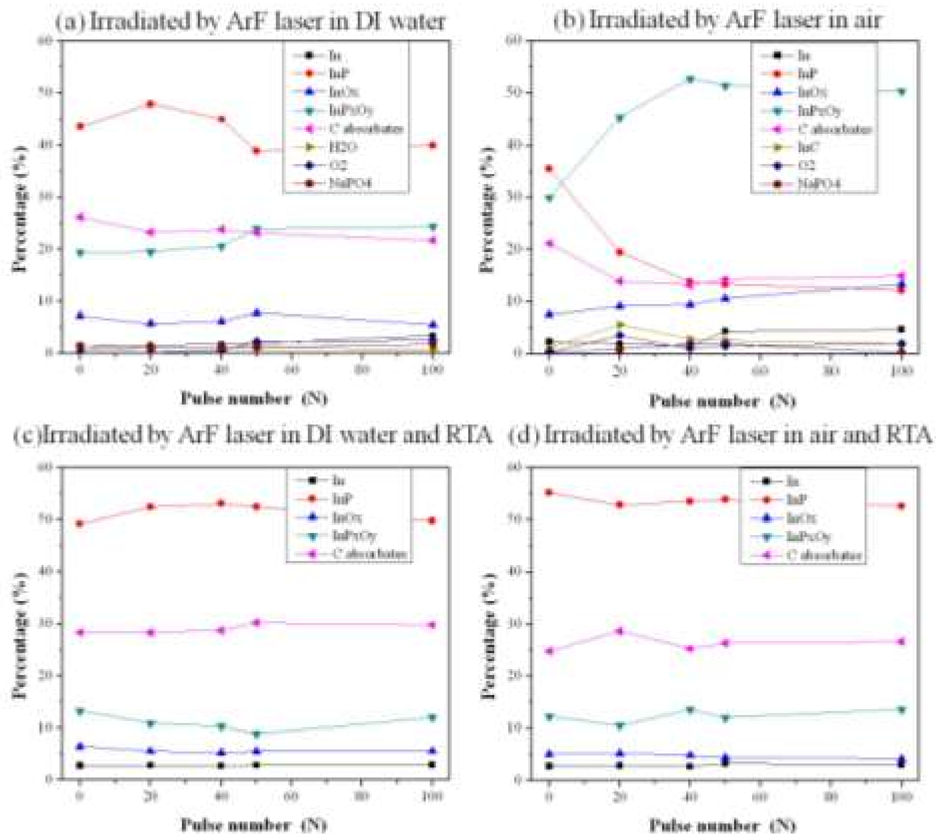

Figure 5. 10 Dependence of XPS atomic concentration of InP and surface adsorbates on pulse number in the samples irradiated with ArF laser in DI water (a), in air (b) and after RTA of the sample irradiated in DI water (c) and in air (d).

Following the RTA treatment at 700°C for 2 minutes, both series of samples show comparable XPS composition profiles for the range of $0 \leq N \leq 100$. It is feasible that the surface oxides have been decomposed and/or evaporated during the RTA step, although some diffusion of the surface adsorbates could take place into the investigated microstructures.

5.2.4.4 SIMS analysis of RTA samples that were irradiated with ArF laser in air and DI water

The TOF-SIMS depth profiles of oxygen in the QW microstructures irradiated with the ArF laser are shown in Figure 5.11. The bars above the figures illustrate the chemical composition of the investigated microstructure. The five InGaAs wells and four InGaAsP barriers separating the wells can clearly be identified from the observed oxygen profiles. The presence of oxygen is a common problem in CBE [T. Kitatani*, et al.* 2000] and MOVPE [T. Tsuchiya*, et al.* 2003] grown materials. The concentration of oxygen in the InGaAs layers reported in Figure 5.11 a is lower than in the InGaAsP layers, consistent with the use of PH_3 for the growth of the barrier material that could also be the source of the oxygen impurity. The SIMS oxygen profiles for the as-grown and irradiated in DI water samples are almost identical. However, the laser irradiation in air has induced a measurable increase of oxygen in the top portion of the microstructure (sputtering time < 600 sec). For the same sample, the diffusion of oxygen into the entire active region of the microstructure has been observed following the RTA step at 700°C for 2 minutes (Figure 5.11 b). For the sample irradiated in DI water, the RTA step increased the oxygen concentration only in the top portion of the microstructure (sputtering time < 500 sec). The oxygen impurity in III-V QW microstructures has been employed as a diffuse source in an MQW sample coated with Al reduced SiO_2 layer to induce intermixing [L. Guido*, et al.* 1989]. It seems reasonable that this impurity is the main source of the QWI effect observed in the investigated here microstructures.

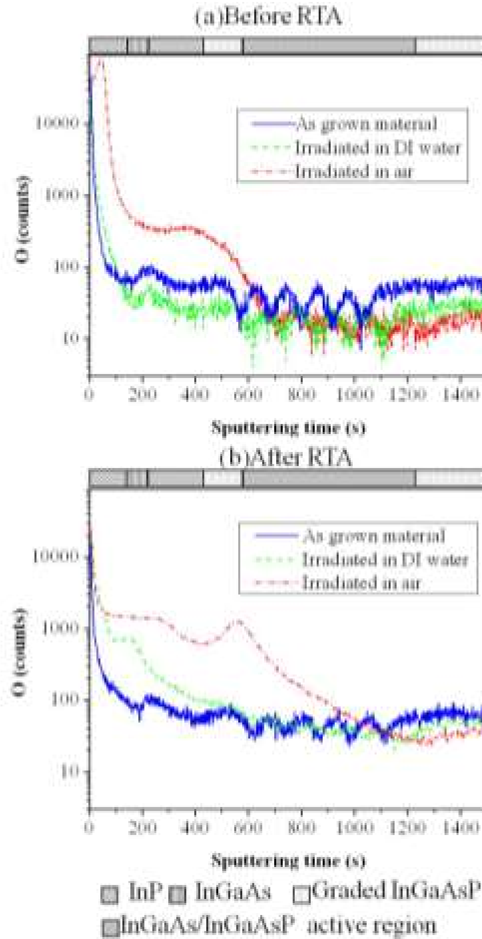

Figure 5. 11 TOF-SIMS oxygen concentration depth profile in as grown sample, and in samples irradiated with ArF laser in DI water and in air before (a) and after (b) RTA at 700°C for 2 minutes.

5.2.4.5 XPS analysis of the samples after KrF laser irradiation in air and in DI water

Qualitatively, similar results have been observed for the KrF laser irradiated samples. Figure 5.12 presents XPS atomic concentrations of In, InP, oxides compounds and major adsorbates observed for the as-grown InP cap layer and a dependence of these concentrations on the laser irradiation pulse number. The irradiation was carried out in DI water and air environments using the KrF laser delivering pulse fluence of 124 mJ/cm^2. For the samples irradiated in DI water, a 25-pulse irradiation increases atomic concentration of InP_xO_y to 28%, while the same irradiation in air results in the increase of the concentration of this oxide to 48%. The XPS InP signal decreases with the pulse number as it has been oxidized into InP_xO_y. This effect is especially evident for samples irradiated in air. For the samples irradiated in air, the concentration of InC_x increased to 4% from 1.5%, observed for the as-grown material. This compound is not observed in the samples irradiated in DI water; instead, they exhibit a traceable amount of H_2O. We

attribute a reduced concentration of InP_xO_y, observed in the as-grown material exposed to DI water (17%) compared to the 29% concentration of this oxide in the as-grown sample exposed to air, to the high solubility of this oxide in DI water. Following the RTA step at 700°C for 2 minutes, the concentration of InP_xO_y, regardless of the pulse number, has been reduced to near 10%. This illustrates the effect of thermal decomposition of oxides and loss of the surface oxygen due to its diffusion into the investigated microstructure. Similar to the results presented in Figure 5.12 c and d, the surface chemical composition of all the RTA processed samples is indistinguishable within the experimental error of the XPS measurements.

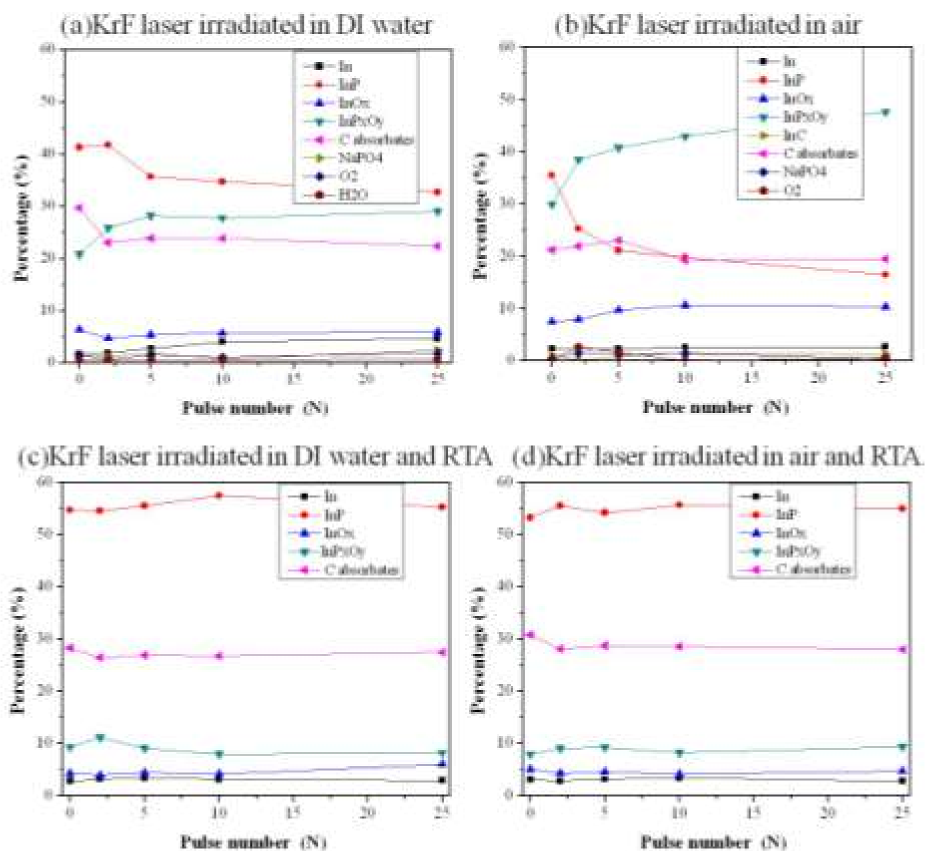

Figure 5. 12 Dependence of XPS atomic concentration of InP and surface adsorbates on pulse number in the sample irradiated with KrF laser in DI water (a), in air (b) and after RTA of the sample irradiated in DI water (c) and in air (d).

5.2.5 Conclusions

We have investigated the surface chemical evolution of InP/InGaAs/InGaAsP QW microstructures irradiated with ArF and KrF lasers in the context of the laser induced QWI effect. The role of laser irradiation, carried out in air and DI water, is to modify the surface of the QW

microstructure and create conditions enhancing atomic intermixing during the RTA step. Our results have indicated that InP_xO_y oxides are the dominating product of the ArF and KrF lasers interaction with InP. Owing to oxide solubility in water, a significantly greater concentration of oxides has been observed in samples irradiated in air than in those irradiated in DI water. The increasing oxide concentration with the laser pulse number has a similar trend as the band gap increment, indicating that oxides play important roles in the excimer laser QWI. The SIMS results show that after RTA, significant amount of oxygen atoms have diffused in the microstructure active region and resulted in an enhanced intermixing. A greater PL shift in samples irradiated in air than that in the samples irradiated in DI water is consistent with this observation. XPS results have also shown that surface chemical composition of samples after the RTA step is comparable, regardless of the environment in which the laser irradiation took place. This suggests that excimer laser processing of InP/InGaAs/InGaAsP microstructures does not lead to a significant modification of the surface chemical composition – a feature attractive for the fabrication of future devices from the laser fabricated QWI material.

5.2.6 Acknowledgements

This work was supported by the Natural Science and Engineering Research Council of Canada (Discovery Grant No. 122795-2010) and the programs of both the Canada Research Chair in Quantum Semiconductors (JJD) and Plasma Québec. Technical assistance of Sonia Blais (Université de Sherbrooke Centre de characterization de materiaux, Sherbrooke) in collecting XPS data, Suzie Poulin (École Polytechnique Laboratoire de service pour analysis de surface des materiaux, Montréal) in collecting SIMS data and help of the technical staff of the Université de Sherbrooke Centre de recherche en nanofabrication et en nanocaracterisation (CRN^2) is greatly appreciated. NL acknowledges the Merit Scholarship Program for Foreign Student, Fonds de recherche du Québec - Nature et technologies, for providing a graduate student scholarship.

5.3 XPS analysis of KrF laser irradiated on InP/InGaAs/InGaAsP microstructures coated with InO_x layers

As discussed in the previous chapter, InP_xO_y oxides are the dominating product of the ArF and KrF lasers interaction with InP, and the increasing oxide concentration with the laser pulse number has a similar trend as the band gap increment. To investigate further the effect of oxide induced QWI, a series of M1580 samples have been coated with a different thickness of InO_x deposited by sputtering with a PLASMONIQUE SPT320 system. Figure 5.13 shows In 3d and O 1s XPS spectra of a sample coated with a 40 nm InO_x layer before and after RTA (725°C for 2 minutes in a forming gas). Before RTA, in In 3d 5/2 XPS spectra, the main components are InO_x (BE = 444.2 eV, FWHM = 1eV) and $In(OH)_x$ (BE = 445.0 eV, FWHM = 1.42 eV) with their BE energies and FWHM consistent with [M. Atashbar, *et al.* 1999]. After RTA, the XPS spectra shows that the main composition of the surface is InP, InO_x and $InPO_x$, which is similar to the result observed for as grown InP cap layer after RTA [N. Liu, *et al.* 2013]. This means that $In(OH)_x$ has discomposed during annealing. The BE of InO_x shifted to BE = 445.1 eV due to the presence of different forms of oxides created by different preparation methods [R. Hewitt, *et al.* 1980]. The AFM surface roughness of an RTA sample is ~6.8 nm, which is smoother than that of a sample before RTA (~ 21 nm).

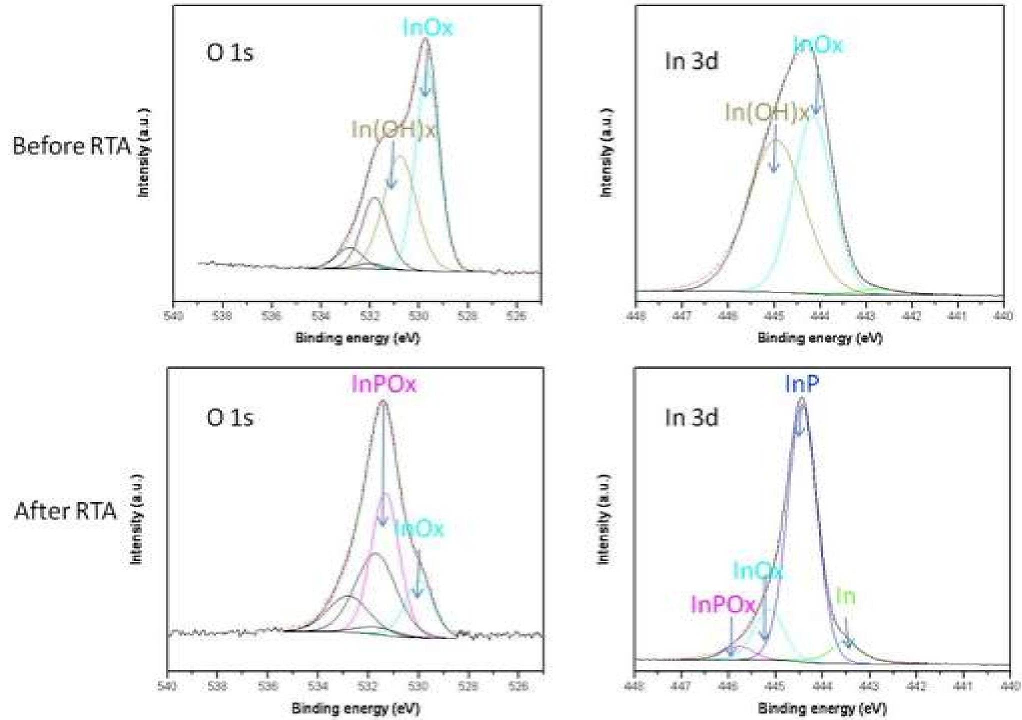

Figure 5. 13 O 1s and In 3d XPS spectra of InO_x layer coated sample before and RTA.

XPS analysis of a sample coated with 10 nm InO_x and irradiated with 2 and 10 pulses of a KrF laser at 124 mJ/cm^2 is shown in Figure 5.14. We find that $In(OH)_3$ decomposed after KrF laser irradiation. However, a great quantity of InP_xO_y has been observed in that sample. In addition, two types of indium oxides, one characterized by BE of 444.1 eV (InO_x) and the other by BE of 444.7 eV (InO_y). XPS spectra show that InO_x originated from the deposited layer (its BE is consistent with InO_x of a non irradiated site). However, the InO_y of higher BE is possibly generated from KrF laser irradiation. $In(PO_3)_y$ and $In_x(PO_4)$ were found on the irradiated sites. With the pulse number increasing to 10 pulses, the oxide percentage increased from 54.5% to 67.8%. As the oxides thickness increases to more than 10 nm, InP becomes undetectable in both In 3d 5/2 and P 2p XPS spectra on sites irradiated with 10 pulses.

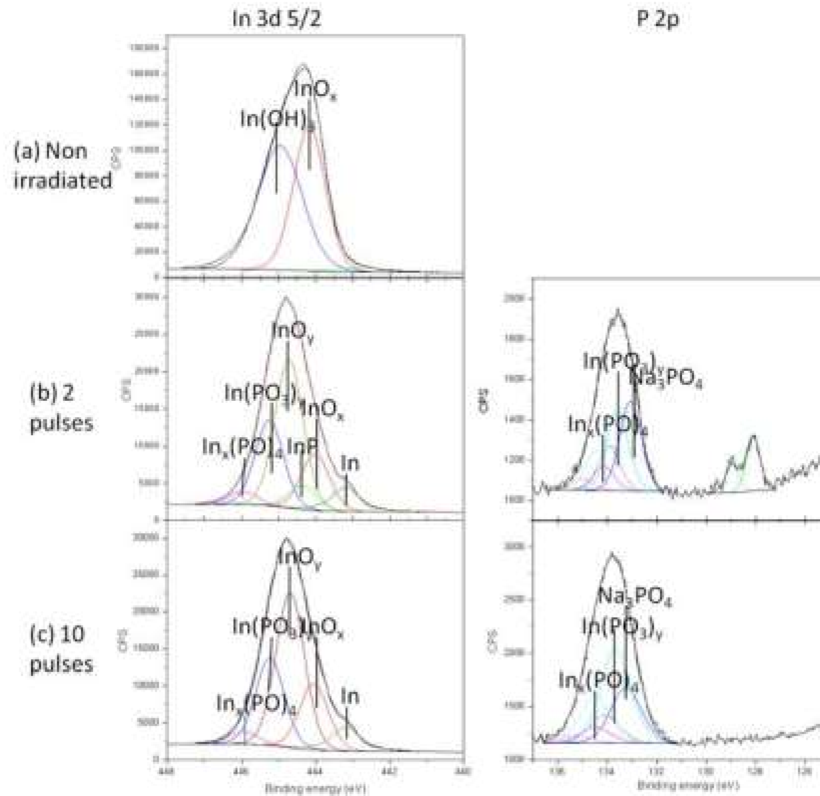

Figure 5. 14 In 3d 5/2 and P 2p XPS spectra of sample coated with 10 nm InO_x layer irradiated by KrF laser with 2 and 10 pulses.

5.4 Summary

In the first part, I investigated surface and interface chemical modification of QW microstructure coated with SiO_2 layer after KrF laser irradiation. XPS shows that there is no obvious modification on SiO_2 layer during irradiation. However, there is an obvious chemical modification of the SiO_2/InP interface. In-depth XPS analysis shows that there were no detectable III or V atoms outdiffused to the SiO_2 layer.

In the second part, I discussed the chemical evolution of InP/InGaAs/InGaAsP microstructure during ArF and KrF laser irradiation in air and DI water and RTA. Significantly more oxides were found on sample irradiated in air by excimer lasers, than that irradiated in DI water. This is caused by laser induced lower temperature and low oxygen concentration in DI water. These oxides were found to disappear after RTA. SIMS has shown that O atoms have diffused as impurity to active regions after annealing to enhance the intermixing. As it will be shown in Chapter 6, 9 times PL intensity enhancement has been found on sample irradiated in DI water due to the oxide layer embedded inside the microstructure. The XPS and SIMS analysis

have confirmed the importance of the environment on the laser-induced chemical modification of the InP surface. In particular, I have demonstrated that irradiation in a DI water environment leads more stoichemical InP surface. The irradiation in different liquid environments could potentially allow fabricating surface layers designed for further moderation of the QWI effect and fabrication of attractive PIC. In Appendix xx, I discuss the application of H_2O_2 and metanol environments for excimer laser induced modification of wettability of Si and *in situ* controlling a hydrophilic-to-hydrophobic transition.

In the third part, we have discussed the chemical evolution of microstructure coated with InO_x layer before and after RTA. The originally deposited InO_x layer has been decomposed and then disappeared after RTA, which is possibly due to O diffusion. After KrF laser irradiation, the InO_x cap was transformed into a thick layer of oxides that screened the XPS InP signal. The significance of laser-induced modification of the InO_x/InP interface in achieving large QWI amplitudes is discussed in the next Chapter 6.

5.5 Bibliography

Abernathy, C., Pearton, S., et al., (1989), Ultrahigh doping of GaAs by carbon during metalorganic molecular beam epitaxy, *Applied Physics Letters*, vol. 55, n°17, 1750-1752.

Arokiaraj, J., Djie, H.S., et al., (2004), Investigations on the blue-shift phenomena in argon plasma intermixed InGaAs/InGaAsP quantum well structures, *Applied Surface Science*, vol. 237, n°1, 256-260.

Aspnes, D., and Studna, A., (1983), Dielectric functions and optical parameters of Si, Ge, GaP, GaAs, GaSb, InP, InAs, and InSb from 1.5 to 6.0 eV, *Physical Review B*, vol. 27, n°2, 985.

Atashbar, M., Gong, B., et al., (1999), Investigation on ozone-sensitive In_2O_3 thin films, *Thin Solid Films*, vol. 354, n°1, 222-226.

Baranzahi, A., Spetz, A.L., et al., (1995), Reversible hydrogen annealing of metal-oxide-silicon carbide devices at high temperatures, *Applied Physics Letters*, vol. 67, 3203.

Barik, S., Fu, L., et al., (2007), Impurity-free disordering of InAs/ InP quantum dots, *Applied Physics Letters*, vol. 90, 243114.

Chen, G., Visbeck, S., et al., (2002), Structure-sensitive oxidation of the indium phosphide (001) surface, *Journal of Applied Physics*, vol. 91, 9362.

Chia, C., Chua, S., et al., (2005), Group-V intermixing in InAs/ InP quantum dots, *Applied Physics Letters*, vol. 86, 051905.

Chiu, C.L., Lin, E.Y., et al., (2009), Argon plasma induced photoluminescence enhancement and quantum well intermixing of InGaAs/InGaAlAs multiple quantum wells, *Physica B*, vol. 404, n°8-11, 1226-1229.

Clarke, T.A., and Rizkalla, E.N., (1976), X-ray photoelectron spectroscopy of some silicates, *Chemical Physics Letters*, vol. 37, n°3, 523-526.

Deppe, D.G., and Holonyak, N., (1988), Atom diffusion and impurity induced layer disordering in quantum well III-V semiconductor heterostructures, *Journal of Applied Physics*, vol. 64, n°12, R93-R113.

Du, S.C., Fu, L., et al., (2011), Investigation of ion implantation induced intermixing in InP based quaternary quantum wells, *Journal of Physics D: Applied Physics*, vol. 44, n°47, 475105.

Dubowski, J., Poole, P., et al., (1999), Enhanced quantum-well photoluminescence in InGaAs/InGaAsP heterostructures following excimer-laser-assisted surface processing, *Applied Physics A: Materials Science & Processing*, vol. 69, 299-303.

Dubowski, J.J.: 'Laser-induced bandgap shifting for photonic device integration' US Patent 6,514,784, 2003.

Fan, J.C.C., and Goodenough, J.B., (1977), X-ray photoemission spectroscopy studies of Sn-doped indium-oxide films, *Journal of Applied Physics*, vol. 48, n°8, 3524-3531.

Feurprier, Y., Cardinaud, C., et al., (1997), Surface modification and etch product detection during reactive ion etching of InP in-plasma, *Plasma Sources Science and Technology*, vol. 6, 334.

Francois, A., Aimez, V., et al., (2006), Enhancement of quantum well intermixing on InP/InGaAs/InGaAsP heterostructures using titanium oxide surface stressors to induce forced point defect diffusion, *Applied Physics Letters*, vol. 89, 164107.

Franke, R., Chasse, T., et al., (1991), Auger parameters and relaxation energies of phosphorus in solid compounds, *Journal of Electron Spectroscopy and Related Phenomena*, vol. 56, n°4, 381-388.

Gallas, B., Kao, C.C., et al., (2002), Laser annealing of SiOx thin films, *Applied Surface Science*, vol. 185, n°3-4, 317-320.

Genest, J., Dubowski, J.J., et al., (2004), UV laser-based process for quantum well intermixing of III-V heterostructures, *Proceeding of SPIE*, vol. 5451, 551.

Genest, J., Dubowski, J., et al., (2007), UV laser controlled quantum well intermixing in InAlGaAs/GaAs heterostructures, *Journal of Physics: Conference Series*, vol. 59, 605-609.

Genest, J., Beal, R., et al., (2008), ArF laser-based quantum well intermixing in InGaAs/InGaAsP heterostructures, *Applied Physics Letters*, vol. 93, 071106.

Ghumman, C.A.A., Moutinho, A.M.C., et al., (2012), An upgraded TOF-SIMS VG Ionex IX23LS: Study on the negative secondary ion emission of IIII-V compound semiconductors with prior neutral cesium deposition, *Applied Surface Science*, vol. 258, n°7, 2490-2497.

Golovanov, V., Maki-Jaskari, M.A., et al., (2005), Experimental and theoretical studies of indium oxide gas sensors fabricated by spray pyrolysis, *Sensors and Actuators B: Chemical*, vol. 106, n°2, 563-571.

Guido, L., Major, J., et al., (1989), Disorder defined buried heterostructure $Al_xGa_{1-x}As$/GaAs quantum well lasers by diffusion of silicon and oxygen from Al-reduced SiO_2, *Applied Physics Letters*, vol. 54, n°13, 1265-1267.

Gunawan, O., Ong, T., et al., (2000), A theoretical analysis of quantum well intermixing using the pulsed laser irradiation technique in InGaAs/InGaAsP laser structure, *Surface and Coatings Technology*, vol. 130, n°1, 116-121.

Heo, J., and Kim, H.J., (2007), Effects of annealing condition on low-k a-SiOC: H thin films, *Electrochemical and Solid-State Letters*, vol. 10, G11.

Hewitt, R., and Winograd, N., (1980), Oxidation of polycrystalline indium studied by x-ray photoelectron spectroscopy and static secondary ion mass spectroscopy, *Journal of Applied Physics*, vol. 51, n°5, 2620-2624.

Hollinger, G., Joseph, J., et al., (1987), On the chemistry of passivated oxide-InP interfaces, *Journal of Vacuum Science & Technology B: Microelectronics and Nanometer Structures*, vol. 5, 1108.

Hollinger, G., Bergignat, E., et al., (2009), On the nature of oxides on InP surfaces, *Journal of Vacuum Science & Technology A: Vacuum, Surfaces, and Films*, vol. 3, n°6, 2082-2088.

Holonyak, N., Jr., (1998), Impurity-induced layer disordering of quantum-well heterostructures: discovery and prospects, *IEEE Journal of Selected Topics in Quantum Electronics*, vol. 4, n°4, 584-594.

Ingrey, S., Lau, W., et al., (1987), An x-ray photoelectron spectroscopy study on ozone treated InP surfaces, *Journal of Vacuum Science & Technology A: Vacuum, Surfaces, and Films*, vol. 5, n°4, 1621-1624.

Iwata, S., and Ishizaka, A., (1996), Electron spectroscopic analysis of the SiO2/Si system and correlation with metal-oxide semiconductor device characteristics, *Journal of Applied Physics*, vol. 79, n°9, 6653-6713.

Jin, Z., Hashizume, T., et al., (2001), In Situ X-Ray Photoelectron Spectroscopy Study of Etch Chemistry of Methane-Based Reactive Ion Beam Etching of InP Using N2, *Japanese Journal of Applied Physics*, vol. 40, 2757.

Kitatani, T., Kondow, M., et al., (2000), Effects of thermal annealing procedure and a strained intermediate layer on a highly-strained GaInNAs/GaAs double-quantum-well structure, *Journal of Crystal Growth*, vol. 221, n°1, 491-495.

Lau, W., Sodhi, R., et al., (1988), Thermal desorption of oxides on InP, *Applied Physics Letters*, vol. 52, n°5, 386-388.

Lianping, H., Haji, M., et al., (2011), 10-GHz Mode-Locked Extended Cavity Laser Integrated With Surface-Etched DBR Fabricated by Quantum-Well Intermixing, *IEEE Photonic Technology Letters*, vol. 23, n°2, 82-84.

Liliental, Z., Krivanek, O., et al., (1985), Structure of the InP/SiO_2 interface, *Applied Physics Letters*, vol. 46, n°9, 889-891.

Liu, N., Blais, S., et al., (2011a), Surface and interface study of SiO coated InP/InGaAs/InGaAsP semiconductor laser microstructures processed in the soft KrF laser irradiation regime, *Proceeding of SPIE*, vol. 8206, 820609.

Liu, N., Moumanis, K., et al., (2011b), Surface morphology of SiO2 coated InP/InGaAs/InGaAsP microstructures following irradiation with the ArF and KrF excimer lasers, *Proceeding of SPIE*, vol. 7920, 79200C.

Liu, N., Moumanis, K., et al., (2012), Self-organized Nano-cone Arrays in InP/InGaAs/InGaAsP Microstructures by Irradiation with ArF and KrF Excimer Lasers, *Journal of Laser Micro/Nano Engineering*, vol. 7, n°2, 130.

Liu, N., and Dubowski, J.J., (2013), Chemical evolution of InP/InGaAs/InGaAsP microstructures irradiated in air and deionized water with ArF and KrF lasers, *Applied Surface Science*, vol. 270, n°13, 16-24.

Liu, Y., Chen, T., et al., (2006), Depth profiling of charging effect of Si nanocrystals embedded in SiO2: A study of charge diffusion among Si nanocrystals, *The Journal of Physical Chemistry B*, vol. 110, n°33, 16499-16502.

McKerracher, I., Fu, L., et al., (2008), Impurity-free vacancy disordering of quantum heterostructures with SiO_xN_y encapsulants deposited by magnetron sputtering, *Proceedings of SPIE,*, vol. 7039, 70390U.

McKerracher, I., Fu, L., et al., (2012), Intermixing of InGaAs/GaAs quantum wells and quantum dots using sputter-deposited silicon oxynitride capping layers, *Journal of Applied Physics*, vol. 112, n°11, 113511.

McLaren, J., Nelson, A., et al., (1983), Surface topography of oxides on InP thermally grown at high temperatures, *Journal of Vacuum Science & Technology A: Vacuum, Surfaces, and Films*, vol. 1, n°3, 1486-1490.

Mikushkin, V., Sysoev, S., et al., (2004), Standardless XPS method for determining the chemical composition of multiphase compounds and its application to studies of InP plasma oxide nanofilms, *Physics of the Solid State*, vol. 46, n°10, 1830-1835.

Miller, D., Biesinger, M., et al., (2002), Interactions of CO_2 and CO at fractional atmosphere pressures with iron and iron oxide surfaces: one possible mechanism for surface contamination?, *Surface and Interface Analysis*, vol. 33, n°4, 299-305.

Neves, P., Arronte, M., et al., (2002), KrF excimer laser dry and steam cleaning of silicon surfaces with metallic particulate contaminants, *Applied Physics A: Materials Science & Processing*, vol. 74, n°2, 191-199.

Nguyen, T.P., Lefrant, S., et al., (1997), Interfacial reactions in poly (phenylene vinylene)-metal systems, *Synthetic Metals*, vol. 84, n°1-3, 659-660.

Nguyen, T.P., Le Rendu, P., et al., (2003), An X-ray photoelectron spectroscopy investigation into the interface formed between poly(2-methoxy-5-(2'-ethyl-hexyloxyl)-p-phenylene vinylene) and indium tin oxide, *Synthetic Metals*, vol. 138, n°1-2, 113-117.

Oswald, S., and Brückner, W., (2004), XPS depth profile analysis of non-stoichiometric NiO films, *Surface and Interface Analysis*, vol. 36, n°1, 17-22.

Pan, J., Tay, S., et al., (1999), XPS study of incident angle effects on the ion beam modification of InP surfaces by 6 keV O_2, *Surface and Interface Analysis*, vol. 27, n°11, 993-997.

Salvia, A.M., and Castle, J.E., (1998), The intrinsic asymmetry of photoelectron peaks: dependence on chemical state and role in curve fitting, *Journal of Electron Spectroscopy and Related Phenomena*, vol. 95, n°1, 45-56.

Schulze, P., Shaffer, S., et al., (1983), Adsorption of water on rhenium studied by XPS, *Journal of Vacuum Science & Technology A: Vacuum, Surfaces, and Films*, vol. 1, n°1, 97-99.

Shibata, N., and Ikoma, H., (1992), X-Ray photoelectron spectroscopic study of oxidation of InP, *Japanese Journal of Applied Physics*, vol. 31, 3976-3980.

Som, T., Chini, T.K., et al., (2009), Formation of nanodots on oblique ion sputtered InP surfaces, *Applied Surface Science*, vol. 256, n°2, 562-566.

Stanowski, R., Voznyy, O., et al., (2006), Finite element model calculations of temperature profiles in Nd: YAG laser annealed GaAs/AlGaAs quantum well microstructures, *J. Laser Micro Nanoengineering*, vol. 1, 17-21.

Stavarache, I., Lepadatu, A.-M., et al., Structural investigations of Ge nanoparticles embedded in an amorphous SiO2 matrix, *Journal of Nanoparticle Research*, vol. 13, n°1, 221-232.

Teng, J., Dong, J., et al., (2002), Controlled group V intermixing in InGaAsP quantum well structures and its application to the fabrication of two section tunable lasers, *Journal of Applied Physics*, vol. 92, 4330.

Thurgate, S., and Erickson, N., (1990), X-ray photoelectron spectroscopy/Ar+ ion profile study of thin oxide layers on InP, *Journal of Vacuum Science & Technology A: Vacuum, Surfaces, and Films*, vol. 8, n°5, 3669-3675.

Truesdale, G., Downing, A., et al., (1955), The solubility of oxygen in pure water and sea-water, *Journal of Applied Chemistry*, vol. 5, n°2, 53-62.

Tsuchiya, T., Shimizu, J., et al., (2003), Selective-area growth of high-crystalline-quality InGaAlAs by metal-organic vapor-phase epitaxy, *Journal of Crystal Growth*, vol. 248, 384-389.

Tsvetkova, T., Sellin, P., et al., (2010), X-ray photoelectron study of high-energy He+ implanted a-SiC: H thin films, *Journal of Physics: Conference Series*, vol. 253, 012052.

Wager, J., and Wilmsen, C., (1982), Plasma enhanced chemical vapor deposited SiO2/InP interface, *Journal of Applied Physics*, vol. 53, n°8, 5789-5797.

Wagner, C., Passoja, D., et al., (1982), Auger and photoelectron line energy relationships in aluminum-xygen and silicon-oxygen compounds, *Journal of Vacuum Science and Technology*, vol. 21, n°4, 933-944.

Weiher, R., and Ley, R., (1963), Thermal Expansion of Indium Oxide, *Journal of Applied Physics*, vol. 34, 1833.

Yamaguchi, M., and Ando, K., (1980), Thermal oxidation of InP and properties of oxide film, *Journal of Applied Physics*, vol. 51, n°9, 5007-5012.

Yang, L.L., Zhao, Q.X., et al., (2011), A SIMS study on Mg diffusion in $Zn_{0.94}Mg_{0.06}O$/ZnO heterostructures grown by metal organic chemical vapor deposition, *Applied Surface Science*, vol. 257, n°20, 8629-8633.

Chapter 6 Excimer laser induced quantum well intermixing amplitudes in III-V microstructures

In this chapter, I will discuss QWI amplitudes achieved in QW microstructures irradiated directly with ArF and KrF excimer lasers in air and DI environments, as well as irradiated through SiO_2, Si_3N_4 and InO_x layers deposited on the surface of InP capping material. I will discuss the role of DI water in achieving high-quality QWI material (a related manuscript "Enhanced photoluminescence from UV laser quantum well intermixed InGaAs/InGaAsP/InP laser microstructures" by N. Liu, S. Poulin, J.J. Dubowski, Journal of Physics D: Applied Physics, Vol. **46**, pp. 445103, (2013). I will also discuss the amplitude of the QWI effect induced in InGaAsP/GaAs microstructure irradiated in air and DI water with KrF laser.

6.1 QWI amplitudes in InP/InGaAs/InGaAsP microstructures coated with different oxides and irradiated with excimer lasers

As we discussed in chapter 2, the PL shift dependens on diffusion length L of atoms in the wells and barriers. The diffusion length is determined by $\mathrm{L} = \sqrt{\mathrm{Dt}}$, D is the intermixing coefficient and t is annealing time. First the net PL shift on the excimer laser irradiated sites is supposed to increase with increasing annealing time and saturates at large annealing time, when all the surface defects generated by excimer laser have moved through the whole QW active region. Figure 6.1 shows the net PL shifts of irradiated sites (A1, A2) from full laser QW microstructure (M1580) and sites (B1, B2) from shallow well QW microstructure (RAC82) dependence on annealing time range from 0 to 6 minutes at 2-min intervals. The RTA temperature is at 700 °C. It shows that all the net PL shifts first increase with annealing time and saturate at 6 minutes.

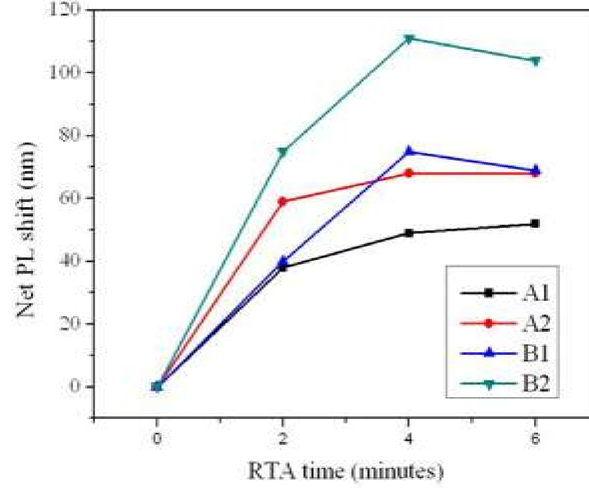

Figure 6. 1 Net PL shifts dependence on RTA time

However, the thermal shifts of QW microstructure increases with increasing RTA time or temperature. In order to investigate the UV laser generated surface defects mechanism, it is required to suppress the thermal shifts to around 10 nm. Therefore, during my projects, 2 minutes RTA at 700°C was used consistly with this expectation. In this situation, the PL shift can be estimated by intermixing coefficient. The UV laser intermixing coefficient D is reported to be related to the pulse number depending on the equation [H. Djie*, et al.* 2006, J. Genest*, et al.* 2008]:

$$D = D_0 + \sum_{i=1}^{M} D_i \left(1 - e^{-k_i (N - N_{th})}\right) \qquad (6.1)$$

where D_0 is the intrinsic diffusion coefficient. D_i is the defect-enhanced intermixing coefficient, k_i is pulse dependent rate of defect generation process, N is pulse number and N_{th} is threshold pulse number. According to this equation, we can find that the intermixing amplitude first increases with pulse number and saturates at $(D_0 + \sum_{i=1}^{M} D_i)$ larger pulse number. The values of D_0 and D_i are different when QW microstructures and laser parameters are different [O. Gunawan*, et al.* 2000, H. Djie*, et al.* 2006, J. Genest*, et al.* 2008]. Secondly, the sacrificial layer damage during excimer laser irradiation at large pulse number will reduce the reservoir of defects generation. This will also cause the PL shift saturation and even reduction at larger pulse number. Thirdly, PL emission from the QW region disappears, as the quantum confinement is lost. At this point, the PL emission from a quaternary ($In_xG_{1-x}As_yP_{1-y}$) could be observed, obviously at a much reduced intensity.

6.1.1 InP/InGaAs/InGaAsP microstruture coated with SiO_2

The InP/InGaAs/InGaAsP microstructure (RAC 82) coated with 243 nm SiO_2 that was irradiated with a KrF laser at 124 mJ/cm^2 and RTA at 700 °C for 2 minutes. A dependence of net blueshift vs. pulse number for both uncoated and SiO_2 coated material, following the KrF laser irradiation and the RTA step, is shown in Figure 6.1. We note that initially (N < 10), greater blueshift amplitudes have been observed for the SiO_2 coated material. For instance, $\delta\lambda = 59$ nm has been achieved following the irradiation with N = 5, which correspond to $\delta\lambda = 51$ nm for the sample irradiated in air. For $10 \leq N < 30$, $\delta\lambda \approx 67$ nm for the SiO_2 coated sample, while it exceeds 80 nm for the uncoated material. A constant $\delta\lambda$, saturating near 70 nm is observed for the SiO_2 coated sample, while a noticeable decrease of $\delta\lambda$ is observed for the uncoated material. The saturation of the blueshift amplitude is likely related to the consumption of oxygen atoms and other defects present at the SiO_2/InP interface that could diffuse towards the active region and promote intermixing. On the other hand, the decrease of $\delta\lambda$ with a pulse number, observed for uncoated sample at N > 30, seems to be related to laser-induced removal of the layer of an altered material that served as a 'reservoir' of intermixing promoting defects that propagate towards the QW region [J. Genest*, et al.* 2008a].

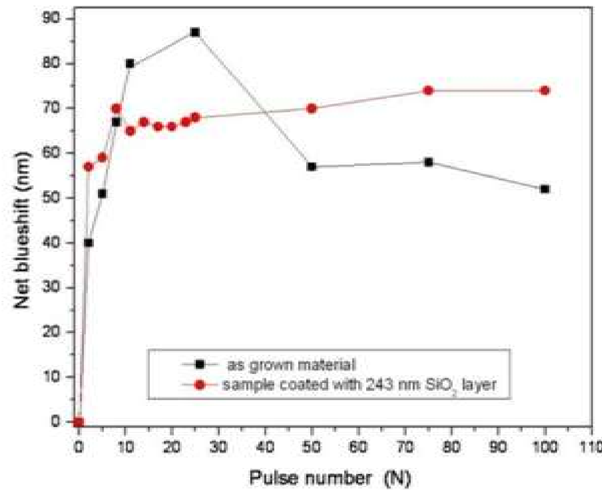

Figure 6. 2 Net blueshift amplitude dependence on the pulse number of the KrF laser at 124 mJ/cm^2 and RTA (InP/InGaAs/InGaAsP QW microstructure).

Table 6.1 shows the blueshift amplitude for a non-irradiated material that underwent RTA. A blueshift of $\delta\lambda = 13$ nm has been measured for the uncoated material. Similar amplitude blueshift

has also been observed for the SiO_2 coated material, regardless of the SiO_2 thickness, $d_{SiO2} = 50$, 150, 190, 243 and 263. These results suggest that no significant outdiffusion of In or P atoms from the InP/InGaAs/InGaAsP QW microstructure take place towards the surface or SiO_2 /InP interface during the RTA step and, therefore, no efficient atomic intermixing occurs at the applied RTA temperature [S. Barik*, et al.* 2007]. Clearly, significant blueshift amplitudes observed in the excimer laser irradiated material illustrate that the initial modification of the surface (SiO_2/InP interface) with an excimer laser, typically extending to a depth not exceeding the material optical absorption ($d_{InP} < 10$ nm), creates the conditions attractive for inducing atomic interdiffusion at elevated (RTA) temperatures.

Table 6. 1 Blueshift amplitude vs. thickness of the SiO_2 layer for non-irradiated QW microstructures.

SiO_2 layer thickness $dSiO_2$ (nm)	0	50	150	190	243	263
Blueshift (nm)	13	11	10	11	13	13

Chapter 4 shows that no obvious III and V group atoms were observed to outdiffuse to SiO_2 layer to promote the intermixing from our indepth XPS analysis as reference [C. Chia*, et al.* 2005]. As there is detection limitation of XPS analysis, SIMS was required to verify the results. Figure 6.2 shows the SIMS analysis of the sample after KrF laser irradiation at 124 mJ/cm^2 with 25 pulses and RTA. The SIMS results show chemical composition profile in SiO_2 layer (0 ~ 250 nm) and InGaAs/InGaAs/InP microstructure (250 ~ 400 nm). Figure 6.3 (a) is the expanded view of top SiO_2 layer (100 ~ 240 nm), it demonstrates that the mainly atoms is Si and O. There are no significant III or V atoms in this SiO_2 layer. Figure 6.3 (b) shows the expanded view of SIMS analysis of InGaAs/InGaAsP/InP microstructure after KrF laser induced QWI. There are 5 P intensity variation periods (350 ~ 400 nm) from the 5 InGaAs wells and 4 InGaAsP barriers. In the top 30 and 40 nm InP layers, the P atom intensity increase sharply around 240 nm, and there is also obvious O and Si atoms. The diffusion length of O atoms is larger than Si atoms due to small mass of O atoms. This confirm the indepth XPS profiling in chapter 5, that there was detectable O atoms (5%) diffuse to the InP layer on the irradiated sites. Before, SIMS results showed that by modifying the g SiO_2 layer, (Si,O) can diffuse as impurity to induce intermixing [L. J. Guido*, et al.* 1990]. So SIMS results verified that O impurities from the KrF laser created defective interface layer have diffused inside QW microstructure to induce the disordering.

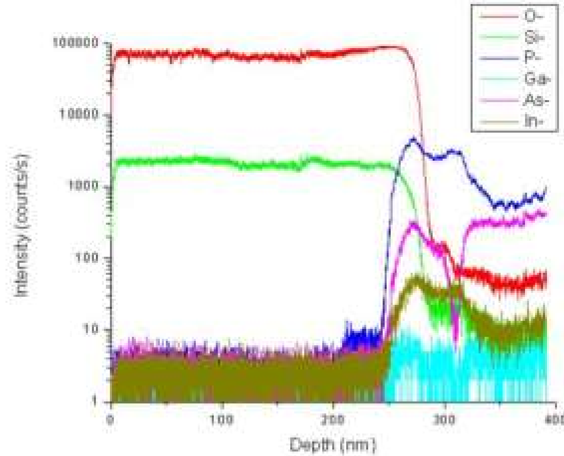

Figure 6. 3 SIMS profiles of O, Si, P, Ga, As and In InP/InGaAs/InGaAsP microstructure coated with a 243 nm thick layer of SiO_2 after KrF laser irradiation and RTA

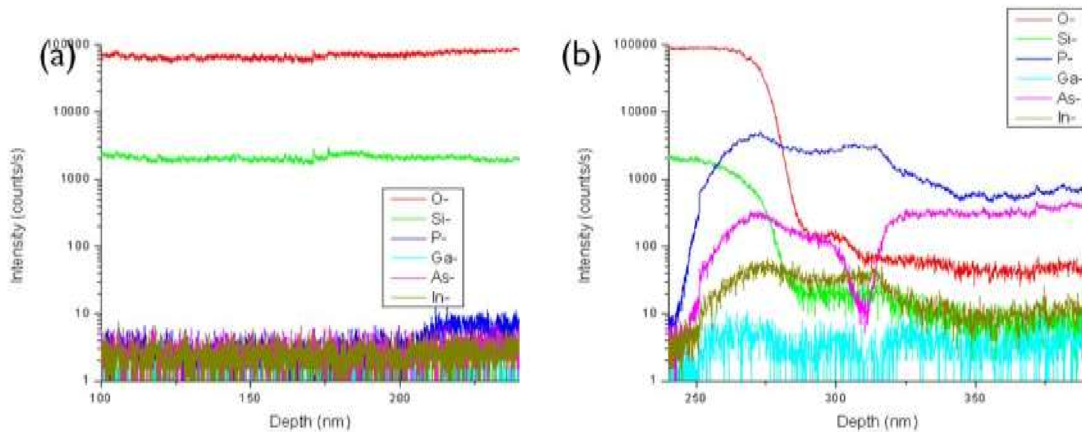

Figure 6. 4 Expanded view of SIMS analysis of InP/InGaAs/InGaAsP microstructure coated with 243 nm SiO_2 layer after KrF laser irradiation and RTA

6.1.2 InP/InGaAs/InGaAsP microstructure coated with Si_3N_4

40 nm Si_3N_4 layer was found to be ablated when irradiated at 67 mJ/cm^2 in chapter 4. Figure 6.4 shows the net blueshift dependence on pulse number after ArF laser irradiated at 67 mJ/cm^2 and RTA at 700°C for 120 seconds on investigated QW microstructure without Si_3N_4 and coated with a 40 nm Si_3N_4 layer. The blueshift increases as the pulse number increases for samples with and without Si_3N_4 coating layer. At lower pulse number ($N < 30$), samples with Si_3N_4 have larger blueshift amplitude than as grown samples after laser irradiation and RTA. This could be attributed to the intermixing induced by laser-driven diffusion of Si impurity into the QW microstructures, similar to the effect reported earlier [J. Epler*, et al.* 1986]. For a large pulse number ($N > 100$), the amplitude of blueshift on as grown samples is larger than for samples

coated with 40 nm Si_3N_4 layer. This could be related to a limited number of defects created during ArF laser irradiation of Si_3N_4 coated QW.

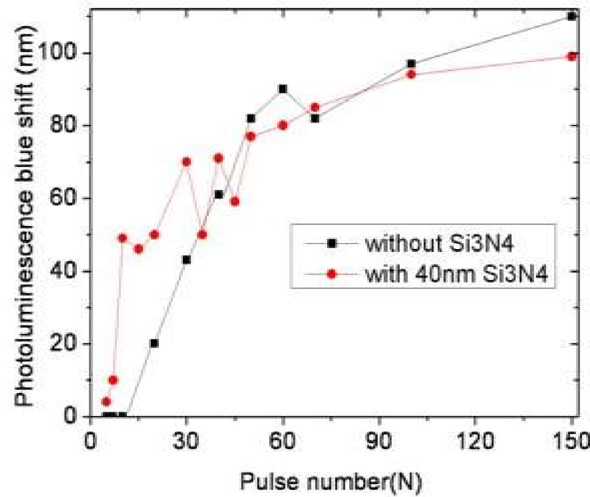

Figure 6. 5 Dependence of amplitude of blueshift on pulse number of samples without Si_3N_4 and coated with 40 nm Si_3N_4 layer after ArF laser irradiation and RTA.

6.1.3 InP/InGaAs/InGaAsP microstructure coated with InO_x

Our previous study demonstrates that eximer laser generated indium oxide layer on InP cap is supposed to promote intermixing, so we sputtering deposit InO_x layer on InP cap and investigate its influence on QWI amplitude. Figure 6.5 shows the non irradiated sites of sample from M1580 InP/InGaAs/InGaAsP microstructure coated with different thickness of InO_x layers after RTA at different temperatures. The samples coated with the InO_x layer have larger blueshift than as grown sample for every RTA temperature. Samples coated with 10 and 20 nm InO_x layer has larger blueshift than sample coated with 40 nm InO_x layer. The maximum blushift always takes place on the sample coated with 20 nm InO_x layer.

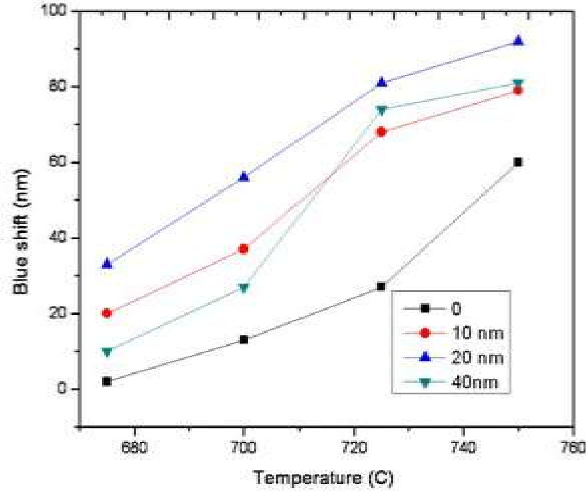

Figure 6. 6 Blueshift of as grown and samples coated with different thickness InO_x layers dependence on RTA temperatures

The SIMS profiles of O, P, Ga, As and In for as grown samples (no InO_x coating) from M1580 microstructure before and after RTA at 725°C are shown in Figure 6.6. After RTA, P atom has obviously diffused from 400 nm InP layer to the adjacent InGaAs layer. O atom from top native oxide layer also diffuse gradient along the InP and InGaAs layer.

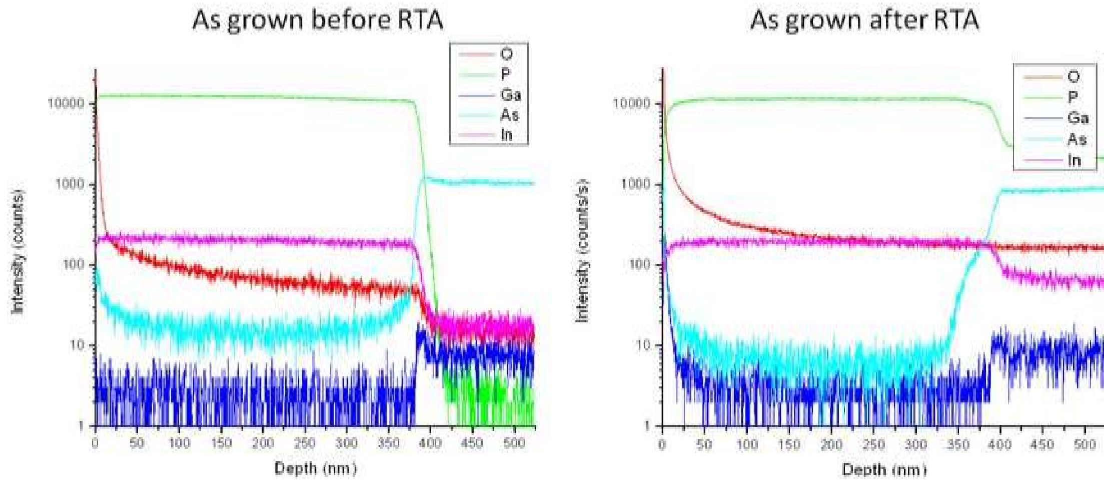

Figure 6. 7 SIMS measurement of as grown samples from M1580 microstructure before and after RTA

Figure 6.7 shows the SIMS results of sample coated with 40 nm InO_x layer before (a) and after (b) RTA at 725°C for 2 minutes. On sample before RTA, we can see that there is high intensity of O and In atoms in the first 40 nm InO_x layer. The top 40 nm InO_x layer has disappeared after RTA. O intensity has increased more than 10 times in the 400 nm InP capping layers and InGaAs layer below due to O diffusion during RTA. The quantity is also 10 times higher than as grown sample after RTA in Figure 6.6. Therefore, these O atoms diffusion are

from the InO_x layer. In constrast, In atoms quantity didn't increase very much. The main defects to promote the intermixing on sample coated with InO_x layer are these O impurities.

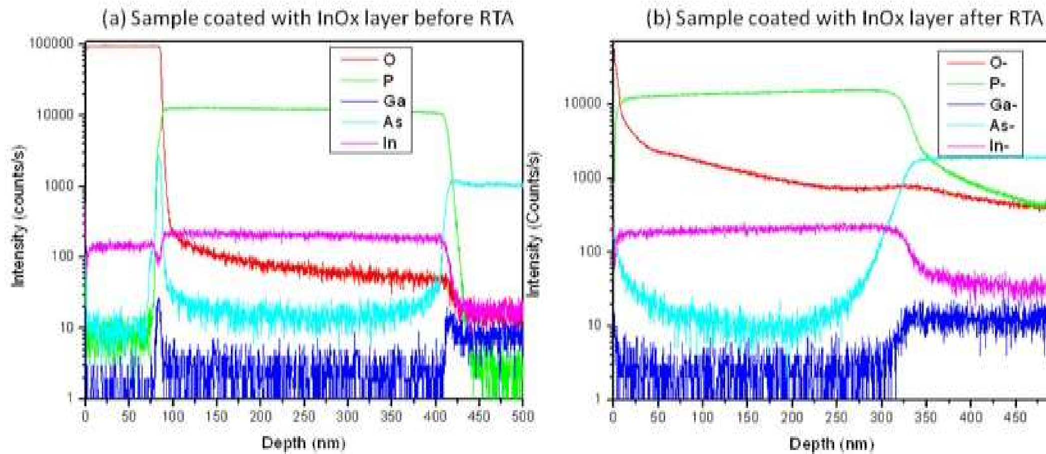

Figure 6. 8 SIMS results of sample coated with 40 nm InOx layer before and after RTA at 725◦C for 2 minutes

Figure 6.8 shows the PL shift dependence on pulse number on as grown sample and samples coated with 10 and 40 nm InO_x layers irradiated by KrF laser at 124 mJ/cm^2. On as grown material, there is no obvious PL shift at this relative lower laser fluence and pulse numbers. However, on samples coated with InO_x layers, there are obvious PL shifts. The PL shift increase with pulse number and the PL shift is larger on sample coated with 10 nm than sample coated with 40 nm. It quickly gets 105 nm PL shifts at 10 pulses irradiation.

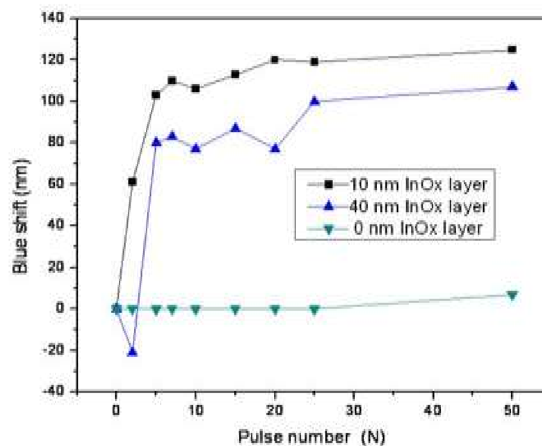

Figure 6. 9 PL shift dependence on pulse number of as grown sample (0 nm) and samples coated with 10 and 40 nm InO_x layer irradiated by KrF laser at 124mJ/cm^2

Figure 6.9 shows the SIMS results of sample coated with 10 nm InO_x layer after KrF laser irradiation at 124mJ/cm^2 and before and after RTA at 725°C for 2 minutes. Before RTA, it shows that the InO_x layer is totally removed after KrF laser irradiation, compared with Figure 6.7

(a). This confirms what we find in surface chemical analysis by XPS discussed in chapter 5. There is more O intensity on the top of 50 nm layer, compared with as grown material before RTA in Figure 6.6. After RTA we can see that there is O diffusion in the top 100 nm layer in Figure 6.9. These O impurities diffusion promote the III-V group atoms interdiffusion as P atoms concentration is higher in InGaAs layer and enhance the intermixing.

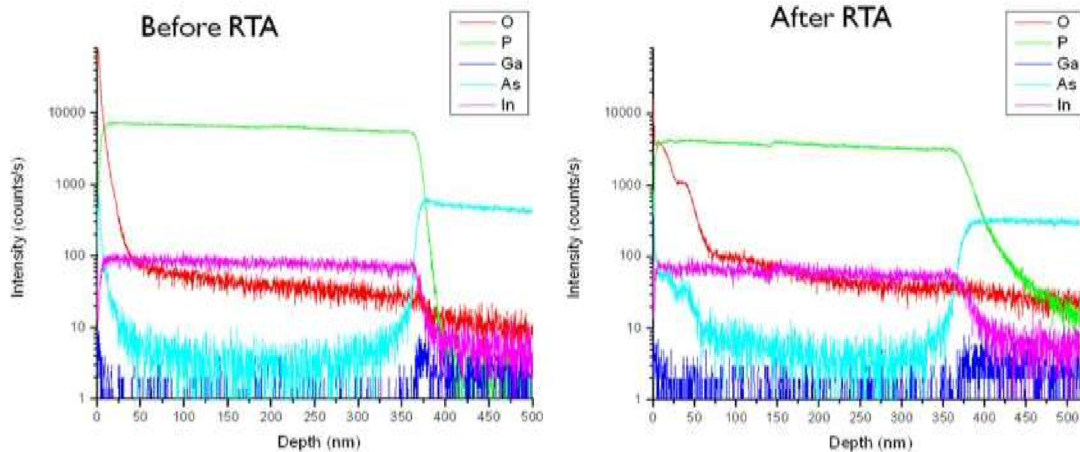

Figure 6. 10 SIMS results of sample coated with 40 nm InO_x layer after KrF laser irradiation with 10 pulses and before and after RTA at 725°C for 2 minutes

Therefore, on sample coated with InO_x layer, we can see that the PL shift is enhanced on both non irradiated and irradiated sites compared with as grown material. This indicates that InO_x layer is important in UV laser QWI on InP based microstructure through O impurity diffusion from these oxides layer during annealing.

6.2 Study of excimer laser induced interface chemical modification InGaAs/InGaAsP/InP laser microstructures in DI water and air by SIMS

Enhanced photoluminescence from UV laser quantum well intermixed InGaAs/InGaAsP/InP laser microstructures

Neng Liu, Suzie Poulin and Jan J. Dubowski, Journal of Physics D: Applied Physics, **46**, 445103, (2013).

Abstract: In spite of many years of research, the quantum well intermixing technique has not been able to deliver multibandgap III-V semiconductor wafers at highly attractive costs. We report that UV laser irradiation of InGaAs/InGaAsP/InP quantum well (QW) microstructures in

deionized water and rapid thermal annealing (RTA) allows achieving, mask-free, wafers with blue-shifted PL emission of intensity exceeding almost 10X that of the RTA-only wafers. Our calculations indicate that a ~ 40-nm-thick InO_x layer formed on top of the investigated microstructure induces compressive strain in the QW region and leads to this record-high enhanced PL amplitude.

Keywords: Quantum well intermixing, InGaAs/InGaAsP/InP microstructures, ArF excimer, laser-matter interaction, XPS, ToF-SIMS, photoluminescence

The selective area control of the bandgap of semiconductor wafers is one of the key factors in the development of photonic integrated circuits (PICs) [S. B. Estrella*, et al.* 2012]. Post-growth quantum well intermixing (QWI) has been reported as a relatively simple and potentially cost-effective method allowing area-selective bandgap tuning of $Si/Si_{1-x}Ge_x$ [J. J. Dubowski*, et al.* 1999c] and III-V quantum well (QW) wafers [E. J. Skogen*, et al.* 2005, J. Genest*, et al.* 2008a, C. Xu*, et al.* 2009, L. A. Coldren*, et al.* 2011]. The quality of the QWI material has frequently been investigated with the photoluminescence (PL) effect. Examples of such studies include material fabricated with ion implantation induced disordering [B. Elman*, et al.* 1989, Z. Jie*, et al.* 2006], sputtered SiO_2 intermixing [S. D. McDougall*, et al.* 1998], Ar ion plasma [H. S. Djie*, et al.* 2003, D. Nie*, et al.* 2006], SiO_2/Si_xN_y cap layers [J. Teng*, et al.* 2002], and both IR [J. J. Dubowski*, et al.* 2002, R. Stanowski*, et al.* 2009] and UV laser [J. J. Dubowski 2003, J. Genest*, et al.* 2007a] induced intermixing. The quality of the QWI material has also been investigated with Raman spectroscopy [T. K. Ong*, et al.* 2000, A. S. Helmy*, et al.* 2006], secondary ion mass spectroscopy (SIMS) [J. Teng*, et al.* 2002] as well as with devices, such as waveguides [J. E. Haysom*, et al.* 1999] and laser diodes [J.-P. Noel*, et al.* 1996, M. Paquette*, et al.* 1997, J. J. Dubowski*, et al.* 2002]. Numerous results have reported some degradation of the optical properties of QWI material manifested, e.g., by reduced QW PL intensity [Z. Jie*, et al.* 2006] and increased both waveguide losses [J. E. Haysom*, et al.* 1999] and laser threshold current [J. J. Dubowski*, et al.* 2002]. While reduced quantum confinement could account for some of these changes, an excessive uptake of impurities from the processing environment has often contributed to the increased intermixing amplitude and reduced device performance. The surface damage of InP cap and formation of defects propagating deep into the active region could lead to significantly decreased PL signals [S. D. McDougall*, et al.* 1998, Z. Jie*, et al.* 2006]. However, a 1.9X

enhanced PL intensity has been reported for a lattice-matched Zn-doped InGaAs/InGaAsP/InP microstructure blueshifted with Ar plasma by 86 nm [H. S. Djie*, et al.* 2003], while the same technique applied to a lattice-matched undoped InGaAs/InGaAsP/InP microstructure, produced a 16 nm blueshifted material emitting PL reduced by 50% [D. Nie*, et al.* 2006]. The importance of a processing environment on the quality of the QWI material has been illustrated with a variety of proximity caps employed during RTA, indicating that annealing with a Si proximity cap could produce a 90 nm blueshifted InGaAs/InGaAsP material emitting PL signal 2X more intense than that from the material capped with an InP proximity cap [O. Hulko*, et al.* 2006].

We have employed an UV laser QWI technique for processing of III-V QW microstructures [J. J. Dubowski 2003], and we have demonstrated large bandgap blueshifts ($\Delta\lambda \sim 130$ nm) in InGaAs/InGaAsP/InP microstructures[J. Genest*, et al.* 2008a, N. Liu*, et al.* 2013], while significant inhibition of the intermixing effect in AlGaAs/GaAs and InAlGaAs/AlGaAs/GaAs microstructures [J. Genest*, et al.* 2007a, J. Genest*, et al.* 2007b]. The irradiation experiments with both 193 and 248 nm excimer lasers carried out for samples surrounded by atmospheric air [J. Genest*, et al.* 2007a, J. Genest*, et al.* 2007b, J. Genest*, et al.* 2008a], deionized water [N. Liu*, et al.* 2013], SiO_x [Neng Liu*, et al.* 2011] and SiN_x [N. Liu*, et al.* 2010] environments have clearly demonstrated a dependence of both blueshifting and QW PL intensity on those environments. For instance, in comparison to the intensity of the RTA only material, a 2X enhanced QW PL intensity has been observed in the lattice matched material irradiated in air with an ArF laser and blueshifted by 74-83 nm [J. Genest*, et al.* 2008a]. Recently, a 1.4X PL intensity enhancement has been reported in a 140 nm blueshifted, compressively strained (~ 1%), InGaAsP/InGaAsP/InP QW heterostructure irradiated in air with a KrF laser [M. Kaleem*, et al.* 2013].

The presence of excessive impurities in the proximity of the QW region, while promoting the QWI effect, could be the source of the reduced amplitude of the QW PL emission due to increased non-radiative recombinations. This effect would intensify in microstructures with the surface-QW distance significantly reduced from its typical 1-2 μm used in laser microstructures. We addressed this issue by investigating the origin of enhanced PL emission in

InGaAs/InGaAsP/InP QW microstructure with the active region located approximately 80 nm below the surface.

The cross-section of the investigated InGaAs/InGaAsP/InP microstructure (RAC 82) is shown in Figure 3.5. The microstructure, grown on S-doped InP (001) substrate, consists of five (5) 6-nm-thick $In_{0.32}Ga_{0.68}As$ QW separated by four (4) 10-nm-thick $In_{0.79}Ga_{0.21}As_{0.42}P_{0.58}$ barriers. The QW stack is under a nominal 0.8 % compressive strain induced by the difference in chemical compositions of barriers and wells. The microstructure is interfaced with a 40-nm thick InP and a 6-nm-thick etch-stop InGaAsP layer and, finally, capped with a 30-nm thick InP layer. The microstructure was designed to emit PL at 1540 nm at room temperature.

The samples of 10 mm x 10 mm dimensions, following their degreasing in Opticlear, acetone, and isopropyl alcohol, were installed in a 0.74 mm tall Teflon chamber covered with a fused silica window. The chamber was filled with an atmospheric pressure air or DI water and the irradiation was carried out with an ArF-based projection system described elsewhere [N. Liu*, et al.* 2013]. A series of 0.9 mm diameter sites were irradiated on each sample, nominally under identical condition, with pulse fluence of 82 mJ/cm^2. The irradiated samples prepared for surface analyses were stored immediately in a N_2 filled box that provided protection against air oxidation. The RTA step was carried out at 700 °C for 2 min in a forming gas environment (N_2:H_2=9:1) using a commercial furnace (JIPELEC, Jetfirst). During RTA, the samples were installed face down on a silicon wafer employed as a capping material.

PL signal from processed samples was collected at room temperature with a commercial PL mapper (Philips, PLM-150) equipped with an Nd:YAG laser (λ = 1.06 μm) excitation source.

The surface chemical modification was investigated with XPS (AXIS Ultra DLD, Kratos Analytical). The analysis was carried with a take-off-angle normal to the sample surface. Quantification of XPS data was carried out using Casa XPS software as detailed in our previous work [N. Liu*, et al.* 2013].

The ArF laser irradiation of InP, due to the relatively strong absorption of the 193 nm radiation (6.4 eV), initially modifies an approximately 8 nm deep layer[D. Aspnes*, et al.* 1983, N. Liu*, et al.* 2012a]. The RTA activated processes and diffusion modify the chemical composition

of that layer and increase further its thickness. The PL shift and intensity of excimer laser irradiated QW microstructures was reported to be affected by the surface chemical state and morphology [J. J. Dubowski*, et al.* 1999c, N. Liu*, et al.* 2012a], but the mechanism of this enhancement has remained relatively unknown. Figure 6.11compares PL spectra from as grown material before and after RTA with those from the sites irradiated with the laser in air and in DI water (Figure 6.10 a and b, respectively). The insets are PL intensity maps of the samples displaying the sites irradiated with the indicated pulse number and annealed in a RTA furnace. The colour scale bars on the right provide a reference to the measured PL intensities. While RTA of the as grown material blueshifts its PL emission by about 15 nm, the irradiation in air with 20 pulses and RTA lead to the fabrication of the QWI material net blueshifted by 72 nm. This compares to the material net blueshifted by only 32 nm that was irradiated in DI water with the same laser parameters (pulse number and fluence). The greater blueshift of the site irradiated in air must be due to the excessive contribution from impurities and/or laser-induced modification of the surface. This is consistent with drastically decreased PL intensities observed from all sites irradiated in air. In contrast, significantly increased PL peak intensities have been measured from the sites irradiated in water. For instance, the 20-pulse irradiated site, blueshifted by 32 nm, emits PL signal at 2300 c.u., which is 2.1X more intense than that of the as grown material, and 9X more intense than the PL signal of the RTA only material.

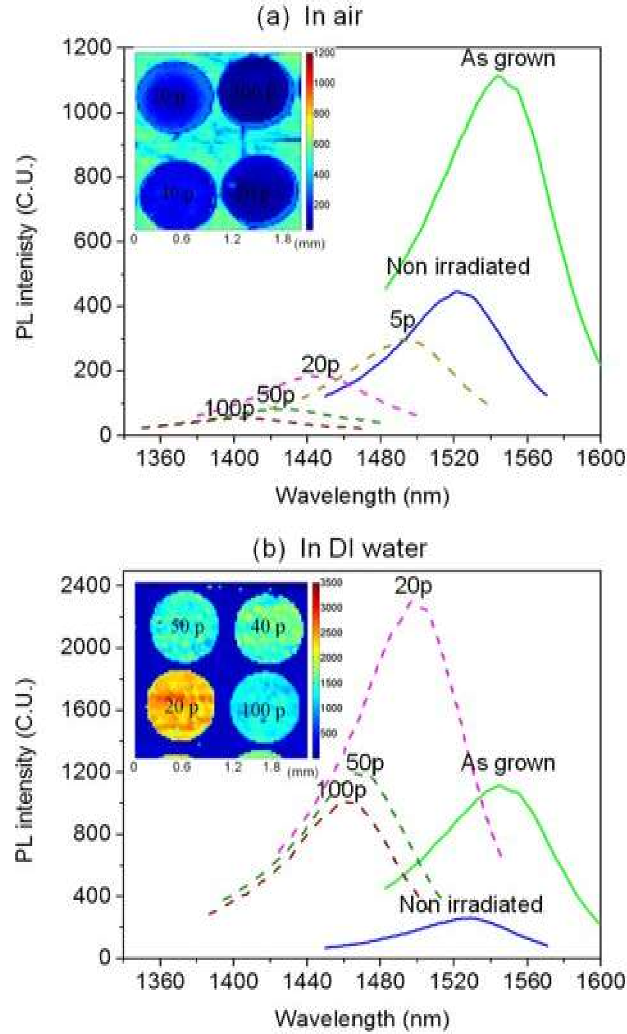

Figure 6. 11 PL spectra of as grown material and sites irradiated in air (a) and DI water (b) following the RTA step.

AFM data revealed only minimal surface roughening of the sites irradiated in air and DI water. The 50-pulse irradiated sites exhibited $\sigma_{RMS} \sim 6$ nm (compared to $\sigma_{RMS} \sim 1$ nm for the as grown material) that was reduced to $\sigma_{RMS} \sim 3.2$ nm after the RTA step. Thus the PL intensity enhancement due to surface nanostructurization is negligible in our samples. The PL full-width-at-half-maximum (PL_{FWHM}) of the as grown material was reduced from 82 nm to 77-75 nm after RTA. The PL_{FWHM} of 77 nm was observed for the sites irradiated with 20 pulses in DI H_2O (following the RTA step), while the sites irradiated with the same number of pulses in air exhibited PL_{FWHM} increased to 84 nm. The irradiation with 50 pulses in DI H_2O produced a material with $PL_{FWHM} \approx 82$ nm, i.e., comparable to that of the as grown material. This suggests that no significant deterioration of the active region is induced by the laser irradiation in DI H_2O.

To investigate the feasibility of a compressive strain increased PL emission intensity due to increased splitting energy between the heavy and light hole bands [T. Tsuchiya, *et al.* 1994a], we studied the chemical composition of the investigated samples using XPS and ToF-SIMS. Figure 6.11 shows the In $3d_{5/2}$ XPS spectra of sites irradiated with 50 pulses of the ArF laser at 82 mJ/cm^2 in air and DI water before (Figure 6.12 a and c) and after the RTA step (Figure 6.11 b and d). A massive amount of InP_xO_y (including $In(PO_3)_3$, $In_y(PO_4)$, $In(PO_3)_x$ and InO_x) can be seen on the sample irradiated in air. In contrast, a significantly smaller amount of InP_xO_y has been observed on the sample irradiated in DI water. The formation of a significantly InP_xO_y-enriched surface seems to be related to the availability of excessive oxygen as well as to a greater surface temperature induced with the laser irradiating the sample in air [N. Liu, *et al.* 2013].

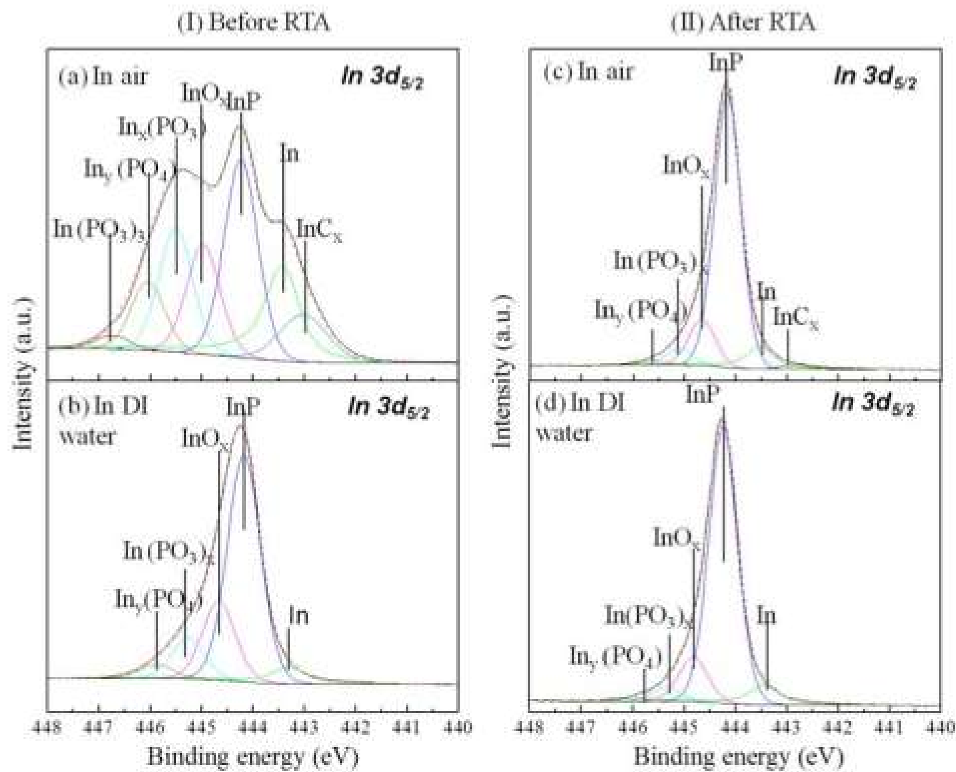

Figure 6. 12 In $3d_{5/2}$ XPS spectra of sample irradiated by ArF laser at 82 mJ/cm^2 with 50 pulses in DI water and air before (I) and after (II) RTA

For the sample irradiated in air, the P/In ratio decreases to 0.8 as the pulse number increases to 50 pulses. A similar P/In ratio was observed in InP capped QW microstructure during Argon-plasma induced QWI [C. Xu, *et al.* 2009]. Since the preferential sputtering of P leads to the formation of P vacancies or In interstitials, enhanced intermixing could be expected in such a case [J. Genest, *et al.* 2008a, C. Xu, *et al.* 2009]. In contrast, the P/In ratio for the 50-pulse site

irradiated in DI water increased by 20%. The preferential loss of In in samples UV laser irradiated in DI water, with P/In ratio of ~1.2 and excessive formation of P-P surface clusters, has been reported in literature [B. Kumar*, et al.* 2009]. This behavior could be traced to the lower surface temperature of InP irradiated in water vs. that irradiated in air for comparable laser parameters [J. A. Zimmerman*, et al.* 1991]. During RTA, the excessive P atoms diffuse into the microstructure and contribute to the formation of interstitial defects via the kick out mechanism as observed, e.g., in InP based QW microstructures coated with a low-temperature deposited P-rich InP cap layer[O. Hulko*, et al.* 2006]. Tables 6.2 and 6.3 summarise the XPS results concerning the P/In ratio observed for the investigated samples before and after the RTA step, respectively

Table 6. 2 XPS P/In ratio in the as grown InP-covered InGaAs/InGaAsP/InP microstructure and ArF irradiated sites before RTA.

	Non irradiated	20 pulses	50 pulses	100 pulses
In DI water	1.0	1.1	1.2	1.1
In air	1.0	0.9	0.8	0.8

Table 6. 3 XPS P/In ratio in the as grown InP-covered InGaAs/InGaAsP/InP microstructure and ArF irradiated sites after 2 min RTA at 700 °C.

	Non irradiated	20 pulses	50 pulses	100 pulses
In DI water	1.1	1.0	1.0	1.0
In air	1.1	1.1	1.1	1.1

It can be seen that, following the RTA step, the stoichiometry of the InP surface, averaged over the XPS probing depth (~10 nm), has been restored for the samples irradiated in DI water. In contrast, the stoichiometric InP surface of non-irradiated microstructures, as well as the P-deficient surface of samples irradiated in air become P-rich due to outdiffusion of this element during the RTA step.

Figure 6.12 compares ToF-SIMS profiles of phosphorus (P^-) (—), arsenic (As^-) (—), oxygen (O^-) (---), and InO^- (—) ions in as-grown material and the 50-pulse material irradiated in air and DI water, all after RTA. We note that InO^- is the main component (~ 80%) of all the In-oxides (InO_2^-, $In_2O_3^-$) observed with ToF-SIMS. The P^- intensity profile in the RTA-only sample (Figure 6.12 (a)) is followed by the weak intensity profile of O^- that follows relatively well the structural composition of the active region. As a reference, the O^- ion signal above 100 counts/s is observed in the top 20 nm thick portion of the microstructure. Our results are consistent with the presence of O reported in MBE [T. Achtnich*, et al.* 1987] and MOCVD [A. Sugg*, et al.* 1993]

grown P-based QW microstructures due to a relatively strong reactivity of P [N. Xiang*, et al.* 2001]. A significantly increased concentration of O^- observed in Figure 6.13 b illustrates an efficient uptake O from air. The O^- ion intensity in this case drops to below 100 counts/s only after about 100 nm of the material has been removed. In contrast, O^- signal drops to below 100 counts/s after about 50 nm removal of the material irradiated in DI water (Figure 6.12 c). Diminishing amplitude of the P^- ion profile in the active region irradiated in air (Figure 6.12 b) illustrates the presence of significant intermixing. The disappearance of the P^- ion minimum related to the presence of the 6-nm thick etch stop InGaAsP layer, originally observed in Figure 6.13a, is also an indication of the strong intermixing phenomenon, although slightly reduced depth resolution is expected during sputtering in ToF-SIMS. In contrast, the presence of the etch stop layer and four (4) InGaAsP barriers are clearly observed in the sample irradiated in DI water (Figure 6.12 c).

Both XPS and ToF-SIMS results confirm the presence of InO_x at significant concentration in the top portion of the investigated material. InO^- profile in the RTA only sample oscillates around 60 counts/s, and it increases to ~500 counts/s at the surface of that sample. This is consistent with the XPS data that revealed InO_x^- as a major component on the surface of RTA samples (see Figure 6.11). For the sample irradiated in air, almost constant InO^- ion intensity at 450 counts/s is observed in the top 70 nm thick layer, while in the active region, it drops to near 100 counts/s. The intensity of InO^- ion profile in the active region of the sample irradiated in DI water is slightly below 100 counts/s, while a compositional gradient of this material is observed over the 70 nm distance, as indicated by the signal increasing from 100 to 800 counts/s at the surface. Thus, it is clear that the top layer of the investigated material consists of the In-P-O mixture, with InO_x dominating its composition.

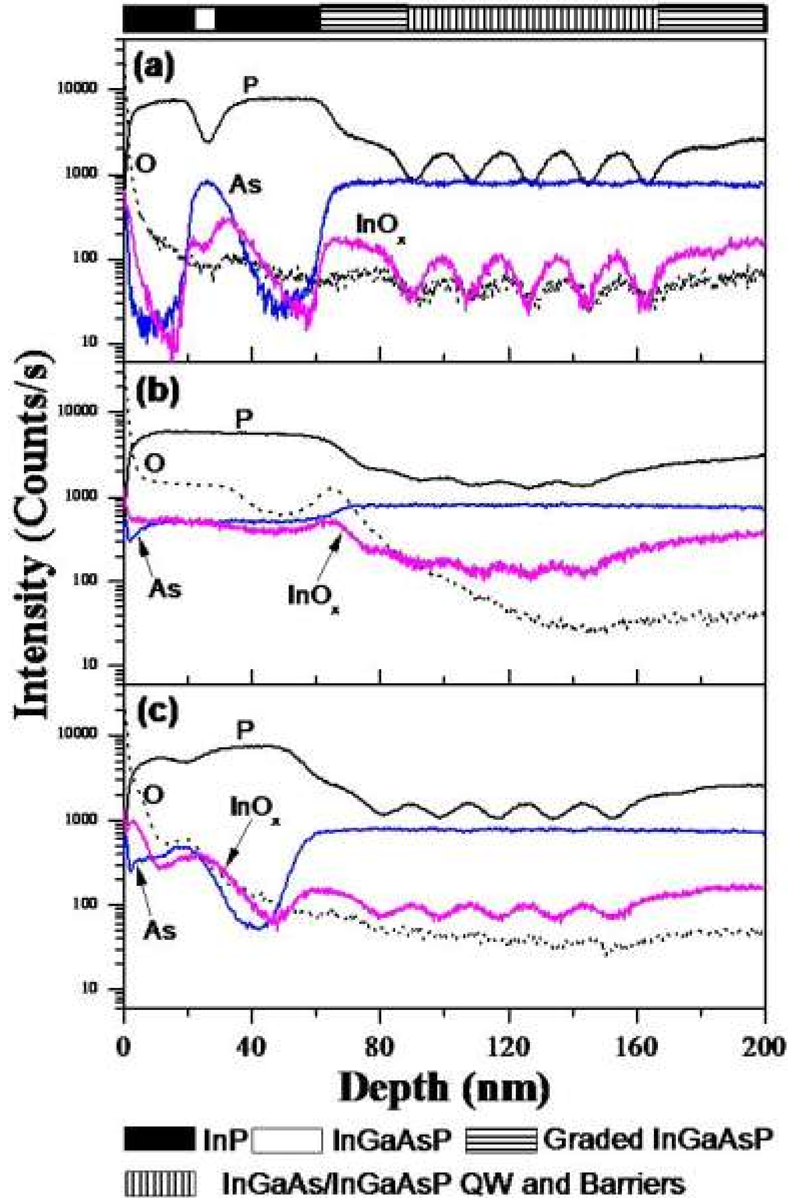

Figure 6. 13 P (—), O (---), As (—) and InO (—) intensity profiles in the microstructure after RTA of as grown sample (a) and samples irradiated by ArF laser at 82mJ/cm^2 with 50 pulses in air (b) and DI water (c) investigated by ToF-SIMS

We have investigated the role of InO_x on the strain induced in the active region. As the atomic radius of O (60 pm) is smaller than P (100 pm), InO_x has a greater coefficient of thermal expansion (CTE): 10.1 x 10^{-6} /K than that of InP: 4.1 x 10^{-6} /K [R. Singh*, et al.* 1978]. Thus, in the In-P-O mixed compound, CTE is supposed to increase with increasing concentration of InO_x. The thermal strain from the capped stressor layer on the QW microstructure is defined as [A. Francois*, et al.* 2006]:

$$\varepsilon = (\alpha_{structure} - \alpha_{stressor})\Delta T \qquad (6.2)$$

where $\alpha_{structure}$ and $\alpha_{stressor}$ is CTE of the microstructure and the stressor, respectively, and ΔT is the difference between the RTA (700 °C) and room (25 °C) temperatures. The negative value of ε indicates a compressive strain. We assumed that the top 76 nm thick layer consists of an interdiffused $In_xGa_{1-x}As_yP_{1-y}$ and an InO_x cap layer of thickness *d* that was used as a parameter in COMSOL calculations. The interdiffused composition profile was calculated based on the PL determined blueshift. Figure 6.13 shows the dependence of the calculated strain in the active region of the microstructure blueshifted by 32 nm on the thickness of the InO_x layer. Note that z = 0 in that figure indicates location of the barrier material above the uppermost QW interfacing the 20 nm thick $In_xGa_{1-x}As_yP_{1-y}$ graded bandgap layer. No significant modification of the strain is observed for *d* < 20 nm. As the InO_x thickness increases to 41 nm, the compressive strain in the QW region increases to almost 1.4%. It was reported that the PL intensity in InGaAsP/InGaAsP QW microstructures could increase by almost 10 times if the compressive strain in the active region increased from 0.8% to 1.4% [T. Tsuchiya*, et al.* 1994a]. Thus, the amplitude of PL enhancement observed in our samples is consistent with these calculations. It is feasible that InO_x nanocrystallites could form in the InGaAsP matrix at depths exceeding 40 nm and, thus, contribute to the strain in the active region of conventional laser microstructures. Nevertheless, we argue that the principal source of the PL intensity enhancement observed in the investigated microstructures is strain induced by the InO_x layer.

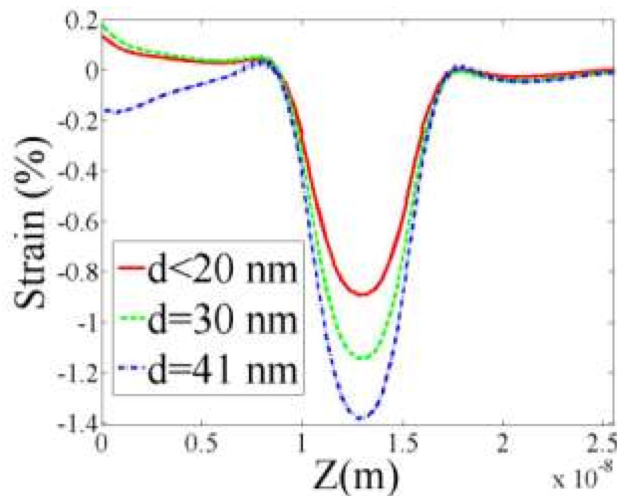

Figure 6. 14 Calculated strain dependence in the 32 nm blueshifted InGaAs/InGaAsP QW region on the thickness, d, of the InO_x stressing layer.

In summary, the ability to fabricate high-quality QWI material, illustrated by high-intensity QW PL and, e.g., low-threshold laser current fabricated from the QWI material, is critically important for the advancement of the QWI technology and fabrication of PICs. We have employed the UV laser QWI technique that allows eliminating parasitical contribution to QWI by surface accumulated impurities. An almost 10 times more intense PL signal was observed from the 32 nm net blueshifted material in comparison to the RTA only material. The XPS results indicate that the stoichiometry of the InP surface irradiated in DI water has been restored after the RTA step. This could contribute to some enhancement of the PL signal due to reduced concentration of the surface non-radiative recombination centres. However, our investigations point out to the increased strain in the QW region as the leading mechanism responsible for enhanced PL intensity in QWI InGaAs/InGaAsP/InP microstructures. The calculations indicate that a 41 nm thick layer of InO_x formed during RTA of the sample laser irradiated in DI H_2O is a source of the observed effect of PL enhancement. These results demonstrate the potential of the UV laser QWI technique in designing experimental conditions attractive for the fabrication of the QWI material with unique optical and electrical characteristics.

Acknowledgements: This work was supported by the Natural Science and Engineering Research Council of Canada (Discovery Grant No. 122795-2010) and the program of the Canada Research Chair in Quantum Semiconductors. Technical assistance of the technical staff of the Université de Sherbrooke Centre de recherche en nanofabrication et en nanocaractérisation (CRN^2) is greatly appreciated. NL acknowledges the Merit Scholarship Program for Foreign Student, Fonds de recherche du Québec - Nature et technologies, for providing a graduate student scholarship.

6.3 KrF laser induced QWI in GaAs based QW microstructure

A suppressed QWI effect was observed in AlGaAs/GaAs and InAlGaAs/AlGaAs/GaAs microstructures irradiated in air with a KrF laser [J. Genest*, et al.* 2007a, J. Genest*, et al.* 2007b]. The mechanism responsible for the reduced intermixing is due to the laser generated Ga_2O_3-induced tensile stress during RTA in the QW microstructures. In order to develop the application of our home made HI-PLM system, who is equipped with green laser, on samples after UV laser selective area QWI, we have employed KrF laser QWI on GaAs based QW

microstructure. As the laser generated oxides quantities on III-V semiconductors are different on sample irradiated in DI water and air as we reported in Chapter 5 and Chapter 6, we have studied the laser generated oxides effect on QWI in GaAs based QW microstructure by KrF laser irradiation in these two environments.

6.3.1 Experiment

The samples from InGaAsP/GaAs (T0808) microstructure were irradiated by KrF laser in air and DI water at 124 mJ/cm^2 with 50 pulses using a custom designed (maple leaf) mask. As Arsenic (As) is easily to evaporate at 825 °C temperature of forming gas, two fresh GaAs proximate caps were used to provide an As overpressure environment and prevent the As outdiffusion during annealing. After RTA, the samples were first going to PL measurement with PLM-150 excited by a green laser (λ = 532 nm). Then these samples were measured by HI-PLM equipment excited with a 532 nm laser.

6.3.2 Results and discussions

Figure 6.14 shows the PL map measured by PLM-150, we can see there is clearly maple leave pattern on these samples with different emission wavelength compared with as grown material. This means KrF laser have succeeded to induce QWI on this GaAs based QW microstructure by irradiation in DI water (a) and air (b). It is interesting to find that after irradiation in DI water, there shows redshift (~ 8 nm) while it has clearly blueshift (~ 9 nm) on sample irradiated in air at same laser fluence and RTA conditions. This is maybe due to the different chemical composition induced by KrF laser in these two different environments. The oxidation rate is reported faster on GaAs when irradiated by UV laser in water vapor than in air [D. Podlesnik*, et al.* 1986]. In addition that, UV light irradiation also leads to As depletion on the surface because of the high solubility of As oxides in water [D. V. Podlesnik*, et al.* 1984]. This indicates that more GaO_x is expected on sample irradiated in DI water and this oxide layers suppressed the intermixing due to thermal stress. On the sites irradiated in air, as the pulse number is smaller than reference [J. Genest*, et al.* 2007a], laser induced defects instead of oxides layer which promote the intermixing. The non irradiated region of samples in DI water emitted at

shorter wavelength than sites in air is possible due to oxides dissolve in DI water. More surface chemical characterizations will be required to verify the results.

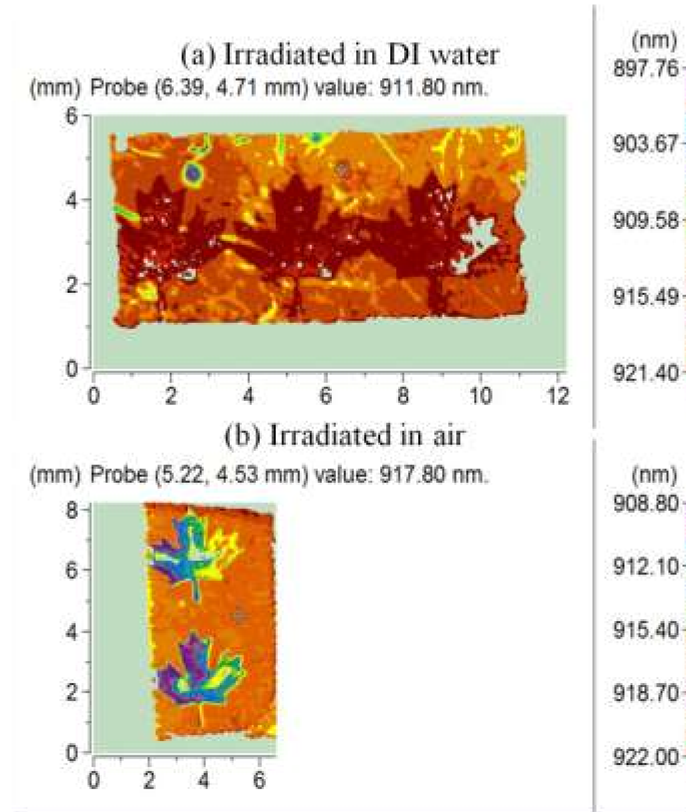

Figure 6. 15 PL map of sample (T0808) irradiated in DI water (a) and air (b) by KrF laser and RTA at 825 °C measured PLM

Figure 6.16 shows the PL map measured by HI-PLM after KrF laser irradiation in DI water (a) and air (b) and then RTA. The different color in the PL map shows the different emission wavelength according to color bar on the right. The maximum red shift in the maple leave region on sample irradiated in DI water is around 8 nm, while the blueshift on sample irradiated in air is around 10 nm, which is consist with PLM-150 measurement. However, all the wavelengths on both irradiated and non irradiated sites of these two samples have shifted by 5 nm compared with PLM-150. This is caused by different calibration standard in these two machines. It shows that HI-PLM measurement can collect good quality of image of PL map with sharp edge contrast of PL variation in both edges and tiny features and with high spatial and spectral resolution, which is useful for characterization of selective area bandgap tuned samples used in integrated photonic circuits fabrication.

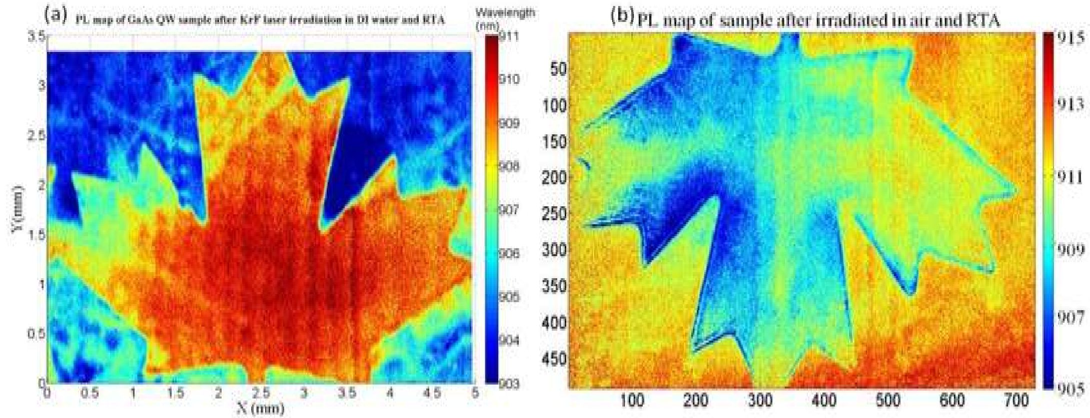

Figure 6. 16 PL map measured by HI-PLM of investigated sample after KrF laser QWI and RTA

6.4 Summary

In the first part, SIMS was used to verify that the defective interfacial layer creation on InGaAs/InGaAsP/InP microstructure coated with 243 nm SiO_x layer after KrF laser QWI. Both Si and O impurities from SiO_x layer have been found to diffuse to the QW microstructures. In contrast, there is no III or V atoms outdiffuse to the SiO_2 layer.

In the second part, 9 times enhanced PL intensities were found on InGaAs/InGaAsP/InP microstructures after ArF laser irradiation in DI water and RTA. XPS results shows that, compared with sites irradiated in air, there is fewer oxides created in DI water and fewer nonstoichiometric defects following RTA. SIMS shows that in the active region, the V atoms interdiffusion level is more obvious on sample irradiated in air, which induce higher PL shift on these sites. More O impurities were found on sites irradiated in air, which is one of the main causes of PL intensity degradation. Besides, there were different InO^- profiles in the interface on these sites irradiated in different environments. As InO has a higher CTE than microstructure, additional compressive strain will be generated in these microstructures. The In-plane strain calculation shows that compressive strain increase from 0.8% to 1.4% in the active regions in a complete confinement. This is supposed to enhance the PL intensity.

In the ending part, we have succeeded to induce QWI on GaAs based QW microstructure by KrF laser in air and DI water. Depending on the irradiation environments, both enhanced and suppressed bandgap engineering have been found. The novel HI-PLM equipment has been used to measure the selective area bandgap engineering with higher spatial resolution.

6.5 Bibliography

Achtnich, T., Burri, G., et al., (1987), Secondary ion mass spectrometry study of oxygen accumulation at GaAs/AlGaAs interfaces grown by molecular beam epitaxy, *Applied Physics Letters*, vol. 50, n°24, 1730-1732.

Aspnes, D., and Studna, A., (1983), Dielectric functions and optical parameters of Si, Ge, GaP, GaAs, GaSb, InP, InAs, and InSb from 1.5 to 6.0 eV, *Physical Review B*, vol. 27, n°2, 985.

Barik, S., Fu, L., et al., (2007), Impurity-free disordering of InAs/ InP quantum dots, *Applied Physics Letters*, vol. 90, 243114.

Chia, C., Chua, S., et al., (2005), Group-V intermixing in InAs/ InP quantum dots, *Applied Physics Letters*, vol. 86, 051905.

Coldren, L.A., Nicholes, S.C., et al., (2011), High Performance InP-Based Photonic ICs-A Tutorial, *Journal of Lightwave Technology*, vol. 29, n°4, 554-570.

Djie, H.S., Mei, T., et al., (2003), Photoluminescence enhancement by inductively coupled argon plasma exposure for quantum-well intermixing, *Applied Physics Letters*, vol. 83, n°1, 60-62.

Dubowski, J.J., Rowell, N., et al., (1999), Laser-induced selective area band-gap tuning in $Si/Si_{1-x}Ge_x$ microstructures, *Applied Physics Letters*, vol. 74, n°14, 1948-1950.

Dubowski, J.J., Feng, Y., et al., (2002), Monolithic multiple wavelength ridge waveguide laser array fabricated by Nd: YAG laser-induced quantum well intermixing, *Journal of Vacuum Science & Technology A: Vacuum, Surfaces, and Films*, vol. 20, n°4, 1426-1429.

Dubowski, J.J.: 'Laser-induced bandgap shifting for photonic device integration' US Patent 6,514,784, 2003.

Elman, B., Koteles, E.S., et al., (1989), GaAs/AlGaAs Quantum-Well Intermixing using shallow Ion-Implantation and Rapid Thermal Annealing, *Journal of Applied Physics*, vol. 66, n°5, 2104-2107.

Epler, J., Burnham, R., et al., (1986), Laser induced disordering of GaAs AlGaAs superlattice and incorporation of Si impurity, *Applied Physics Letters*, vol. 49, 1447.

Estrella, S.B., Johansson, L.A., et al., (2012), Widely Tunable Compact Monolithically Integrated Photonic Coherent Receiver, *IEEE Photonics Technology Letters*, vol. 24, n°5, 365-367.

Francois, A., Aimez, V., et al., (2006), Enhancement of quantum well intermixing on InP/InGaAs/InGaAsP heterostructures using titanium oxide surface stressors to induce forced point defect diffusion, *Applied Physics Letters*, vol. 89, 164107.

Genest, J., Dubowski, J., et al., (2007a), Suppressed intermixing in InAlGaAs/AlGaAs/GaAs and AlGaAs/GaAs quantum well heterostructures irradiated with a KrF excimer laser, *Applied Physics A: Materials Science & Processing*, vol. 89, n°2, 423-426.

Genest, J., Dubowski, J., et al., (2007b), UV laser controlled quantum well intermixing in InAlGaAs/GaAs heterostructures, *Journal of Physics: Conference Series*, vol. 59, 605-609.

Genest, J., Beal, R., et al., (2008), ArF laser-based quantum well intermixing in InGaAs/InGaAsP heterostructures, *Applied physics letters*, vol. 93, 071106.

Guido, L.J., Major, J.S., et al., (1990), Column III vacancy and impurityinduced layer disordering of $Al_xGa_{1-x}As_xGaAs$ heterostructures with SiO_2 or Si_3N_4 diffusion sources, *Journal of Applied Physics*, vol. 67, n°11, 6813-6818.

Haysom, J.E., Delage, A., et al., (1999), Experimental analysis and modeling of buried waveguides fabricated by quantum-well intermixing, *IEEE Journal of Quantum Electronics*, vol. 35, n°9, 1354-1363.

Helmy, A.S., Martin, P., et al., (2006), Spatially resolved photoluminescence and Raman spectroscopy of bandgap gratings fabricated in GaAs/AlAs superlattice waveguide using quantum well intermixing, *Journal of Crystal Growth*, vol. 288, n°1, 53-56.

Hulko, O., Thompson, D., et al., (2006), The effect of different proximity caps on quantum well intermixing in InGaAsP/InP QW structures, *Semiconductor Science and Technology*, vol. 21, n°7, 870.

Jie, Z., Jie, C., et al., (2006), Implant Depth Influence on InGaAsP/InP Double Quantum Well Intermixing Induced by Phosphorus Ion Implantation, *Chinese Physics Letters*, vol. 23, n°4, 919.

Kaleem, M., Zhang, X., et al., (2013), UV laser induced selective-area bandgap engineering for fabrication of InGaAsP/InP laser devices, *Optics and Laser Technology*, vol. 51, 36-42.

Kumar, B., and Soni, R., (2009), Pulsed-laser-induced photochemical growth of the periodic surface structure on InP, *Semiconductor Science and Technology*, vol. 24, n°9, 095007.

Liu, N., Moumanis, K., et al., ArF excimer laser-induced quantum well intermixing in dielectric layer coated InGaAs/InGaAsP microstructures, *PICALO 2010*, unpublished.

Liu, N., Blais, S., et al., (2012) Surface and interface study of SiO_{2-x} coated InP/InGaAs/InGaAsP semiconductor laser microstructures processed in the soft KrF laser irradiation regime, *Proc. SPIE 8206, Pacific Rim Laser Damage 2011: Optical Materials for High Power Lasers*, SPIE, 820609.

Liu, N., Moumanis, K., et al., (2012), Self-organized Nano-cone Arrays in InP/InGaAs/InGaAsP Microstructures by Irradiation with ArF and KrF Excimer Lasers, *Journal of Laser Micro/Nano Engineering*, vol. 7, n°2, 130.

Liu, N., and Dubowski, J.J., (2013), Chemical evolution of InP/InGaAs/InGaAsP microstructures irradiated in air and deionized water with ArF and KrF lasers, *Applied Surface Science*, vol. 270, n°13, 16-24.

McDougall, S.D., Kowalski, O.P., et al., (1998), Monolithic integration via a universal damage enhanced quantum-well intermixing technique, *IEEE Journal of Selected Topics in Quantum Electronics*, vol. 4, n°4, 636-646.

Nie, D., Mei, T., et al., (2006), Argon plasma exposure enhanced intermixing in an undoped InGaAsP/InP quantum-well structure, *Journal of Applied Physics*, vol. 100, 046103.

Noel, J.-P., Melville, D., et al., (1996), High-reliability blue shifted InGaAsP/InP lasers, *Applied Physics Letters*, vol. 69, n°23, 3516-3518.

Ong, T.K., Gunawan, O., et al., (2000), High-spatial-resolution quantum-well intermixing process in GaInAs/GaInAsP laser structure using pulsed-photoabsorption-induced disordering, *Journal of Applied Physics*, vol. 87, n°6, 2775-2779.

Paquette, M., Beauvais, J., et al., (1997), Blueshifting of InGaAsP/InP laser diodes by low-energy ion implantation, *Applied Physics Letters*, vol. 71, n°26, 3749-3751.

Podlesnik, D., Gilgen, H., et al., (1986), Interaction of deep-ultraviolet laser light with GaAs surfaces in aqueous solutions, *Journal of the Optical Society of Ameica B*, vol. 3, n°5, 775-784.

Podlesnik, D.V., Gilgen, H.H., et al., (1984), Deep-ultraviolet induced wet etching of GaAs, *Applied physics letters*, vol. 45, n°5, 563-565.

Singh, R., and Shewchun, J., (1978), A possible explanation for the photovoltaic effect in indium tin oxide on InP solar cells, *Journal of Applied Physics*, vol. 49, n°8, 4588-4591.

Skogen, E.J., Raring, J.W., et al., (2005), Monolithically integrated active components: a quantum-well intermixing approach, *IEEE Journal of Selected Topics in Quantum Electronics*, vol. 11, n°2, 343-355.

Stanowski, R., and Dubowski, J., (2009), Laser rapid thermal annealing of quantum semiconductor wafers: a one step bandgap engineering technique, *Applied Physics A*, vol. 94, n°3, 667-674.

Sugg, A., Chen, E., et al., (1993), Effects of low-temperature annealing on the native oxide of Al_xGa_{1-x} As, *Journal of Applied Physics*, vol. 74, n°6, 3880-3885.

Teng, J., Dong, J., et al., (2002), Controlled group V intermixing in InGaAsP quantum well structures and its application to the fabrication of two section tunable lasers, *Journal of Applied Physics*, vol. 92, 4330.

Tsuchiya, T., Komori, M., et al., (1994), Investigation of effect of strain on low-threshold 1.3 um InGaAsP strained-layer quantum well lasers, *Electronics Letters*, vol. 30, n°10, 788-789.

Xiang, N., Tukiainen, A., et al., (2001), Oxygen-related deep level defects in solid-source MBE grown GaInP, *Journal of Crystal Growth*, vol. 227, n°0, 244-248.

Xu, C., and Mei, T., (2009), Inductively Coupled Argon Plasma-Enhanced Quantum-Well Intermixing: Cap Layer Effect and Plasma Process Influence, *IEEE Journal of Quantum Electronics*, vol. 45, n°8, 920-926.

Zimmerman, J.A., Bach, S.B.H., et al., (1991), Ion/molecule reactions of arsenic and phosphorus cluster ions: ionization potentials and novel reaction pathways, *The Journal of Chemical Physics*, vol. 95, n°1, 98-104.

Chapter 7 Laser diodes in KrF laser QWI InGaAs/InGaAsP/InP microstructures

The development of the UV laser QWI technology addresses the integration field of optoelectronic devices. In this section, I will first discuss KrF laser QWI in samples coated with Al mask and designed for the fabrication of laser diodes – the fundamental blocks of PIC. The results carried out in collaboration with the Zhejiang University in Hangzhou (China), have been published by Kaleem et al. in the Journal of Optics & Laser Technology 51 (2013) 36-41. In the second part of this chapter, I will discuss some properties of laser diodes fabricated in ZJU QW microstructures. The fabrication of large area QWI material by applying the UdeS KrF laser processing setup induced QWI samples on.

7.1 KrF laser QWI for integrated laser diode fabrication

7.1.1 Experimental

A dedicated sample was coated with a 70 nm thick Al mask with arrays of 40 µm x 200 µm rectangular windows. The mask, originally designed to fabricate 16 x 100 GHz digitally wavelength-switchable V-coupled-cavity laser diodes [J. Jin*, et al.* 2012], manufactures using a standard photolithography process comprising inductive coupled plasma (ICP) etching and a lift-off process. The sample was irradiated in a KrF laser with a rectangular mask of 40 mm x 4 mm in an air environment with 200 pulses of 156 mJ/cm^2. Following the laser irradiation step, the Al film was removed by etching the sample for 5 minutes in a diluted 2.5% Tetramethylammonium hydroxide (TMAH) (Sigma-Aldrich Canada) solution. The cleaned sample was annealed for 2 min at 700 °C in a forming gas, resulting in the 15 nm blueshift of the non-irradiated material.

7.1.2 Results and discussions

Figure 7.1 shows the PL spectra of the microstructure irradiated with 75 and 100 pulses of a homogenized KrF laser beam. It can be seen that the non-irradiated material, after the RTA step, is blueshifted by about 15 nm and the PL intensity of the active region (QW) decreased by 20% in comparison to the as grown sample before RTA. However, the FWHM of the PL signal

remained unchanged at around 72 nm. The irradiation with 75 and 100 pulses leads (after RTA) to the fabrication of 76 and 81 nm blueshifted material of PL intensity almost 1.35 times greater than that of the as grown material. This result confirms that KrF laser QWI could lead to the fabrication of a high-quality material, or at least it doesn't lead to the significant deterioration of the optical properties of the QWI microstructure [M. Kaleem*, et al.* 2013].

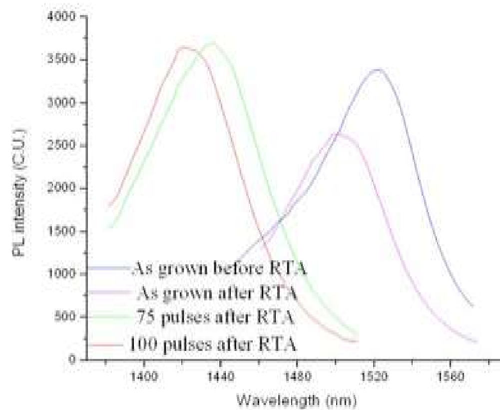

Figure 7. 1 PL spectra of as grown material, irradiated with 75 and 100 pulses by KrF laser at 153 mJ/cm^2 in air and RTA

Figure 7.2 shows the PL map of as-grown sample coated with Al mask. The emission at 1530 nm of the QW microstructure can clearly be seen from 40 µm x 200 µm windows. Note that the "1440 nm" signal is an arbitrary background corresponding to the region with the negligible PL emission.

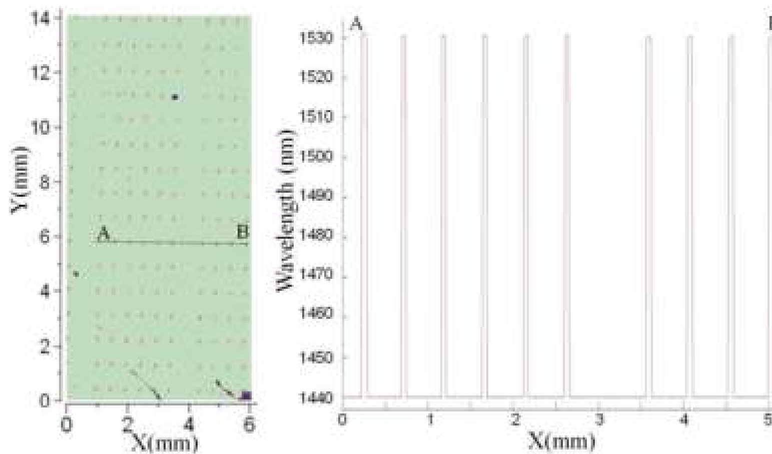

Figure 7. 2 PL map of the sample before KrF laser QWI. The "1440 nm" signal is an arbitrary background corresponding to the region with the negligible PL emission.

Figure 7.3 (left panel) shows the PL map of an array of sites from a fragment of QW sample irradiated with the KrF laser and RTA (Al mask was removed before annealing). A cross-section

scan covering a region with 5 blue shifted windows, shown in the right panel of Figure 7.3, provides more details of the processed microstructure. A uniform emission at near 1442 nm is observed from each window, while the background emits at 1515 nm. Figure 7.4 shows a high-resolution PL map of a 3-window area. The right pannel illustrates the uniformity of the QWI process, as indicated by the wavelength scans along the long (top) and short (botton) axis of one of the windows. A relatively uniform blueshift PL amplitude of 73 nm is observed inside of the window. Some PL wavelength fluctuations at the window edge are possibly caused by the limited spatial resolution of the PL mapping setup and/or by light scattering during the excimer laser irradiation. The blueshift amplitude achieved in this case is a promising result towards the fabrication of enhanced performance digitally wavelength-switchable V-coupled-cavity laser diodes [J. Jin*, et al.* 2012] or other devices taking advantage of the multibandgap wafers.

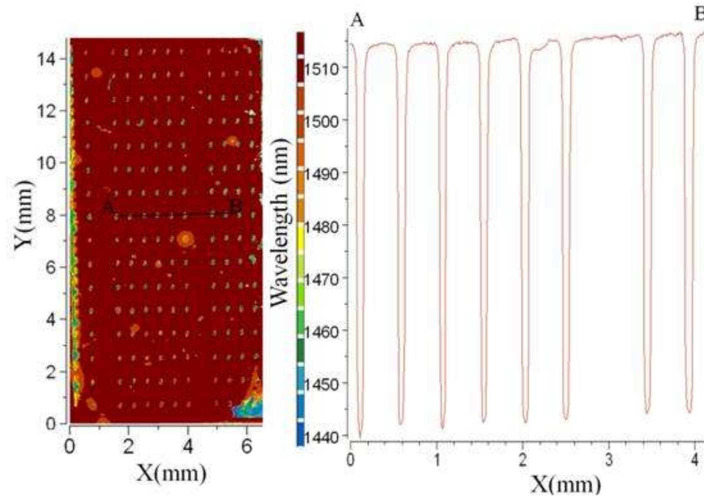

Figure 7. 3 PL map (left) and PL scanning profile (right), line from A to B, of InGaAs/InP QW microstructure after KrF laser irradiation at 156 mJ/cm^2 with 200 pulses through Al film mask with 40 µm x 200 µm windows and RTA at 700°C for 2 minutes.

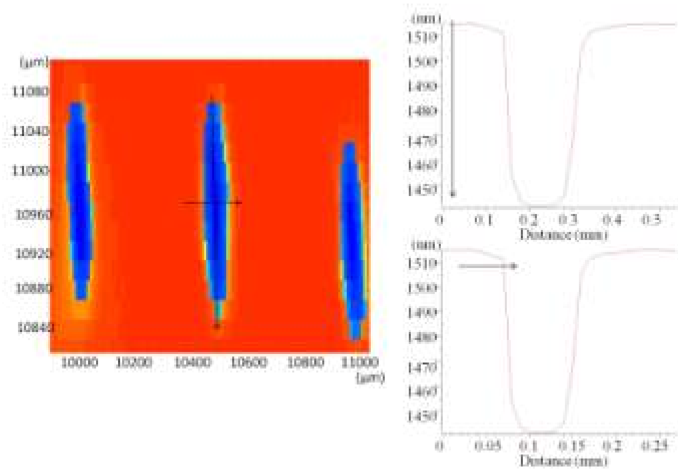

Figure 7. 4 Detailed PL map and scanning line of small windows of InGaAs/InP QW microstructure after KrF laser irradiation at 156 mJ/cm^2 with 200 pulses and RTA at 700 °C for 2 minutes

7.2 Laser diode fabricated on KrF laser intermixed material

A series of single LDs have been fabricated in KrF laser irradiated and RTA on one sample from ZJU QW microstructure. Figure 7.5 shows PL map of a sample irradiated with 75 and 150 pulses at 156 mJ/cm^2 and RTA. The background (non-irradiated) material emit at 1527 nm and 80 and 120 nm net blueshifted QWI material has been obtained following the irradiation with 75 pulses (A and B) and 150 pulses (C and D), respectively.

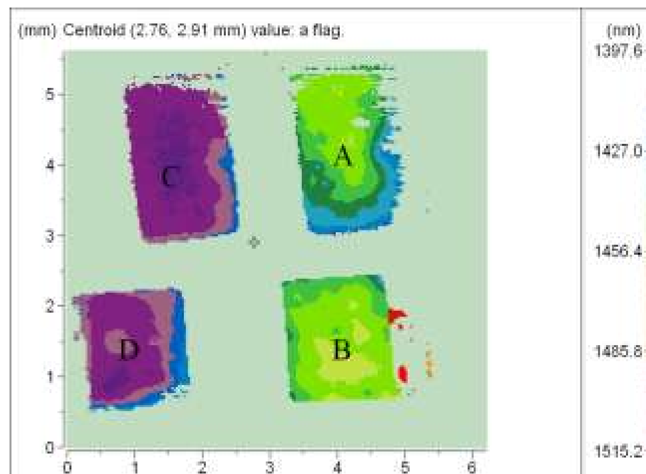

Figure 7. 5 PL map of a ZJU sample after KrF laser irradiation at 156 mJ/cm^2 and RTA. Sites A and B irradiated with 75 pulses (80 nm net blue shift) and sites C and D with 150 pulses (120 nm net blue shift).

The top 500 nm InP layer was removed by etching in HCl:H_2O=1:1 solution at the etching rate of 70 nm/min [S. Adachi, *et al.* 1982]. The fabrication of LDs was obtained following the steps listed in Table 7.1.

Table 7. 1 Laser diode fabrication steps

Steps	Description
1	PECVD deposition of a 200 nm SiO_2 layer
2	Spin coating of Shipley 1813 photo-resist
3	Photolithography of 40 µm width X 3000 µm waveguide
4	SiO_2 etch in a buffered oxide etchant solution
5	Electron beam evaporation of the front side contact layer: Cr (15 nm), Ti (30 nm), Pd (30 nm) and Au (100 nm)
6	Mechanical thinning and polishing of the samples back sides (t < 150 µm)
7	Electron beam evaporation of the back side contact layer: Au (14 nm), Ge (14 nm), Au (14 nm), Ni (11 nm) and Au (200 nm)
8	Alloy annealing (400°C, 60 seconds)

9	Laser diodes cleave and separation

The light-current density (L-J) characteristics were taken by directly shining the LDs emission onto a detector while the spectra measurements were achieved by injecting the laser signal into an optical fiber connected to an optical spectrum analyzer. Figure 7.6 (a) shows emission spectra of LDs fabricated from the KrF laser QWI material (samples 1-3), LD from as grown sample emitted at 1565 nm and non irradiated sites (RTA only) emitted at 1550 nm. The maximum shift from the intermixed LD is around 133 nm (KrF QWI 3). The spectra from the intermixed LDs also show that by varying the number of pulses, it is possible to cover a relatively large range of emission wavelengths from 1430 to 1563 nm. Figure 7.6 (b) shows the the normailized intensity vs. threshold current density of laser diodes fabricated from samples. The threshold current density of laser diodes from as-grown sample is around 1750 kA/cm^2, which is comparable to the threshold current density of laser diodes (1-2 kA/cm^2) from the references [L. V. Asryan*, et al.* 2000, N. A. Pikhtin*, et al.* 2002]. J_{th} values from the other PL shifted laser diodes do not show significant increase. The maximum J_{th} value found on the sample $\Delta\lambda$=133 nm, slightly increased by 8%. These results are comparable to the laser diodes fabricated with low energy ion implantation (≤ 20 keV) QWI on InP based QWs, which have 120 nm PL shift and the increase of threshold current up to 15% [V. Aimez*, et al.* 2002]. Therefore, the quality of the KrF laser intermixed material is comparable to non laser treated sites. The injected current vs. voltage, I-V curve, of these laser diodes are shown in Figure 7.6 (c). The resistance (R) of intermixed laser diode p-n junction fabricated from the intermixed material is greater than that from as grown and RTA-only sample. This could be related to the increased atoms diffusion in the intermixed material [N. Li*, et al.* 1999].

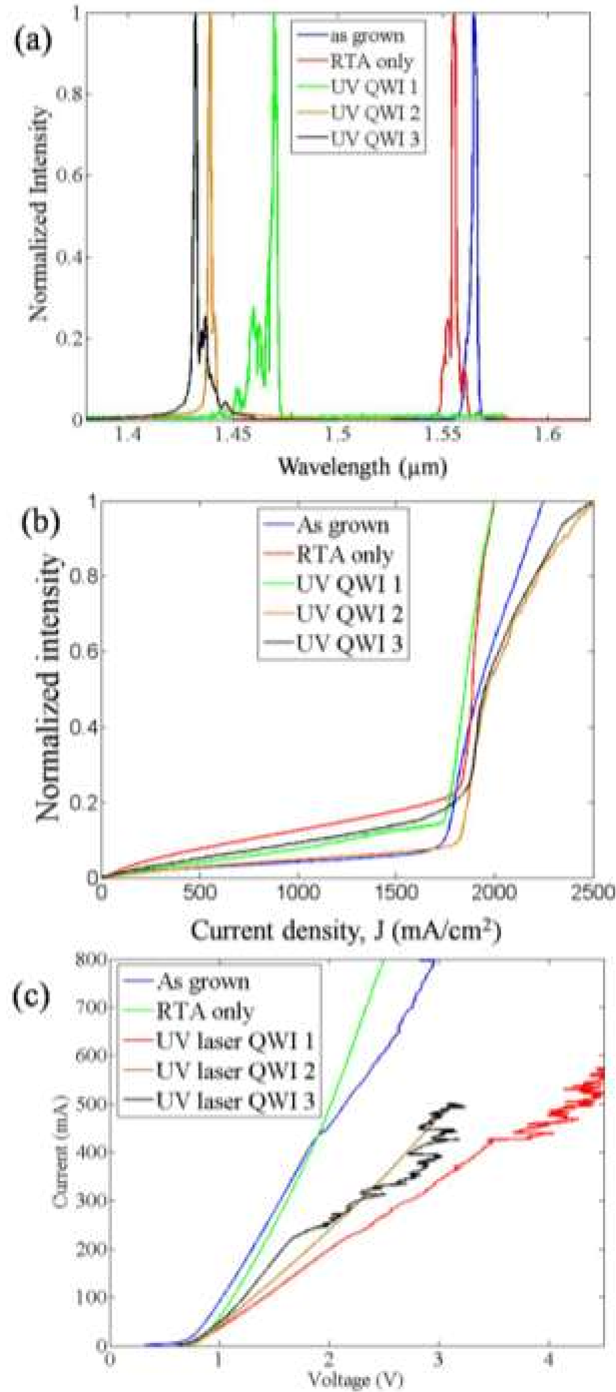

Figure 7. 6 Emission spectra (a), L-J curve (b) and I-V (c) of LD devices fabricated in the QWI (Sample 1-3) and RTA as grown sample and RTA only sample.

7.3 Summary

The KrF QWI material has been investigated for the fabrication of high-performance LDs and digitally wavelength-switchable V-coupled-cavity laser diodes [J. Jin, *et al.* 2012]. To

monolithically integrate these laser diode arrays based on the discussed new technique to use the Al film mask with 40 μm X 200 μm opening to get uniform bandgap shift (~73 nm) on samples from a full LD InGaAsP/InGaAsP/InP microstructure with one step KrF laser irradiation and RTA is more attractive. By changing the laser parameters and projection beam size on the sample, we are supposed to have different bandgap in different windows precisely and simply. However, in present PICs fabrication, ion implantation QWI is popularly used to achieve multibandgap on one wafer, which require amounts of circles of lithographical removal and annealing. The number of bandgap is limited by practical lithographic process steps [E. J. Skogen, *et al.* 2005, S. Jain, *et al.* 2011]. Also, KrF laser induced QWI on this microstructure shows no obvious degradation on this strained QW microstructure and even with PL intensity enhancement. LD fabrication and test experiment shows that the quality of intermixed material did not have significant damage, as the threshold is comparable with that fabricated on RTA only sample. Therefore, it demonstrates the KrF laser QWI with Al mask will make a breakthrough for the PICs fabrication.

7.4 Bibliography

Adachi, S., Noguchi, Y., et al., (1982), Chemical etching of InGaAsP/InP DH wafer, *Journal of the Electrochemical Society*, vol. 129, n°5, 1053-1062.

Aimez, V., Beauvais, J., et al., (2002), Low-energy ion-implantation-induced quantum-well intermixing, *IEEE Journal of Selected Topics in Quantum Electronics*, vol. 8, n°4, 870-879.

Asryan, L.V., Gun'ko, N.A., et al., (2000), Threshold characteristics of InGaAsP/InP multiple quantum well lasers, *Semiconductor Science and Technology*, vol. 15, n°12, 1131.

Jain, S., Sysak, M., et al., (2011), Integrated hybrid silicon DFB laser-EAM array using quantum well intermixing, *Optical express*, vol. 19, n°14, 13692-13699.

Jin, J., Wang, L., et al., (2012), Digital wavelength switching by thermal and carrier injection effects in V-coupled cavity semiconductor laser, *Chinese Optics Letters*, vol. 10, n°10, 102501-102501.

Kaleem, M., Zhang, X., et al., (2013), UV laser induced selective-area bandgap engineering for fabrication of InGaAsP/InP laser devices, *Optics and Laser Technology*, vol. 51, 36-42.

Li, N., Li, N., et al., (1999), Proton implantation and rapid thermal annealing effects on GaAs/AlGaAs quantum well infrared photodetectors, *Superlattices and microstructures*, vol. 26, n°5, 317-324.

Pikhtin, N.A., Sliptchenko, S.O., et al., (2002), Analysis of threshold current density and optical gain in InGaAsP quantum well lasers, *Semiconductors*, vol. 36, n°3, 344-353.

Skogen, E.J., Raring, J.W., et al., (2005), Monolithically integrated active components: a quantum-well intermixing approach, *IEEE Journal of Selected Topics in Quantum Electronics*, vol. 11, n°2, 343-355.

Chapter 8 Conclusions and perspectives

This thesis aimed at studying the origin of excimer laser induced QWI in III-V semiconductor microstructures by investigating surface/interface morphology and chemical modification of the microstructures irradiated in different environments, including air, DI water, SiO_2, Si_3N_4 and InO_x and annealed in an RTA furnace. Through these researches, we have proposed new solutions for the development of a controllable UV laser QWI process and its application for the fabrication of high quality PICs. This chapter presents a review of the major findings of the project and suggestions of future work required to address some of the questions invoked in the course of this study.

8.1 Conclusions

In order to meet the demands of PICs development, amounts of integration approaches have been developed. QWI is one of the approaches with many unique advantages: simpler and cheaper post growth procedure than regular epitaxial growth; equipments compatible with the regular semiconductor industry and, usually, it can address a selective area modification of the bandgap in a broad range on one wafer. However, QWI techniques are still not popular in the industry. Most problems are related to its relatively low reproducibility and controllability. For instance, conventional QWI techniques have been assisted by the unintentional introduction of unknown impurities during the intermixing process that could degrade the quality of the intermixed material.

The Université de Sherbrooke QS Group previous works have demonstrated that UV laser QWI is applicable to control the bandgap engineering in the InP and GaAs based QW, QD and quantum stick microstructures [J. Genest*, et al.* 2007a, J. Genest*, et al.* 2007b, J. Genest 2008, J. Genest*, et al.* 2008a]. Both increased bandgap and suppression of bandgap shifting have been observed depending on the material and laser parameters. In order to understand the role of surface chemistry of material capping QW microstructures in the QWI process, I have used both ArF and KrF lasers to irradiate InP epitaxial grown on top of selected QW microstructures. The irradiation in an atmospheric air, in DI and in other environments provided by SiO_2, Si_3N_4 and InO_x films deposited on InP, allowed to investigate the dynamics, the amplitude and the

reproducibility of the UV Laser QWI process in chapter 4, 5, 6. The analysis of processed samples was carried out with numerous spectroscopic and surface characterization techniques, including photoluminescence, XPS, SIMS, AFM, SEM and optical microscopy.

As the dielectric layers (SiO_2 and Si_3N_4) coatings are always important steps in PICs fabrication, we have coated InP/InGaAs/InGaAsP microstructure with dielectric layers of different thicknesses. In most cases, the PL shift was only found when SiO_2/Si_3N_4 layer is ablated away by ArF and KrF laser. However, the obvious PL shifts were found in an InP QW sample coated with a 243 nm (~ λ_{krF}) thick SiO_2 layer and irradiated with KrF laser without any obvious SiO_2 layer ablation. One of the causes of different surface modification during laser irradiation is that excimer laser induced temperatures depends on the cap layer thicknesses and chemistry. AFM, XPS SEM and ellipsometry results show that there is laser induced modification in the interface between InP and SiO_2 layer, see chapter 4.3 and 5.1. Indepth XPS and SIMS results show that there is no III-V atoms outdiffusion to the SiO_2 layer. Instead, the SIMS results demonstrate that O atoms diffuse from the laser altered interface layer to the QW that promotes the intermixing.

To verify the importance of laser induced oxide layer and O impurities diffusion are important in UV laser QWI, InO_x layers have been deposited before UV laser irradiation. On sample coated with InO_x layer, the interdiffusion enhancement is found on both irradiated sample and non irradiated sample after RTA, see 6.1.3. The SIMS results show that there is significant O impurity diffusion in the microstructure, which verifies the importance of O impurity in UV laser QWI.

To study the surface modification effects on QWI, a MQW microstructure with active region 76 nm below surface were mainly discussed, which is different from full laser QW microstructure (~2 µm). When irradiated in air, it always has the larger PL shift (maximum 128 nm) than irradiated in DI water (~ 60 nm). However, the PL intensity is found to be significantly enhanced (~9 times) in the sample irradiated in DI water, while the PL intensity degraded in the material irradiated in air and RTA. The XPS shows that there were more oxides in sample irradiated in air and these oxides increased with pulse number. However, on sample irradiated in DI water, there was no obvious oxides increment on irradiated sites. SIMS shows that more O

atoms from the oxide layer have diffused to the active region of sample irradiated in air than that in DI water. These O impurities enhance the intermixing and degrade the quality of QW. High coefficient of thermal expansion InO_x layer is clearly found in the interface till to active region on sample after ArF laser QWI, which is estimated to affect the compressive strain in the active region. The increment of compressive strain is supposed to enhance the PL intensity on sample irradiated in DI water. Also, fewer nonstoichemical surface defects of sample irradiated in DI water and then RTA is possible another cause of PL intensity enhancement.

In order to test the quality of excimer laser intermixed samples, I have fabricated laser diodes, with up to 120 nm PL shift. The threshold current of irradiated samples are comparable to the non irradiated samples. Also, with an Al mask, we have shown that our excimer laser QWI can create arrays of the QWI material in small windows (40 µm X 200 µm), which is an attractive approach towards the fabrication of arrays of tunable lasers.

In addition to bandgap engineering, I have found that excimer laser can be used to create self organized nanocone structures on InP (001) surface, when the laser parameters are outside of the range useful for QWI (excessive laser fluence and pulse number). The diameter, period and height of these nanocones depend on laser fluence, pulse number and laser wavelength. Due to the increased efficiency of the light extraction from QWs, the nanocone covered. InP/InGaAs/InGaAsP microstructure exhibited PL intensity increased by 1.4 times in comparison to the PL signal emitted by the as-grown material.

I have also employed the experience of excimer laser induced modification of physical and chemical properties of III-V surfaces in a test study aiming an investigation of laser induced chemical modification of bulk Si (001) that would lead to a strongly hydrophobic/hydrophilic surface with laser fluence below Si ablation threshold. The irradiation in a methanol environment leads to the formation of $Si\text{-}O\text{-}CH_3$ which results in a strongly hydrophobic surface (contact angle ~ 109°). In contrast, a super hydrophilic surface (contact angle ≤ 15°) was found when Si was irradiated in a low concentration H_2O_2 solution (≤ 0. 2%). This is mainly due to the laser induced Si-OH and Si-O, as observed by XPS. These results have been discussed in Appendix.

8. 2 Future work

A nine-fold enhancement of PL intensity in the InP/InGaAs/InGaAsP QW microstructure processed with ArF laser in DI water represents, to date, record-high enhanced PL amplitude ever observed in the QWI material. It is clear that this approach deserves further investigation. It would be interesting to investigate the performance of both passive and active devices fabricated with this technique. The UV Laser QWI technique could lead to the development of a new generation of high performance PICs obtained in a cost-attractive manner. SIMS results show the presence of oxygen and III-V atoms diffusion after ArF laser irradiation, even before RTA. This seems to be related to photo-activated process of atom diffusion or displacement. Investigation of this subject requires extensive studies that could shed more light on the problem of UV laser interaction with quantum semiconductor microstructures and excimer laser induced annealing or doping.

The results obtained in the frame of this thesis have not shown the advantage of the UV Laser QWI approach in processing of high-temperature oxide (SiO_2) or silicon-nitride (Si_3N_4) coated samples. However, laser irradiation of InO_x coated samples has produced potentially attractive results. A more precise model should be built that would take inot account both the surface presence on InO_x and InO_x distribution inside InP/InGaAs/InGaAsP QW microstructures. The influence of InO_x deposited and/or formed as a result of excimer laser irradiation should be discussed on example of other InP based QW passive and active devices. This theoretical model should be investigated/verified for GaAs based QW devices that have been reported to have enhanced PL intensity after KrF laser induced intermixing.

The excimer laser irradiation of III-V semiconductor surfaces in liquid environments, other than DI water, has been suggested as another interesting subject relevant to the problem of increased blueshifting amplitudes obtained in an impurity-free environment.

8.3 Bibliography

Genest, J., Dubowski, J., et al., (2007), Suppressed intermixing in InAlGaAs/AlGaAs/GaAs and AlGaAs/GaAs quantum well heterostructures irradiated with a KrF excimer laser, *Applied Physics A: Materials Science & Processing*, vol. 89, n°2, 423-426.

Genest, J., Dubowski, J., et al., (2007), UV laser controlled quantum well intermixing in InAlGaAs/GaAs heterostructures, *Journal of Physics: Conference Series*, vol. 59, 605-609.

Genest, J.: 'Interdiffusion de puits Quantiques controllee par irradiation laser excimere pour l'intergration de compasants photoniques'. Doctor Thesis, University of Sherbrooke,Department of Electrical and Computer Engineering 2008

Genest, J., Beal, R., et al., (2008), ArF laser-based quantum well intermixing in InGaAs/InGaAsP heterostructures, *Applied Physics Letters*, vol. 93, 071106.

Chapitre 8 Conclusions et perspectives

Cette thèse vise à étudier l'origine de l'interdiffusion de puits quantiques (QWI) induite par laser excimer dans des microstructures de semi-conducteurs III-V en étudiant la morphologie de la surface/interface et la modification chimique des microstructures irradiées dans des différents environnements, y compris l'air, l'eau déionisée (DI), SiO_2, Si_3N_4 et InO_x et recuites dans un four RTA. Grâce à ces recherches, nous avons proposé de nouvelles solutions pour le développement d'un processus contrôlable de QWI par laser UV et de son application pour la fabrication des circuits photoniques intégrés (PICs) de haute qualité. Ce chapitre présente une revue des principaux résultats du projet et des suggestions de travaux futurs nécessaires pour répondre à certaines des questions invoquées dans le cadre de cette étude.

8.1 Conclusions

Afin de répondre aux exigences de développement des circuits photoniques intégrés, plusieurs approches d'intégration ont été développées. QWI est l'une des approches avec de nombreux avantages uniques : le processus de post-épitaxie est plus simple et moins cher que l'épitaxie standard ; les équipements sont compatibles avec l'industrie régulière de semi-conducteurs et, en général, cette technique peut répondre à une modification sélective d'une zone de la bande interdite dans un large domaine sur une gaufre. Cependant, les techniques de QWI ne sont toujours pas populaires dans l'industrie. La plupart des problèmes sont liés à sa faible reproductibilité et contrôlabilité. Par exemple, les techniques classiques de QWI ont été contaminées par l'introduction involontaire d'impuretés inconnues pendant le processus de l'interdiffusion qui pourraient dégrader la qualité de la matière interdiffusée.

Les travaux antérieurs du Groupe QS de l'Université de Sherbrooke ont démontré que la technique QWI par laser UV est applicable à contrôler l'ingénierie de la bande interdite dans des puits quantiques (QW), des points quantiques (QD) et des microstructures de bâtonnets quantiques à base de InP et GaAs, [J Genest, et al. 2007, J. Genest, et al. 2008]. Les deux effets, l'augmentation et la suppression du déplacement de la bande interdite ont été observés en fonction des paramètres du matériau et du laser. Afin de comprendre le rôle de la chimie de surface du matériau de recouvrement des microstructures QW dans le processus du QWI, j'ai

utilisé deux lasers ArF et KrF pour irradier l'InP épitaxié au-dessus des microstructures de QW sélectionnés. L'irradiation dans l'air atmosphérique, l'eau déionisée (DI) et dans d'autres environnements sous forme de couches de SiO_2, Si_3N_4 et InO_x déposés sur InP, a permis d'étudier la dynamique, l'amplitude et la reproductibilité du processus du QWI par laser UV dans les chapitres 4, 5 et 6. L'analyse des échantillons traités a été effectuée avec de nombreuses techniques de caractérisation spectroscopiques et de surface, y compris la photoluminescence, XPS, SIMS, AFM, SEM et la microscopie optique.

Comme le revêtement ou le dépôt des couches diélectriques (SiO_2 et Si_3N_4) est toujours une étape importante dans la fabrication des PICs, nous avons recouvert les microstructures InP/InGaAs/InGaAsP par des couches diélectriques de différentes épaisseurs. Dans la plupart des cas, le déplacement de la PL n'a été mesuré que lorsque la couche SiO_2/Si_3N_4 est enlevée par le laser (ArF ou KrF). Cependant, des décalages évidents de PL ont été obtenus sur un échantillon InP QW revêtu d'une couche de SiO_2 d'épaisseur 243 nm ($\sim \lambda_{KrF}$) et irradiée par le laser KrF sans l'ablation de la couche de SiO_2. L'une des causes de différente modification de surface pendant l'irradiation au laser est que les températures induites par les lasers excimer dépendent des épaisseurs de la couche de couverture et de la chimie de surface. Les résultats d'AFM, XPS, SEM et d'ellipsométrie montrent qu'il existe une modification induite par laser dans l'interface entre InP et la couche de SiO_2 (voir chapitre 4.3 et 5.1). Les résultats de XPS et SIMS montrent qu'il n'y a pas de diffusion d'atomes III-V de l'hétérostructure vers la couche de SiO_2. Plutôt, les résultats de SIMS montrent que des atomes d'O diffusent à partir de la couche d'interface modifiée par le laser vers le QW qui favorise l'interdiffusion.

Pour vérifier l'importance de la couche d'oxyde induite par laser et le rôle important de la diffusion des impuretés d'O dans le QWI, des couches d'InO_x ont été déposés avant l'irradiation par laser UV. Sur l'échantillon recouvert d'une couche d'InO_x, l'augmentation de l'interdiffusion s'est révélée à la fois sur l'échantillon irradié et sur celui non irradié après RTA (voir 6.1.3). Les résultats de SIMS montrent aussi qu'il existe de la diffusion des 'impuretés significatives d'O dans la microstructure, ce qui confirme l'importance de l'impureté d'O durant le processus de QWI par laser UV.

Pour étudier les effets de modification de surface sur QWI, juste une microstructure de MQW avec une région active à 76 nm sous la surface qui était principalement interprété, ce qui est différent par rapport à toute la microstructure laser à QW (~ 2 μm). Lorsqu'elle est irradiée dans l'air, elle avait toujours le plus grand décalage de PL (maximum 128 nm) par rapport à l'irradiation dans l'eau DI (~ 60 nm). Cependant, l'intensité de la PL se trouvait être augmentée de manière significative (~ 9 fois) dans l'échantillon irradié dans l'eau DI, tandis que cette intensité s'est dégradée dans la matière irradiée dans l'air et après l'étape de RTA. La mesure de XPS montre qu'il y avait plusieurs oxydes dans l'échantillon irradié dans l'air qui se sont intensifiés en fonction du nombre des pulses. Cependant, sur échantillon irradié dans l'eau DI, il n'y avait pas d'évident accroissement d'oxydes sur les sites irradiés. Les résultats de SIMS ont montré que plusieurs atomes d'O ont diffusé à partir de la couche d'oxyde vers la région active de l'échantillon irradié dans l'air par rapport à l'eau DI. Ces impuretés d'O améliorent l'interdiffusion et dégradent la qualité du QW. Un coefficient de dilatation thermique élevé de la couche InO_x a été clairement identifié dans l'interface jusqu'à la zone active de l'échantillon après l'interdiffusion par ArF laser, ce qui est prévu affecter la déformation compressive dans la région active. L'accroissement de cette déformation est censé augmenter l'intensité de la PL sur l'échantillon irradié dans l'eau DI. En outre, les quelques défauts non-stœchiométriques de surface de l'échantillon irradié dans de l'eau DI et traité par RTA, peuvent être une autre cause possible de l'augmentation de l'intensité de la PL.

Afin de tester la qualité des échantillons interdiffusés par le laser excimer, j'ai fabriqué des diodes laser, avec un maximum de 120 nm de décalage de la PL. Le courant de seuil des échantillons irradiés est comparable à celui des échantillons non irradiés. En outre, avec un masque d'Al, nous avons montré que notre technique de QWI par laser excimer peut créer des matrices de matière interdiffusée dans de petites fenêtres (40 μm x 200 μm), ce qui est une approche intéressante pour la fabrication de réseaux de lasers accordables.

En plus de l'ingénierie de la bande interdite, j'ai constaté que le laser excimer peut être utilisé pour créer des structures de nano-cône organisées sur des surfaces d'InP (001), lorsque les paramètres du laser sont en dehors de la plage utile pour QWI (quand la fluence de laser et le nombre d'impulsions sont excessifs). Le diamètre, la période et la hauteur de ces nano-cônes

dépendent de la fluence de laser, de nombre d'impulsions et de la longueur d'onde du laser. En raison de l'efficacité accrue de l'extraction de la lumière des QW, les nano-cônes couvrent la microstructure InP/InGaAs/InGaAsP dont l'intensité de la PL a augmenté de 1.4 fois par rapport à celle émise par le matériau non-interdiffusé.

J'ai aussi utilisé l'effet induit par laser excimer pour la modification des propriétés physiques et chimiques des surfaces III-V dans une étude d'essai visant l'investigation de la modification chimique induite par laser de Si (001) qui mènerait à une surface fortement hydrophobe/hydrophile avec une fluence du laser au-dessous du seuil d'ablation de Si. L'irradiation dans un environnement de méthanol conduit à la formation de liaisons Si-O-CH_3 ce qui se traduit par une surface fortement hydrophobe (angle de contact ~109°). En revanche, une surface super-hydrophile (angle de contact ≤ 15°) a été trouvée lorsque la surface de Si a été irradiée dans une solution à faible concentration de H_2O_2 (≤ 0.2%). Ceci est principalement dû au Si-OH et Si-O induite par laser, comme observé par XPS. Ces résultats ont été discutés dans l'Annexe.

8.2 Les travaux futurs

L'augmentation de l'intensité PL de 9 fois dans la microstructure InP/InGaAs/ InGaAsP QW iradiée par le laser ArF dans l'eau DI représente, à ce jour, un grand record d'augmentation d'amplitude de PL jamais observé dans un matériel QWI. Il est clair que cette approche mérite d'être étudiée. Il serait intéressant d'étudier la performance des deux dispositifs passifs et actifs fabriqués avec cette méthode. La technique UV laser QWI pourrait mener au développement d'une nouvelle génération de PICs de haute performance obtenus d'une manière économique et attrayante. Les résultats SIMS montrent la présence d'oxygène et la diffusion des atomes III-V après l'irradiation par le laser ArF, avant même le processus de RTA. Cela semble être en rapport avec le procédé de la photo-activation de diffusion des atomes ou de déplacement. L'investigation sur ce sujet nécessite des études approfondies qui pourraient éclaircir et jeter plus de lumière sur le problème de l'interaction laser UV avec les microstructures de semi-conducteurs quantiques et le recuit par laser excimer ou le dopage induit.

Les résultats obtenus dans le cadre de cette thèse n'ont pas démontré l'avantage de l'approche UV laser QWI pour le traitement à haute température des échantillons enrobés d'oxyde (SiO_2) ou de nitrure de silicium (Si_3N_4). Cependant, l'irradiation par laser des échantillons revêtus d'InO_x a produit des résultats potentiellement intéressants. Un modèle plus précis devrait être conçuen tenant en considération la présence à la fois d'InO_x sur la surface et de la distribution d'InO_x à l'intérieure de la microstructure de QW InP/InGaAs/InGaAsP. L'influence de la couche d'InO_x déposée et/ou formée à la suite de l'irradiation par laser excimer devrait être discutée comme un exemple par rapport aux autres dispositifs passifs et actifs à base de QW sur InP. Ce modèle théorique doit être étudié/vérifié pour des dispositifs à base de QW sur de GaAs qui ont été rapportés d'avoir une meilleure intensité PL après l'interdiffusion induite par le laser KrF.

L'irradiation par laser excimer de surfaces de semi-conducteurs III-V dans des environnements liquides, autres que l'eau DI, a été suggérée comme un autre sujet intéressant en rapport avec le problème de l'augmentation des amplitudes de décalage « blue-shifting » de PL, obtenus dans un environnement exempt d'impuretés.

8.3 Bibliographie

Genest, J., Dubowski, J., et al., (2007), Suppressed intermixing in InAlGaAs/AlGaAs/GaAs and AlGaAs/GaAs quantum well heterostructures irradiated with a KrF excimer laser, *Applied Physics A: Materials Science & Processing*, vol. 89, n°2, 423-426.

Genest, J., Dubowski, J., et al., (2007), UV laser controlled quantum well intermixing in InAlGaAs/GaAs heterostructures, *Journal of Physics: Conference Series*, vol. 59, 605-609.

Genest, J.: 'Interdiffusion de puits Quantiques controllee par irradiation laser excimere pour l'intergration de compasants photoniques'. Doctor Thesis, University of Sherbrooke,Department of Electrical and Computer Engineering 2008

Genest, J., Beal, R., et al., (2008), ArF laser-based quantum well intermixing in InGaAs/InGaAsP heterostructures, *Applied Physics Letters*, vol. 93, 071106.

Appendix: Study of excimer laser control Si wettability in different aqueous environments

In this chapter, I will present excimer laser induced Si wettability modification in different aqueous environments. Firstly, the theory background of Si wettability and its application in biofunctionization, and the contact angle (CA) measurement were presented. Then, KrF and ArF lasers were used to induce a superhydrophilic surface by irradiation in low concentration H_2O_2 solution. Fluorescence nanospheres were successfully selective area functionized on laser patterned surface. These results were presented in the manuscript '*Selective area in situ conversion of Si (001) hydrophobic to hydrophilic surface by excimer laser irradiation in hydrogen peroxide*' (submitted to Journal of Physics D). In the ending part, I present excimer laser induced hydrophobic Si surface by irradiation in methanol solution. The results were presented in manuscript 'Excimer laser assisted chemical process for formation of hydrophobic surface of Si (001)' (Applied Physic A, published on line, DOI: 10.1007/s00339-014-8380-9).

A.1 Si wettability and bionfunctionization

The degree of wettability Si is always determined by a force balance between adhesive and cohesive forces, presented by CA, which provides an inverse measure of wettability. CA is the angle at which the liquid–vapor interface meets the solid–liquid interface. For water, a drop with larger CA is hydrophobic, which is exemplified by poor wetting, poor adhesiveness and low surface energy. A drop with a small CA is hydrophilic, which reflects better wetting, better adhesiveness and higher surface energy. For an ideal rigid flat surface, which is perfectly smooth, chemically homogeneous, CA is dependent on surface energy between interfaces, as equation [R. N. Wenzel 1949] :

$$\gamma_{SG} = \gamma_{SL} + \gamma_{LG} cos\theta \quad \text{(A-1)}$$

where γ_{SG} is the surface energy between solid and gas, γ_{SL} is the surface energy between solid and liquid, and γ_{LG} is the surface energy between liquid and gas. This is similar as Young's equation and CA is called Young's CA [G. Whyman, *et al.* 2008]. Unlike flat surface, the rough surface textures are classified into two categories: homogeneous or heterogeneous. A

homogeneous wetting regime is where the liquid fills in the rough grooves of a surface. A heterogeneous wetting regime is where the air fills the rough grooves of a surface [A. Marmur 2003]. Figure A.1 gives the schematic illustration of rigid flat surface (A), homogeneous (B) and heterogeneous (C) wetting regime. Wenzel and Cassie–Baxter are the two main models that attempt to describe the homogeneous and heterogeneous wetting of textured surfaces, respectively [G. Whyman, *et al.* 2008].

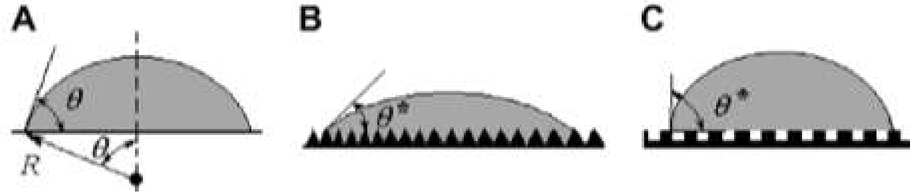

Figure A. 1 Schemes of different wetting regimes, (A) flat rigid surface (B) homogeneous wetting regime (C) heterogeneous wetting regime [G. Whyman, *et al.* 2008].

The equation of Wenzel model is [G. Whyman, *et al.* 2008]:

$$cos\theta_W = r * cos\theta \quad \text{(A-2)}$$

where θ is Young's CA, θ_W is Wenzel CA on the real rough surface, and r is roughness ratio which is the ratio of true area of the surface to the nominal surface, always >1. So this means when the surface is hydrophobic ($\theta \geq \pi/2$), the homogeneous roughness increases CA.

The equation of the Cassie–Baxter mode is [G. Whyman, *et al.* 2008]:

$$cos\theta_{CB} = r_f \text{ x } f \text{ x } cos\theta + f \quad \text{(A-3)}$$

where θ_{CB} is Cassie-Baxter CA on the real rough surface, r_f is roughness ratio of the wet area and f is fraction of solid surface area wet by the liquid. It seems that the Cassie-Baxter can also increase CA when the surface is hydrophobic but with a different rate with Wenzel model.

Figure A.2 (b) shows the SEM image of lotus leave indicating the water expelling effect on lotus leave, as shown in Figure A.2 (a), is due to the nature surface nanostructure. As we discussed before, Fs laser can generate similar nanostructure on Si surface, as shown in SEM image of Figure A.2 (c) by controlling the laser parameters and induce a superhydrophobic (CA ≥ 150°) Si surface, as shown in Figure A.2 (d) [T. O. Yoon, *et al.* 2008a]. Therefore, laser induced specific texturing surface can induce a superhydrophobic surface, for the applications such as self-cleaning surfaces, biological scaffolds, microfluidics, and lab-on-chip devices.

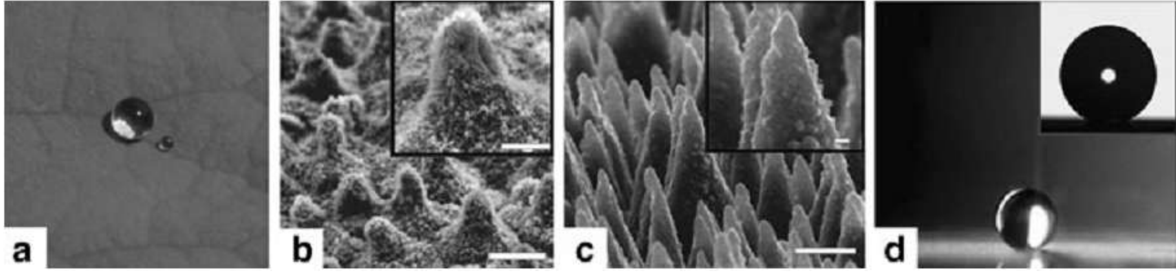

Figure A. 2 (a) a bead of water on lotus leave (b) SEM image of microscale (scale bar 10μm) on the surface of a lotus leaf, (c) SEM images of femto second laser textured Si surface showing microscale (scale bar 5 μm) structures.(d) Image of a water droplet on a laser-structured, silane-coated, Si surface with a static CA θ=154° [T. O. Yoon*, et al.* 2008a].

The remarkable electronic properties and high mechanical strength have made Si as an ideal choice for microchips, especially biochips. In addition, Si is commonly used as packaging material for biosensors. So, Si based biosensors have undergo tremendous development [A. Ranella*, et al.* 2010b, A. Vorobyev*, et al.* 2010]. However, as the Si surface bioactivity and biocompatibility is very poor, Si based biosensors always suffer problems associated with undesirable interaction between Si based biosensors and bimolecular [Y. Niu*, et al.* 2007]. It has been identified as a major long term hurdle for the Si based biosensor development [X. Liu*, et al.* 2007]. Also, to further develop biosensor chips, for instance microfluidic biochips, it critically requires to specific area increase Si biocompatibility, control adsorption and non specific bind biomelecules as well as precisely pattern functional biomaterials on Si [C. G. K. Malek 2006]. The bioactivity and biocompatibility of biosensor depends on the surface chemistry, surface morphology and wettability of Si substrate [Y. Niu*, et al.* 2007]. To control the wettability is always more important and direct to test the quality of biocompatibility, especially in microfluidic biochips. Figure A.3 (a) and (b) shows the SEM images of cones prepared by laser irradiation with different laser fluences. Figure A.3 (c) and (d) shows the attached cell per area (d) decrease as CA increases due to laser created surface nanocone structures, which means this cell attachment is more favorable on hydrophilic surface [A. Ranella*, et al.* 2010b].

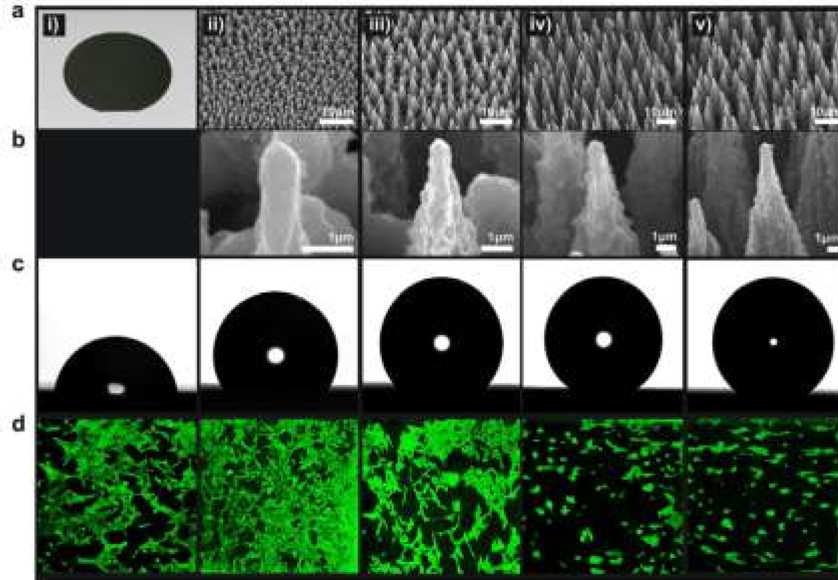

Figure A. 3 (a) SEM image of Si wafer i) and cones prepared on Si wafer at four different laser fluencies (b) high magnification SEM image of Si cones (c) image of CA on respective Si surface (d) microscopy images of cells functionalized after three days on respective Si surface [A. Ranella, *et al.* 2010b].

In the semiconductor fabrication industry, several different physical and chemical patterning approaches have been employed for structuring surfaces and tailoring their wettability, including photolithography [D. Oner, *et al.* 2000], template electrochemical deposition [P. N. Bartlett, *et al.* 2002], plasma treatments [I. Woodward, *et al.* 2003], electron-beam lithography [E. Martines, *et al.* 2005], and selective growth of carbon nanotubes [K. K. S. Lau, *et al.* 2003]. Recently, various laser techniques have been used to fabricate specific micro/nano surface structures to create superhydrophobic Si surface, as shown in Figure A.2 and Figure A.3. On the other hand, scientists have reported to induce a new special microgroove pattern to make the Si wettable and superwicking with Fs laser depending on the capillary effect [A. Vorobyev, *et al.* 2010]. Compared with other techniques, laser techniques demonstrate their advantages in simple step but with reproducible and efficient results. Other techniques always need either complicated multistep patterning procedures and materials or strict reactive conditions, especially for making wettability gradient on one sample [V. Zorba, *et al.* 2006a, C. Sun, *et al.* 2008, A. Vorobyev, *et al.* 2010]. However, as the high ablation threshold (~1 J/cm^2) of Si wafer during laser irradiation, the laser etching process always requires high power laser or special or toxic gas environments (e.g. SF_6).

Besides texturing surface, hydrophobic Si surface is obtained by Si-H, Si-CH_x or Si-F groups, while the hydrophilicity is caused by singular and associated OH groups on the surface [M. Grundner*, et al.* 1986b]. So, different sorts or concentration of materials with low surface free energy such as fluoroalkylsilane, siloxane, and chlorosilane have been chosen to modify surfaces for creating hydrophobic surface [T. Kajiyama*, et al.* 1996, S. Suzuki*, et al.* 2004]. However, to selective area control the wettability of Si, it always requires complex patterning steps with these chemical solution treatment. Therefore, scientists have tried to use various standard microfabrication methods to create chemical monolayer on Si substrate to modify the hydrophilicity/hydrophobility. Multistep patterned a-Si:H or hydrogenated amorphous Si suboxides (a-SiO_x:H) films were deposited by plasma enhanced chemical vapor deposition (PECVD) on Si for selective area cell adhesion [C. Dahmen*, et al.* 2003]. As UV laser has higher chemical activity, it has also been used to anneal or react with organic/inorganic film which has been deposited on Si in different chemical steps [X.-M. Li*, et al.* 2007]. The general process of UV irradiation induced reversibly switchable wettability Si surface always includes complicated steps: pattern pillars on predeposited SU-8 photoresist on Si using photolithography; deposit TiO_x nanorodes whose wettability is switchable during UV laser irradiation [G. Caputo*, et al.* 2009]. It will be more attractive if we can simply and directly modify Si surface chemical bonds by UV laser irradiation in different environments, e.g. liquid environments, to obtain the switchable wettability.

A.2 Contact angle measurement

CA can be measured by producing a drop of liquid on a solid, looking at the profile of the drop and measuring two-dimensionally the angle formed between the solid and the drop profile with the vertex at the three-phase line. Up to now, various measurement methods have been developed, including static sessile drop method, tilting plate method, time-dependant dynamic method and Wilhelmy plate method. Among these, static sessile drop method is simple but most widely used measurements, as shown in Figure A.4. In this method, the drop is deposited by a syringe pointed vertically down onto the sample surface, and a high resolution camera captures the image, which can then be analyzed either by eye or using image analysis software. The size

of the drop can be increased gradually and proportionally, so CA remains congruent. By taking pictures incrementally as the drop grows, the user can acquire a set of data to get a good average.

Figure A. 4 Schematic of ramé-hart contact angle goniometer used to measure CA

In this project, static CA measurement was operated on a goniometer (Rame-Hart NRL, Model 100) at room temperature and ambient humidity. The profile images of the sessile water drop on the samples were captured by CCD camera (Logitech). Four different and independent measurements were performed on the sites irradiated with same conditions. Drop image for analysis was processed by VP-eye 6.0 software (MMedia) on PC and CA was determined by drop analysis plugins of public ImageJ software.

A.3 Selective area in situ conversion of Si (001) hydrophobic to hydrophilic surface by excimer laser irradiation in hydrogen peroxide

Neng Liu, Xiaohuan Huang and Jan J. Dubowski

A.3.1 Abstract

We report on a method of a rapid conversion of hydrophobic to hydrophilic state of Si (001) surface irradiated with a relatively low number of pulses of an excimer laser. Hydrophilic Si (001), characterized by the surface contact angle (CA) of near 15°, has been fabricated following irradiation with either KrF or ArF excimer lasers of hydrophobic samples (CA ~75°) immersed in a 0.01% H_2O_2/H_2O solution. The chemical and structural analysis carried with X-ray

photoelectron spectroscopy and atomic force microscopy measurements confirmed the formation of OH-terminated Si (001) surface with no detectable change in the surface morphology of the laser-irradiated material. To investigate the efficiency of this laser-induced hydrophilization process, we demonstrate a selective area immobilization of biotin-conjugated fluorescein stained nanospheres outside of the laser-irradiated area. The results demonstrate the potential of the method for the fabrication of biosensing architectures and advancements of the Si-based microfluidic device technology.

Keywords: silicon, surface wettability, laser-surface interaction, selective area processing, X-ray photoelectron spectroscopy

A.3.2 Introduction

The remarkable electronic properties and high mechanical strength have made silicon (Si) an attractive choice for applications involving microfluidic technology and biochip fabrication [Y. Guo, *et al.* , X. M. Li, *et al.* 2007]. The wettability of Si in such applications is one of the key parameters important to control attachment and/or displacement of molecules [S. Daniel, *et al.* 2001, P. Bayiati, *et al.* 2007]. Typically, strongly hydrophobic surfaces have been obtained by modification of Si surface morphology involving nanostructures fabrication [X. M. Li, *et al.* 2007, S. J. Cho, *et al.* 2011], while hydrophilic surfaces have been obtained by modification of Si both surface roughness and chemistry [C. Sun, *et al.* 2008]. The structuring to produce a variety of wetting-controlled microstructures on the Si surface includes photolithography [T. N. Krupenkin, *et al.* 2004], ion-beam lithography [E. Martines, *et al.* 2005] and laser techniques [T. Baldacchini, *et al.* 2006, A. Ranella, *et al.* 2010]. In comparison to conventional techniques, laser surface micro/nanostructuring is a direct (mask-free) approach. Thus, it has the potential to offer design flexibility as well as economically attractive solutions [V. Zorba, *et al.* 2006b]. However, as Si has a relatively high texturing threshold of ~ 500 mJ/cm^2 [R. Tsu, *et al.* 1991], the low-damage micro/nanostructuring of this material requires the assistance of reactive gases, such as SF_6 [V. Zorba, *et al.* 2006a, C. Sun, *et al.* 2008, A. Ranella, *et al.* 2010]. Numerous works addressing wettability of Si have employed lasers to induce or assist modification of the Si surface chemical composition by depositing organic or metal oxide films on the surface before laser irradiation . For instance, a UV laser has been successfully applied to irradiate TiO_2 coated Si and generate oxygen vacancies with affinity to water, resulting in the surface CA of near 10°

[G. Caputo, *et al.* 2008]. It is known that hydrophilicity of Si originating from the presence of singular and associated OH groups on its surface could be obtained by boiling it in an H_2O_2 solution at 100 °C for several minutes [J. Bal, *et al.* 2010a]. In contrast, the hydrophobic Si surface state, mainly characterized by Si-H or Si-O-CH_3 groups, could be obtained by wet chemical treatment involving HF acid or photoresists [M. Grundner, *et al.* 1986, J. Bal, *et al.* 2010a, J. Bal, *et al.* 2010b]. UV lasers have also been used to induce chemical or thermal dissociation and adsorption of different gases (methanol, water vapor, etc.) on the Si surface [B. G. Koehler, *et al.* 1989, K. Tanaka, *et al.* 1993]. However, a limited volume of work has been devoted to the study of the chemical modification of the Si surface in the context of surface wettability of this material. XPS measurements have shown that both C/Si and O/Si ratios of an air exposed Si (100) decrease after KrF laser irradiation in air, illustrating the so called 'laser cleaning effect' [R. Tsu, *et al.* 1991]. At the same time, as the C content decreased with the pulse number, CA was found decreasing from 75° to near 52°, similarly to the effect of coating Si with thermal oxide [R. Tsu, *et al.* 1991]. In our previous work, UV laser was successfully used to modify surface chemical composition of GaAs, InGaAs and InP irradiated in air [J. J. Dubowski, *et al.* 1999, J. Genest, *et al.* 2007, J. Genest, *et al.* 2008] and NH_3 [J. M. Wrobel, *et al.* 1998]. We found that UV laser irradiation of in deionized (DI) water reduces the presence of surface oxides and carbides, while it enhances adsorption of water on the surface of a semiconductor [N. Liu, *et al.* 2013b]. Following these observations, we have employed an ArF laser for the irradiation of Si samples immersed in methanol and we have demonstrated the formation of strongly hydrophobic surfaces (CA~103°), primarily due to the ability of the ArF laser to induce photodissociation of CH_3OH [N. Liu, *et al.* 2014].

Here, we report on the KrF and ArF excimer laser induced modification of the hydrophobic state of Si (001) samples immersed in a low concentration of H_2O_2 solution with the purpose of selective area formation of a strongly hydrophilic surface.

A.3.3 Experimental

One-side polished, 3 inch diameter, 380 μm thick n-type (P-doped) Si (100) wafers (resistivity 3.1~4.8 Ωm) were employed in this study. Small coupons of 12 mm x 6 mm were cleaved from the wafer. The coupons were first cleaned with Opticlear, Acetone and isopropyl

alcohol, each for 5 minutes, then they were lightly etched in a diluted 1:50 HF (48%) (Anachemia Science) solution for 1 minute to remove the native oxide [K. Mizuno, *et al.* 1991]. Following the etching step, the samples were rinsed with DI water and dried with high-purity (99.999%) nitrogen. The samples were placed in a 0.74 mm tall chamber that was sealed with a fused silica window transmitting more than 90% of UV radiation. The chamber was filled with water diluted H_2O_2 (Fisher Scientific) in the range of 0.01 - 0.2 %. The samples were irradiated with KrF (λ=248 nm) and ArF (λ=193 nm) lasers (Lumonics, Pulse master 800) operating at 2 Hz. For each laser pulse fluence, only 2 sites were irradiated on each coupon with 100/200, 300/400, or with 500/600 pulses. A double micro-lens fly-eye-array homogenized laser beam was used to project circular and "maple leaf" masks on the sample surface at the demagnification ratio of 1.8. With a computer controlled X-Y-Z-Theta positioning of the sample, the whole beam shaping and delivery setup (MBX JPSA Sercel, Manchester, NH) allowed for precise changing of the sample position and carrying out irradiation of numerous sites. Following the laser irradiation, samples were rinsed with DI water, dried with nitrogen and installed in a sealed nitrogen container to limit their exposure to an atmospheric environment before further surface characterization experiments.

Static CA measurements were carried out with a goniometer (Rame-Hart NRL, Model 100) at room temperature and ambient humidity, as we discussed in A.2. Excimer laser induced surface chemical modification was investigated with a $1x10^{-9}$ Torr base pressure XPS spectrometer (Kratos Analytical, AXIS Ultra DLD) equipped with an Al Kα source operating at 150 W. Two Lorentzian asymmetric line shape peaks were applied to Si 2p, including Si 2p 3/2 and Si 2p 1/2 spin states with equal FWHM. The area ratio and energy separation of Si 2p 1/2 to Si 2p 3/2 was taken as 0.5 and 0.61 eV, respectively [P. J. Grunthaner, *et al.* 1987a]. FTIR data were collected with a Bruker Optics Vertex80 spectrometer operating under ambient conditions. The signal was collected and focused on a liquid N_2 cooled HgCdTe broadband detector with a resolution of 4 cm^{-1}. The analyzed area was approximately 3 mm in diameter.

Upon irradiation through a "maple leaf" mask and washing with DI water, the samples were immersed for 2 hours in a pH 7.4 phosphate buffered saline (PBS, 1X) solution (Sigma, Canada) of biotin-conjugated and fluorescein stained 40-nm-diameter nanospheres (Invitrogen, Burlington, Canada). This step was followed by washing the sample with PBS to remove

nanospheres weakly bound to the surface. The laser fabricated hydrophilic surface of Si was expected to prevent the nanospheres from immobilization, as the biotin protein is hydrophobic in nature [J. L. Swift*, et al.* 2008]. The fluorescence was excited with a blue light source emitting between 450 and 490 nm. The fluorescent images were observed at 515 nm using a fluorescence inverted microscope (Olympus, IX71) equipped with a DP71 digital camera. Surface morphology of samples, after laser irradiation and functionalized with biotin-conjugated nanospheres, was imaged with AFM (Digital Instrument, Nanoscope III) operating in a tapping mode. The AFM images were collected over the 5 μm x 5 μm region with 512 points per line at a rate of 1.97 Hz, allowing for high accuracy roughness measurement and surface morphology imaging [N. Liu*, et al.* 2012a].

A.3.4 Results and discussions

A.3.4.1 CA measurements

Figure A.5 demonstrates the CA dependence on pulse number for sites irradiated in DI water and 0.01, 0.02, 0.05 and 0.2% H_2O_2 solutions using a KrF laser at 250 mJ/cm^2. The insets show examples of profile images of water drops on (a) non-irradiated sample (CA=75°) and on (b) sites irradiated with 200 pulses (CA=38°) and (c) 500 pulses (CA=15°) of samples immersed in the 0.01 % H_2O_2 solution. We can see that the CA decreases as the pulse number increases for all the H_2O_2 solutions. The CA for 0.02 and 0.01% H_2O_2 solutions, decreased to 15° at 500 pulses. Somewhat greater CA has been observed for 0.05 and 0.2 % H_2O_2 solutions. At the same time, CA of the non-irradiated material (N = 0) decreased from 75° to 43° as the H_2O_2 concentration increased from 0.02 to 0.2%. The results for the non-irradiated material, obtained after an average 10 min exposure to H_2O_2 solutions, likely represent the CA saturation values obtainable at respective H_2O_2 concentrations. Note that hydrophilic OH terminated Si surfaces, with CA near 10°~15° and ~25°, have been fabricated by boiling Si samples at 100°C for 10 minutes in solutions of H_2O: NH_4OH: 30% H_2O_2=2:1:1 and H_2O: HCl: 30% H_2O_2=1:1:6, respectively [K. Hermansson*, et al.* 1991, J. K. Bal*, et al.* 2010]. Our results indicate that the exposure of Si to a 0.01% H_2O_2 solution alone has not been able to induce a significant change to its CA. Furthermore, as show in figure A.5, CA of the sites irradiated in DI water show no obvious change for the pulse number as large as 600.

Table A. 1 Parameters of Si used in calculation of spatial and transient temperature profiles.

Thermal Conductivity	Specific heat	Density	Optical absorption
34 [W/(m.K)]	678 [J/(kg.K)]	2320 [kg/m^3]	1.64x10^8 [m^{-1}]
[C. Glassbrenner, *et al.* 1964]	[P. Flubacher, *et al.* 1959]	[I. Lukeš, *et al.* 1992]	[D. E. Aspnes, *et al.* 1983]

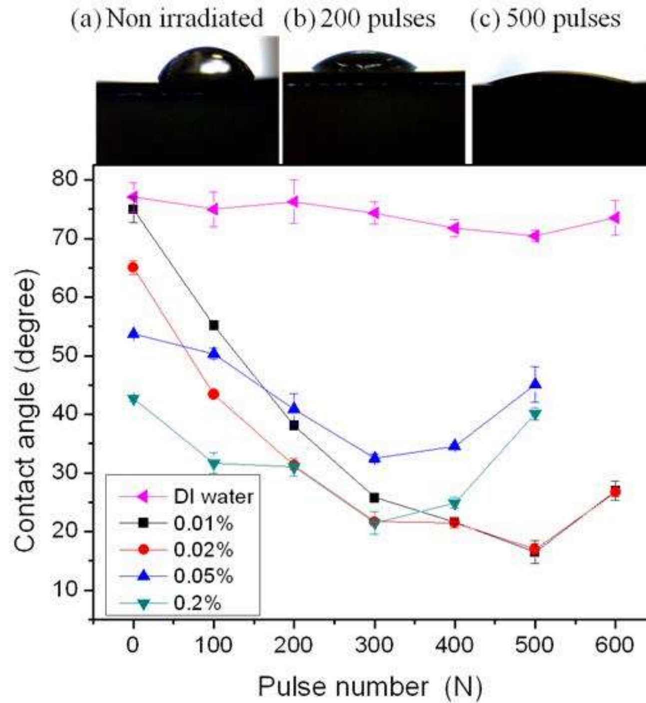

Figure A. 5 Contact angle vs. pulse number of KrF laser irradiated Si (001) at 250 mJ/cm^2 in DI water, and in 0.01, 0.02, 0.05 and 0.2% H_2O_2/DI water solutions. Experimental points are indicated by the respective symbols and the solid lines have been included as a guide to an eye. The insets shows profile images of water drops on (a) non-irradiated Si with CA=75°, and sites irradiated with (b) 200 pulses (CA=38°) and (c) 500 pulses (CA=15°) by KrF laser in a 0.01% H_2O_2/DI water solution.

The ability of the KrF laser pulse fluence of 320 mJ/cm^2 to induce the surface temperature near the boiling point of H_2O coincides with our observation of a large concentration of bubbles formed in this case at the sample-liquid interface, especially for large pulse number. The accumulative effect of the laser induced heating of the Si-liquid interface has also been observed for the portion of the coupon that remained non-irradiated during this experiment. As shown in figure A.6, the CA value of a material at N=0 has decreased from 75 to 69°, suggesting the presence of a temperature enhanced hydrophilization process. Consistent with the less efficient heating of Si at reduced pulse fluence was the observation that CA of 75°, characterizing the HF etched material, was not significantly affected by the accumulative (indirect) heating of coupons

irradiated with pulses at 183 and 250 mJ/cm^2. Generally, the formation of bubbles made it difficult to collect a reliable set of data for N > 400 and 600 and pulse fluence of 320 and 250 mJ/cm^2, respectively.

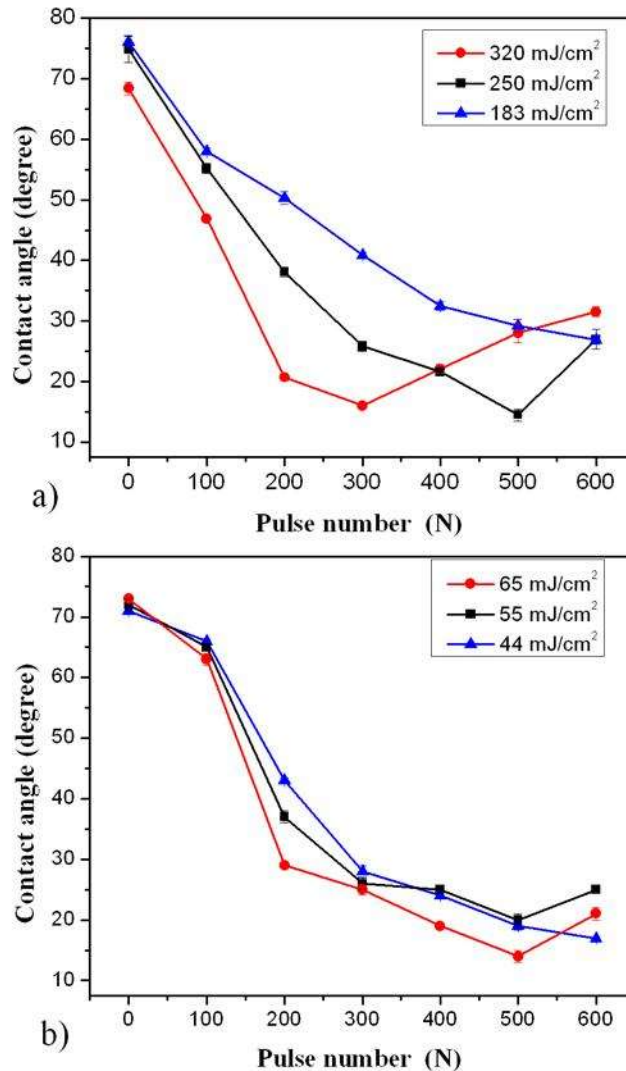

Figure A. 6 Contact angle vs. pulse number after irradiation in a 0.01% H_2O_2 solution with KrF (a) and ArF (b) lasers of different pulse fluences.

For the ArF laser, the smallest CA value of ~14° was achieved with 500 pulses of the 65 mJ/cm^2 pulse fluence. As the surface peak temperature induced in this case is only 40 °C, it seems that the formation of a hydrophilic surface has been affected by enhanced photo-dissociation of H_2O_2. It is important to note that H_2O_2 absorption at 193 nm is 7X stronger than at 248 nm [A. Schiffman, *et al.* 1993]. This process could be further enhanced by the laser heating of water that absorbs approximately 32X stronger at 196 nm (α = 126 x 10^{-2} m^{-1}) than at

248 nm (α = 3.92 x 10^{-2} m^{-1}) [T. I. Quickenden*, et al.* 1980]. The net result of enhanced photo-dissociation would be an increased concentration of OH radicals available for the reaction with Si and its hydrophilization. We found it impractical to irradiate the samples with ArF laser at the fluence exceeding 65 mJ/cm^2 due to the formation of a large number of bubbles increasing in proportion to the number of laser pulses delivered to the surface.

A.3.4.2 AFM analysis

Surface morphology of Si samples was investigated to address the possible modification of CA due to the increased surface roughness [V. Zorba*, et al.* 2006b]. Figure A.7 shows an AFM image of (a) a fragment of the HF etched sample that was not laser irradiated, but remained in the 0.01% H_2O_2/H_2O solution for approximately 10 min during laser processing, and (b) a site on the same sample irradiated with 500 pulses of the KrF laser at 250 mJ/cm^2. We found that the roughness (σ_{RMS}) of the non-irradiated material and that of the irradiated site is 0.30 nm and 0.38 nm, respectively. This indicates that there is no obvious surface morphology modification during laser irradiation of Si samples immersed in the H_2O_2/H_2O solution.

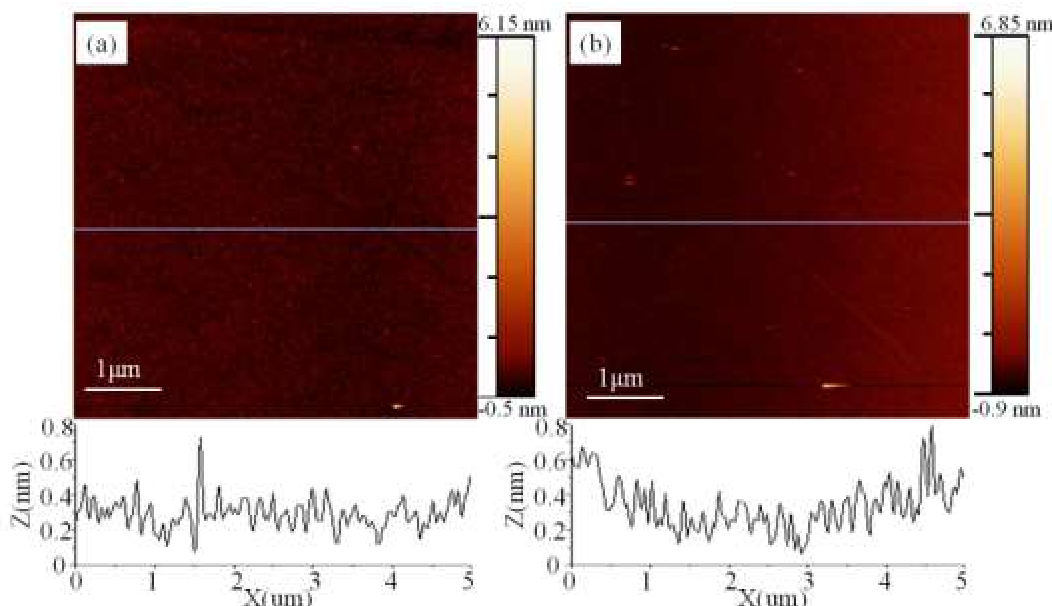

Figure A. 7 AFM images of a non irradiated sample (a) and a site irradiated with KrF laser at 250 mJ/cm^2 with 500 pulses (b) of the sample kept for ~ 10 min in a 0.01% H_2O_2/H_2Osolution.

A.3.4.3 XPS analysis

Figure A.8 shows Si 2p and O 1s XPS spectra of a freshly HF etched Si surface (a,d), non-irradiated Si surface exposed to 0.01% H_2O_2 solution for approximately 10 min (b, e), and Si

sites exposed to 0.01% H_2O_2/H_2O solution and irradiated with 500 pulses of the KrF laser at 250 mJ/cm^2 (4c, 4f). The Si 2p XPS spectra were fitted with Si, Si sub-oxides (SiO_x, $x < 2$), oxides (SiO_2) and silicon hydroxides (SiOH) [P. J. Grunthaner, *et al.* 1987a]. The Si 2p 3/2 of elemental Si was fixed at BE = 99.2±0.1 eV, while the peaks of SiO_x and SiO_2 were shifted by 0.7 and 3.8 eV, respectively [P. J. Grunthaner, *et al.* 1987a]. The OH replacing the oxygen atom has little impact on the Si 2p, so the SiO_2 and SiOH peaks were fixed at the same position in the Si 2p spectra [J. Heo, *et al.* 2007b].

In comparison to the as-received material, HF etching significantly reduces the XPS concentration of oxygen originating from the surface present of SiO_2 (data not shown). Consistent with this is the CA value of the as-received material, determined to be 51°, that increased to 75° following the etching procedure (see table A.2). The 500-pulse irradiated sites exhibit significantly increased concentrations of both SiOH and SiO_2, consistent with the increased material hydrophilicity. In the O 1s spectra, the peaks at 531.8±0.1, 532.6±0.1 and 533.7±0.1 eV were assigned to SiO_x, SiO_2 and SiOH, respectively [P. J. Grunthaner, *et al.* 1987b, J. Heo, *et al.* 2007b]. Since OH has a direct effect on the O 1s, there is observed a BE shift between SiO_2 and SiOH in the O 1s spectra [J. Heo, *et al.* 2007b]. After etching in the HF solution, most of SiO_2 and SiO_x have been removed, as shown in figure 4d. The quantity of SiO_2 and SiOH is greater for the irradiated site (e) than that for the non-irradiated material (f). Depending on the O/Si ratio, the minimum CA values of SiO_2 coated Si have been reported to be 45°~55° [M. Chasse, *et al.* 2002], while the minimum CA of 13° has been reported for a SiOH monolayer covered Si surface [Y. Chen, *et al.* 1991]. Thus, the increase of SiOH plays a dominating role in decreasing CA to 14° at 500 pulses. The XPS fitting of the O 1s spectra allowed to determine that the $SiOH/SiO_2$ ratio increased from 0.10 to 0.17 when pulse number increased from 100 (not shown here) to 500. The formation of the Si-OH bond is possibly due to the availability of negatively charged OH radicals formed by the UV laser induced photolysis of H_2O_2, as discussed in Sec. 3.1. The interaction of OH radicals with Si is facilitated by the excimer laser induced photoelectric effect, which leads to the formation of a positively charged Si surface [L. Chen, *et al.* 1988]. The increased concentration of OH reacting with Si is expected to increase its hydrophilicity [M. Grundner, *et al.* 1986a]. Furthermore, it is known that H_2O_2 is thermodynamically unstable, and its decomposition described by $2H_2O_2 \rightarrow 2H_2O + O_2$, could be

accelerated by impurities [F. Rice*, et al.* 1927, B. Averill*, et al.* 2007] and/or catalysts, such as iron oxides [S.-S. Lin*, et al.* 1998]. It is feasible that similar decomposition channels are present in our experiment and lead to the formation of an excessive presence of O_2 in the vicinity of the Si surface. While the potentially important consequence of this process in achieving a hydrophilic surface of Si would be the formation of SiO_2, the presence of O_2 molecules could also be the source of bubbles forming near the irradiated surface. As discussed above, we have observed significantly increased bubble formation in experiments involving ArF laser at 65 mJ/cm^2 and KrF laser at 320 mJ/cm^2, which is consistent with the increased possibility of thermally driven decomposition of H_2O_2. As the minimum CA for SiO_2 coated Si is known to be near 45° (see discussed above), the increase of CA observed for the sites irradiated with a large pulse number could be related to the formation SiO_2 enriched Si.

The dashed lines in the O 1s spectra correspond to carbon (C) adsorbates, whose quantities are calculated from the known ratios of oxygen to carbon in the C 1s spectra originating from C-O, C=O and O-C=O bonds [D. Miller*, et al.* 2002b]. It can be seen that the concentration of C is greater on the surface of a non-irradiated but exposed to the H_2O_2/H_2O solution material, than on the freshly etched sample. As shown in figure 4f, the concentration of C absorbates is reduced with the increasing pulse number due to the known excimer laser cleaning effect [R. Tsu*, et al.* 1991]. Since the C absorbates contribute to the hydrophobic nature of Si [M. Grundner*, et al.* 1986a], the laser induced cleaning of the Si surface of the C adsorbates helps to enhance the hydrophilic properties of the Si surface.

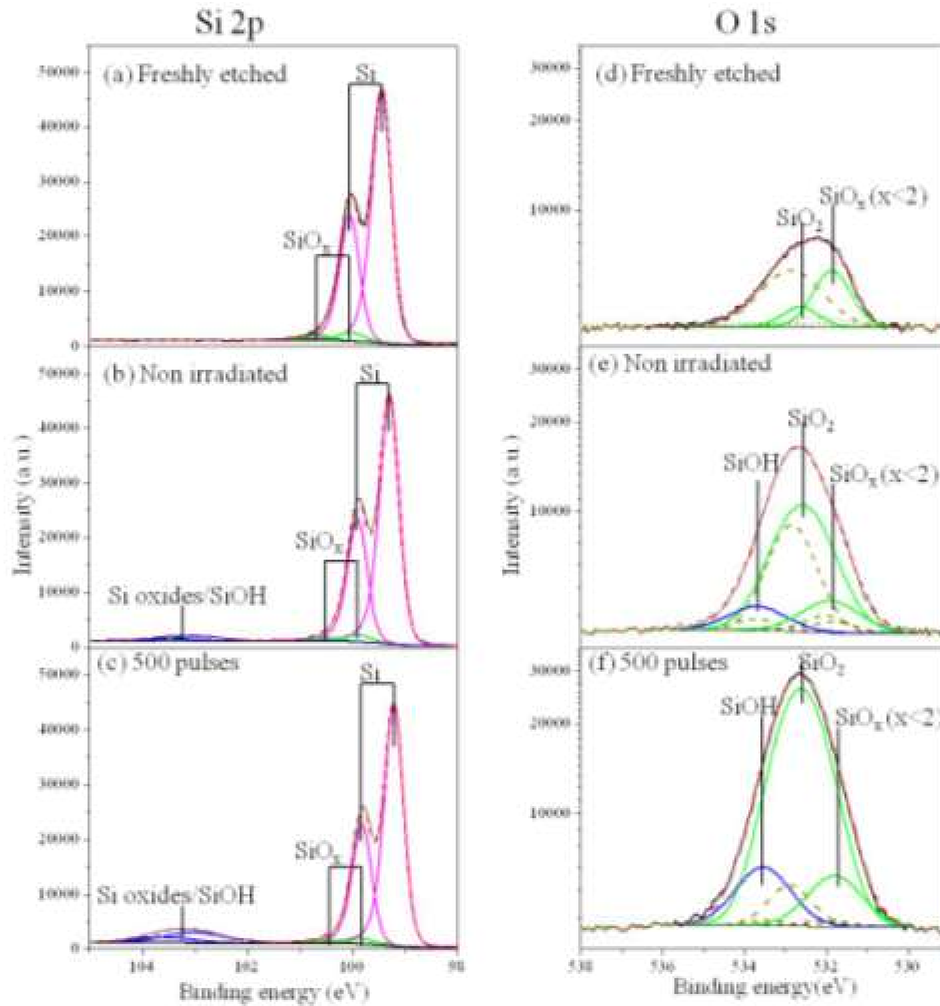

Figure A. 8 Si 2p and O 1s XPS spectra of a freshly etched site (a), (d), non irradiated sample kept for 10 min in a 0.01% H_2O_2/H_2O solution (b), (e) and a site exposed to a 0.01% H_2O_2 solution and irradiated with 500 pulses of the KrF laser (c), (f).

Table A.2 shows atomic concentrations of Si, O, C, F and the CA values observed for as-received, etched and KrF laser irradiated at 250 mJ/cm^2 samples. Due to the high coverage with native oxide (O/Si~1.4), CA of as-received material is 51°. As this oxide is removed by HF treatment, CA increased to 75°. Following the sample exposure to 0.01% H_2O_2 solution, the oxygen atomic percentage and the O/Si ratio increase with pulse number due to UV laser induced formation of SiOH. Table A.3 shows the values of atomic concentrations of Si, O, C, F and CA observed for as-received, etched and ArF laser irradiated samples at 65 mJ/cm^2 with 100 and 500 pulses. XPS fitting shows that SiOH/SiO_2 increased in this case from 0.15 to 0.22 for the sites irradiated with 100 and 500 pulses.

Table A. 2 Atomic percentage and CA of as-received, etched and KrF laser processed Si samples with 100 and 500 pulses of 250 mJ/cm^2.

	Si (%)	O (%)	C (%)	F (%)	CA
As-received	39.92	54.50	9.58	0	51±2.1°
Freshly etched	83.36	9.75	6.61	0.08	75±1.6°
Non-irradiated exposed to 0.01% H_2O_2	75.73	11.14	13.13	0	74±2.2°
100-pulse irradiated in 0.01% H_2O_2	75.82	12.43	11.75	0	55.2±0.8°
500-pulse irradiated in 0.01% H_2O_2	67.98	23.83	8.19	0	14.5±1°

Table A. 3 Atomic percentage and CA of as-received, etched and ArF laser processed Si samples with 100 and 500 pulses of 65 mJ/cm^2.

	Si (%)	O (%)	C (%)	F (%)	CA
Non-irradiated exposed to 0.01% H_2O_2	77.05	9.75	12.92	0.28	73±0.3°
100-pulse irradiated in 0.01% H_2O_2	75.95	11.58	12.31	0.11	63±1°
500-pulse irradiated in 0.01% H_2O_2	68.23	25.75	6.01	0.05	14±1°

A.3.4.4 FTIR analysis

A series of FTIR spectra characterizing a non-irradiated material exposed to a 0.01% H_2O_2 solution for approx. 10 min and the sites irradiated in a 0.01% H_2O_2 solution with 100 and 500 pulses of a KrF laser operating at 250 mJ/cm^2 are shown in figure A.9. The peaks at 3750 cm^{-1} and 3745 cm^{-1} correspond to the Si-OH and Si-$(OH)_2$ vibrational modes, respectively, while the peak at 3735 cm^{-1} is ascribed to the SiO-H stretching vibrational mode [B. A. Morrow*, et al.* 1988, P. Gupta*, et al.* 1991, D. B. Mawhinney*, et al.* 1997]. It can be seen that the absorbance intensities of these peaks increase with the laser pulse number, thus, indicating a growing concentration of these compounds. This result is consistent with the XPS data discussed above. The insignificant presence of Si-oxides in our samples has been also suggested by our inability to detect an FTIR peak at 1108 cm^{-1} that originates from the Si-O-Si vibrational modes related to oxides created by thermal oxidation of Si in an O_2 environment [P. Gupta*, et al.* 1991, D. B. Mawhinney*, et al.* 1997].

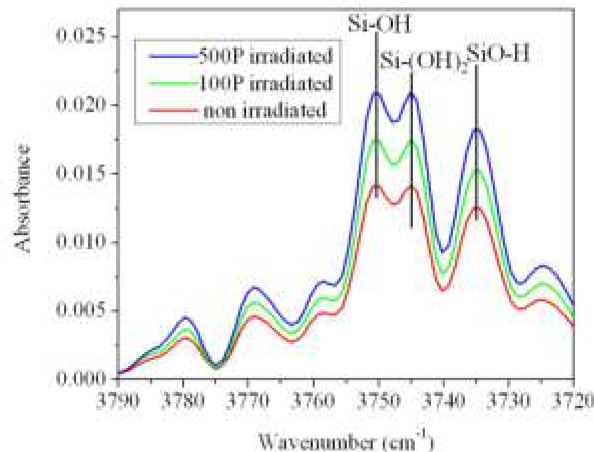

Figure A. 9 FTIR spectra of non irradiated site and sites irradiated by KrF laser in 0.01% H_2O_2 solution with 100 pulses (100P) and 500 pulses (500P)

A.3.4.5 Selective area immobilization of biotinylated nanospheres

Figure A.10a shows a fluorescence image of the Si sample that, after KrF laser irradiation through the maple leaf mask with 400 pulses at 250 mJ/cm^2 in a 0.01% H_2O_2/H_2O solution, was exposed to a solution of fluorescein stained nanospheres and, consequently, washed with PBS to remove nanospheres weakly bound to the surface. As expected, a dense accumulation of nanospheres took place on the non-irradiated portion of the sample surface. The morphology of this nanosphere-coated surface is illustrated with an AFM image shown in figure A.10b. Although a sharp contrast of the hydrophilic/hydrophobic interface is well depicted in figure A.10a, the presence of some defects related to the local increase of the surface hydrophobicity has been illustrated by the nanospheres trapped inside of the laser-irradiated zone. The likely source of these defects is formation of a SiO_2 or SiO_x rich surface in hot spots associated with the formation of bubbles as discussed in A3.4.3. A possible strategy towards correction of this problem could include a careful preparation of the Si surface to minimize the presence of surface impurities, and adjusting the conditions of the irradiation, e.g., by reducing the pulse number and/or fluence.

The Si surface selectively patterned with biotin-conjugated nanospheres is important for the fabrication of microbiosensors and bimolecular electronic devices [R. N. Orth*, et al.* 2003, S. E. Stanca*, et al.* 2005]. Furthermore, our results illustrate the potential of the excimer laser technique for the fabrication of such devices without the need of an ablative patterning that could

lead, e.g., to the excessive accumulation of the ablated material in the vicinity of patterned structures.

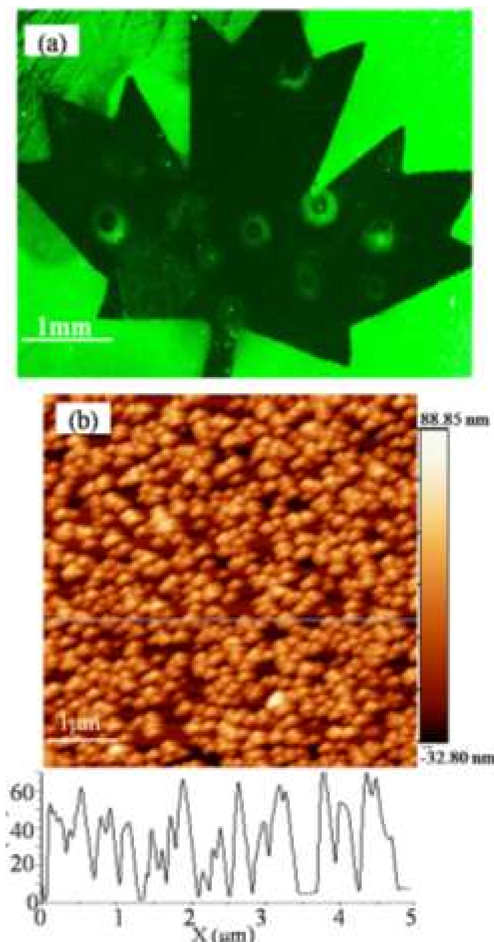

Figure A. 10 (a) Fluorescence image of a sample that, following the irradiation through a maple leaf mask with 400 pulses of a KrF laser at 250 mJ/cm2, was exposed to a solution of fluorescein stained nanospheres and washed with PBS; (b) AFM image of a non-irradiated portion of the sample.

A.3.5 Conclusion

Modification of the Si surface wettability, initially characterized by CA ~75°, has been investigated with a series of samples immersed in low concentrations of H_2O_2/H_2O solutions and irradiated with KrF and ArF lasers. Superhydrophilic surface, characterized by CA ~14°, of Si samples immersed in a 0.01% H_2O_2/H_2O solution has been fabricated following the 500-pulse irradiation with 250 and 65 mJ/cm^2 pulse fluence of the KrF and ArF laser, respectively. Owing to the relatively low laser pulse fluence, the surface morphology of processed samples remained unaffected as evidenced by the AFM results. XPS and FTIR measurements showed that the

formation of a highly hydrophilic surface is associated with the formation of Si-OH bonds. The laser fabricated hydrophilic surface of Si inhibits the immobilization of biotin-coated nanospheres that naturally stick to the hydrophobic surface of Si. The investigated method of laser-induced modification of the Si surface wettability is compatible with the microfluidic device technology.

Thus, the same approach could be applied to fabricate highly hydrophobic surfaces of Si as we have demonstrated it recently [N. Liu*, et al.* 2014]. Although we have not carried out repetitive wetting/dewetting experiments in this work, it is reasonable to expect that such a process could be implemented for *in situ* selective area functionalization of Si surfaces investigated, e.g., for the applications involving molecular chemistry research and fabrication of advanced microfluidic devices for (bio)sensing applications.

A.3.6 Acknowledgement

This work was supported by the Natural Science and Engineering Research Council of Canada (Discovery Grant No. 122795-2010) and the program of the Canada Research Chair in Quantum Semiconductors (JJD). Technical assistance of Centre de characterization de materiaux in collecting XPS data, Centre de recherche en nanofabrication et en nanocaracterisation (CRN^2), Universite de Sherbrooke is greatly appreciated. NL acknowledges the Merit Scholarship Program for Foreign Student, Fonds de recherche du Québec - Nature et technologies, for providing a graduate student scholarship.

A.4 Excimer laser assisted chemical process for formation of hydrophobic surface of Si (001)

Neng Liu, Walid Mohamed Hassen, Jan J. Dubowski, Applied Physics A, DOI: 10.1007/s00339-014-8380-9, (2014);

A 4.1 Abstract

Silicon (Si) wettability is one of the important parameters in the development of Si based biosensing and lab-on-chip devices. We report on UV laser induced hydrophobicity of Si (001)

wafers immersed in methanol during the irradiation with an ArF excimer laser. The irradiation with 800 pulses of the laser operating at 65 mJ/cm^2 allowed to significantly increase the hydrophobicity of investigated samples as characterized by the static contact angle change from 77° to 103°. Owing to the irradiation with relatively low laser fluence, no measurable change of surface morphology of the irradiated samples has been observed with atomic force microscopy measurements. The nature of the hydrophobic surface of investigated samples is consistent with X-ray photoelectron spectroscopy analysis that indicates formation of Si-O-CH_3 bonds on the surface of the laser-irradiated material.

Key words: Hydrophobic silicon, UV laser, methanol, X-ray photoelectron spectroscopy, AFM

A 4.2 Introduction

Reduced wettability is often obtained by both increasing surface roughness and surface chemical modification [C. Sun*, et al.* 2008]. Laser structuring of surfaces is a relatively simple process with the potential to offer nanostructuring with high spatial resolution [V. Zorba*, et al.* 2006a]. Femtosecond laser has been reported to generate nanostructures on the Si surface and induce a superhydrophobic surface with a CA exceeding 150° [T. O. Yoon*, et al.* 2008b]. However, as Si has a high laser texturing threshold (~500 mJ/cm^2) [R. Tsu*, et al.* 1991], surface nanostructuring always requires a relatively high power laser irradiation, frequently carried out in an atmosphere of reactive gasses [V. Zorba*, et al.* 2006a, C. Sun*, et al.* 2008, A. Ranella*, et al.*]. To avoid this complication, numerous experiments have been focused on laser-induced/-assisted surface chemical modification, involving deposition of organic/metal oxide films on the Si substrate before irradiation [X. M. Li*, et al.* 2007, G. Caputo*, et al.* 2008]. It is known that a hydrophobicity is mainly due to the presence of Si-H and/or Si-(O)-CH_x groups [M. Grundner*, et al.* 1986a]. To achieve selective area control of wettability of Si, complex patterning steps are usually required, including treatment in chemical solutions [Y. Li*, et al.* 2001]. High chemical reactivity of UV laser radiation has also been used to selective area process organic film coated solid substrates and modify their hydrophobicity [X. M. Li*, et al.* 2007]. However, a limited amount of data is available on laser-assisted modification of Si wettability by irradiation of samples immersed in different chemical solutions. It has been reported that a 1% HF treated Si surface immersed in methanol (CH_3OH) solution for 20 minutes becomes coated with –OCH_3

through the reaction with Si dangling bonds [K. Mizuno, *et al.* 1991]. Furthermore, the CH_3OH vapor is known to have a strong absorption band in the 105-200 nm region, and it can be dissociated relatively easily with 157 and 193 nm lasers to form H atoms and $–OCH_3$ radicals [S. Satyapal, *et al.* 1989, B. Cheng, *et al.* 2002, Z. Chen, *et al.* 2011].

In our previous work, a UV laser was used to modify the chemical composition of InP surfaces exposed to air, SiO_2 or deionized water environments [J. Genest, *et al.* 2008, N. Liu, *et al.* 2013a, N. Liu, *et al.* 2013b]. In this paper, we expand this approach on studying laser-assisted modification of surface chemistry of Si (001) samples immersed in CH_3OH, aiming for the formation of a strongly hydrophobic material.

A 4.3 Experimental

The Si samples were cleaned and the native oxides were removed as we discussed in section A3.3. The samples were immersed into a 0.74 mm tall microfluidic chamber filled with a degassed methanol solution. The chamber was capped with a UV transparent (transmission > 90%) fused silica window, and designed to provide a continuous injection of methanol above the sample surface during irradiation. The irradiation was carried out with ArF and KrF excimer laser (Lumonics, Pulse Master 800) based systems described in section A 3.2. Following irradiation, samples were rinsed with DI water, dried with N_2 and installed in a sealed N_2 container designed to eliminate their exposure to an atmospheric environment, and transported for further surface characterization.

Static CA measurements were carried out using a goniometer (Rame-Hart NRL, Model 100) operating at room temperature and ambient humidity. Excimer laser processed surfaces were analysed with a Kratos Analytical, AXIS Ultra DLD XPS operating at a take-off angle (TOF) of 60°. Sample surface morphology was imaged with a Digital Instrument, Nanoscope III AFM operating in a tapping mode over the 5 μm x 5 μm region.

A 4.4 Results and Discussion

A4.4.1 Contact angle measurements

Figure A.11 shows the CA values measured for Si (001) samples that were immersed in methanol and irradiated with the ArF laser at pulse fluence of 30, 65 and 80 mJ/cm^2. It can be seen that CA of the sites irradiated with 800 pulses at 65 mJ/cm^2 increases from its initial value of 77° to 103°. A comparable result is observed for the 1000-pulse irradiated sites. This suggests that the laser induced CA modification of the Si surface saturates for the applied laser fluence. A more intense dynamic of the CA increase has been observed for 80 mJ/cm^2 and low number of laser pulses ($N < 200$), as indicated by the full circle symbols in Figure A.11. However, the formation of bubbles on the samples irradiated with $N > 200$ pulses, and a related uncontrolled modification of the sample surface morphology prevented us from collecting reliable data under such conditions. Using an approach described elsewhere [R. Stanowski*, et al.* 2006, Neng Liu*, et al.* 2013b], we estimated that a 65 mJ/cm^2 pulse of the ArF laser induces peak temperature on the Si surface comparable to the methanol boiling point, i.e., 65 °C [J. W. Westwater*, et al.* 1955]. Thus, the irradiation with greater laser fluence leads to the formation of a large amount of bubbles. We have observed that, indeed, the surface concentration of bubbles increased in this case drastically, in proportion to the number of laser pulses delivered to the surface. Consistent with this was our inability to fabricate Si samples of satisfactory characteristics with the laser fluence of 80 mJ/cm^2 and $N > 200$ pulses. In contrast, the irradiation of 30 mJ/cm^2 showed only a weak increase of CA to 78° for the 1000-pulse irradiated sites.

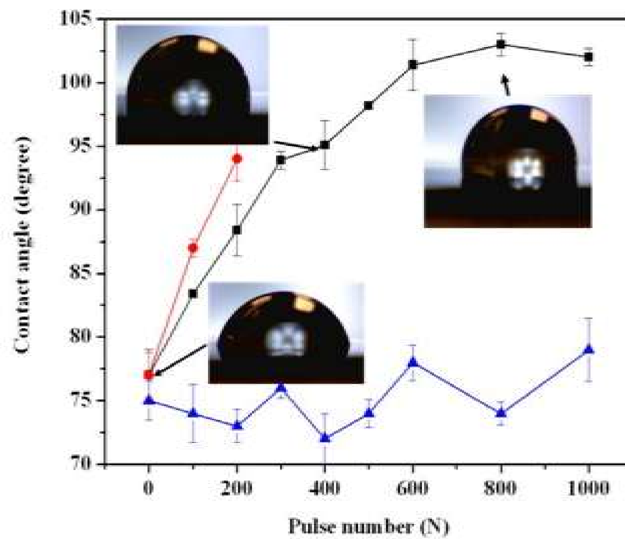

Figure A. 11 Contact angle of Si (001) samples immersed in methanol and irradiated with an ArF laser at 30 mJ/cm2 (▲), 65 mJ/cm2 (■) and 80 mJ/cm2 (●). The error bars are calculated based on the measurements of 4 independent sites.

Experiments involving KrF laser revealed no significant change of CA for samples irradiated up to 182 mJ/cm^2. The irradiation with fluence of 250 mJ/cm^2 resulted in an intensive formation of bubbles, consistent with the ability of an individual pulse of such a fluence to increase the temperature of the Si wafer (immersed in methanol) to the boiling point of methanol. No measurable increase of CA could be recorded for samples irradiated under these conditions with up to 1000 pulses. A negative response of Si to KrF laser-induced chemical modification of its surface in methanol seems to be related to the inability of this laser to photodissociate CH_3OH and create $-OCH_3$ radicals required in the formation of a hydrophobic surface [S. Satyapal*, et al.* 1989, Z. Chen*, et al.* 2011].

The CA values of the ArF laser irradiated samples remained unchanged for up to 4 hours if the samples were stored in N_2. However, following a 20-hour storage in air environment, we observed CA decreased to 56°, which is likely related to the oxidation of Si and formation of SiO_2 on its surface [M. Chasse*, et al.* 2002]. Note that CA ~50-65° has been reported for Si samples passivated with naturally grown SiO_2 [R. Williams*, et al.* 2003].

A 4.4.2 AFM analysis

Figure A.12 shows AFM images of a non irradiated Si sample that was etched with HF and rinsed with DI water, and a sample (site) immersed in methanol and irradiated with 500 pulses with ArF laser at 65 mJ/cm^2. The AFM roughness (σ_{RMS}) measured for the 500 pulse irradiated site is 0.37 nm, which is comparable to $\sigma_{RMS} = 0.31$ nm for the non irradiated sample. Clearly, no obvious laser induced surface morphology modification could be indentified with the AFM measurements. Thus, the hydrophobic nature of the material irradiated in methanol must be related to the laser induced chemical modification of its surface.

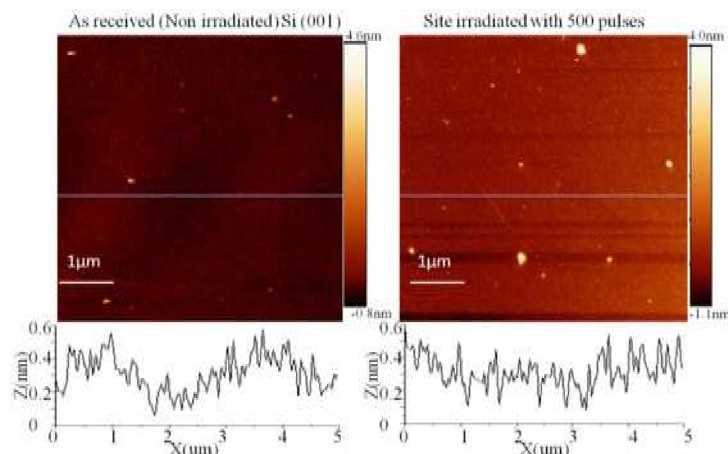

Figure A. 12 AFM image of a non-irradiated Si (001) sample and a site irradiated with 500 pulses by an ArF laser operating at 65 mJ/cm^2.

A4.4.3 XPS analysis

Figure A.13 shows XPS spectra of Si 2p, O 1s and C 1s for a non-irradiated sample (a-c), and a sample immersed in methanol and irradiated with 500 pulses of the ArF laser at 65 mJ/cm^2 (d-f). A weak feature, indicated as Si-O-C in the Si 2p spectrum of the non-irradiated site (Fig. 3a) can be seen around BE=102.7 eV. This feature has been reported to originate from the Si-$(OCH_3)_x$ bond [J. W. Kim*, et al.*]. The atomic concentration of this compound was estimated at 0.7%, which probably is slightly underestimated due to the relatively small (60°) TOF applied while collecting our XPS data [M. Grundner*, et al.* 1986a, K. Mizuno*, et al.* 1991]. On the irradiated site shown in d, the atomic concentration of Si-$(OCH_3)_x$ has been estimated at 3.5%, which indicates a significant 5-fold increase of the surface concentration of this compound. In the O 1s spectra (b and e), the Si-$(OCH_3)_x$ peak (BE=532.6 eV) increases from 1% for the non-irradiated material to 2.5% for the irradiated site. In the C 1s spectra (c and f), the C-O bond from original C absorbates overlaps with Si-$(OCH_3)_x$, so the C-O increment ratio is not as significant as in the Si 2p and O 1s spectra. As Si-$(OCH_3)_x$ is responsible for the hydrophobic nature of the Si surface [M. Grundner*, et al.* 1986a, A. Jákli*, et al.* 1999, T. Ishizaki*, et al.* 2006], the increase of the surface concentration of this compound appears to be the main reason for the observed enhancement of the hydrophobic characteristics of the ArF irradiated Si samples. With increasing laser fluence, more -OCH_3 is expected to be created and absorbed on the Si surface [G. L. Vaghjiani*, et al.* 1990]. The saturation of CA around 103° is related to the CH_3 surface energy. The lower the surface energy, the higher the hydrophobicity is expected. It has been reported that

the closest hexagonal packing of $–CF_3$ groups gives the lowest surface free energy of any solid, with CA of near 120° [T. Nishino*, et al.* 1999].

In the O 1s spectra, besides Si-O-C and C-O, there are also SiO_x and OH related peaks. The increase of the SiO_x peak is possibly due to the OCH_3 bond to the sub-oxides (SiO_{x+1}-CH_3) [J. W. Kim*, et al.*]. As the HF treated Si sample didn't show the presence of OH (not shown here), the OH peak is possibly due to CH_3OH physically absorbed on the surface.

XPS study of the samples irradiated in methanol with up to 500 pulses of the KrF laser at 250 mJ/cm^2 showed no evidence of the increased surface concentration of Si-O-C. This result is consistent with the inability of the KrF laser, in contrast to the ArF laser, to photodissociate methanol and create -OCH_3 radicals [B. Cheng*, et al.* 2002, Z. Chen*, et al.* 2011].

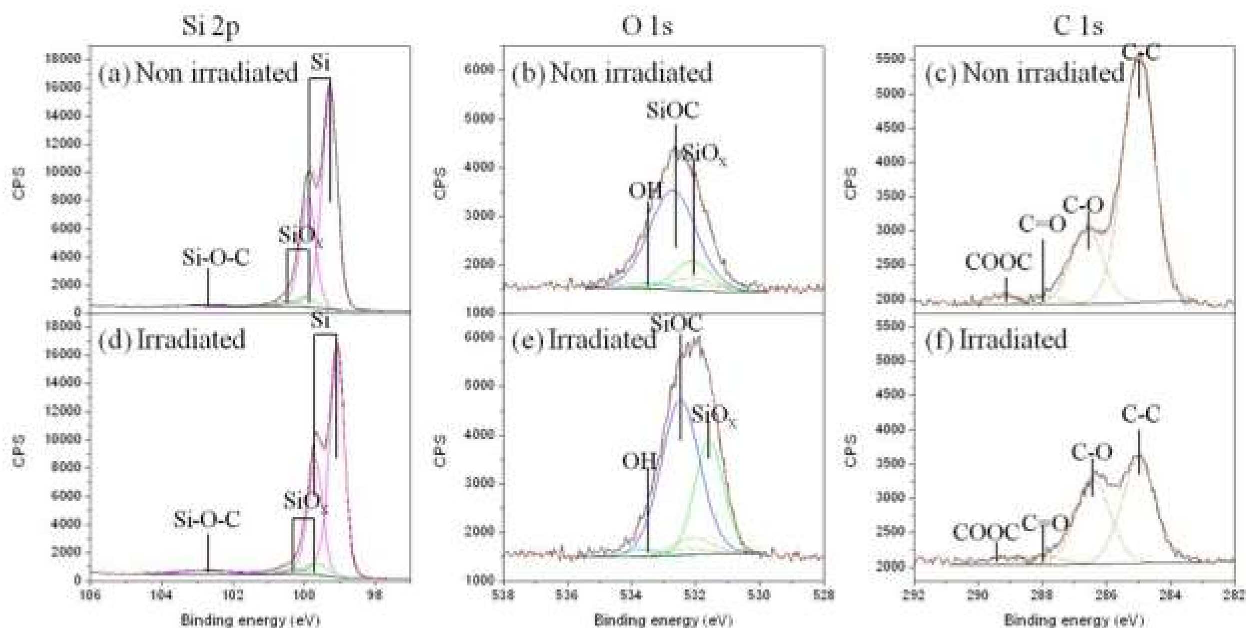

Figure A. 13 XPS Si 2p, O 1s and C 1s spectra of a reference (non-irradiated) sample (a-c), and a sample immersed in methanol and irradiated with 500 pulses of an ArF laser at 65 mJ/cm^2 (d-f).

A 4.5 Conclusion

The mechanism of laser-induced wettability of Si surface has been investigated by irradiation of samples immersed in methanol using ArF and KrF excimer lasers. The formation of Si (001) hydrophobic surface, CA~103° (an increase for the initial CA of 77°) has been observed for irradiation with 800-1000 pulses of the ArF laser at 65 mJ/cm^2. XPS

results suggest laser-induced formation of Si-$(OCH_3)_x$ compounds, consistent with the observed increase of the Si surface hydrophobicity. It appears that the Si-$(OCH_3)_x$ is formed by ArF laser induced decomposition of CH_3OH. This innovative technique of laser induced formation of a hydrophobic surface of Si (001), without AFM detectable surface morphology deterioration, is potentially attractive for *in situ* functionalization of Si wafers employed in the process of fabrication of microfluidic and lab-on-chip devices. We note that the same approach could be applied to fabricate highly hydrophilic surfaces of Si, and our preliminary experiments seem to confirm this expectation. Although we have not carried out repetitive wetting/dewetting experiments in this work, it is reasonable to expect that oxidized samples could be enriched with Si-$(OCH_3)_x$ if irradiated in methanol with the 193 nm laser. Thus, this research paves a new way to selective area *in situ* modification of Si surfaces from strongly hydrophobic to strongly hydrophilic and *vice versa*.

A 4.6 Acknowledgement

This work was supported by the Natural Science and Engineering Research Council of Canada (Discovery Grant No. 122795-2010) and the programs of the Canada Research Chair in Quantum Semiconductors, Plasma Québec and Regroupement québécois sur les matériaux de pointe (RQMP). Technical assistance of the Université de Sherbrooke Centre de characterization de materiaux (CCM) in collecting XPS data and Centre de recherche en nanofabrication et en nanocaracterisation (CRN^2) as well as the support from NanoQuébec are greatly appreciated. NL acknowledges the Merit Scholarship Program for Foreign Student, Fonds de recherche du Québec-Nature et technologies (FRQNT), for providing a graduate student scholarship.

A.5 Summary

The wettability of Si surface has been modified by excimer laser low fluence direct irradiation in different aqueous environments. After irradiation by KrF and ArF laser in low concentration (~0.01%) H_2O_2 solution, CA decreased with pulse number to ~14° (superhydrophilic) at 500 pulses. XPS, AFM and FTIR measurements show that this hydrophilicity improvement is induced by excimer laser induced formation of mainly Si-OH

and also SiO_2 instead of surface texturing. Carboxylic acid group coated fluorescence nanospheres have succeeded in selective area immobilization on the irradiated surface which indicates the great potential of this novel technique in biosensor region. In contrast, ArF laser has been used to irradiate Si surface in microchamber filled with methanol to increase CA to 103° (hydrophobic) as the pulse number increases. XPS results show that this is caused by ArF laser induced decomposition of CH_3OH and formation of hydrophobic $SiOCH_3$.

A.6 Bibliography

Aspnes, D.E., and Studna, A.A., (1983), Dielectric functions and optical parameters of Si, Ge, GaP, GaAs, GaSb, InP, InAs, and InSb from 1.5 to 6.0 eV, *Physical Review B*, vol. 27, n°2, 985-1009.

Averill, B., and Eldredge, P.: (2007), Chemistry: Principles, Patterns, and Applications (Pearson Benjamin Cummings), 1131p.

Bal, J., Kundu, S., et al., (2010a), Growth and stability of Langmuir-Blodgett films on OH-, H-, or Br-terminated Si (001), *Physical Review B*, vol. 81, n°4, 045404.

Bal, J., Kundu, S., et al., (2010b), Hydrophobic to hydrophilic transition of HF-treated Si surface during Langmuir lodgett film deposition, *Chemistry Physics Letters*, vol. 500, n°1, 90-95.

Baldacchini, T., Carey, J.E., et al., (2006), Superhydrophobic surfaces prepared by microstructuring of silicon using a femtosecond laser, *Langmuir*, vol. 22, n°11, 4917-4919.

Bartlett, P.N., Baumberg, J.J., et al., (2002), Highly Ordered Macroporous Gold and Platinum Films Formed by Electrochemical Deposition through Templates Assembled from Submicron Diameter Monodisperse Polystyrene Spheres, *Chemistry of Materials*, vol. 14, n°5, 2199-2208.

Bayiati, P., Tserepi, A., et al., (2007), Electrowetting on plasma-deposited fluorocarbon hydrophobic films for biofluid transport in microfluidics, *Journal of Applied Physics*, vol. 101, n°10, 103306-103309.

Caputo, G., Nobile, C., et al., (2008), Reversible wettability changes in colloidal TiO_2 nanorod thin-film coatings under selective UV laser irradiation, *The Journal of Physical Chemistry C*, vol. 112, n°3, 701-714.

Caputo, G., Cortese, B., et al., (2009), Reversibly Light-Switchable Wettability of Hybrid Organic/Inorganic Surfaces With Dual Micro-/Nanoscale Roughness, *Advanced Functional Materials*, vol. 19, n°8, 1149-1157.

Chasse, M., and Ross, G., (2002), Effect of aging on wettability of silicon surfaces modified by Ar implantation, *Journal of Applied Physics*, vol. 92, n°10, 5872-5877.

Chen, L., Liberman, V., et al., (1988), Ultraviolet laser-induced ion emission from silicon, *Journal of Vacuum Science & Technology A: Vacuum, Surfaces, and Films*, vol. 6, n°3, 1426-1427.

Chen, Y., Helm, C., et al., (1991), Molecular mechanisms associated with adhesion and contact angle hysteresis of monolayer surfaces, *The Journal of Physical Chemistry*, vol. 95, n°26, 10736-10747.

Chen, Z., Eppink, A., et al., (2011), Product pair correlation in CH_3OH photodissociation at 157 nm: the OH+ CH_3 channel, *Physical Chemistry Chemical Physics*, vol. 13, 2550.

Cheng, B., Bahou, M., et al., (2002), Experimental and theoretical studies on vacuum ultraviolet absorption cross sections and photodissociation of CH_3OH, CH_3OD, CD_3OH, and CD_3OD, *The Journal of Chemistry Physics*, vol. 117, n°4, 1633-1640.

Cho, S.J., An, T., et al., (2011), Superhydrophobic nanostructured silicon surfaces with controllable broadband reflectance, *Chemical Communications*, vol. 47, n°21, 6108-6110.

Dahmen, C., Janotta, A., et al., (2003), Surface functionalization of amorphous silicon and silicon suboxides for biological applications, *Thin Solid Films*, vol. 427, n°1-2, 201-207.

Daniel, S., Chaudhury, M.K., et al., (2001), Fast drop movements resulting from the phase change on a gradient surface, *Science*, vol. 291, n°5504, 633-636.

Dubowski, J.J., Poole, P., et al., (1999), Enhanced quantum-well photoluminescence in InGaAs/InGaAsP heterostructures following excimer-laser-assisted surface processing, *Applied Physics A: Materials Science & Processing*, vol. 69, 299-303.

Flubacher, P., Leadbetter, A., et al., (1959), The heat capacity of pure silicon and germanium and properties of their vibrational frequency spectra, *Philosophical Magazine*, vol. 4, n°39, 273-294.

Genest, J., Dubowski, J.J., et al., (2007), Suppressed intermixing in InAlGaAs/AlGaAs/GaAs and AlGaAs/GaAs quantum well heterostructures irradiated with a KrF excimer laser, *Applied Physics A: Materials Science & Processing*, vol. 89, n°2, 423-426.

Genest, J., Beal, R., et al., (2008), ArF laser-based quantum well intermixing in InGaAs/InGaAsP heterostructures, *Applied Physics Letters*, vol. 93, 071106.

Glassbrenner, C., and Slack, G.A., (1964), Thermal conductivity of silicon and germanium from 3 K to the melting point, *Physical Review*, vol. 134, n°4A, A1058.

Grundner, M., and Jacob, H., (1986), Investigations on hydrophilic and hydrophobic silicon (100) wafer surfaces by X-ray photoelectron and high-resolution electron energy loss-spectroscopy, *Applied Physics A: Materials Science & Processing*, vol. 39, n°2, 73-82.

Grunthaner, P.J., Hecht, M.H., et al., (1987), The localization and crystallographic dependence of Si suboxide species at the SiO_2/Si interface, *Journal of Applied Physics*, vol. 61, n°2, 629-638.

Guo, Y., Su, S., et al., A silicon-based electrochemical sensor for highly sensitive, specific, label-free and real-time DNA detection, *Nanotechnology*, vol. 24, n°44, 444012.

Gupta, P., Dillon, A., et al., (1991), FTIR studies of H_2O and D_2O decomposition on porous silicon surfaces, *Surface Science*, vol. 245, n°3, 360-372.

Heo, J., and Kim, H.J., (2007), Effects of annealing condition on low-k a-SiOC: H thin films, *Electrochemical and Solid-state Letters*, vol. 10, G11.

Hermansson, K., Lindberg, U., et al., (1991), Wetting properties of silicon surfaces, *International Conference on Solid-State Sensors and Actuators*, IEEE, 193-196

Ishizaki, T., Saito, N., et al., (2006), Fabrication and characterization of ultra-water-repellent alumina-silica composite films, *Journal of Physics D: Applied Physics*, vol. 40, n°1, 192.

Jákli, A., Almásy, L., et al., (1999), Memory of silica aggregates dispersed in smectic liquid crystals: Effect of the interface properties, *The European Physical Journal B - Condensed Matter and Complex Systems*, vol. 10, n°3, 509-513.

Kajiyama, T., Ge, S., et al., (1996), Scanning force microscopic study of surface structure and properties of (alkylsilane/ fluoroalkylsilane) mixed monolayers, *Supramolecular Science*, vol. 3, n°1-3, 123-130.

Kim, J.W., Kim, H.B., et al., (2010), Correlation Study on the Low-Dielectric Characteristics of a SiOC (-H) Thin Film from a BTMSM/O_2 Precursor, *Journal of the Korean Physical Society*, vol. 56, n°1, 89-95.

Koehler, B.G., Mak, C.H., et al., (1989), Decomposition of H_2O ON Si(111)7 × 7 studied using laser-induced thermal desorption, *Surface Science*, vol. 221, n°3, 565-589.

Krupenkin, T.N., Taylor, J.A., et al., (2004), From Rolling Ball to Complete Wetting:The Dynamic Tuning of Liquids on Nanostructured Surfaces, *Langmuir*, vol. 20, n°10, 3824-3827.

Lau, K.K.S., Bico, J., et al., (2003), Superhydrophobic Carbon Nanotube Forests, *Nano Letters*, vol. 3, n°12, 1701-1705.

Li, X.-M., Reinhoudt, D., et al., (2007), What do we need for a superhydrophobic surface? A review on the recent progress in the preparation of superhydrophobic surfaces, *Chemical Society Reviews*, vol. 36, n°8, 1350-1368.

Li, X.M., Reinhoudt, D., et al., (2007), What do we need for a superhydrophobic surface? A review on the recent progress in the preparation of superhydrophobic surfaces, *Chemical Society Reviews*, vol. 36, n°8, 1350-1368.

Li, Y., Pfohl, T., et al., (2001), Selective surface modification in silicon microfluidic channels for micromanipulation of biological macromolecules, *Biomed Microdevices*, vol. 3, n°3, 239-244.

Lin, S.-S., and Gurol, M.D., (1998), Catalytic Decomposition of Hydrogen Peroxide on Iron Oxide: Kinetics, Mechanism, and Implications, *Environmental Science & Technology*, vol. 32, n°10, 1417-1423.

Liu, N., Moumanis, K., et al., (2012), Self-organized Nano-cone Arrays in InP/InGaAs/InGaAsP Microstructures by Irradiation with ArF and KrF Excimer Lasers, *Journal of laser micro/nano Engineering*, vol. 7, n°2, 130.

Liu, N., and Dubowski, J.J., (2013a), Chemical evolution of InP/InGaAs/InGaAsP microstructures irradiated in air and deionized water with ArF and KrF lasers, *Applied Surface Science*, vol. 270, n°13, 16-24.

Liu, N., Poulin, S., et al., (2013b), Enhanced photoluminescence emission from bandgap shifted InGaAs/InGaAsP/InP microstructures processed with UV laser quantum well intermixing, *Journal of Physics D: Applied Physics*, vol. 46, n°44, 445103.

Liu, N., Hassen, W.M., et al., (2014), Excimer laser assisted chemical process for formation of hydrophobic surface of Si (001), *Applied Physics A: Materials Science & Processing*, vol., in print.

Liu, X., Fu, R.K.Y., et al., (2007), Hydrogen plasma surface activation of silicon for biomedical applications, *Biomolecular Engineering*, vol. 24, n°1, 113-117.

Lukeš, I., and Černý, R., (1992), Study of excimer laser induced melting and solidification of Si by time-resolved reflectivity measurements, *Applied Physics A: Materials Science & Processing*, vol. 54, n°4, 327-333.

Malek, C.G.K., (2006), Laser processing for bio-microfluidics applications (part I), *Analytical and Bioanalytical Chemistry*, vol. 385, n°8, 1351-1361.

Marmur, A., (2003), Wetting on Hydrophobic Rough Surfaces:To Be Heterogeneous or Not To Be?, *Langmuir*, vol. 19, n°20, 8343-8348.

Martines, E., Seunarine, K., et al., (2005), Superhydrophobicity and superhydrophilicity of regular nanopatterns, *Nano Letters*, vol. 5, n°10, 2097-2103.

Mawhinney, D.B., Glass, J.A., et al., (1997), FTIR Study of the Oxidation of Porous Silicon, *Journal of Physics Chemical B*, vol. 101, n°7, 1202-1206.

Miller, D., Biesinger, M., et al., (2002), Interactions of CO_2 and CO at fractional atmosphere pressures with iron and iron oxide surfaces: one possible mechanism for surface contamination?, *Surface and interface analysis*, vol. 33, n°4, 299-305.

Mizuno, K., Maeda, S., et al., (1991), Photoelectron emission from silicon wafer surface with adsorption of organic molecules, *Analytical Science*, vol. 7, 345.

Morrow, B.A., and Gay, I.D., (1988), Silicon-29 cross-polarization/magic angle spinning NMR evidence for geminal silanols on vacuum-activated aerosil silica, *The Journal of Physics Chemistry*, vol. 92, n°20, 5569-5571.

Nishino, T., Meguro, M., et al., (1999), The lowest surface free energy based on -CF3 alignment, *Langmuir*, vol. 15, n°13, 4321-4323.

Niu, Y., Liu, X., et al., (2007), Bioactivity and cytocompatibility of silicon wafers treated by water, *Journal of Biomedical Materials Research Part A*, vol. 83, n°4, 1047-1053.

Oner, D., and McCarthy, T.J., (2000), Ultrahydrophobic Surfaces. Effects of Topography Length Scales on Wettability, *Langmuir*, vol. 16, n°20, 7777-7782.

Orth, R.N., Clark, T., et al., (2003), Avidin-biotin micropatterning methods for biosensor applications, *Biomed. Microdevices*, vol. 5, n°1, 29-34.

Quickenden, T.I., and Irvin, J.A., (1980), The ultraviolet absorption spectrum of liquid water, *The Journal of Chemistry Physics*, vol. 72, n°8, 4416-4428.

Ranella, A., Barberoglou, M., et al., (2010), Tuning cell adhesion by controlling the roughness and wettability of 3D micro/nano silicon structures, *Acta Biomaterialia*, vol. 6, n°7, 2711-2720.

Rice, F., and Reiff, O., (1927), The thermal decomposition of hydrogen peroxide, *The Journal of Physical Chemistry*, vol. 31, n°9, 1352-1356.

Satyapal, S., Park, J., et al., (1989), Dissociation of methanol and ethanol activated by a chemical reaction or by light, *The Journal of Chemistry Physics*, vol. 91, 6873.

Schiffman, A., Nelson Jr, D., et al., (1993), Quantum yields for OH production from 193 and 248 nm photolysis of HNO_3 and H_2O_2, *The Journal of Chemistry Physics*, vol. 98, n°9, 6935-6946.

Stanca, S.E., Ongaro, A., et al., (2005), DNA-templated assembly of nanoscale architectures, *Nanotechnology*, vol. 16, n°9, 1905.

Stanowski, R., Voznyy, O., et al., (2006), Finite element model calculations of temperature profiles in Nd: YAG laser annealed GaAs/AlGaAs quantum well microstructures, *Journal of Laser Micro/Nanoengineering*, vol. 1, 17-21.

Sun, C., Zhao, X.W., et al., (2008), Control of water droplet motion by alteration of roughness gradient on silicon wafer by laser surface treatment, *Thin Solid Films*, vol. 516, n°12, 4059-4063.

Suzuki, S., Nakajima, A., et al., (2004), Elongation and contraction of water droplet during sliding on the silicon surface treated by fluoroalkylsilane, *Surface Science*, vol. 557, n°1-3, L163-L168.

Swift, J.L., and Cramb, D.T., (2008), Nanoparticles as Fluorescence Labels: Is Size All that Matters?, *Biophysical Journal*, vol. 95, n°2, 865-876.

Tanaka, K., Matsuzaki, S., et al., (1993), Photodecomposition of adsorbed methoxy species by UV light and formaldehyde adsorption on silicon(111) studied by XPS and UPS, *The Journal of Chemical Physics*, vol. 97, n°21, 5673-5677.

Tsu, R., Lubben, D., et al., (1991), Mechanisms of excimer laser cleaning of air-exposed Si (100) surfaces studied by Auger electron spectroscopy, electron energy-loss spectroscopy, reflection high-energy electron diffraction, and secondary-ion mass spectrometry, *Journal of Vacuum Science & Technology A: Vacuum, Surfaces, and Films*, vol. 9, n°2, 223-227.

Vaghjiani, G.L., and Ravishankara, A.R., (1990), Photodissociation of H_2O_2 and CH_3OOH at 248 nm and 298 K: Quantum yields for OH, $O(_3P)$ and $H(_2S)$, *The Journal of Chemistry Physics*, vol. 92, n°2, 996-1003.

Vorobyev, A., and Guo, C., (2010), Laser turns silicon superwicking, *Optics Express*, vol. 18, n°7, 6455-6460.

Wenzel, R.N., (1949), Surface Roughness and Contact Angle, *The Journal of Physical Chemistry*, vol. 53, n°9, 1466-1467.

Westwater, J.W., and Santangelo, J.G., (1955), Photographic Study of Boiling, *Industrial&Engineering Chemistry*, vol. 47, n°8, 1605-1610.

Whyman, G., Bormashenko, E., et al., (2008), The rigorous derivation of Young, Cassier-Baxter and Wenzel equations and the analysis of the contact angle hysteresis phenomenon, *Chemical Physics Letters*, vol. 450, n°4-6, 355-359.

Williams, R., and Goodman, A.M., (2003), Wetting of thin layers of SiO_2 by water, *Applied Physics Letters*, vol. 25, n°10, 531-532.

Woodward, I., Schofield, W.C.E., et al., (2003), Super-hydrophobic Surfaces Produced by Plasma Fluorination of Polybutadiene Films, *Langmuir*, vol. 19, n°8, 3432-3438.

Wrobel, J.M., Moffitt, C.E., et al., (1998), XPS study of XeCl excimer-laser-etched InP, *Applied Surface Science*, vol. 127-129, 805-809.

Yoon, T.O., Shin, H.J., et al., (2008), Formation of superhydrophobic poly (dimethysiloxane) by ultrafast laser-induced surface modification, *Optics Express*, vol. 16, n°17, 12715-12725.

Zorba, V., Persano, L., et al., (2006a), Making silicon hydrophobic: wettability control by two-lengthscale simultaneous patterning with femtosecond laser irradiation, *Nanotechnology*, vol. 17, 3234.

Zorba, V., Tzanetakis, P., et al., (2006b), Silicon electron emitters fabricated by ultraviolet laser pulses, *Applied Physics Letters*, vol. 88, 081103.